


3-24-2021

Uranium Fate and Mineral Transformations upon Remediation with Ammonia (NH₃) Gas

Silvina A. Di Pietro
sdipi001@fiu.edu

Follow this and additional works at: <https://digitalcommons.fiu.edu/etd>

 Part of the [Analytical Chemistry Commons](#), [Environmental Chemistry Commons](#), [Inorganic Chemistry Commons](#), and the [Radiochemistry Commons](#)

Recommended Citation

Di Pietro, Silvina A., "Uranium Fate and Mineral Transformations upon Remediation with Ammonia (NH₃) Gas" (2021). *FIU Electronic Theses and Dissertations*. 4645.
<https://digitalcommons.fiu.edu/etd/4645>

This work is brought to you for free and open access by the University Graduate School at FIU Digital Commons. It has been accepted for inclusion in FIU Electronic Theses and Dissertations by an authorized administrator of FIU Digital Commons. For more information, please contact dcc@fiu.edu.

FLORIDA INTERNATIONAL UNIVERSITY

Miami, Florida

URANIUM FATE AND MINERAL TRANSFORMATIONS UPON REMEDIATION
WITH AMMONIA GAS

A dissertation submitted in partial fulfillment of the

requirements for the degree of

DOCTOR OF PHILOSOPHY

in

CHEMISTRY

by

Silvina A. Di Pietro

2021

To: Dean Michael R. Heithaus
College of Arts, Sciences and Education

This dissertation, written by Silvina A. Di Pietro and entitled, Uranium Fate and Mineral Transformations upon Remediation with Ammonia Gas, having been approved in respect to style and intellectual content, is referred to you for judgment.

We have read this dissertation and recommend that it be approved.

Hilary P. Emerson

Yelena Katsenovich

Jim E. Szecsody

Christopher J. Dares

David Chatfield

Yong Cai, Major Professor

Date of Defense: March 24, 2021

The dissertation of Silvina A. Di Pietro is approved.

Dean Michael R. Heithaus
College of Arts, Sciences and Education

Andrés G. Gil
Vice President of Research and Economic Development
and Dean of the University Graduate School

Florida International University, 2021

© Copyright 2021 by Silvana A. Di Pietro

All rights reserved.

DEDICATION

To my parents, Rodolfo Di Pietro and Maria Sugameli Di Pietro. To my brother, Mauro. Without their patience, understanding, support, and love, the completion of this work would not have been possible.

To my nonni. My grandparents fleeing World War II in search of a new life in unknown lands. Their sacrifice taught me that anything is possible, especially in uncertain times. Particularly to my angel nonna, Caterina Sammartanno, who was my #1 fan and believed in the power of education. As my nonno Vincenzo Sugameli would say, “chi va piano va sano e va lontano,” which can be translated to “slow and steady wins the race.”

ACKNOWLEDGMENTS

Writing this section is a dissertation on itself. This monumental milestone would not have been accomplished if it weren't for the various people that have helped me in the past five years and half. And thus, I would like to take the time to formally acknowledge all of the people who assisted me through this very arduous and trying process.

First of all, I thank my major professor and eminent environmental chemistry professor at FIU, Dr. Yong Cai. At a time when one door had closed, Dr. Cai opened the opportunity for graduate school. Dr. Cai believed in my capabilities to pursue a Ph.D. and helped me with identifying a source of funding my studies. I am fortunate to have found a professor who taught me analytical and environmental chemistry and provided me with strong support throughout my undergraduate and graduate studies. The enthusiasm he demonstrated in his lectures and the integrity he showed in his work ignited my curiosity and passion for pursuing research in environmental chemistry. I would also like to thank my Chemistry department committee members, Drs. Christopher Dares and David Chatfield who were more than generous with their expertise and precious time.

Next, I would like to thank my second family: the Applied Research Center (ARC). First and foremost, to our Principal Investigator, Director of the DOE-FIU Science and Technology Workforce Development Program, and my boss Dr. Leonel Lagos. Thank you for 'hiring' me into the best program I could have been part of as a graduate student. I hope I was able to personify your statement: GANAS! I thank you for giving me the space to put in 'muchas ganas' in every ARC opportunity, whether it was a scholarship or travel conference. I extend my gratitude to the rest of ARC staff: Margoth Osco, Claudia Benitez,

and Gloria Dingeldein... thank you for helping me with travel arrangements and financial paperwork. Special thanks to Angelique Lawrence for reviewing my dissertation. Thank you also to former ARC post-docs, Drs. Daria Boglaienko, Kirstin Sockwell, and Shambhu Kandel, for assisting me with instrumental set-ups in OU108 and EC1227 labs. A very special thanks goes to Dr. Ravi Gudavalli who was like a second mentor to me. Thank you for your patience, guidance, and troubleshooting methods.

The DOE fellowship experience would not have been as unique and fun if it weren't for my fellow DOE Fellows. To those who are still part of the DOE Fellows program and those that have graduated (basically all my predecessors, as I am the most senior current DOE fellow 😊), thank you for the smiles, friendship, support, and ideas. Special thanks go to my lab and cubicle mate Dr. Hansell Gonzalez-Raymat, who guided me through the doctoral program, answering countless questions about cumes, environmental-track graduate classes, and uranium chemistry. And last but certainly not least, I would like to thank a very special ARC scientist and committee member Dr. Yelena Katsenovich. I thank Dr. Yelena for giving me the opportunity to be part of her Soil and Groundwater research group. From helping me with laboratory work to Geochemist Workbench modeling support to personal recommendations, Dr. Yelena has always been there for me, especially when she took the role as my ARC mentor. Despite overseeing a team of two undergraduate students, five graduate students, two post-docs, and two research scientists to direct, help, and advise, she still found the time to review documents, such as draft manuscripts and excerpts of my dissertation. I kindly appreciate your profound patience and unwavering support during my graduate studies since day one at ARC.

Furthermore, I wish to express my sincere gratitude to two VIS (“Very Important Scientists”) in my life: Drs. Jim E. Szecsody and Hilary P. Emerson from Pacific Northwest National Laboratory (PNNL). First, I would like to thank Dr. Jim for allowing me to work in his laboratory and use his instruments during my 10-week internship in the summer of 2016 and 2018. But most importantly, I thank Dr. Jim for his invaluable mentorship. Not only was he by my side through the many steps of my Aim 1 mineral dissolution experimental setup and procedures, but he continued to offer intellectual guidance through the data analysis and writing processes (both internship reports and manuscript preparation). I have learned an immense amount of geochemistry, nuclear waste legacy, and DOE/PNNL history by working alongside him, and I will never be able to thank him enough for all of his unwavering support. Your contribution to this project was paramount and for that, I am grateful to have chosen you as my external committee member.

My deepest and most sincere gratitude goes to the very special Dr. Hilary P. Emerson without whom this work would not have been possible. Working alongside her, I have developed several skills which I cannot explain in this small paragraph. Indeed, words cannot describe how grateful I am to have been able to pursue my Ph.D. while being a graduate research assistant at ARC under her advisement. I thank you for spending countless hours in helping me with every single aspect of my training as a scientist. I thank you for enormously helping me in my technical writing capabilities, especially when it comes to manuscript writing. I thank you for constantly challenging me to be the best researcher and independent thinker I can possibly be. From assisting me with my CV/figures and calculations to writing letters of recommendation to laboratory work to providing technical help, Dr. Hilary has been tirelessly by my side through every step of

my graduate research career. Over the past five and half years, Dr. Hilary has not only challenged me to become a better scientist, but also a better person. Dr. Hilary is inspiring and unparalleled as a researcher, and transitioning from her mentee to her colleague has been a tremendous honor.

Lastly, I would like to thank our national laboratories collaborators. From PNNL, I would like to thank Tom Resch and Dr. Sarah Saslow for laboratory guidance, and a very special mention goes to Dr. Nikolla P. Qafoku for his expertise, manuscript revision, and analytical support. From Lawrence Livermore National Laboratory (LLNL), I would like to thank Drs. Maxwell Marple, April Sawvel, and Harris Mason for allowing me to use their Nuclear Magnetic Resonance (NMR) instrumentation and accepting to be collaborators to my second publication, and particularly to Dr. Mavrik Zavarin for providing NMR financial support and endless assistance during my Glenn T. Seaborg internship experience.

I also wish to acknowledge two fundamental mentors that shaped my academic career prior to graduate school. I would like to formally thank my very first mentor throughout my college career, Dr. Lulrick Balzora. Dr. Balzora taught me to maximize like a true Honors Student Committee (HSC) member would. He believed in me and supported me in every scholarship application, tennis tournament, and when I had to miss his IDH Honors class for 10 days. Dr. Balzora pushed me when I did not want to be pushed. Most importantly, however, Dr. Balzora taught me to question everything, a very powerful skill any good scientist should acquire. Secondly, major thanks to my very first chemistry teacher, Dr. Iris Payan. Dr. Payan saw something in me that I was unable to see in myself. She is the one person who defined my choice to pursue a career in chemistry. Although I

always enjoyed my middle and high school science classes, Dr. Payan piqued my interest in chemistry. Not only was she the first scientist I was ever exposed to, but also she made learning the subject extremely fun. Her sense of humor and undivided willingness to answer my inquisitive questions made me fall in love and form a bond (no pun intended) with chemistry.

I would also like to greatly acknowledge all fellow chemistry graduate students and now Drs., Ingrid Lehman-Andino, María Eugenia De Cabrera, Marcela Jaramillo, and Valery Liamtsau, Class of 2015. Thank you for leading a hand when I needed help, making the time to be my study buddies, or providing a shoulder to cry on when things did not go as planned.

My deepest appreciation is also extended to all my friends: childhood, high school, undergraduate buddies who were incredibly supportive. They have all made this journey so much more bearable and enjoyable, particularly when I would Facetime, Whatsapp call, or simply say hi to my amazing childhood friends Denisse Brödl, Rochi Salado, and Clara Bertucci (cuánto las extraño!). Thanks for believing in me unconditionally, even at times where I did not believe in myself, especially my friends Anna Sobczyszyn and former roommate Erika Collante whose encouragement and moral support made this experience that much easier. Last but certainly not least, I would like to thank my family both in Argentina and Italy for their unconditional love, unwavering and never-ending support in everything I do.

♡ THANK YOU. GRAZIE. GRACIAS. ♡

-Silvi

This research was supported by the DOE-FIU Science and Technology Workforce Development Program, sponsored and funded by the U.S. Department of Energy, Office of Environmental Management (DOE-EM), under Cooperative Agreement #DE-EM0005213.

ABSTRACT OF THE DISSERTATION
URANIUM FATE AND MINERAL TRANSFORMATIONS UPON REMEDIATION
WITH AMMONIA GAS

by

Silvina A. Di Pietro

Florida International University, 2021

Miami, Florida

Professor Yong Cai, Major Professor

The fission of uranium (U) for plutonium production was a major activity at the U.S. Department of Energy's (DOE) Hanford Site in Washington State during World War II and Cold War. This endeavor resulted in the generation of over two million liters of high-level radioactive waste, most of which still remains in 177 underground storage tanks. Due to the improper storage and aging of these tanks in addition to other waste releases across the Site, approximately 200,000 kg of U have been released into the vadose zone. The objective of this study was to determine whether the application of the reactive gas, ammonia (NH₃), could be effective for sequestration of U in vadose zone conditions such as those at the Hanford Site.

The goal of this novel technique is to elevate the pH and induce mineral dissolution. As the NH₃ dissipates and the pH returns to neutral conditions, adsorption and co-precipitation processes are expected to immobilize U. The targeted mineral dissolution and secondary precipitate formation processes are not well understood at these conditions including their impact on U behavior.

The experimental results suggest that, as a result of pH manipulation with NH_3 , investigated minerals (illite, muscovite, and montmorillonite) undergo incongruent dissolution. In addition, several analytical techniques were applied to compare ammonia-treated and circumneutral pH-treated minerals. Characterization studies showed that physicochemical transformations occurred, such as recrystallization of mineral edges and particle size and surface area increase. These behaviors are indicative of secondary precipitate formation, which was confirmed by comparisons of Al:Si ratios in solution and the solid phase, suggesting U sequestration. Furthermore, U distribution calculations between the solid and liquid phases indicate a significant increase in solid phase U with treatment, while geochemical software modeling provided a way to predict U species and secondary mineral phases upon alkaline treatment.

These findings show the scientific community that NH_3 gas injection is an effective technology to decrease the mobility of the uranyl ion. This technology may be particularly valuable to unsaturated areas where contamination remedies are needed *in situ* without the addition of liquid amendments.

TABLE OF CONTENTS

CHAPTER	PAGE
1 CHAPTER 1: INTRODUCTION	2
1.1 Uranium History	2
1.2 Uranium Chemistry.....	4
1.2.1 Environmental Chemistry of Uranium.....	6
1.2.2 Occurrence and Sources of Uranium	12
1.2.3 Immobilization of Uranium and Apparent Partitioning Coefficient K_d	15
1.3 Uranium Toxicity	19
1.4 DOE Hanford Site Case Study.....	23
1.5 Hanford Site Mineralogy	26
1.5.1 Phyllosilicates	28
1.5.2 Uranium Phases at the Hanford Site	31
1.6 Ammonia (NH ₃) Gas Treatment	33
1.6.1 Ammonia Background and Speciation	34
1.6.2 Geochemical and Physical Processes.....	37
1.6.3 Summary of the Ammonia Gas Reaction with Sediments.....	37
1.7 Aims and Research Gaps	38
1.7.1 Aim 1: Mineral Dissolution and Precipitation Processes under Highly Alkaline Conditions	39
1.7.2 Aim 2: Characterization of Physicochemical Mineral Phase Alterations with Treatment	40
1.7.3 Aim 3: Determination of the Dominant Solid Phases and the Stability of U	42
1.8 Research Hypothesis.....	43
1.9 References.....	44
2 CHAPTER 2: MINERAL DISSOLUTION AND PRECIPITATION PROCESSES UNDER HIGHLY ALKALINE CONDITIONS.....	55
2.1 Abstract.....	55
2.2 Introduction.....	56
2.3 Experimental Methodology	61
2.3.1 Materials	61
2.3.2 Mineral Characterization	62

2.4	Results.....	65
2.4.1	Mineral Dissolution Based on Aqueous Si.....	65
2.4.2	Evidence for Incongruent Dissolution Under Alkaline Treatments	70
2.4.3	Effect of Alkaline Treatments.....	75
2.4.4	Effect of Redox and pH Conditions.....	79
2.5	Discussion.....	82
2.6	Conclusion	84
2.7	References.....	85
3	CHAPTER 3: CHARACTERIZATION OF PHYSICOCHEMICAL MINERAL PHASE ALTERATIONS WITH TREATMENT.....	92
3.1	Abstract.....	92
3.2	Introduction.....	93
3.3	Experimental Methodology	98
3.3.1	Mineral Characterization	98
3.3.2	Materials	106
3.3.3	Batch Protocol.....	106
3.4	Results and Discussion	107
3.4.1	Characterization of Illite Prior to Treatment.....	107
3.4.2	Illite Physical Alterations.....	112
3.4.3	Effect of Ammonia Intercalation into Mineral's Interlayer.....	116
3.4.4	Evidence of Incongruent Dissolution Phenomena.....	122
3.4.5	Characterization of Mineral Transformations.....	125
3.5	Conclusion	131
3.6	References.....	132
4	CHAPTER 4: DETERMINATION OF SOLID PHASES SPECIATION AND MOBILITY OF URANIUM.....	143
4.1	Abstract.....	143
4.2	Introduction.....	144
4.3	Experimental Methodology	147
4.3.1	Materials	147
4.3.2	Batch Protocol.....	148
4.3.3	Mineral Characterization	154
4.3.4	Geochemical Speciation Modeling.....	159

4.4	Results and Discussion	160
4.4.1	Mineral Transformation and U Interaction Mechanism	160
4.4.2	Uranium K_d Values for Phyllosilicate Minerals and Hanford Site Sediments.....	173
4.4.3	Predicting Solid Phases upon Ammonia Gas Technology using Geochemist Workbench Modeling	177
4.5	Conclusions.....	181
4.6	References.....	183
5	CHAPTER 5: GENERAL CONCLUSIONS	191
5.1	Conclusion Summary.....	191
5.2	Future Work	193
A.	APPENDIX	195
	VITA.....	228

LIST OF TABLES

TABLE	PAGE
Table 1.1. Thermodynamic data, $\log K_{sp}^\circ$ at standard state, $I=0$ and 25°C , for solid U(IV) and U(VI) (Fujiwara et al., 2005; Grenthe et al., 1992; Neck & Kim, 2001).....	9
Table 1.2. Typical natural abundance of U in the Earth’s crust (Langmuir, 1997).....	12
Table 1.3. Hanford Site bulk fraction (in weight %) minerals.....	28
Table 1.4. General characteristics of the aluminosilicates clay minerals relevant Hanford Site (Moore & Reynolds Jr, 1989; Nesse, 2012).....	31
Table 3.1. PH readings post 5% $\text{NH}_3/95\% \text{N}_2$ injection (~30 d) and post aeration step (24 h). Note: standard deviations are based on triplicate measurements.....	104
Table 3.2. Theoretical Ratios and Cation Exchange Capacity (CEC) for Pure Minerals Illite and Montmorillonite Pure Minerals	104
Table 3.3. Chemical Composition of illite (SWy-1, Clay Minerals Society, Cambrian Hole, Silver Hill Mount) and montmorillonite (Clay Mineral Society, Crook County, Wyoming) used, in oxide % wt based on SEM-EDS analyses of minerals prior to treatments. Note: standard deviations are based on the average composition of nine data points.....	105
Table 3.4. BET surface area measurements (average and standard deviation based on triplicate measurements) for illite mineral exposed to ammonia (pH 12) and aeration (pH 8) treatments	110
Table 3.5. Descriptive statistics (ANOVA: two-factor with replication) and particle size measurements of illite ammonia- and aerated- treated samples taken from magnification 1000x SEM images.....	115
Table 3.6. FTIR % transmission ratios of Al-Al-OH/Si-O-Si peak heights (at 913 cm^{-1} and 1022 cm^{-1} , respectively) for illite mineral.....	125
Table 3.7. <i>t</i> -Test (average, variance, observation number and <i>p</i> value) for Al/Si illite ratios (pH 12 and 8) assuming unequal variances	125
Table 4.1. SGW composition for aging of mica minerals and Hanford Site sediments batch protocol (7.2 mM total ionic strength).	150
Table 4.2. Summary of batch initial conditions for Experiments 1, 2, and 3	151

Table 4.3. Summary of U loading ($\mu\text{g/g}$) for Experiments 1, 2, and 3 for all investigated solid phases at both ammonia and aerated treatments	151
Table 4.4. XANES U L_{III} -Edge Linear Combination Analysis (LCA) Results in Percentages for Calcite NH_3 -gas, Illite NH_3 -gas, and Illite-aerated treated samples sent to Argonne National Laboratory	165
Table 4.5. Summary SEM-EDS showing Al/Si ratios for U-spiked, ammonia and aerated sample experiments	172
Table 4.6. Uranyl mineral phases used in the Geochemist Workbench [®] speciation modeling	180
Table A.1. Chemical Analysis (CEC and BET) and Theoretical Ratios for Minerals ...	197
Table A.2. Pseudo second order dissolution rates as measured by monitoring of aqueous Si over time (rate law, standard deviation from linear regression, and R^2 values) for the minerals investigated (illite, muscovite, and montmorillonite) in 0.01 M NaOH and 3.1 M NH_4OH alkaline solutions under anaerobic and aerobic conditions ..	197
Table A.3. Pseudo first order dissolution rates as measured by monitoring of aqueous Al over time (rate law, standard deviation from linear regression, and R^2 values) for the minerals investigated (illite, muscovite, and montmorillonite) in 0.01 M NaOH and 3.1 M NH_4OH alkaline solutions under anaerobic and aerobic conditions	198
Table A.4. Pseudo second order dissolution rates as measured by monitoring of aqueous Al over time (rate law, standard deviation from linear regression, and R^2 values) for the minerals investigated (illite, muscovite, and montmorillonite) in 0.01 M NaOH and 3.1 M NH_4OH alkaline solutions under anaerobic and aerobic conditions ..	198
Table A.5. SGW composition for batch protocol (7.2 mM total ionic strength)	207
Table A.6. Indexed absorption bands for illite (Clay Minerals Society, Cambrian Hole, Silver Hill Mount) FTIR spectra.....	208
Table A.7. Summary of descriptive statistics (ANOVA: Two-Factor with Replication) and particle size measurements of illite ammonia- and aerated- treated samples taken from magnification 1000x SEM images	213
Table A.8. Indexed absorption bands for montmorillonite (Clay Minerals Society, Crook County, Wyoming) FTIR spectra.	215
Table A.9. Phyllosilicate minerals and Hanford sediments (~ 25 g/L) pH and ORP readings during 5% $\text{NH}_3/95\%$ N_2 and aeration treatments	219
Table A.10. Hanford Sediment XRF-EDS Molar Quantity (normalized to MW) and Al/Si ratios for Experiment 2	220

Table A.11. X-ray powder diffraction patterns for illite (IMt-2, Cambrian Hole, Silver Hill Mount, Clay Mineral Society) comparing *d*-spacing (in Å) and 2Theta (°) values for theoretical (obtained from the listed reference) and experimental measurements for untreated (control) and treatment (NH₃ and aerated at pH 12 and 8), respectively 224

Table A.12. X-ray powder diffraction patterns for montmorillonite (SWy-2, Crook County, Wyoming, Clay Mineral Society) comparing *d*-spacing (in Å) and 2Theta (°) values for theoretical (obtained from the listed reference) and experimental measurements for untreated (control) and treatment (NH₃ and aerated at pH 12 and 8), respectively 225

LIST OF FIGURES

FIGURE	PAGE
Figure 1.1. Nuclear fission chain reaction in ^{235}U (Ling et al., 2016).	5
Figure 1.2. The three types of uranyl ion. U^{6+} cations are shown in yellow, potential anions are shown in white, and oxygen atoms are shown in blue. Drawing made by <i>Chem 3D</i> software (Burns et al., 1996).....	7
Figure 1.3. Pourbaix diagram for a closed system for U concentration at 10^{-8} M, 25°C , and 1.0 atm pressure. Note: diagram is carbonate-free.	8
Figure 1.4. Uranium speciation at variable pH and U concentration of $1.0\ \mu\text{mol/L}$ in synthetic groundwater (SGW) with Geochemist’s WorkBench® modeling software using Thermo-Minteq database in the system open to the atmosphere. Note: only species at $> 10^{-10}$ M are shown (Katsenovich et al., 2018).	11
Figure 1.5. Overview of a schematic nuclear fuel cycle (Karpas, 2014).....	14
Figure 1.6. Hypothetical equilibrium contaminant partitioning curve for a generic sorbing contaminant (i.e., U). Note: the system is closed and the curve is determined by adsorption at low concentration and precipitation at high concentration (Zachara et al., 2007).	17
Figure 1.7. Mechanisms by which U mobility can be retarded in the surface and subsurface geologic environment. A) Precipitation of U(VI) and U(IV) phases. B) U microbial uptake. C) Sorption of U by organic or inorganic matter such as humic materials and Fe oxides, respectively. D) Immobilization of U by clay and metal oxide coatings. E) Under reducing conditions, the formation of surface rinds of U(IV) on U(VI) minerals can also limit U mobility because U(IV) solids are less soluble. F) Co-precipitation of U with amorphous and crystalline host minerals may limit U mobility (Duff et al., 2002).....	19
Figure 1.8. Geographical location and principal facilities at the Hanford Site in Washington State (DOE, 2020).	24
Figure 1.9. Hanford Site’s 177 waste tanks. A) Schematic of Hanford’s single-shell tanks, depicting the sludge and saltcake in yellow. B) Image showing the mixture of liquids, solids, and sludges inside the storage tanks. C) Hanford tank showing leakage (white surrounding) (Gallucci, 2020).	26
Figure 1.10. Phyllosilicate minerals investigated in this study: illite, muscovite, and montmorillonite.....	29
Figure 1.11. Octahedral (O) and tetrahedral (T) sheets in layered phyllosilicate minerals (Nesse, 2012).....	30

Figure 1.12. Crystallography structure for phyllosilicates: a) mica and b) smectite family minerals created via <i>VESTA</i> software program.	30
Figure 1.13. Conceptual diagram of U contamination in the Hanford 200 Area vadose zone with respect to depth (diagram) and mineral fraction and percentage (table) (Szecsody et al., 2010).	33
Figure 1.14. Waste discharges to the Hanford Site vadose zone (Gee et al., 2007).	34
Figure 1.15. Ammonium-ammonia speciation as a function of pH for a closed system (a), where the total initial concentration (3.12 mol/L) is equal to ammonia solubility at 25 °C in pure water and an open system (b), where ammonia gas is constantly mixing with liquid phase and assumes equilibrium highlighting the maximum solubility of these species.	36
Figure 1.16. Overview of the processes that occur with injection of ammonia vapor into an unsaturated, U-contaminated sediment (Zhong et al., 2015).	38
Figure 2.1. Aqueous Si, in $\mu\text{M/g}$, with time for batch experiments with 33 g/L minerals, including: montmorillonite (triangles), muscovite (squares), and illite (circles) with exposure to 3.1 M NH_4OH (closed black) and 0.01 M NaOH (open gray) under aerobic (top) and anaerobic (bottom) conditions. Note: error is based on analysis of triplicate samples.	68
Figure 2.2. Aqueous Al, in $\mu\text{M/g}$, with time for batch experiments with 33 g/L minerals, including: montmorillonite (triangles), muscovite (squares), and illite (circles) with exposure to 3.1 M NH_4OH (closed black) and 0.01 M NaOH (open gray) under aerobic (top) and anaerobic (bottom) conditions. Note: error is based on analysis of triplicate samples.	71
Figure 2.3. Aqueous Si (black) and Al (gray), in mol/L after reaction of 33 g/L suspension of minerals [illite (top), muscovite (middle) and montmorillonite (bottom)] over time (24-, 240-, 745- and 1440-h) with 3.1 M NH_4OH under anaerobic conditions, dashed lines represent congruent Al dissolution based on measured Si in the aqueous phase.	72
Figure 2.4. Comparison of Si removal during alkaline treatments (3.1 M NH_4OH – black and 0.01 M NaOH – gray) for minerals (33 g/L) illite (top), muscovite (middle) and montmorillonite (bottom) under aerobic condition. Note: error bars are based on analysis of triplicate samples.	77
Figure 2.5. ORP, in mV, measurements for investigated minerals under anaerobic (red) and aerobic (light blue) conditions exposed to alkaline treatments (NaOH – pattern and NH_4OH – solid) after two months of reaction. Note: values printed above and below bars correspond to pH measurements and error bars are based on analysis of triplicate samples.	80

Figure 2.6. Total Fe dissolution with variable redox conditions for illite (top) and montmorillonite (below) across all sampling events (24-, 240-, 745-, 1440 h) for NH ₄ OH (solid) and NaOH (pattern) alkaline treatment with color darkening with time. Note*: missing measurements for illite mineral at 745 h sampling were below limit of detection; error based on analysis of triplicate samples.....	83
Figure 3.1. X-ray diffraction pattern of illite clay. I, illite; K, kaolinite; Q, quartz; M, microcline; C, calcite.	110
Figure 3.2. Infrared spectra of illite mineral (untreated in black) (a) prior to 95% N ₂ /5% NH ₃ gas treatment, during gas treatment at pH 12 (light blue) and post treatment (darker blue) for 30-day contact time in SGW solution (7.2 mM) at pH 8 and (b) during 95% N ₂ /5% NH ₃ gas treatment at pH 12 (dark blue) and aerated treated at pH 8 (light blue) in comparison with untreated illite (black) showing the Si-O-Si and Al-Al-OH bands at ~ 1000 and ~ 915 cm ⁻¹ (dotted circle).	111
Figure 3.3. SEM images of (a) control untreated illite mineral taken in backscatter mode, (b) illite treated with 95% N ₂ /5% NH ₃ gas treatment at pH 12, and (c) post treatment in secondary mode for 30-day contact time in SGW solution (7.2 mM).....	115
Figure 3.4. Infrared spectra of aluminosilicate minerals (illite-blue and montmorillonite-red) showing (a) the effect of ammonium intercalation as evidenced by the stretching vibrations of N-H groups at ~ 3100 cm ⁻¹ and (b) the bending vibrational modes of N-H groups at ~ 1404 cm ⁻¹ prior to 95% N ₂ /5% NH ₃ gas treatment (control, darker) and post treatment (lighter) for 30-day contact time in SGW solution (7.2 mM) at pH 12.....	120
Figure 3.5. Selected area electron diffraction (SAED) image patterns of the crystalline aluminosilicate minerals (illite, top; montmorillonite, bottom) for untreated minerals (a and d), treated with 95% N ₂ /5% NH ₃ gas for 30-day contact time in SGW solution (7.2 mM) at pH 12 (b and e) and aerated-treated at pH 8 (c and f). Bottom right show inset micrographs of Transmission Electron Microscope (TEM) images at 100 and 200 nm resolution.....	121
Figure 3.6. ²⁹ Si NMR for illite control (black), ammonia-treated (orange), and aerated (green). Shapes above spectra represent where within the illite phyllosilicate structure are splitting and shifting (ppm). Note: “T” and “O” are representative of tetrahedral and octahedral layers, respectively.	129
Figure 3.7. Plot of the Q2, Q3, and Q4 content (in %) according to ²⁹ Si NMR spectroscopy for illite (untreated), ammonia-treated (orange), and aerated (green). Note: the bottom image shows the extent to Si polymerization according to Q orientation.	130
Figure 3.8. ²⁷ Al MAS (y-axis) NMR for illite control (black), ammonia-treated (orange), and aerated (green).	131

Figure 4.1. EMPA micrographs and corresponding elemental maps for U and Fe showing a correlation on illite particle (top) and particles (bottom) post-ammonia (5% NH ₃ /95% N ₂) and aerated treatments in Experiment 3.....	162
Figure 4.2. Uranium L _{III} -edge XANES spectra shown in black for (a) Illite-NH ₃ at pH 12, (b) Illite-aerated, and (c) calcite-NH ₃ at pH 8 in Experiment 1. Fraction-adjusted standards contributing to total fit shown for UO ₂ (gray) and UO ₃ (blue), and total U fit (red).....	165
Figure 4.3. XRD patterns for (a) illite, (b) muscovite, and (c) montmorillonite showing (blue circle) calcite (CaCO ₃) formation peaks during ammonia (orange) and aeration (purple) treatments	169
Figure 4.4. EMPA micrographs and corresponding elemental maps for Al and Si showing a correlation on illite particle (top) and particles (bottom) post-ammonia (5% NH ₃ /95% N ₂) and aerated treatments in Experiment 3.....	172
Figure 4.5. Partitioning coefficient K _d (mL/g) U measurements of phyllosilicate minerals and Hanford Site sediments upon ammonia (gray) or aerated (orange) treatment during three-day (pattern) or six-month (solid) contact time for Experiment 3. Note*: there was no measurement recorded for illite 3-day, ammonia treatment.	176
Figure 4.6. Partitioning coefficient K _d (mL/g) U measurements of illite (blue), muscovite (red), montmorillonite (green) and Hanford Site sediment (orange) minerals upon ammonia (left) or aerated (right) treatment during three-day (pattern) or six-month (solid) contact time for Experiment 3. Note*: there was no measurement recorded for illite 3-day, ammonia treatment.	177
Figure 4.7. Saturation index of U-bearing mineral phases diagram plotted as a function of pH for 5.0% of NH ₃ [3.1 mol/L NH _{3(aq)}] in SGW.....	180
Figure 4.8. Saturation index of Ca-bearing mineral phases diagram plotted as a function of pH for 5.0% of NH ₃ [3.1 mol/L NH _{3(aq)}] in SGW.....	181
Figure A.1. XRD patterns for illite (green, top), muscovite (red, middle) and montmorillonite (blue, bottom). Note: major 2θ peak values are listed with reference to best fit PDF card.	196
Figure A.2. The proposed mechanism of dissolution for phyllosilicates in alkaline solutions in three steps: a) individual Al atoms from the solid phase react with OH ⁻ ions; b) silicate tetrahedra at the surface depart intact, and c) the products from a) and b) steps react in solution. At high pH, aluminosilicate formation such as those produced in d) can precipitate, according to our system (Crundwell, 2014).	197
Figure A.3. Aqueous Si (black) and Al (gray), in mol/L after reaction of 33 g/L suspension of minerals [illite (top), muscovite (middle) and montmorillonite (bottom)]	

over time (24-, 240-, 745- and 1440-h) with 0.01 M NaOH under anaerobic conditions. Dashed lines represent theoretical Al dissolution based on triplicate measurements of Si in the aqueous phase.....	199
Figure A.4. Aqueous Si (black) and Al (gray), in mol/L after reaction of 33 g/L suspension of minerals [illite (top), muscovite (middle) and montmorillonite (bottom)] over time (24-, 240-, 745- and 1440-h) with 3.1 M NH ₄ OH under aerobic conditions. Dashed lines represent theoretical Al dissolution based on triplicate measurements of Si in the aqueous phase.	200
Figure A.5. Aqueous Si (black) and Al (gray), in mol/L after reaction of 33 g/L suspension of minerals [illite (top), muscovite (middle) and montmorillonite (bottom)] over time (24-, 240-, 745- and 1440-h) with 0.01 M NaOH under aerobic conditions. Dashed lines represent theoretical Al dissolution based on triplicate measurements of Si in the aqueous phase.	201
Figure A.6. Comparison of aqueous Al (orange) or Si (green), in μM/g, for minerals investigated at 24 h (solid) and 1440 h (pattern) contact-time via NaOH or NH ₄ OH treatment under aerobic (top) or anaerobic (bottom) conditions.	202
Figure A.7. Comparison of Si removal during alkaline treatments (3.1 M NH ₄ OH – black and 0.01 M NaOH – gray) for minerals (33g/L) illite (top), muscovite (middle) and montmorillonite (bottom) under anaerobic condition. Note: error bars are based on analysis of triplicate samples; montmorillonite at 240 h was unable to be sampled due to artifact problems.	203
Figure A.8. pH measurements as a function of time for investigated minerals exposed to alkaline treatments (NaOH - gray and NH ₄ OH - black) under aerobic (top) and anaerobic conditions (bottom) for control (diamonds), illite (circles), muscovite (square), and montmorillonite (triangles).	204
Figure A.9. Concept map identifying the differences and similarities between the various solid phase characterization techniques completed throughout this dissertation. Note: highlighted in yellow show the analytical techniques confirming incongruent dissolution phenomena and purple arrow show complementary characterization techniques.	205
Figure A.10. Concept map identifying the differences between Scanning (SEM) and Transmission (TEM) electron microscopy.	206
Figure A.11. X-ray diffraction pattern of untreated (control) illite clay (Silver Hill). ...	207
Figure A.12. SEM micrographs of untreated (left column) and treated illite (ammonia- middle column; aerated-right column) at various magnifications (90x, 150x, 200x, 300x, 500x, 4300x, and 10Kx).....	212

Figure A.13. X-ray diffraction pattern of montmorillonite clay (PDF: 01-076-8291). M, montmorillonite; Mi, mica; Q(c), quartz cristobalite; Mc, microcline; Mu, muscovite.	214
Figure A.14. Transmission Electron Microscope (TEM) micrographs of aluminosilicate minerals (illite, top; montmorillonite, bottom) untreated (a and d) and treated with 95% N ₂ /5% NH ₃ gas for 30-day contact time in SGW solution (7.2 mM) at pH 12 (b and e) and 8 (c and f), ammonia- and aerated-treated, respectively.	217
Figure A.15. Uranium L _{III} -edge XANES spectra of the reference compounds used for XANES LCA fitting. LCF fit shown in red for UO ₂ and in black for UO ₃	219
Figure A.16. EMPA micrograph and corresponding elemental maps for U and Fe showing a correlation on illite particles post-ammonia (5% NH ₃ /95% N ₂) and aerated treatment in Experiment 3.	220
Figure A.17. EMPA backscatter micrograph and corresponding elemental maps for Al, U, Si, and Fe showing a correlation on illite particle post-ammonia (5% NH ₃ /95% N ₂) and aerated treatment in Experiment 3.	221
Figure A.18. EMPA backscatter micrograph and corresponding elemental maps for Al, Si, and Fe showing a correlation on illite particles post-ammonia (5% NH ₃ /95% N ₂) and aerated treatment in Experiment 3.	222
Figure A.19. EMPA micrographs and corresponding elemental maps for Al and Si showing a correlation on illite particles post-ammonia (5% NH ₃ /95% N ₂) and aerated treatment in Experiment 3.	223
Figure A.20. U loading (µg/g) of phyllosilicate minerals and Hanford Site sediments upon ammonia (green) or aerated (red) treatment during three-day (pattern) or six- month (solid) contact time for Experiment 3. Notes: surface area in m ² /g represented next to the solid phase; *: there was no measurement recorded for illite 3-day, ammonia treatment.	227

ABBREVIATION AND ACRONYMS

ABS	absorbance
AFM	atomic force microscopy
AMD	acid mine drainage
ATM	one atmosphere of pressure
BET	Brunauer–Emmet–Teller
CEC	cation exchange capacity
DIW	deionized water
DOE	Department of Energy
EDS	energy dispersive X-ray spectroscopy
E_h	redox potential
EMPA	electron microprobe analysis
Fe	iron
FTIR	Fourier-transform infrared spectroscopy
GWB	Geochemist Workbench [®]
ICP-OES	inductively coupled plasma optical emission mass spectrometry
ICP-MS	inductively coupled plasma mass spectrometry
ISL	in-situ leaching
K_d	apparent partitioning coefficient
KPA	kinetic phosphorescence analyzer
nano-SIMS	nanoscale secondary ion mass spectrometry
NaOH	sodium hydroxide

NH ₃	ammonia
NH ₄ OH	ammonium hydroxide
NMR	nuclear magnetic resonance
ORP	oxidation-reduction potential
PNNL	Pacific Northwest National Laboratory
ppb	parts per billion
ppm	parts per million
PZC	point of zero charge
SI or Ω	saturation index
SAED	selected area electron diffraction
SEM	scanning electron microscopy
SGW	synthetic groundwater
STEM	scanning transmission electron microscopy
STW	simulated tank waste
U	uranium
U(IV)	uranium (IV)
U(VI)	uranium (VI)
UO ₂ ²⁺ _(aq)	aqueous uranyl ion
TEM	transmission electron microscope
XANES	X-ray absorption near edge spectroscopy
XRD	X-ray diffraction
Z	atomic number

CHAPTER I

Introduction

1 CHAPTER 1: INTRODUCTION

1.1 Uranium History

The discovery of the element uranium (U) is credited to German chemist Martin Heinrich Klaproth. In 1789, Klaproth dissolved the mineral pitchblende in nitric acid (HNO_3). According to early mineralogists, pitchblende was thought to be an ore of zinc (Zn) and iron (Fe). However, after a greenish-yellow crystal precipitated, it was concluded that the salt contained a new element. In honor of the newly discovered planet Uranus in 1781 by the English astronomer Herschel, Klaproth proposed the name “uranium” (Edelstein et al., 2011).

Although the element had been included in Mendeleev’s periodic table, the metallic U could not be isolated for several decades. It was not until 1841 when French chemist Eugène-Melchior Péligot succeeded in producing a powder of pure U (Kragh, 2018). As a result, it was concluded that Klaproth had isolated the oxide uraninite (UO_2), the primary composition of pitchblende. Péligot may thus be properly considered the founder of modern U chemistry as he was the first to use the word uranyl to describe the U structure in the greenish-yellow salt crystals (Edelstein et al., 2011).

Within the first century after its discovery, the principal use of U was as a colorant for ceramics and manufacture of yellow-green fluorescent glasses. Such usage quickly dissipated when French engineer and physicist Antoine-Henri Becquerel demonstrated that U and its salts emitted penetrating rays (Fry & Thoennessen, 2013). In 1896, Becquerel proved its radioactive character by developing images of U crystals in photographic plates of non-phosphorescent U salts wrapped in black paper. Although Becquerel had exposed the material to sunlight, the experiment was delayed because the Parisian skies were

overcast. To his surprise, the images were clear, distinct, and definite. Thus, Becquerel concluded that U-containing materials emit spontaneous radiation without any need for excitation by an external energy source such as the Sun (The Health Physics Society, 2020).

The newly discovered topic of penetrating “uranic” rays seemed most interesting to doctoral student Marie Curie and her husband Pierre Curie, a professor at the Ecole Municipale de Physique et de Chimie. Under Becquerel’s mentorship, the couple found that the same material Becquerel used for his experiment, pitchblende, was four times as active as metallic U (Mould, 1999). Thus, they concluded it contained other elements present at trace levels. After a series of chemical separations, they managed to extract two previously unknown elements, polonium (Po) and radium (Ra), both more radioactive than U. In 1903, the collaboration allowed Becquerel and the Curies to share the Nobel Prize in Physics for their work on radioactivity (NobelPrize, 2020).

The crucial importance of U was not established until 1938 when German chemists Otto Hahn and Fritz Strassman discovered nuclear fission (Grenthe et al., 1992). Inspired by the work of Italian physicist Enrico Fermi, the team irradiated U with neutrons. Expecting Fermi's radioactive products to be beyond U (heaviest naturally occurring element in the periodic table at the time), they unexpectedly produced barium (Ba), a significantly lighter element than U. News of the splitting of the atom rapidly reached scientists in the United States *a priori* the outbreak of World War II. The implications of such discovery led to study possible military developments that ultimately resulted in the end of World War II. Since then, U has occupied a central position in the field of nuclear energy.

1.2 Uranium Chemistry

Uranium (U) is one of nature's most intriguing and chemically complex elements. In fact, U is the most studied actinide and heaviest naturally occurring element found in significant quantities. With an atomic number (Z) of 92, U is a heavy, silver-white, flexible, weakly radioactive, and strongly electropositive metal exhibiting poor electrical conductivity. Sixty-five percent higher than lead (Pb), U has a density of 19.05 g/cm^3 (Závodská et al., 2008). Uranium has very interesting physical properties. In the presence of air, water, and oxygen (O_2), U powder can spontaneously burn at room temperature. At a $\sim 25^\circ\text{C}$ temperature, U is also malleable and as the temperature increases, it behaves as a plastic material. When the temperature exceeds 200°C , the powder may self-ignite when exposed to atmospheric gases such as carbon dioxide (CO_2) or nitrogen (N_2) (Edelstein et al., 2011). Then, when reaching 1132°C , the powdered metal melts.

Uranium is an easily oxidizable element; thus, U mainly occurs in oxidized forms. Like electropositive elements aluminum (Al) and magnesium (Mg), U needs to be reduced by hydrogen (H_2) to create its metallic form (Edelstein et al., 2011). In its elemental state, the metal reacts with almost all non-metallic elements. The reactivity of the metal-non-metal interaction increments with increasing temperature.

Along with its metallic properties, all isotopes of U are radioactive. Twenty-three U isotopes ($Z = 217 - 242$) have been identified, with $^{220,221}\text{U}$ and ^{241}U yet to be observed. Proving the complexity of U, a 2007 study regarding neutron-rich nuclei (the *Hartree-Fock-Bogoliubov-14* method model) concluded that about 80 additional U isotopes could exist (Fry & Thoennessen, 2013; Goriely et al., 2007). However, the U isotopes found in the environment are ^{238}U (99.3% abundance), ^{235}U (0.7% abundance), and ^{234}U (0.006%

abundance), with half-lives of 4.46 billion years, 704 million years and 245,000 years, respectively (Edelstein et al., 2011; Grenthe et al., 1992; Nilsson, 2016). Among the U isotopes that occur naturally in any significant abundance, ^{235}U is special. Discovered in 1935 by Canadian-American physicist Arthur Dempster using mass spectrometry (Nilsson, 2016), ^{235}U isotope is unique in that it has the ability to be split into two atoms (fission fragments) following impact with a slowly moving neutron while releasing energy given by Eq. 1.1 and Figure 1.1 (Edelstein et al., 2011; Langmuir, 1997).

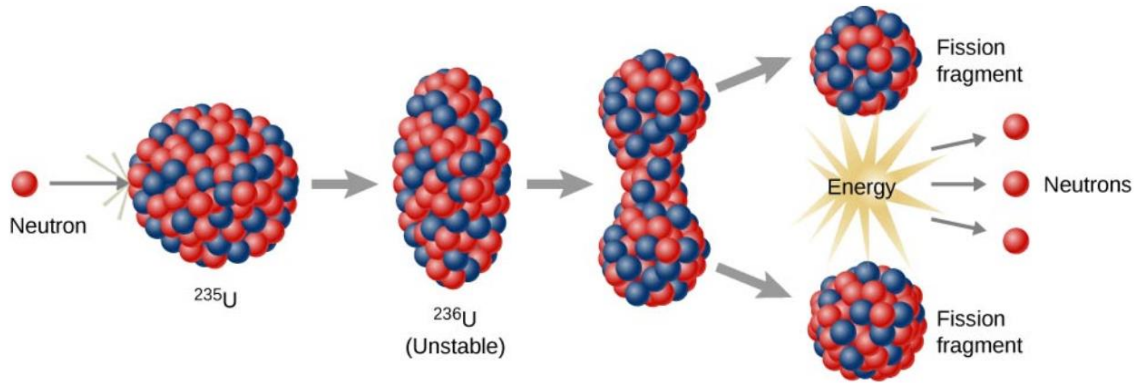
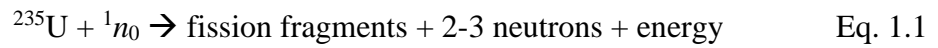
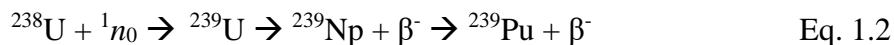


Figure 1.1. Nuclear fission chain reaction in ^{235}U (Ling et al., 2016).

The advantage of the fissionability of ^{235}U generates two main uses. First, the reaction in Eq. 1.1 produces heat to drive steam generators to produce electricity (Frost, 1986). In fact, the complete fission of ^{235}U gives rise to an incredibly large amount of energy, approximately 2.0×10^7 kWh/kg or 200 MeV per fission reaction (compared to ~ 4 eV per atom in the oxidation of carbon to CO_2) (Walls et al., 2011). Second, the reaction allows for the synthesis of other important actinide elements. These reactions are used both in commercial nuclear power and in nuclear weapons (e.g., “Little Man” which was dropped

on Hiroshima, Japan on August 6, 1945). The more abundant isotope, ^{238}U , can be converted into ^{239}Pu by absorption of a neutron followed by two beta decays, as given by Eq. 1.2.



Beta decay is the process by which a neutron is converted into a proton, electron, and neutrino (weakly interacting subatomic particle). The energetic electron, or β^- , is a byproduct of the decay (Tomoda, 1991; Wilson, 1968). Ultimately, the release of neutrons during fission is controlled to help sustain an ample supply of thermal neutrons to continue the chain reaction and maintain fission without an external source of neutrons (Edelstein et al., 2011; Langmuir, 1997). Like ^{235}U , ^{239}Pu is also thermally fissile. Plutonium-239 served as fuel for the world's first atomic bomb explosion, the Trinity Test, which occurred on July 16, 1945 in New Mexico (Brix & Salander, 1990). Less than one month later, the “Fat Man” nuclear weapon, an implosion-type plutonium bomb, was dropped on Nagasaki, Japan on August 9, 1945 contributing to the end of the World War II (Harvey, 2000).

1.2.1 Environmental Chemistry of Uranium

The geochemical speciation of U influences its solubility, mobility, and biologic availability in the environment. Uranium exists in four potential oxidation states: +3, +4, +5, +6, although only the +4 and +6 oxidation states are found in significant amounts in the natural environment (Bethke, 2008; Grenthe et al., 1992). The reduction of uranyl ion (UO_2^{2+}) is a reaction important to geochemists because it transforms oxidized U to an insoluble, reduced form uranous (U^{4+}). One reason why uranyl, U(VI), is readily found is because of its stability in aquatic environments. U(VI) has a strongly positive nucleus requiring two axial oxygen atoms to stabilize with a linear geometry (O-U-O axial bond

angle rarely diverges from linearity of 4°). The linear geometry creates an overall formal charge of +2. However, when in aqueous solution, it has an effective charge of +3.3. Both the uranyl ion and uranous, U(IV), have the highest effective charges, +3.3 and +4, respectively. The effective charge is directly correlated to the actinide's likelihood for hydrolysis, sorption, and complexation (Powell, 2012). Further, Wadt (1981) found that the configuration with the axial oxygen atoms for the uranyl ion is energetically most favorable because of its electron configuration (5f levels). On the other hand, the equatorial U^{6+} -O bonds are dependent on coordination number. In crystal structures (Figure 1.2), the uranyl ion (in addition to its two axial oxygens) is coordinated by four, five, or six anions, such that the coordinating anions are coplanar with the U^{6+} cation. These anions could be carbonates, hydroxides, phosphates, etc. (Burns et al., 1996; Wadt, 1981).

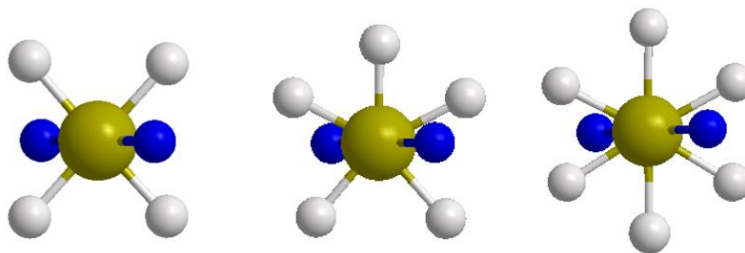


Figure 1.2. The three types of uranyl ion. U^{6+} cations are shown in yellow, potential anions are shown in white, and oxygen atoms are shown in blue. Drawing made by *Chem 3D* software (Burns et al., 1996).

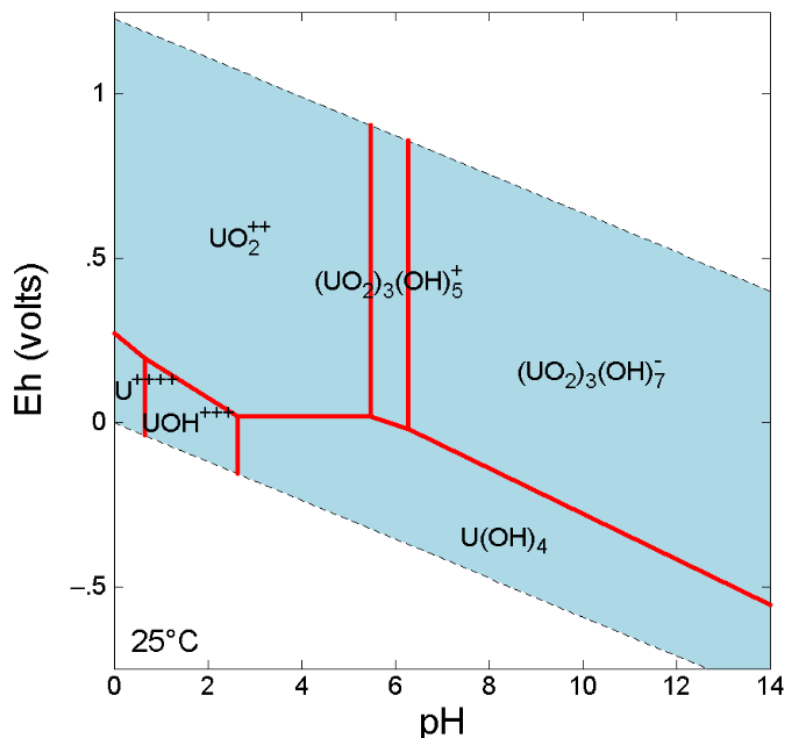


Figure 1.3. Pourbaix diagram for a closed system for U concentration at 10^{-8} M, 25° C, and 1.0 atm pressure. Note: diagram is carbonate-free.

Because of these two oxidation states with extremely different chemistries, the environmental chemistry of U is complex and heavily affected by pH. Figure 1.3 shows the dominant U oxidation states and speciation across the range of pH and E_h conditions at which water is stable. At low pH and high E_h , the free uranyl ion is dominant. However, as E_h potential is reduced, uranous is dominant (Figure 1.3) (Powell, 2012). For this to occur, reduction potential needs to be less than 0.25 V. The extent to which Eq. 1.3 proceeds to the product side to form insoluble U is strongly influenced by three main characteristics: (1) complexing species in the system, (2) aqueous U concentration, and (3) concentration of oxidants [e.g., O_2 , Mn(III)] or reductants [e.g., Fe(II), H_2S] (Grenthe et al., 1992; Zachara et al., 2007).



Furthermore, experimental data and geochemical modeling show tetravalent U precipitates predominate over U(IV) aqueous complexes under most conditions (Langmuir, 1997). Minimum solubility can be shown by solubility products (K_{sp}). The reported $-\log K_{\text{sp}}$ value is -61.0 for crystalline U(IV)O₂, whereas for the U(VI)O₂OH₂ form reported value is -22.5, as shown in Table 1.1 with theoretical calculations for pH 7.5 (Fujiwara et al., 2005; Neck & Kim, 2001). Because the aqueous U(IV) molar concentration is smaller than U(VI) (by several orders of magnitude), it confirms that the U(IV) is more likely to precipitate out of suspension than UO₂²⁺.

Table 1.1. Thermodynamic data, $\log K_{\text{sp}}^\circ$ at standard state, I=0 and 25°C, for solid U(IV) and U(VI) (Fujiwara et al., 2005; Grenthe et al., 1992; Neck & Kim, 2001)

Aqueous U hydrolysis reaction	Oxidation state	$\log K_{\text{sp}}^\circ$	Calculated molar solubility at pH 7.5, M
$\text{U}(\text{OH})_4(\text{s}) \rightleftharpoons \text{U}^{4+}(\text{aq}) + 4 \text{OH}^-(\text{aq})$	U(IV)	-61.0	10^{-35}
$\text{U}(\text{O}_2)_2(\text{OH})_2(\text{s}) \rightleftharpoons \text{UO}_2^{2+}(\text{aq}) + 2\text{OH}^-(\text{aq})$	U(VI)	-22.5	$10^{-9.5}$

It must be noted that these calculations are representative of simple systems without complexing ligands. The uranyl ion, considered a Lewis acid and a hard electron acceptor, forms highly soluble complexes with hard bases such as with hydroxide anions (OH⁻) and carbonate (CO₃²⁻). The general trend for inorganic ligand complexation is: OH⁻, CO₃²⁻ > HPO₄²⁻, SO₄²⁻, F⁻ > NO₃⁻, Cl⁻ (Langmuir, 1997). It can also adsorb to organic matter and Fe-hydroxides or precipitate with various anions, such as hydroxide, silicate, vanadate, arsenate, and phosphate (Grenthe et al., 1992). Further, the uranyl ion extensively

hydrolyzes at pH higher than 6 (Figure 1.3). Although at elevated pH, carbonate complexes begin to outcompete hydrolysis in solutions in equilibrium with air or calcite (CaCO_3).

The precipitation of hydroxide solids as a function of pH is a relatively straightforward exercise for simple systems since the hydroxide concentration is known at any given pH. Nonetheless, this precipitation is not the case with other ligands such as carbonate whose free concentration depends not only on pH but also on the metal concentration and the ligand concentration which may be determined by its partial pressure (e.g., carbon dioxide in air) (Morel & Hering, 1993). When the free uranyl ion is present in alkaline subsurface environments, anionic aqueous species such as $\text{UO}_2(\text{CO}_3)_2^{2-}$ and $\text{UO}_2(\text{CO}_3)_3^{4-}$ are formed. Not only can these complexes freely move in groundwater, but they are also repelled by the negatively charged mineral surfaces commonly found in contaminated subsurface systems. Thus, one potential U removal process is the reduction to uranous that may temporarily immobilize U through formation of precipitates (Zachara et al., 2007). However, when reducing conditions are not optimal for prolonged periods of time, neutrally charged U(VI)-carbonate and U(VI)-hydroxide species may precipitate when their concentrations reach solubility limits. This process may allow for coating of co-precipitated U (Emerson et al., 2017, 2018; Szecsody et al., 2012).

As shown, the U chemistry can be very complex. As U-carbonate complexes form, the system is further complicated with the presence of calcium (Ca) and Mg as it significantly changes uranyl speciation above pH 7.0. As the pH increases, the solubility of these cations decreases.

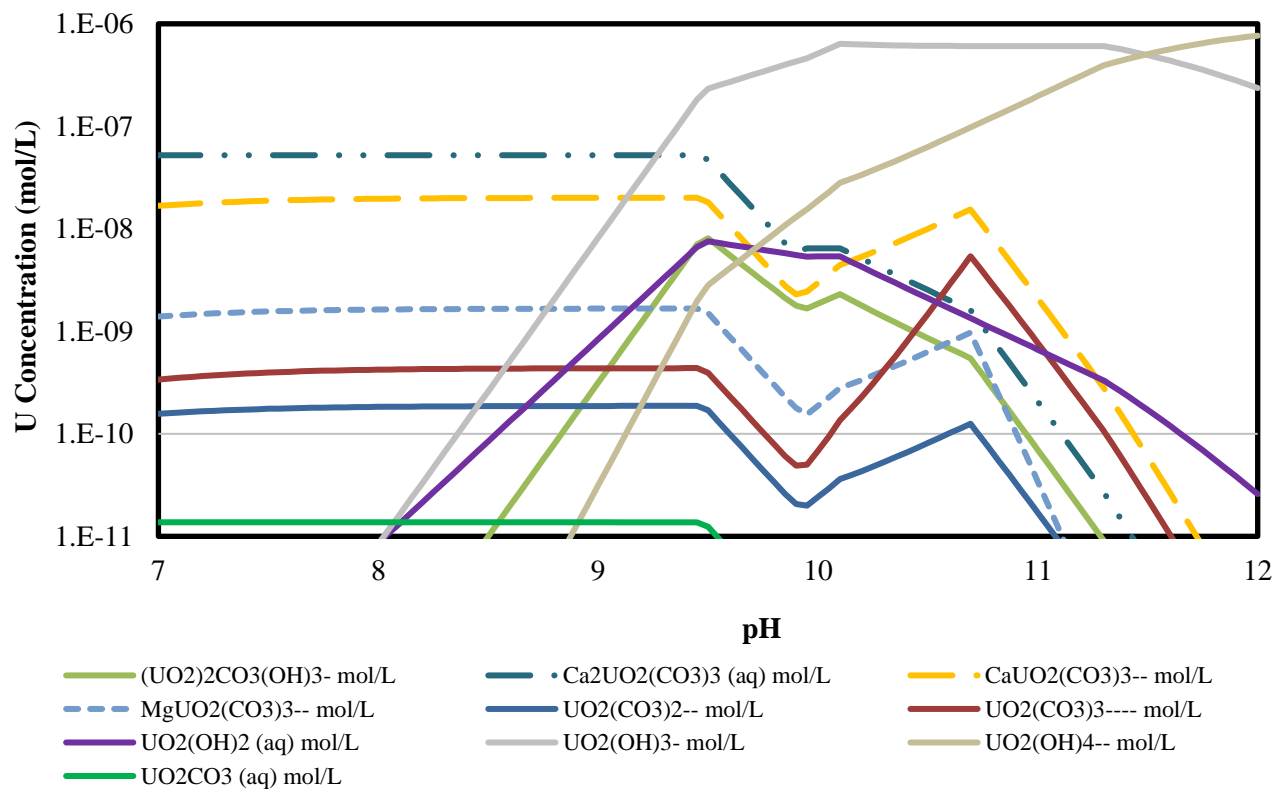


Figure 1.4. Uranium speciation at variable pH and U concentration of 1.0 $\mu\text{mol/L}$ in synthetic groundwater (SGW) with Geochemist's WorkBench® modeling software using Thermo-Minteq database in the system open to the atmosphere. Note: only species at $> 10^{-10}$ M are shown (Katsenovich et al., 2018).

1.2.2 Occurrence and Sources of Uranium

Uranium is ubiquitous in our planet. Uranium averages 2.7 $\mu\text{g/g}$ in the Earth's crust, 1.2 $\mu\text{g/g}$ in sedimentary rocks, 5.0×10^{-6} mg/L in the ocean, 0.003 mg/L in seawater and freshwater and 0.001 to 0.01 mg/L in groundwater (Horne, 1978; Langmuir, 1997; Zachara et al., 2007). Table 1.2 lists the natural U concentration of aquatic and terrestrial systems.

Table 1.2. Typical natural abundance of U in the Earth's crust (Langmuir, 1997)

Terrestrial	U ($\mu\text{g/g}$)	Aqueous	U ($\mu\text{g/L}$)
Earth's crust (average continental)	2.7	Seawater	3.3
Granites	4.4	Oxidizing groundwater	<0.1-100
Basalt	0.8	Reducing groundwater	<0.1
Shale	3.8		
Phyllosilicates	20		
K-feldspar	1.5		
Zircon	2500		

In terrestrial environments, U is a major component of rocks and, thus, is classified as a lithophilic element. In fact, more than 5% of all known minerals contain U (Závodská et al., 2008) with 155 minerals currently identified contain U as an essential component (Karpas, 2014). The most common minerals are pitchblende (U_3O_8), uraninite (UO_2) in oxide form, uranophane [$\text{Ca}(\text{UO}_2)_2(\text{SiO}_3\text{OH})_2(\text{H}_2\text{O})_5$] and coffinite [$\text{U}(\text{SiO}_4)_{1-x}(\text{OH})_{4x}$] in uranyl silicate form. Uranium is also present in accessory minerals such as zircon (ZrSiO_4), as well as secondary U minerals formed in the presence of other anions, such as carnotite [$\text{K}_2(\text{UO}_2)_2(\text{VO}_4)_2 \cdot 1-3\text{H}_2\text{O}$] and autunite [$\text{Ca}(\text{UO}_2)_2(\text{PO}_4)_2 \cdot 8-12\text{H}_2\text{O}$] (Edelstein et al., 2011; Karpas, 2014). Currently, the main geographical locations of U minerals include Australia, Canada (Ontario), Congo, France, Great Britain (Cornwall), Russia, South Africa, and the United States (Colorado, Utah, New Mexico) (Ribera et al., 1996).

The movement of the radionuclide U into aquatic ecosystems is known to occur via physical transfer. Transportation methods include rainfall, snowmelt, flooding, erosion, dissolution, and leaching of U minerals (US Environmental Protection Agency, 2002). In aquatic systems, U is mostly found either in surface water or groundwater. The amount of U released to the water system is dependent on physical transfers such as dissolution and solubility as a function of pH. As mentioned in section 1.2.1, U(VI) is stable in aquatic environments; therefore, U is often mobile in the near surface zone (Ribera et al., 1996; Závodská et al., 2008). In groundwater systems, reduction of U(VI) to U(IV) is mostly via hydrogen sulfide (H₂S), while other reducing agents may be humic material (Baohua Gu et al., 2005; Q. Wang et al., 2019) bacteria (Chen et al., 2015; Baohua Gu et al., 2005; Lovley et al., 1996) or Fe-hydroxide phases (Duff et al., 2002; Jang et al., 2008; Wehrli et al., 1989).

Data on U particle concentrations measured in the atmosphere are sparse as U in metallic form quickly oxidizes when exposed to air. A 1987 study conducted analysis of airborne radionuclides near nuclear industries. Results determined that U effects are greatly affected by concentration and dust cloud particle size, which may have dimensions from 1.0 to 10 µm (Bigu, 1987). More recently, the United Nations Scientific Committee on the Effects of Atomic Radiation (UNSCEAR, 2000) estimated a worldwide average concentration of 0.1 ng/m³ in ambient air. In the United States, the threshold limit in workspace air is fixed to 200 µg/m³ (Ribera et al., 1996). A special case of U inhalation exposure has historically occurred in war zones where fine U oxide aerosols were produced as a result of U munition weapons burning (Karpas, 2014). Additional details will be presented in section 1.3.

A major source of U distribution in the environment is the anthropogenic activities of U mining and milling (processing of U ores) products of the nuclear fuel cycle. Figure 1.5 provides a general overview of the cycle.

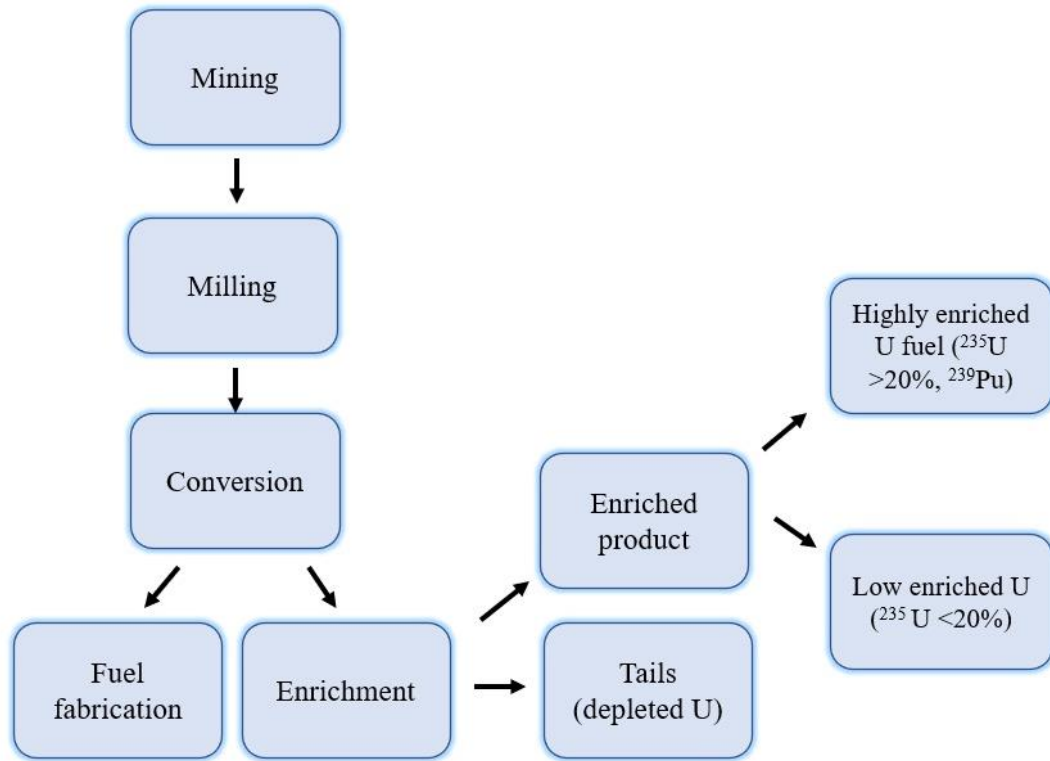


Figure 1.5. Overview of a schematic nuclear fuel cycle (Karpas, 2014).

Briefly, the cycle starts with exploration for U deposits. Mining can be done by underground excavation, open pits, or by in-situ leaching (ISL) techniques for U recovery. Then, the U ore is transported to mills for chemical processing to be converted into a concentrated form known as yellowcake (U_2O_8). The calcined and impure material (65%–85% U_2O_8) is not sufficient for reactor use, thus it is further augmented in U and refined to produce nuclear grade material. After the fuel fabrication step, U can be placed in a reactor to undergo fission, splitting into smaller parts when bombarded with neutrons. According to the European Nuclear Fuel Management, 20,000 tons of U ore produce approximately

23 tons of U, ~240 kg of Pu, and ~720 kg of various fission daughters result as a byproduct of the nuclear fuel cycle (Karpas, 2014). It is important to note that since 1975, 80% of the mined U in the United States has been produced from ISL. The ISL approach has the advantage to both reduce mining costs and eliminate large volumes of tailings. However, it is impossible to restore groundwater quality to its initial state (Schweitzer et al., 2009). As a result, commercial and defense-related activities produced vast volumes of contaminated sediments and groundwater (Knox et al., 2008). In the United States, Department of Energy (DOE) sites such as Savannah River Site (SRS) in Aiken, South Carolina and Hanford Site in Richland, Washington State have recognized U as one of the most frequently occurring radionuclides in groundwater, soils, and sediment (Reynolds et al., 2018; Wellman et al., 2008).

1.2.3 Immobilization of Uranium and Apparent Partitioning Coefficient K_d

Approximately 50% of the United States population consumes its drinking water from groundwater (US Environmental Protection Agency, 1999). Thus, it is important to understand the long-term behavior and fate and transport of contaminants in the subsurface. In the case of U, its vertical transport to groundwater and mobility within sediments depends on the system's properties. These include pH, redox potential, water availability, soil porosity, particle size, etc. (Závodská et al., 2008). For the purpose of the present work, focus was placed on pH, redox potential, and amount of water. Uranium uptake and its retention in soil is a complex function. The contaminant interaction results in several processes happening simultaneously. They may consist of competitive adsorption-

desorption, multi-component ion exchange, complexation¹, and precipitation-dissolution reactions or their combination. However, a common approach is to incorporate all of these “sorption” reactions into one value (commonly represented as *apparent*) to describe the distribution of the contaminant between the solid and liquid phase (Edelstein et al., 2011; Emerson et al., 2018; Zachara et al., 2007). The *apparent partition coefficient* (K_d) is one of the most important parameters used in estimating the migration potential of contaminants present in aqueous solutions in contact with the solid phase (i.e., surface, subsurface and suspended solids) (Knox et al., 2008; US Environmental Protection Agency, 1999). To understand the concept of migration, it is important to understand the different components the empirical K_d equation (Eq. 1.4) consists of.

$$K_d = \left[\frac{\text{total } U(VI) \text{ sorbed}}{\text{total } U(VI) \text{ in solution}} \right] \cdot \frac{\text{volume solution}}{\text{mass sediment}} \quad \text{Eq. 1.4}$$

Equation 1.4 displays the components of laboratory-measured or *in situ*-collected values. However, in the literature, the simplest form of the K_d value is commonly represented as the ratio of the contaminant concentration sorbed to the solid phase, given by Eq. 1.5.

$$K_d = \frac{[\text{solid}]}{[\text{liquid}]} \quad \text{Eq. 1.5}$$

Where [solid] (mol/g) and [liquid] (mol/mL) are the concentrations of the contaminant in the solid and liquid phases at equilibrium, respectively (Zachara et al., 2007). To place the solid-liquid distribution parameter into context, Figure 1.6 depicts a hypothetical contaminant-partitioning curve for a generic scenario. Although for simplification not

¹ Complexation (i.e., complex formation): any combination of dissolved cations with molecules or anions containing free pairs of electrons (Stumm & Morgan, 1991).

accounted for in Figure 1.6 (i.e., values remain constant), pH, ionic strength, and the surface site distribution are important factors in complex real-world environmental conditions relative to its adsorption behavior on reactive solid phase surfaces (Stumm & Morgan, 1991).

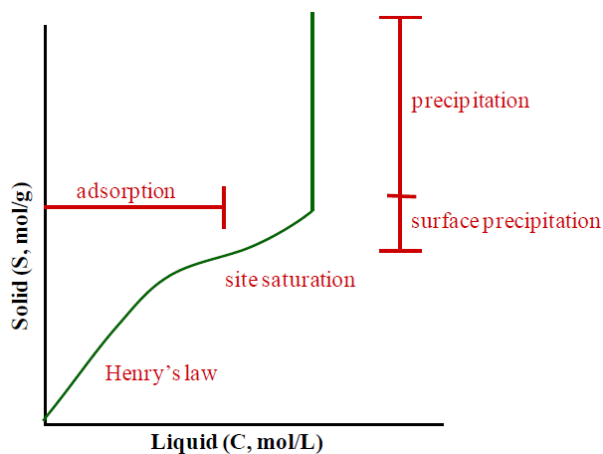


Figure 1.6. Hypothetical equilibrium contaminant partitioning curve for a generic sorbing contaminant (i.e., U). Note: the system is closed and the curve is determined by adsorption at low concentration and precipitation at high concentration (Zachara et al., 2007).

As the contaminant partitions into the solid phase, ion exchange or surface complexation reactions occur linearly or at a constant rate (Henry's Law region). As adsorption sites become filled or saturated, the slope of Henry's Law region becomes less pronounced. Continuing to increase U concentration above the site saturation may result in surface precipitation; however, when U liquid phase is no longer available, precipitation of a contaminant-bearing solid phase takes place.

While Figure 1.6 presents a generic overview of a solid phase-contaminant distribution, there are several mechanisms by which U can be immobilized in environmental systems. Figure 1.7 shows six processes that influence the potential decrease of U contamination. To begin, when uranyl minerals (i.e., uranophane, uraninite, etc.) are

present in biotic reducing condition, they may precipitate to their insoluble, reduced form U(IV) in the presence of a microbial source (Figure 1.7a) (Duff et al., 2002; Knox et al., 2008). In addition, microbes, such as *Thiobacillus denitrificans* (DiSpirito & Tuovinen, 1982) and *Pseudomonas* sp. (Vijay et al., 2020) can catalyze the U(VI) reduction or *Geobacter metallireducens* may perform redox-coupled reactions to limit the mobility of U (Finneran et al., 2002) (Figure 1.7b). Figure 1.7c represents the capability of Fe-oxide minerals (Duff et al., 2002; Jang et al., 2008) and organic matter (Mikutta et al., 2016; Sachs & Bernhard, 2008) to sorb U when complex formation is not possible. Also, U can be sequestered by ubiquitous Fe-oxide mineral coatings (B Gu et al., 1998; Stewart et al., 2011; Yuan, 2015) or clays (Dong & Wan, 2014; Emerson et al., 2018; Moyes et al., 2000; Olivelli et al., 2013) represented in Figure 1.7d. As Figure 1.7a, reductive system can reduce U(VI) mineral; however, in this process a surface coating of less soluble U-bearing mineral forms, thus, limiting the U mobility, as depicted in Figure 1.7e (Katsenovich et al., 2018; Szecsody et al., 2012). Finally, another potential process (Figure 1.7f) that could influence U transport is the co-precipitation of U with oxide minerals or other naturally occurring mineral phases such as the carbonates (Dong et al., 2005; Duff et al., 2002; Emerson et al., 2017; Mashal et al., 2004; Mason et al., 1997; Reeder et al., 2000). For the purpose of the present study, focus was given on processes depicted in Figure 1.7d-f.

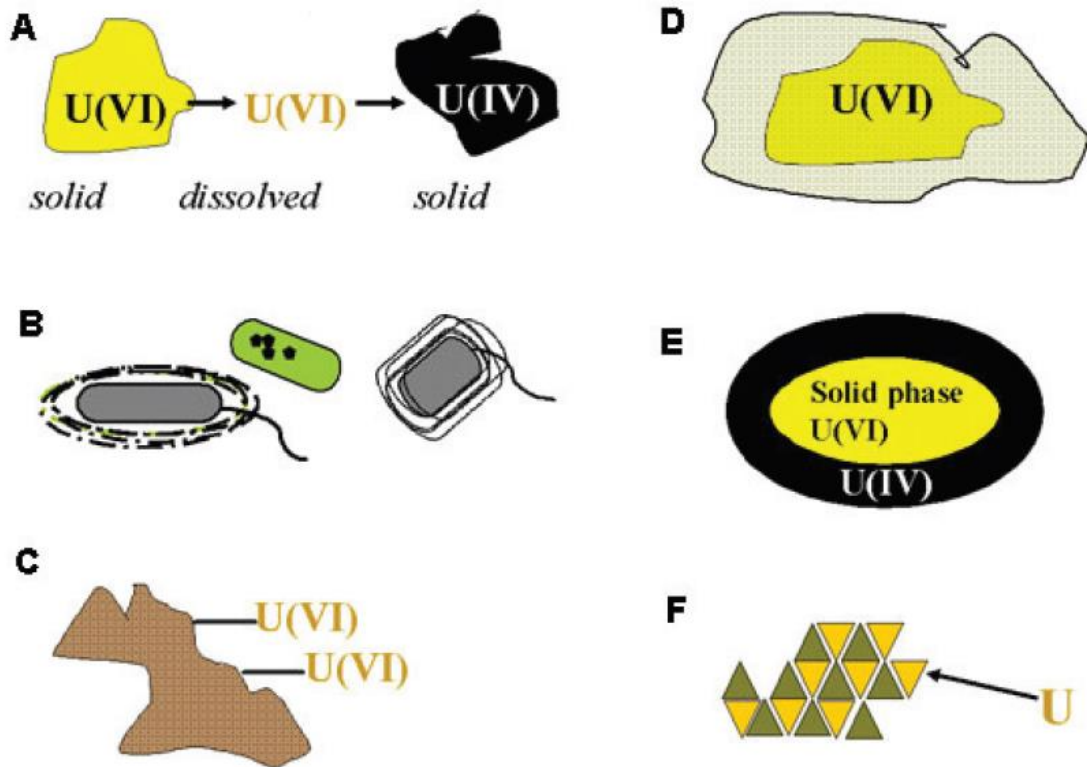


Figure 1.7. Mechanisms by which U mobility can be retarded in the surface and subsurface geologic environment. A) Precipitation of U(VI) and U(IV) phases. B) U microbial uptake. C) Sorption of U by organic or inorganic matter such as humic materials and Fe oxides, respectively. D) Immobilization of U by clay and metal oxide coatings. E) Under reducing conditions, the formation of surface rinds of U(IV) on U(VI) minerals can also limit U mobility because U(IV) solids are less soluble. F) Co-precipitation of U with amorphous and crystalline host minerals may limit U mobility (Duff et al., 2002).

1.3 Uranium Toxicity

As stated in section 1.2.2, U is a ubiquitous naturally radioactive and radiotoxic element because of its heavy metal properties. Thus, its effects on human health should not be ignored. Human exposure could be both natural (surface water, natural U-minerals, U-containing aerosols etc.) or anthropogenic (mine tailings, nuclear industry, military munitions, etc.) (Anke et al., 2009; Gao et al., 2019; Karpas, 2014). The human body

naturally contains ~ 56 µg of U, those of which 56% and 20% are found in the skeleton and muscle tissues, respectively, where the total body threshold in human beings is estimated to be 40 µg/L (Závodská et al., 2008). Uranium enters the organism by different pathways. In descending order of hazard, the routes are: bloodstream, inhalation, oral, and dermal (Karpas, 2014). For this reason, ingestion of soluble U in food and water and inhalation of aerosol particles will be discussed.

The distribution and retention of U in organisms is divided into two parts: a biological aspect and a physical aspect. While the biological is associated with the radiotoxic transport between the organs, the physical aspect is attributed to the radioactivity of the element (Ribera et al., 1996). In fact, it is widely known that the toxic effects of U exposure are the result of its chemical properties and, to a lesser degree, to its radioactive characteristics (Gao et al., 2019; Karpas, 2014; Zamora et al., 1998, 2009; Závodská et al., 2008).

The incorporation of U through ingestion of food or contaminated drinking water is the main route to which the general population is exposed to U-compounds. Ingestion of plant-based foods is a major source of U. In fact, vegetables account for 33% of the U ingested by adults (Anke et al., 2009). The cause is primarily because plants serve as bioaccumulators. A study concluded by Caldwell *et al.*, noted that plants contained higher U concentrations than soil and sediment, particularly in the roots, in U-contaminated locations. The team concluded that plant species can act as bio-monitors, and should be given special attention especially after nuclear accidents such as the Chernobyl and Fukushima nuclear power plant disasters (Caldwell et al., 2012). Similarly, Gao *et al.*, found that U can affect the growth of plant roots and leaves, resulting in the inhibition of electron transfer needed for photosynthesis in two different plant species (*Arabidopsis*

thaliana and *Chlamydomonas reinhardtii*). This growth effect was most prominent at low pH (< 4.5) and pH values of 5-7 for mean U concentrations of $2.4 - 2.8 \times 10^{-5}$ M, where the uranyl ion is most stable, concluding that this U species is highly toxic for the (*Arabidopsis thaliana* and *Chlamydomonas reinhardtii*) biological organisms, respectively (Gao et al., 2019). Thus, the toxic level stresses the importance of the potential leakage of nuclear industry wastes or mine tailings running into soil and groundwater.

Although U is toxic at high concentrations (>40 µg/L), U has no known essential biological functions even at low concentrations. As previously mentioned, because of its stability [i.e., U(VI)], the non-essential metal readily accumulates in aquatic biota. In comparison to Ra and Th, U accumulates the most when it is present in sediments and aquatic plants (Ribera et al., 1996). As a result, its biological effects are described in literature as early as the 1820s (Zamora et al., 1998). More recently, ample studies have concluded that U in contaminated drinking water induces kidney damage (Abed et al., 2019; Bjørklund et al., 2020; Corlin et al., 2016; Grison et al., 2019; Kurttio et al., 2002; Zamora et al., 2009). Identified as a nephrotoxin, its chemical property (i.e., solubility and oxidation state) determines its detrimental effect to the kidneys.

While ingestion of insoluble U compounds has little health effects as practically all the material will be excreted in feces (gastrointestinal tract absorbs < 0.1 – 6.0 % U), soluble U compounds are toxic by inhalation because of absorption from the lungs into the blood (Závodská et al., 2008). As mentioned, the bloodstream is the only carrier of U to organs. Transported in the oxidation state +6, the uranyl ion may form complexes with protein and biological anions, such as bicarbonate (HCO_3^-). According to Závodská, the biological half-life of U for retention are estimated to be 11 days in bone and 2-6 days in the kidney

(Závodská et al., 2008). As a result, it is inferred that the nephrotoxicity effects are primarily the result of high-level acute exposure rather than to low-level chronic exposure (Corlin et al., 2016). To regulate toxicity effects, the legal limit for the concentration of U in drinking water is set between 15 – 30 µg/L worldwide (Karpas, 2014). In the United States, the Office of Ground and Drinking Water set a maximum level of 30 µg/L (US Environmental Protection Agency, 2002).

As stated in section 0, United Nations Scientific Committee on the Effects of Atomic Radiation estimates low concentrations of U in the air (0.1 ng/m³). However, its exposure is of special case when the population was exposed to U munitions used in war zones. With the start of the nuclear war era, there was a need for enriched U. The by-product of enrichment is *depleted* in the ²³⁵U isotope as the stream concentrated in ²³⁵U is used in reactors and weapons (Figure 1.5). The abundance of depleted U, (≤ 0.2 % atom of ²³⁵U) (Walls et al., 2011), led to its wide application in shielding materials, kinetic energy weapons, and armor. The properties of depleted U make it useful as munition (e.g., high density). Consequently, it was used as projectiles in three recent conflicts: Bosnia-Herzegovina (1995), Kosovo (1999), and Iraq (2003). Even though depleted U emits 40% less radioactivity than natural U, it retains all of its chemical properties (Miller & McClain, 2007). As a result, soldier personnel, populations near war zones, or even occupational workers may have been exposed through the four main pathways: bloodstream (munitions fragments entering in cut-open wounds), inhalation (U-oxide aerosols products of the depleted U burning), oral (drinking water containing depleted U or tailing), and dermal (depleted U embedded in soft tissues). The latter being the least detrimental as U primarily emits alpha particles, with limited penetrating power. Such low levels of ionizing radiation

exposure could cause DNA damage or fragmentation in the long term. However, to date, no human cancer has been reported as either direct or indirect, chronic or acute as a result of U hazardous exposure (Bjørklund et al., 2020; Corlin et al., 2016).

1.4 DOE Hanford Site Case Study

With the paramount discovery of Hahn and Strassman's nuclear fission and concerns that Nazi Germany might develop an atomic bomb in 1939, President Franklin Roosevelt accelerated efforts in developing technology for nuclear weapons. The combined efforts of Dr. Fermi's experimental designs and Lieutenant General Leslie Richard Groves' construction made possible to build, in secrecy, the world's first full scale nuclear reactor, the B reactor. Between March 1943 and April 1945, the Hanford Site became the nation's first Pu production facility with the sole purpose to end World War II with the "Fat Man" bomb. The Hanford Site sets on a 586 mi² of semi-arid desert (~16 cm of rainfall per year) in southeastern Washington State (DOE-ORP, 2016; Ginder-Vogel et al., 2005; Harvey, 2000). As shown in Figure 1.8, the Hanford Site is divided into four areas: 100 Area, 200 Area (West and East), 300 Area, and 1100 Area. The 200 and 300 Areas are particularly important to this study. The fabrication enriched ²³⁵U reactor fuel in Hanford's 300 Area, and the reprocessing of irradiated fuel in Hanford's 200 Areas to recover Pu, has led to significant U contamination in the vadose zone and groundwater at the Hanford Site (Zachara et al., 2007).

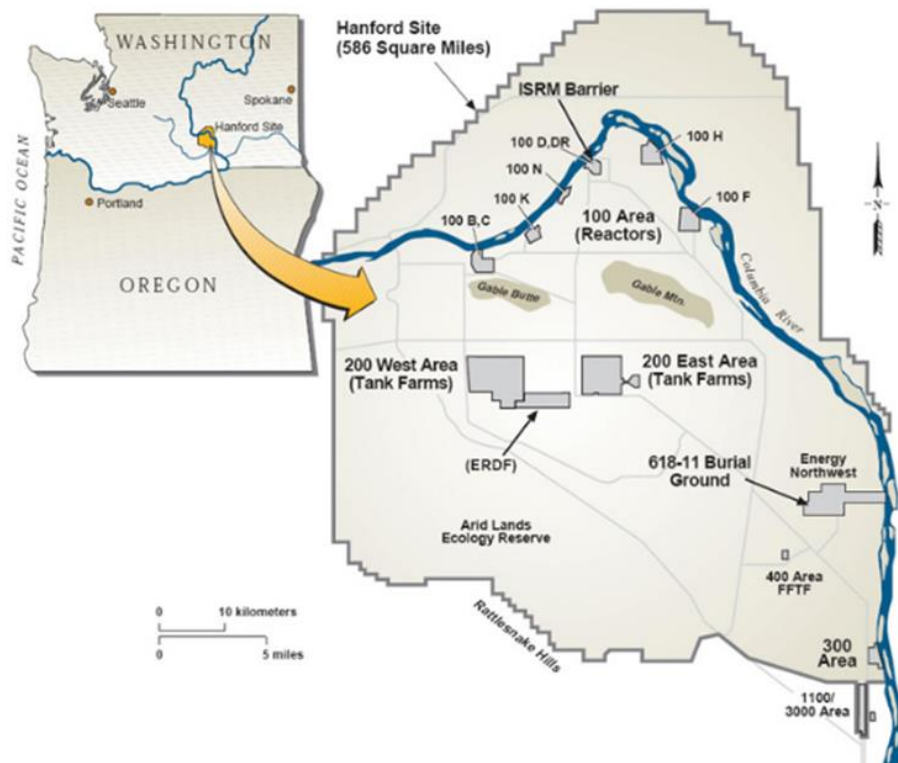


Figure 1.8. Geographical location and principal facilities at the Hanford Site in Washington State (DOE, 2020).

Currently, the site is considered the most polluted place in the Western Hemisphere, containing 1.92 – 3.80 million L of high-level radioactive liquid waste inside underground waste tanks (Gallucci, 2020). The Tank Waste Inventory Network Systems estimates that $\sim 6.5 \times 10^5$ kg of U are still stored in the 177 underground waste tanks at the Hanford Site (Reynolds et al., 2018) and the tank clean-up efforts are expected to last 60 more years, with a cost estimated at \$550 billion (Gallucci, 2020). The waste consists of metal oxide sludges and concentrated hydroxide solutions with concentrations and pH as high as 5.0 M and 13, respectively. The mixed electrolyte solutions are varied (sodium nitrate, nitrite, hydroxide, aluminate, sulfate, phosphate, carbonate, etc.). With highly concentrated solutions, salts have precipitated, leaving some tanks filled with solid salt layers referred

to as saltcake (Figure 1.9a). Some of the generated waste was also released through accidental spills and intentionally into the subsurface through engineered structures (e.g., unlined seepage basins or concrete cribs, Figure 1.9b). The release and subsequent percolation into the vadose zone has caused a risk to the local environment including the Columbia River, the largest river in the Pacific Northwest and fourth-largest in the U.S (Kammerer, 1992; Qafoku, Ainsworth, Szecsody, Qafoku, et al., 2003). For the past 30 years, the DOE has focused on remediating legacy contaminated sites, spending approximately \$6 billion annually.

The release of over 200,000 kg of U at the Hanford Site has created a long-term threat to the area's groundwater as most of this U still resides in the deep vadose zone (Szecsody et al., 2013; Zachara et al., 2007). The contamination has been measured down to 170 feet below the ground surface and represents a large proportion of the total Hanford vadose zone (up to 300 feet thick) (Serne et al., 2008; Wellman et al., 2008). The hydrology at the site is composed of three main aquatic systems: porewater² from the vadose zone, groundwater aquifers, and the Columbia River. Referring to Figure 1.4, U(VI) will exist mostly as neutral and anionic uranyl-carbonate complexes under conditions relevant to the Hanford Site. It is these complexes, from both pore and groundwaters, that suppress adsorption, enhance U(VI) solubility, and lower retardation. Apparent partitioning coefficients (K_d) range between 0.11 – 4 mL/g at pH ~ 8 highlighting that U mobility is high. Ultimately the migration of U(VI) in the Hanford subsurface may be retarded by adsorption (complexation to mineral surfaces), precipitation (formation of U-containing

² Porewater: water residing in the interstitial space left by the grains of sediments

mineral phases), co-precipitation, and coating of surfaces with secondary mineral phases through our proposed remediation option (Zachara et al., 2007).

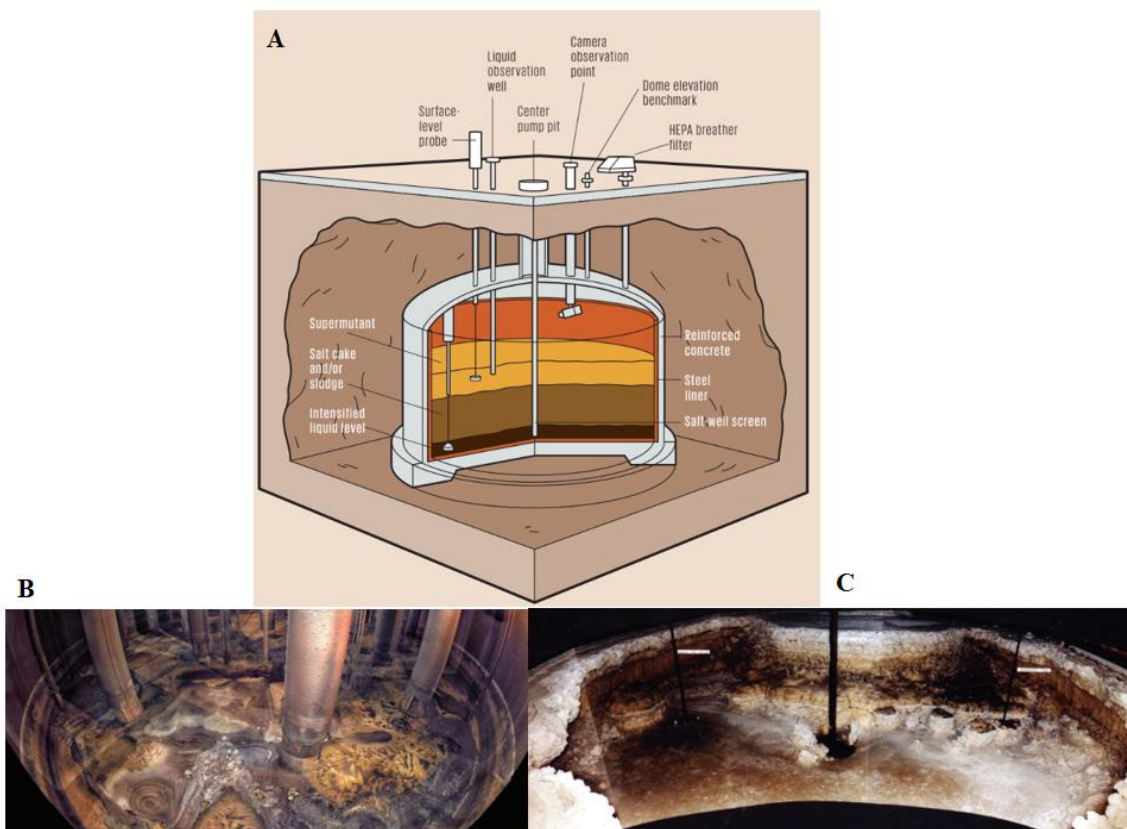


Figure 1.9. Hanford Site's 177 waste tanks. A) Schematic of Hanford's single-shell tanks, depicting the sludge and saltcake in yellow. B) Image showing the mixture of liquids, solids, and sludges inside the storage tanks. C) Hanford tank showing leakage (white surrounding) (Gallucci, 2020).

1.5 Hanford Site Mineralogy

Upon implementation of the proposed ammonia gas technology, a significant increase in Hanford porewater pH from a natural level (~ 8.0) to 11–12 range will cause dissolution of mineral phases. As mentioned in section 1.4, the 200 and 300 Areas currently contain significant U contamination. The mineralogy located in the 200 Area region (also called Central Plateau) is the focus of this research. The 200 Area encompass an extensive area

of vadose zone known as the Hanford formation with 80–100 m in depth which is approximately 2,500,000 years in age. Because the sediments in the Hanford formation are considered youthful in age, they are only modestly weathered (Serne, 2012). The Hanford formation is at the base of most waste disposal facilities and consists of pebble to boulder gravel (4.0 mm – 25.6 cm), fine- to coarse-grained sand (0.25 mm – 1.0 mm), and silt (< 62.5 μm), typically dominated by quartz, various feldspars, and micas (minerals). The latter consists of the solid phase material that U mostly interacts (neutralizes and dissolves) with upon ammonia injection.

To quantify the type of mineralogy within the Hanford sediments, various studies were completed, as shown in Table 1.3. Truex *et al.*, concluded that Hanford sediments are dominated by 30–80% quartz, 5–20% plagioclase (tectosilicate minerals), with minor amounts of K-feldspar (rock-forming tectosilicate minerals) and amphibole (dark, inosilicate minerals) (Truex et al., 2014). Further, a 2012 ammonia gas treatment study completed by Szecsody and team used Hanford formation sediments from the 200 Area (collected at 6-m in depth) and concluded it was composed of 32% quartz, 25% plagioclase, 13% K-feldspar, 19.8% mica (muscovite, biotite, and illite), 1.2% montmorillonite, and other clays (Szecsody et al., 2012). Similarly, a 2008 mineralogical study completed by Xie and team determined that, from 55 collected samples, the sediments consisted of 38% quartz, 19% plagioclase, 17% microcline, 6.0% calcite, 2.0% micas (muscovite, biotite, and illite), and other clays (Xie et al., 2003). However, it is important to know how the clays are fractioned according to their size, in addition to the bulk. Truex and Serne studies of clay-size fractions (<2 μm) in Hanford sediment samples concluded that there four clay minerals that pronominally exist: illite, smectite (montmorillonite and bentonite) family,

chlorite, and kaolinite with minor amounts of quartz, feldspar, and amphibole. Finally, the authors evidenced that the clay fraction of the Hanford Site vadose zone sediments is “remarkably consistent between different vadose zone samples” (Serne, 2012; Truex et al., 2014).

Table 1.3. Hanford Site bulk fraction (in weight %) minerals

Mineral	Hanford Site bulk fraction (weight %)		
Quartz	30-80	32	38
Plagioclase	5-20	25	19
K-feldspar	< 5	13	1.0
Amphibole	< 5	ND/NA	ND/NA
Mica	ND/NA	19.8	2.0
Smectite	ND/NA	1.2	< 5
Microcline	ND/NA	ND/NA	17
Calcite	ND/NA	ND/NA	6.0
Reference	(Truex et al., 2014)	(Szecsody et al., 2012)	(Xie et al., 2003)

ND/NA: not detected and/or not analyzed

1.5.1 Phyllosilicates

The present research focused on three minerals readily found at the Hanford Site: illite, muscovite, and montmorillonite (Figure 1.10). These clay aluminosilicate minerals belong to the family of phyllosilicate, which are constructed by layered sheets of two different types: O (octahedral sheets) and T (tetrahedral sheets). An octahedral sheet consists of two close-packed planes of OH⁻ with di- or trivalent cations occupying the sites in between (Figure 1.11, bottom), while tetrahedral sheets are composed of polymeric sheets of SiO₄ tetrahedra (Figure 1.11, top). In many sheet silicates, Al³⁺ (or Fe³⁺) substitutes for Si, increasing the net negative charge of the T sheet. The TOT are products of chemical weathering of other silicate minerals at the Earth’s surface, following order muscovite → montmorillonite → illite (Hibbard, 2002; Sposito et al., 1999). Figure 1.12 depicts the

crystallography of the studied minerals and Table 1.4 represents a summary of these minerals. Because of their high cation exchange capacity (CEC), clay minerals have been used as adsorbents for the adsorption of hazardous substances (heavy metals, dyes, etc.) (Ismadji et al., 2015).



Figure 1.10. Phyllosilicate minerals investigated in this study: illite, muscovite, and montmorillonite.

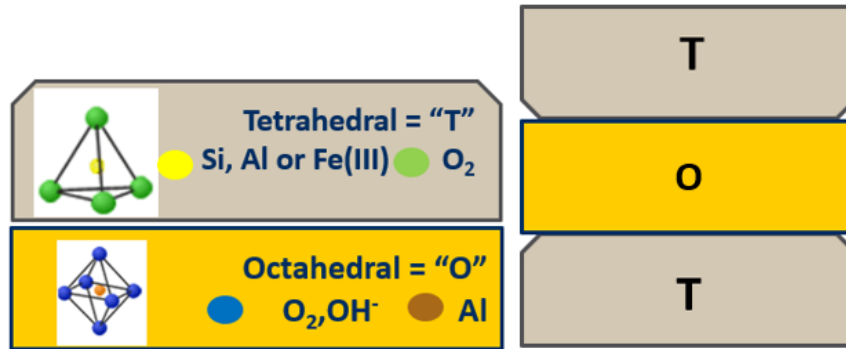


Figure 1.11. Octahedral (O) and tetrahedral (T) sheets in layered phyllosilicate minerals (Nesse, 2012).

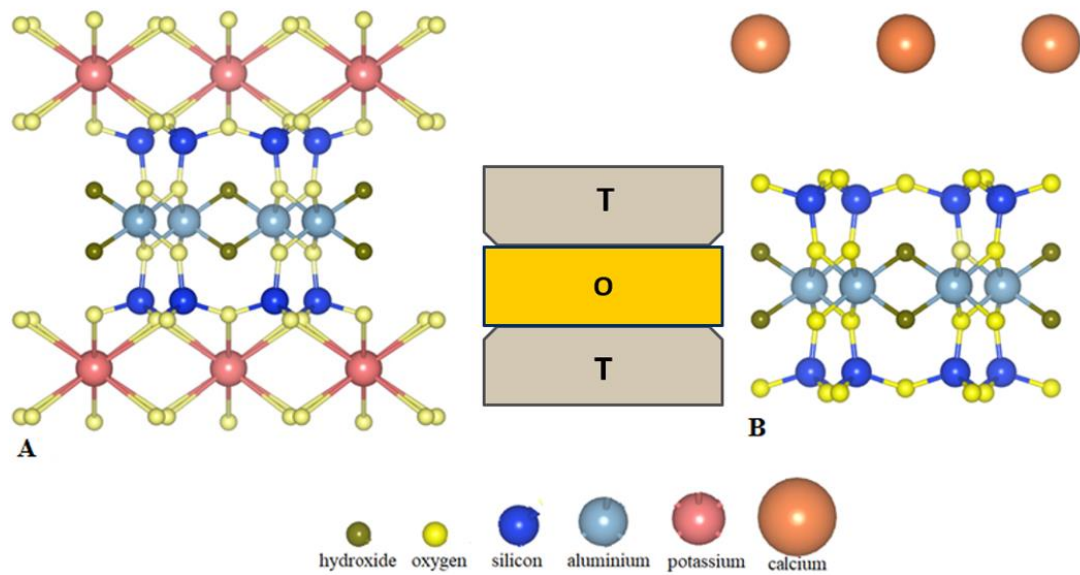


Figure 1.12. Crystallography structure for phyllosilicates: a) mica and b) smectite family minerals created via *VESTA* software program.

Table 1.4. General characteristics of the aluminosilicates clay minerals relevant Hanford Site (Moore & Reynolds Jr, 1989; Nesse, 2012)

Phyllosilicate Clay Mineral	Chemical formula	Group	Type	Cation Exchange Capacity (CEC)	Expandable
Montmorillonite	$\text{Ca}_{0.2}(\text{Al,Mg,Fe})_2(\text{Si}_4\text{O}_{10})(\text{OH})_2 \cdot n\text{H}_2\text{O}$	Smectite	2:1	9.73	✓
Muscovite	$(\text{K,H}_3\text{O})\text{Al}_2[\text{AlSi}_3\text{O}_{10}](\text{OH})_2$	True mica	2:1	16.2	x
Illite	$\text{K}(\text{Mg})_3(\text{Al,Fe})\text{Si}_3\text{O}_{10}](\text{OH})_2$	Interlayer-deficient mica	2:1	17.6	x

1.5.2 Uranium Phases at the Hanford Site

At the Hanford Site, U is found in sediments occurring naturally and anthropogenically because of the discharges of wastes from development of nuclear weapons. To assess the environmental impact associated with vadose zone contamination and groundwater plumes in the 200 and 300 Areas, additional characterization has been conducted. Zachara *et al.*, conducted a comprehensive field-sampling campaign to analyze Hanford aquifer groundwater and sediments. Results show that the background U concentration in unconfined aquifer and sediment samples collected had an overall range of 0.51–12.8 µg/L and 0.39–5.10 µg/g, respectively. In addition, the study found that betafite, $(\text{Ca,U})_2(\text{Ti,Nb,Ta})_2\text{O}_6(\text{OH})$, a naturally occurring U(IV)-primary mineral is present at the Site (15%–35%) and U-coprecipitated with CaCO_3 , a common component in the Hanford sediments (Zachara *et al.*, 2007). Alternatively, mineralogical studies from shallow sediments at the Hanford Site’s Central Plateau waste sites included the following three main U-phases (from least to most mobile): hydrous U-silicates (Na-boltwoodite;

uranophane), U-CaCO₃ co-precipitates, and aqueous or adsorbed U-carbonate complexes (Figure 1.13) (Szecsody et al., 2010; Truex et al., 2014).

The aqueous or adsorbed U-carbonate complexes found across the Hanford Site are most mobile due to two major characteristics: (1) sediments exhibit a porewater pH between 7 and 8 and (2) major groundwater ions groundwater are Ca²⁺, Mg²⁺, and CO₃²⁻. Although the porewater is over-saturated with the aforementioned ions, CO₃²⁻ is of particular interest to the Hanford Site (Szecsody et al., 2010). Carbonate, a hard-base ligand, significantly controls the U adsorption, as all major aqueous complexes present between pH 7 and 8 include CO₃²⁻ (Figure 1.4). Consequently, the U-carbonate aqueous complexes formed (1–7% shown in Figure 1.13) exhibit low adsorption to Hanford sediments (K_d value 0.11–4 mL/g) (Zachara et al., 2007). As a result, this mobility creates

a physical transport of U contamination in the vadose zone, potentially reaching impact receptors (Figure 1.14).

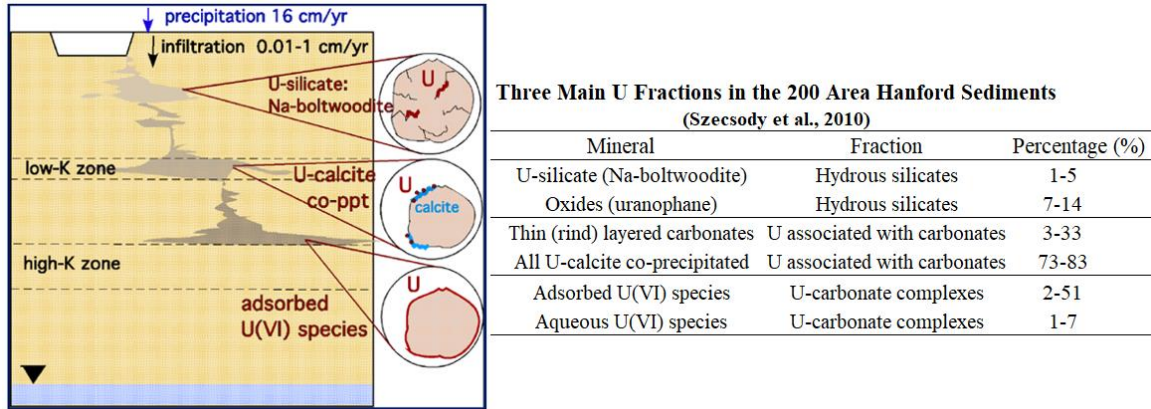


Figure 1.13. Conceptual diagram of U contamination in the Hanford 200 Area vadose zone with respect to depth (diagram) and mineral fraction and percentage (table) (Szecsody et al., 2010).

1.6 Ammonia (NH₃) Gas Treatment

As mentioned in section 1.4, the ongoing U contamination is at significant depth (up to 170 ft) within the deep vadose zone at the Hanford Site. Such depth is of major concern for two main reasons: (1) it represents a potential source of contamination to the groundwater and associated impact receptors (Figure 1.14) and (2) options for deep vadose zone remediation are less developed than shallow contaminated systems (Dresel et al., 2011).

Of the remediation methods that the DOE is currently considering, NH₃ gas injection poses advantages. First, due to U high mobility at the Site from the presence of aqueous carbonates and oxidizing conditions, there is a desire to avoid input of additional liquid as this could increase U flux to the groundwater. Secondly, minimal vadose surface disturbance as NH₃ gas can be injected through injection well. Lastly, due to the vast

vadose zone depth, there is a requirement for relatively even distribution of particles through the treatment zone (Dresel et al., 2011; Emerson et al., 2017). Gas injection has been previously described as a viable remediation technique for inorganic radionuclides because they are highly affected by solution chemistry (Denham & Looney, 2007; Dresel et al., 2011).

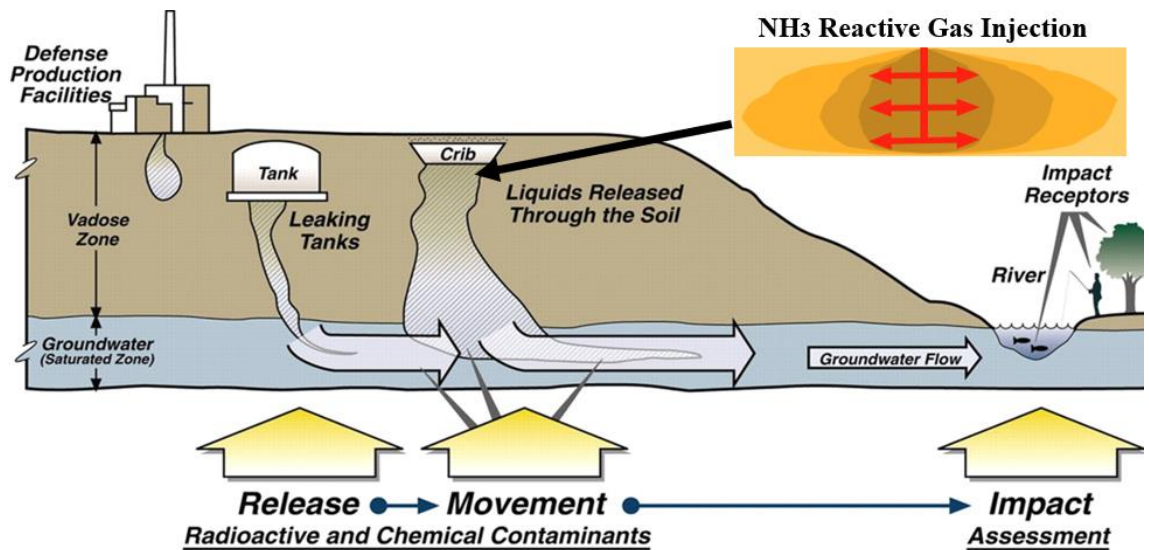


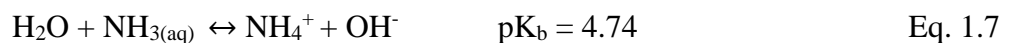
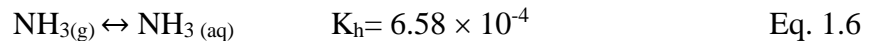
Figure 1.14. Waste discharges to the Hanford Site vadose zone (Gee et al., 2007).

1.6.1 Ammonia Background and Speciation

Ammonia is one of the most widely produced chemicals in the United States. Ammonia is a colorless and highly irritating gas commonly found in nature. It is not highly flammable; however, containers of NH₃ may explode when exposed to high heat (NY Department of Health, 2011). Known to undergo phase transformations, NH₃ can be easily compressed and form a clear, colorless liquid under pressure. Because of its existence under extreme conditions (high pressures and temperatures), NH₃ is among the major constituents in the gas giant planets, such as Neptune and Uranus (Song et al., 2019). Ammonia is widely used for fertilizer, refrigerant gas, plastic and fabric manufacturing,

explosives, household and industrial cleaning solutions, and more recently, as a renewable fuel option (NY Department of Health, 2011; Service, 2018; Shutske, 1996).

Ammonia is a molecule with a central nitrogen atom bonded to three hydrogen atoms (sp^3 hybridization). With a bonding angle of 107° between the atoms, the molecule has a distorted tetrahedral shape. Due to nitrogen's lone pairs, the molecule exhibits a triangular pyramid geometry and a large dipole moment (Tro et al., 2017). The dipole moment allows for hydrogen bonding capacity (17.6 %), and as a result, it extensively solubilizes in water (Song et al., 2019). In fact, this capability is an important factor applicable to NH_3 treatment. The ability for NH_3 gas to partition into the aqueous phase (Eq. 1.6) is relatively quick, as shown by its low Henry's Law constant (a dimensionless value of $\sim 6.58 \times 10^{-4}$). In a NH_3 gas treatment study of vadose zone sediments where the water content was 4% (weight/weight), Szecsody and team concluded that 99.7% of the NH_3 mass was in the porewater when at equilibrium (Szecsody et al., 2012). Consequently, during injection when gaseous NH_3 is in contact with moist sediments, it partitions and reacts with water to form ammonium (NH_4^+) and OH^- ions causing the pH to increase (Eq. 1.7). Furthermore, speciation diagram for closed system is shown in Figure 1.15a.



It is important to note that NH_3 volatilization exponentially increases by an order of magnitude for every unit above pH 6.0. Therefore, it is expected to be higher in alkaline sediments (Emerson et al., 2017).

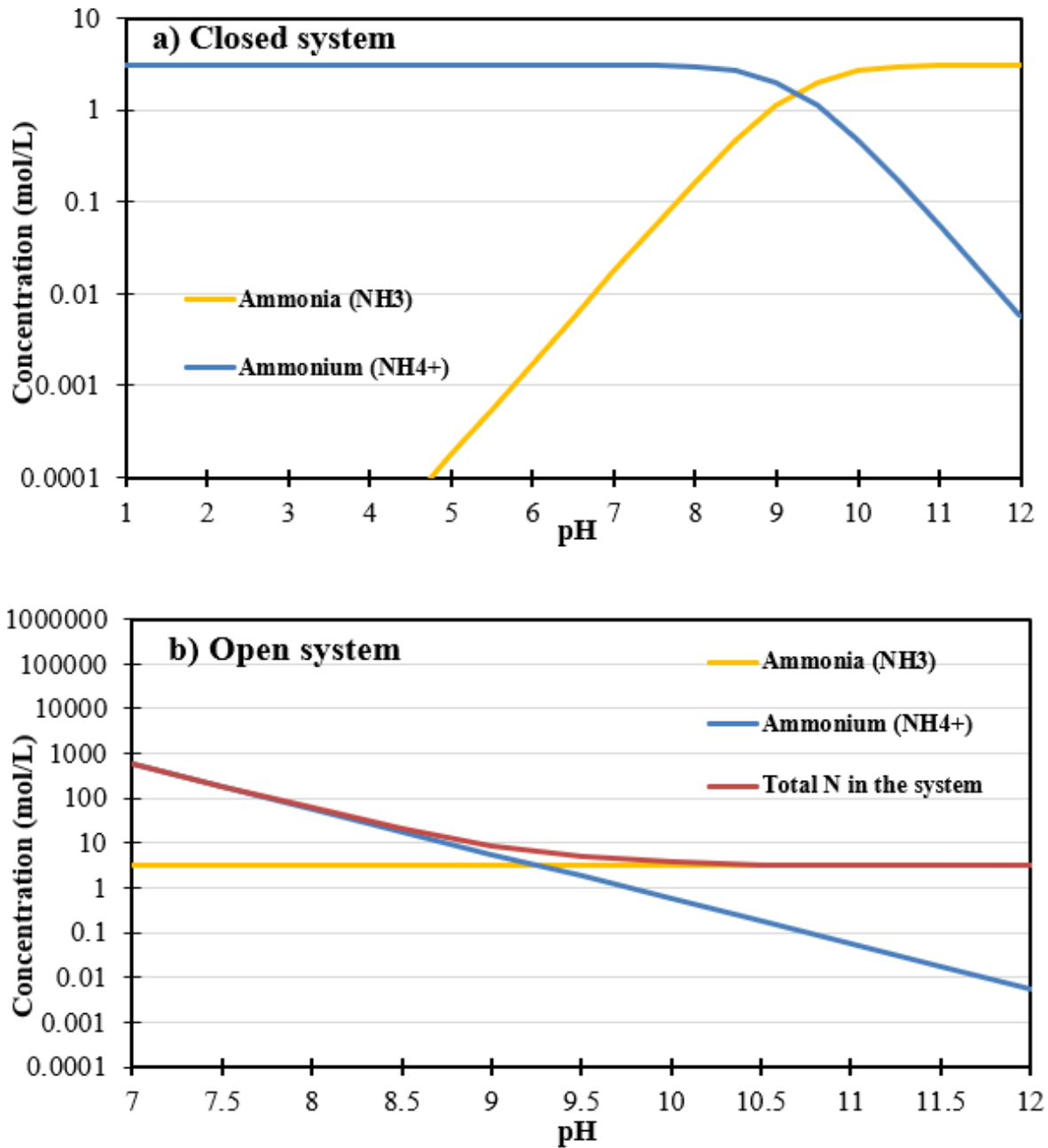


Figure 1.15. Ammonium-ammonia speciation as a function of pH for a closed system (a), where the total initial concentration (3.12 mol/L) is equal to ammonia solubility at 25 °C in pure water and an open system (b), where ammonia gas is constantly mixing with liquid phase and assumes equilibrium highlighting the maximum solubility of these species.

1.6.2 Geochemical and Physical Processes

As NH_3 gas partitions into the porewater within the sediments of the vadose zone, there are several geochemical processes occurring simultaneously. To begin, NH_3 gas will be transported to the surface by diffusion and advection³ modes. Due to the lower density of NH_3 gas (0.726 kg/m^3 at 16°C) relative to air (1.22 kg/m^3 at 16°C), unreacted NH_3 will migrate upward by advection more rapidly than by diffusion. The diffusion rate through Hanford sediment was calculated to be low, at 2.0 % (weight/weight) content, determined by Szecsody and team. Furthermore, the pH of porewaters reacted with injected NH_3 will be impacted by speciation and adsorption processes. As Figure 1.15a-b demonstrate, at $\text{pH} > 9.4$, aqueous NH_3 is the major species. This neutral species exhibits minimal sorption to the mineral surfaces. However, this species will slowly transform into NH_4^+ due to reaction with the sediment's porewater (as per Eq. 1.7). In addition, the oxygen and hydroxide-containing octahedral layers from the phyllosilicates in the system will be neutralized by the NH_4^+ cation, acting as a buffer capacitor and decreasing the pH as a function of time given by volatilization (diffusion and advection) and adsorption processes.

1.6.3 Summary of the Ammonia Gas Reaction with Sediments

Figure 1.16 (1) summarizes the processes mentioned in sections 1.6.1 and 1.6.2 and (2) depicts the three primary steps when NH_3 is injected into the vadose zone. Step 1 shows gas-liquid reaction when NH_3 partitions (Eq. 1.6). Following partitioning, NH_3 increases the ambient porewater pH from 8 to ~ 11.5 , allowing for the aluminosilicates to dissolve (step 2). When sediments have dissolved, precipitates start to form, especially as pH is

³ Advection: dominant transport process in a moving fluid consisting of fluid rearrangement within any given space (Neufeld & Hernandez-Garcia, 2009).

neutralized by reaction with sediments and NH_3 escape from the aqueous phase (step 3). These processes may allow for (1) removal of U from the aqueous phase by adsorption of U, formation of U-precipitates (e.g., forming Na-boltwoodite; $\text{NaUO}_2\text{SiO}_3\text{OH}\cdot\text{H}_2\text{O}$), or formation of co-precipitates with other minerals (e.g., CaCO_3) followed by (2) formation of additional phases that could form secondary coatings with U already precipitated or adsorbed on the sediment surfaces (Qafoku et al., 2003; Zhong et al., 2015). In this dissertation, focus was given on the dissolution and precipitation processes of mineral phases, and as well the adsorption and co-precipitation processes of U with these mineral phases.

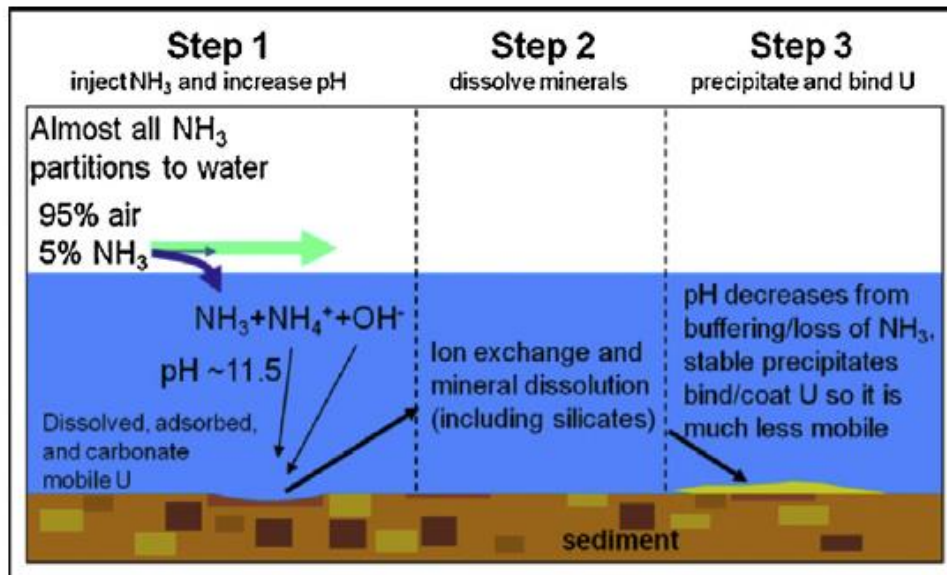


Figure 1.16. Overview of the processes that occur with injection of ammonia vapor into an unsaturated, U-contaminated sediment (Zhong et al., 2015).

1.7 Aims and Research Gaps

The principal goal of the present study was to better understand the fundamental processes and reactions controlling the removal of U from the aqueous phase during and

after reaction of NH_3 gas with subsurface porewaters and clays relevant to Hanford Site sediments. The objective was subdivided into three aims with their associated research gaps.

1.7.1 Aim 1: Mineral Dissolution and Precipitation Processes under Highly Alkaline Conditions

In the alkaline pH range, dissolution occurs due to OH^- deprotonating groups on mineral surfaces (Stumm and Morgan, 1997). Following dissolution, as described in Figure 1.16 – step 3, many metals precipitate when pH is > 7 due to hydrolysis leading to *incongruent dissolution* (Hudak, 2004). However, there is a lack of understanding of mineral dissolution under hyperalkaline conditions at room temperature. Recent work analyzing Hanford site sediments under hyperalkaline (pH 13.4-14.0) conditions found that soil minerals dissolved relatively rapidly (as observed via release of Si and Fe to the aqueous phase) in NaOH and NaNO_3 (Qafoku et al., 2003). Szecsody *et al.* also found elevated concentrations of Si, Al, Ca, Mg, Sr, Na, K, and Fe at short times (i.e., 24 hours) after NH_3 gas injection. However, there is still a lack of understanding of the mineral phase transformations induced by alkaline conditions especially when considering NH_3 gas (Zhong et al., 2015). Therefore, the objective of this aim was to understand how dissolution at high pH (11.5-12.0) affects clay minerals pertinent to the Hanford Site with alkaline treatments (NaOH and NH_4OH). The experiments conducted as part of this aim were in accordance with batch experimental protocols of previous research by Qafoku and Szecsody (Qafoku, Ainsworth, Szecsody, Qafoku, et al., 2003; Szecsody et al., 2012, 2013).

However, batch mineral dissolution experiments were conducted with significantly more liquid than solid in a batch setup where the solid phase is covered by solution as compared to Szecsody's previous work with low water content to simplify conditions for identification of controlling processes. It should be noted that Aim 1 experiments are quite different from unsaturated column experiments conducted previously by Szecsody which has a significantly higher solid to liquid ratio and pore spaces filled with air. In addition, experiments utilized a simplified synthetic groundwater (SGW) in a controlled environment (benchtop laboratories) as compared to the Hanford Site's field-scale experiments (Mashal et al., 2004; Mashal et al., 2005). Lastly, batch experiments were exposed to systematic and comparative alkaline treatments. While previous research utilized alkaline treatments via NaOH or NH₃-injection, there is a lack of understanding of the difference between each treatment (Qafoku, Ainsworth, Szecsody, & Qafoku, 2003; Szecsody et al., 2012). In conclusion, this aim served to investigate (1) the difference between alkaline treatments (NaOH and NH₄OH), (2) the Si and Al behavior while dissolution-precipitation processes are occurring and (3) effects of variable oxidative-reduction (redox) conditions.

1.7.2 Aim 2: Characterization of Physicochemical Mineral Phase Alterations with Treatment

The site mineralogy consists largely of quartz and basaltic glass, plagioclase, K-feldspar, mica (muscovite, biotite, and illite), calcite, and clays (with the clay fraction consisting largely of illite, smectite, kaolinite and chlorite) (Serne, 2012; Serne et al., 2008; Szecsody et al., 2010, 2020; Zachara et al., 2007). Some dissolution work has been performed on specific minerals, such as kaolinite, muscovite and montmorillonite. Qafoku

et al. studied soil mineral dissolution in NaOH-NaNO₃-H₂O solution and Szecsody and Zachara used NH₃ gas injection in the 200 Area Hanford Site (Carroll & Walther, 1990; Qafoku et al., 2003; Szecsody et al., 2013; Zachara et al., 2007). These studies are relevant and provide the basis for work presented in this dissertation; however, sediments and minerals from the 200 Area at the Hanford Site have not been systematically analyzed during and after NH₃ gas treatment. Furthermore, many studies have been conducted on the transformation of aluminosilicates at high pH (Emerson et al., 2018; Katsenovich et al., 2018; Mashal et al., 2004, 2005; Qafoku, Ainsworth, Szecsody, Qafoku, et al., 2003), but few reports are available on the type of minerals that could form *in situ* during and after treatment. Moreover, no research was found in literature that systematically measured mineral phase alteration upon pH manipulation for reaction with NH₃ gas. The objective of this aim was to identify the major physicochemical changes in the solid phase of clean bulk minerals following treatment with NH₃ gas. For this aim, results are presented for minerals characterized following batch experiments conducted with exposure to 5% NH₃/95% N₂ gas and consequently ultrapure air using various analytical techniques such as Brunauer–Emmet–Teller (BET), X-ray diffraction (XRD), and Scanning Electron Microscope with Energy Dispersive X-ray spectroscopy (SEM-EDS). These solid phase characterization techniques fulfilled the endeavor to identify mineral transformations and confirm incongruent dissolution phenomena. In conclusion, pH manipulation needs to be understood in order to (1) describe mineral alteration mechanisms and (2) predict the fate and transport of contaminants.

1.7.3 Aim 3: Determination of the Dominant Solid Phases and the Stability of U

While dissolution may occur from hours to years, precipitation covers a wider time span ranging from seconds to centuries (Qafoku et al., 2003; Sposito, 1994). For example, Qafoku *et. al* found that soil minerals rapidly dissolved after 48 hours of contact with 1.0 M NaOH and 1.0 M NaNO₃ (Qafoku et al., 2003). Meanwhile, Mashal *et al.* found that newly formed cancrinite and sodalite secondary minerals increased with time when in contact with simulated tank waste (STW) at high temperatures (Mashal et al., 2005). Although these research findings and the data presented in Aim 1 and 2 provide evidence of secondary precipitates under hyperalkaline conditions, studies were not conducted under NH₃-injection technology with U.

In order to accomplish this aim, batch experiments and solid phase characterization techniques were part of a continuation from the previous two aims, yet with the distinction that the solid phase was exposed to U. After confirmation that alkaline solution promotes significant Si dissolution (> 1440 h) and there is a rapid decrease in aqueous Al, it can be concluded that incongruent dissolution phenomena occurs (Di Pietro et al., 2020). As a result of such phenomenon, a more in-depth, molecular investigation was conducted in Aim 2 to explain where such clay mineral alteration takes place. After detailed solid phase characterization studies, results suggested that minerals demonstrate an alteration in morphology and recrystallization following aeration treatment. Particularly, solid phase NMR spectra demonstrated modified edged-sites due to Si and Al rearrangement. It is important to note; however, that U was not a variable in the aforementioned aims. Therefore, the objective of this aim was to follow the same batch protocol, yet exposing U to the solid phase, to further understand the complex precipitation and secondary coating

processes controlling U as the system returns to neutral pH (Figure 1.16 – step 3). Analytical instrumentation included SEM-EDS, XRD, electron microprobe (EMPA), and X-ray absorption near edge spectroscopy (XANES). Phyllosilicate clay minerals and Hanford sediments were exposed to U, treated with 95% N₂/5% NH₃ gas, and set to age for approximately six months. The time period chosen was intentional as Szecsody *et al.* previously estimated that the pH may remain elevated for this period in a large-scale system. Similarly to Aim 2, the SGW suspensions were duplicated as both were NH₃-treated with only the second undergoing aeration to simulate a return natural condition. Although U is expected to be associated with the solid phase based on previous experiments (Emerson et al., 2017), there is a need to identify the dominant phases which U will be associated with. In addition, there has been no attempt to study incongruent dissolution phenomena occurrence suggesting formation of secondary precipitates in U-spiked suspensions because of pH manipulation. As a result, there is a knowledge gap in understanding the mechanism of U involving the K_d multi-component processes (section 1.2.3) upon systematic pH manipulation of clays and Hanford Site sediments.

1.8 Research Hypothesis

The present study hypothesized NH₃ gas injection as a viable remediation solution for the sequestration of U in subsurface environments, particularly in vadose zone environments, such as at the Hanford Site in Washington State with a deep unsaturated zone and relatively low rainfall. To begin, NH₃ gas prevents the disturbance of the vadose zone, serving as an *in situ* remediation amendment. In addition, its intrinsic alkaline conditions allow for the partial dissolution of aluminosilicates present in the system to be promoted. Lastly, at vadose zone depth, NH₃ gas favors an even distribution of sediment

and clay particles through the treatment zone. The first aim of this study investigated the geochemical reactions occurring with comparative alkaline aqueous solutions and redox conditions. It was hypothesized that the strong base (NaOH) and the anaerobic conditions will lead to a great dissolution of the phyllosilicate minerals. In addition, it was hypothesized that the Si and Al dissolution rate would not be equal as a function of time, leading to the incongruent dissolution phenomena. This phenomenon itself suggests secondary phase precipitation, an effective method for sequestration of contaminants.

The second aim of this study investigated both the NH₃ gas injection and its the volatilization and adsorption processes from the batch system via solid phase characterization techniques. It is hypothesized that NH₃ gas alters the surface area, particle size, and the octahedral (edges) layers of the phyllosilicate clay minerals, as a result, these mineral transformations allow for U contaminant sequestration.

Lastly, the third aim served to investigate the complex U-precipitation and secondary coating processes that control the U stability at circumneutral pH. It is hypothesized that the U-mineral phases formed upon pH neutralization allows for (1) U-CaCO₃ precipitation and/or (2) aluminosilicate coating of U-species (i.e., Na-boltwoodite). The hypothesis was formed on the basis that NH₃ gas volatilization stabilizes the once mobile U, preventing further contamination to the groundwater system found at the Hanford Site.

1.9 References

Abed, M. M., Mahdi, K. H., & Al-Hamadany, W. S. (2019). Estimation of uranium concentration in blood samples of kidneys failure patients in Al-Muthanna governorate. *AIP Conference Proceedings*, 2123(1), 20057.

Anke, M., Seeber, O., Müller, R., Schäfer, U., & Zerull, J. (2009). Uranium transfer in the food chain from soil to plants, animals and man. *Geochemistry*, 69, 75–90.

- Bethke, C. (2008). *Geochemical and biogeochemical reaction modeling* (2nd ed.). Oxford University Press.
- Bigu, J. (1987). *Characterization of long-lived radioactive dust clouds generated in uranium mill operations*. Atomic Energy Control Board.
- Bjørklund, G., Semenova, Y., Pivina, L., Dadar, M., Rahman, M. M., Aaseth, J., & Chirumbolo, S. (2020). Uranium in drinking water: a public health threat. *Archives of Toxicology*, *94*(5), 1551–1560.
- Brix, P., & Salander, C. (1990). The Discovery of Uranium Fission Its Intricate History and Far-Reaching Consequences. *Interdisciplinary Science Reviews*, *15*(4), 314–326.
- Burns, P. C., Miller, M. L., & Ewing, R. C. (1996). U₆₊ minerals and inorganic phases: a comparison and hierarchy of crystal structures. *The Canadian Mineralogist*, *34*(4), 845–880.
- Caldwell, E. F., Duff, M. C., Ferguson, C. ., Coughlin, D. ., Hicks, R. A., & Dixon, E. (2012). Bio-monitoring for uranium using stream-side terrestrial plants and macrophytes. *Journal of Environmental Monitoring*.
- Chen, Thornton, S. F., & Small, J. (2015). Influence of Hyper-Alkaline pH Leachate on Mineral and Porosity Evolution in the Chemically Disturbed Zone Developed in the Near-Field Host Rock for a Nuclear Waste Repository. *Transport in Porous Media*, *107*(2), 489–505.
- Corlin, L., Rock, T., Cordova, J., Woodin, M., Durant, J. L., Gute, D. M., Ingram, J., & Brugge, D. (2016). Health Effects and Environmental Justice Concerns of Exposure to Uranium in Drinking Water. *Current Environmental Health Reports*, *3*(4), 434–442.
- Denham, M. E., & Looney, B. B. (2007). *Gas: A neglected phase in remediation of metals and radionuclides*. ACS Publications.
- Di Pietro, S. A., Emerson, H. P., Katsenovich, Y., Qafoku, N. P., & Szecsody, J. E. (2020). Phyllosilicate mineral dissolution upon alkaline treatment under aerobic and anaerobic conditions. *Applied Clay Science*, *189*.
- DiSpirito, A. A., & Tuovinen, O. H. (1982). Uranous ion oxidation and carbon dioxide fixation by *Thiobacillus ferrooxidans*. *Archives of Microbiology*, *133*(1), 28–32.
- DOE-ORP. (2016). *B reactor*. <http://www.hanford.gov/page.cfm/BReactor>

- DOE. (2020). *Projects & Facilities*. Hanford.Gov.
<https://www.hanford.gov/page.cfm/ProjectsFacilities>
- Dong, W., Ball, W. P., Liu, C., Wang, Z., Stone, A. T., Bai, J., & Zachara, J. M. (2005). Influence of Calcite and Dissolved Calcium on Uranium(VI) Sorption to a Hanford Subsurface Sediment. *Environmental Science & Technology*, 39(20), 7949–7955.
- Dong, W., & Wan, J. (2014). Additive surface complexation modeling of uranium (VI) adsorption onto quartz-sand dominated sediments. *Environmental Science & Technology*, 48(12), 6569–6577.
- Dresel, P. E., Wellman, D. M., Cantrell, K. J., & Truex, M. J. (2011). Review: Technical and policy challenges in deep vadose zone remediation of metals and radionuclides. *Environmental Science & Technology*, 45(10), 4207–4216.
- Duff, M. C., Coughlin, J. U., & Hunter, D. B. (2002). Uranium co-precipitation with iron oxide minerals. *Geochimica et Cosmochimica Acta*, 66(20), 3533–3547.
- Edelstein, N., Katz, J. J., Fuger, J., & Morss, L. R. (2011). *The Chemistry of the Actinide and Transactinide Elements* (Third). Springer.
- Emerson, H. P., Di Pietro, S., Katsenovich, Y., & Szecsody, J. (2017). Effects of ammonium on uranium partitioning and kaolinite mineral dissolution. *Journal of Environmental Radioactivity*, 167.
- Emerson, H. P., Di Pietro, S., Katsenovich, Y., & Szecsody, J. (2018). Potential for U sequestration with select minerals and sediments via base treatment. *Journal of Environmental Management*, 223.
- Finneran, K. T., Housewright, M. E., & Lovley, D. R. (2002). Multiple influences of nitrate on uranium solubility during bioremediation of uranium-contaminated subsurface sediments. *Environmental Microbiology*, 4(9), 510–516.
- Frost, B. R. T. (1986). Nuclear materials: An overview. In *Encyclopedia of Materials Science and Engineering*: (Vol. 4). Pergamon Press.
- Fry, C., & Thoennessen, M. (2013). Discovery of Actinium, Thorium, Protactinium, and Uranium Isotopes. *Atomic Data and Nuclear Data Tables*, 99(3), 345–364.
- Fujiwara, K., Yamana, H., Fujii, T., Kawamoto, K., Sasaki, T., & Moriyama, H. (2005). Solubility product of hexavalent uranium hydrous oxide. *Journal of Nuclear Science and Technology*, 42(3), 289–294.

- Gallucci, M. (2020). What to do with 177 giant tanks of radioactive sludge. *IEEE Spectrum*, 57(5), 24–33.
- Gao, N., Huang, Z., Liu, H., Hou, J., & Liu, X. (2019). Advances on the toxicity of uranium to different organisms. *Chemosphere*, 237, 124548.
- Ginder-Vogel, M., Borch, T., Mayes, M. A., Jardine, P. M., & Fendorf, S. (2005). Chromate reduction and retention processes within arid subsurface environments. *Environmental Science & Technology*, 39(20), 7833–7839.
- Goriely, S., Samyn, M., & Pearson, J. M. (2007). Further explorations of Skyrme-Hartree-Fock-Bogoliubov mass formulas. VII. Simultaneous fits to masses and fission barriers. *Physical Review C*, 75(6), 064312.
- Grenthe, I., Wanner, H., & Forest, I. (1992). *Chemical thermodynamics of uranium*. North-Holland.
- Grison, S., Kereselidze, D., Cohen, D., Gloaguen, C., Elie, C., Lestaevel, P., Legendre, A., Manens, L., Habchi, B., & Benadjaoud, M. A. (2019). Applying a multiscale systems biology approach to study the effect of chronic low-dose exposure to uranium in rat kidneys. *International Journal of Radiation Biology*, 95(6), 737–752.
- Gu, B., Liang, L., Dickey, M. J., Yin, X., & Dai, S. (1998). Reductive precipitation of uranium (VI) by zero-valent iron. *Environmental Science & Technology*, 32(21), 3366–3373.
- Gu, Baohua, Yan, H., Zhou, P., Watson, D. B., Park, M., & Istok, J. (2005). Natural Humics Impact Uranium Bioreduction and Oxidation. *Environmental Science & Technology*, 39(14), 5268–5275.
- Harvey, D. W. (2000). *History of the Hanford Site: 1943-1990*. Pacific Northwest National Laboratory (PNNL), Richland, WA.
- Hibbard, M. J. (2002). *Mineralogy. A View Point of Geology*, McGraw-Hill.
- Horne, R. A. (1978). *The chemistry of our environment*. Wiley.
- Ismadji, S., Soetaredjo, F. E., & Ayucitra, A. (2015). *Clay materials for environmental remediation*. Springer.
- Jang, J.-H., Dempsey, B. A., & Burgos, W. D. (2008). Reduction of U(VI) by Fe(II) in the presence of hydrous ferric oxide and hematite: Effects of solid transformation, surface coverage, and humic acid. *Water Research*, 42(8), 2269–2277.

- Kammerer, J. C. (1992). Water Fact Sheet. *US Geological Survey*, Fact Sheet No. 87-242. <http://pubs.usgs.gov/of/1987/ofr87-242/pdf/ofr87242.pdf>;
- Karpas, Z. (2014). *Analytical chemistry of uranium: environmental, forensic, nuclear, and toxicological applications*. CRC press.
- Katsenovich, Y. P., Cardona, C., Szecsody, J., Lagos, L. E., & Tang, W. (2018). Assessment of calcium addition on the removal of U(VI) in the alkaline conditions created by NH₃ gas. *Applied Geochemistry*, 92, 94–103.
- Knox, A. S., Brigmon, R. L., Kaplan, D. I., & Paller, M. H. (2008). Interactions among phosphate amendments, microbes and uranium mobility in contaminated sediments. *Science of the Total Environment*, 395(2–3), 63–71.
- Kragh, H. (2018). Beyond Uranium, Ca. 1890–1950. In *From Transuranic to Superheavy Elements* (pp. 1–16). Springer.
- Kurtio, P., Auvinen, A., Salonen, L., Saha, H., Pekkanen, J., Mäkeläinen, I., Väisänen, S. B., Penttilä, I. M., & Komulainen, H. (2002). Renal effects of uranium in drinking water. *Environmental Health Perspectives*, 110(4), 337–342.
- Langmuir, D. (1997). Aqueous geochemistry of uranium. *Aqueous Environmental Chemistry*, 494–512.
- Ling, S. J., Sanny, J., Moebis, W., Friedman, G., Druger, S. D., Kolakowska, A., Anderson, D., Bowman, D., Demaree, D., & Ginsberg, E. (2016). *University Physics Volume 2*.
- Lovley, D. R., Coates, J. D., Blunt-Harris, E. L., Phillips, E. J. P., & Woodward, J. C. (1996). Humic substances as electron acceptors for microbial respiration. *Nature*, 382(6590), 445–448.
- Mashal, K., Harsh, J. B., & Flury, M. (2005). Clay mineralogical transformations over time in Hanford sediments reacted with simulated tank waste. *Soil Science Society of America Journal*, 69(2), 531–538.
- Mashal, K., Harsh, J. B., Flury, M., Felmy, A. R., & Zhao, H. (2004). Colloid formation in Hanford sediments reacted with simulated tank waste. *Environmental Science & Technology*, 38(21), 5750–5756.
- Mason, C. F. V, Turney, W. R. J. R., Thomson, B. M., Lu, N., Longmire, P. A., & Chisholm-Brause, C. J. (1997). Carbonate Leaching of Uranium from Contaminated Soils. *Environmental Science & Technology*, 31(10), 2707–2711.

- Mikutta, C., Langner, P., Bargar, J. R., & Kretzschmar, R. (2016). Tetra- and hexavalent uranium forms bidentate-mono-nuclear complexes with particulate organic matter in a naturally uranium-enriched peatland. *Environmental Science & Technology*, 50(19), 10465–10475.
- Miller, A. C., & McClain, D. (2007). A review of depleted uranium biological effects: in vitro and in vivo studies. *Reviews on Environmental Health*, 22(1), 75–89.
- Moore, D. M., & Reynolds Jr, R. C. (1989). *X-ray Diffraction and the Identification and Analysis of Clay Minerals*. (Second). Oxford University Press (OUP).
- Morel, F., & Hering, J. G. (1993). *Principles and applications of aquatic chemistry*. John Wiley & Sons.
- Mould, R. F. (1999). Marie and Pierre Curie and radium: history, mystery, and discovery. *Medical Physics*, 26(9), 1766–1772.
- Moyes, L. N., Parkman, R. H., Charnock, J. M., Vaughan, D. J., Livens, F. R., Hughes, C. R., & Braithwaite, A. (2000). Uranium uptake from aqueous solution by interaction with goethite, lepidocrocite, muscovite, and mackinawite: An X-ray absorption spectroscopy study. *Environmental Science & Technology*, 34(6), 1062–1068.
- Neck, V., & Kim, J. I. (2001). Solubility and hydrolysis of tetravalent actinides. *Radiochimica Acta*, 89(1), 1–16.
- Nesse, W. D. (2012). *Introduction to Mineralogy* (2nd Ed., Issue 549 NES). Oxford University Press.
- Neufeld, Z., & Hernandez-Garcia, E. (2009). *Chemical And Biological Processes In Fluid Flows: A Dynamical Systems Approach*. World Scientific Publishing Company. <http://ebookcentral.proquest.com/lib/fiu/detail.action?docID=1681190>
- Nilsson, M. (2016). *Uranium Chemistry - General Properties of Uranium*. National Analytical Management Program - US DOE Carlsbad Field Office.
- NobelPrize. (2020). *Pierre Curie - Facts*. Nobel Media AB. <https://www.nobelprize.org/prizes/physics/1903/pierre-curie/facts/>
- NY Department of Health. (2011). *The Facts About Ammonia*. https://www.health.ny.gov/environmental/emergency/chemical_terrorism/ammonia_general.htm

- Olivelli, M. S., Curutchet, G. A., & Torres Sánchez, R. M. (2013). Uranium uptake by montmorillonite-biomass complexes. *Industrial & Engineering Chemistry Research*, 52(6), 2273–2279.
- Powell, B. A. (2012). *Environmental chemistry of uranium and plutonium, part II (uranium)*. US Department of Energy NAMP Radiochemistry. <https://foodshield.vids.io/videos/4c9bd8b5191eeac8c4/environmental-chemistry-part-2>
- Qafoku, Ainsworth, C. C., Szecsody, J. E., & Qafoku, O. S. (2003). Aluminum Effect on Dissolution and Precipitation under Hyperalkaline Conditions: I. Liquid Phase Transformations. *Journal of Environmental Quality*, 32(6), 2354–2363.
- Qafoku, Ainsworth, C. C., Szecsody, J., Qafoku, O. S., & Young, J. S. (2003). Aluminum Effect on Dissolution and Precipitation under Hyperalkaline Conditions: II. solid Phase Transformations. *Journal of Environmental Quality*, 32(6), 2364–2372.
- Reeder, R. J., Nugent, M., Lamble, G. M., Tait, C. D., & Morris, D. E. (2000). Uranyl incorporation into calcite and aragonite: XAFS and luminescence studies. *Environmental Science & Technology*, 34(4), 638–644.
- Reynolds, J. G., Cooke, G. A., Page, J. S., & Warrant, R. W. (2018). Uranium-bearing phases in Hanford nuclear waste. *Journal of Radioanalytical and Nuclear Chemistry*, 316(1), 289–299.
- Ribera, D., Labrot, F., Tisnerat, G., & Narbonne, J.-F. (1996). Uranium in the environment: occurrence, transfer, and biological effects. In *Reviews of environmental contamination and toxicology* (pp. 53–89). Springer.
- Sachs, S., & Bernhard, G. (2008). Sorption of U (VI) onto an artificial humic substance-kaolinite-associate. *Chemosphere*, 72(10), 1441–1447.
- Schweitzer, G. E., Parker, F. L., Robbins, K., Sciences, R. A. of, Council, N. R., Affairs, P. and G., Development and Cooperation, S., Eurasia, O. for C. E. and, & Experience, C. on C. U. of R. C. R. C. and U. S. (2009). *Cleaning up Sites Contaminated with Radioactive Materials : International Workshop Proceedings*. National Academies Press.
- Serne. (2012). Hanford Site Vadose Zone Sediment Mineralogy-Emphasis on Central Plateau. Richland, WA. *Pacific Northwest National Laboratory*.

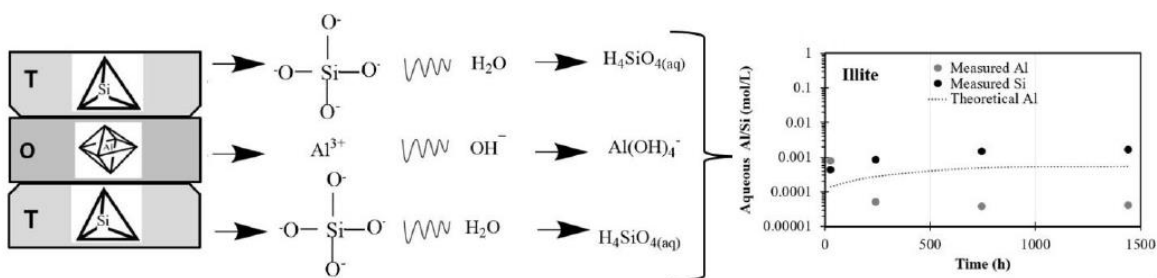
- Serne, Last, G. V., Gee, G. W., Schaef, H. T., Lanigan, D. C., Lindenmeier, C. W., Lindberg, M. J., Clayton, R. E., Legore, V. L., & Orr, R. D. (2008). *Characterization of vadose zone sediment: Borehole 299-E33-45 near BX-102 in the B-BX-BY waste management area*. Pacific Northwest National Lab.(PNNL), Richland, WA (United States).
- Service, R. (2018). Ammonia—A Renewable Fuel Made From Sun, Air, and Water— Could Power the Globe Without Carbon. *Science*, aau7489.
- Shutske, J. M. (1996). *Using anhydrous ammonia safely on the farm*. Minnesota Extension Service, University of Minnesota.
- Song, Yin, K., Wang, Y., Hermann, A., Liu, H., Lv, J., Li, Q., Chen, C., & Ma, Y. (2019). Exotic hydrogen bonding in compressed ammonia hydrides. *The Journal of Physical Chemistry Letters*, 10(11), 2761–2766.
- Sposito, G., Skipper, N. T., Sutton, R., Park, S., Soper, A. K., & Greathouse, J. A. (1999). Surface geochemistry of the clay minerals. *Proceedings of the National Academy of Sciences*, 96(7), 3358–3364.
- Stewart, B. D., Amos, R. T., Nico, P. S., & Fendorf, S. (2011). Influence of uranyl speciation and iron oxides on uranium biogeochemical redox reactions. *Geomicrobiology Journal*, 28(5–6), 444–456.
- Stumm, W., & Morgan, J. J. (1991). Aquatic chemistry. In *John Willey and Son, New York*. John Willey and Son.
- Szecsody, Bagwell, C., Mackley, R., & Hoyle, S. (2020). *Evaluation of Ammonia Discharge into PUREX Crib 216-A-37-1 and Nitrogen Species Fate in the Subsurface*.
- Szecsody, Truex, M. J., Qafoku, N. P., Wellman, D. M., Resch, T., & Zhong, L. (2013). Influence of acidic and alkaline waste solution properties on uranium migration in subsurface sediments. *Journal of Contaminant Hydrology*, 151, 155–175.
- Szecsody, Truex, M. J., Zhong, L., Johnson, T. C., Qafoku, N. P., Williams, M. D., Greenwood, W. J., Wallin, E. L., Bargar, J. D., & Faurie, D. K. (2012). Geochemical and Geophysical Changes during Ammonia Gas Treatment of Vadose Zone Sediments for Uranium Remediation. *Vadose Zone Journal*, 11(4).
- Szecsody, Truex, M., Zhong, L., Williams, M., Resch, C., & McKinley, J. (2010). Remediation of Uranium in the Hanford Vadose Zone Using Gas-Transported Reactants : Laboratory-Scale Experiments. *Contract*, January, 65.

- The Health Physics Society. (2020). *Antoine Henri Becquerel*. Environmental Health & Safety. <https://ehs.msu.edu/lab-clinic/rad/hist-figures/becquerel.html>
- Tro, N. J., Fridgen, T. D., Shaw, L., & Boikess, R. S. (2017). *Chemistry: A molecular approach*. Pearson Boston, MA.
- Truex, M. J., Szecsody, J. E., Qafoku, N., & Serne, J. R. (2014). Conceptual Model of Uranium in the Vadose Zone for Acidic and Alkaline Wastes Discharged at the Hanford Site Central Plateau. PNNL-23666. *Pacific Northwest National Laboratory, Richland, WA*.
- UNSCEAR. (2000). United Nations Scientific Committee on the Effects of Atomic Radiation. In *Sources and effects of ionizing radiation* (Vol. 2). United Nations New York.
- US Environmental Protection Agency. (1999). *Understanding Variation in Partition Coefficient, K_d, Values* (p. 212). Office of Air and Radiation.
- US Environmental Protection Agency. (2002). *Radionuclides in Drinking Water: A Small Entity Compliance Guide*.
- Vijay, A., Khandelwal, A., Chhabra, M., & Vincent, T. (2020). Microbial fuel cell for simultaneous removal of uranium (VI) and nitrate. *Chemical Engineering Journal*, 388, 124157.
- Wadt, W. R. (1981). Why uranyl ion(2+) is linear and isoelectronic thorium dioxide is bent. *Journal of the American Chemical Society*, 103(20), 6053–6057.
- Walls, J., Sharrard, C., Livens, F., Smith, J., Lloyd, J., Banford, A., Morris, K., Renshaw, J., Howard, B., & Pentreath, J. (2011). *Nuclear Power and the Environment*. Royal Society of Chemistry.
- Wang, Q., Zhu, C., Huang, X., & Yang, G. (2019). Abiotic reduction of uranium(VI) with humic acid at mineral surfaces: Competing mechanisms, ligand and substituent effects, and electronic structure and vibrational properties. *Environmental Pollution*, 254, 113110.
- Wehrli, B., Sulzberger, B., & Stumm, W. (1989). Redox processes catalyzed by hydrous oxide surfaces. *Chem. Geol*, 78(3–4), 167–179.
- Wellman, D. M., Gamerding, A. P., Kaplan, D. I., & Serne, R. J. (2008). Effect of particle-scale heterogeneity on Uranium(VI) transport in unsaturated porous media. In *Vadose Zone Journal* (Vol. 7, Issue 1, pp. 67–78).

- Xie, Y., Murray, C. J., Last, G. V., & Mackley, R. D. (2003). *Mineralogical and bulk-rock geochemical signatures of Ringold and Hanford Formation sediments*. Pacific Northwest National Lab., Richland, WA (US).
- Yuan, K. (2015). *Electrochemical Investigations of Redox Reactions of Uranyl (VI) on Magnetite and Computational Modeling of the UO₂-HfO₂ Solid Solution*. Doctoral dissertation.
- Zachara, J., Brown, C., Christensen, J., Davis, J. A., Dresel, E., Kelly, S., Liu, C., McKinley, J., Serne, J., & Um, W. (2007). *A Site-Wide Perspective on Uranium Geochemistry at the Hanford Site*.
- Zamora, M., Tracy, B. L., Zielinski, J. M., Meyerhof, D. P., & Moss, M. A. (1998). Chronic ingestion of uranium in drinking water: a study of kidney bioeffects in humans. *Toxicological Sciences*, 43(1), 68–77.
- Zamora, M., Zielinski, J. M., Moodie, G. B., Falcomer, R. A. F., Hunt, W. C., & Capello, K. (2009). Uranium in Drinking Water: Renal Effects of Long-Term Ingestion by an Aboriginal Community. *Archives of Environmental & Occupational Health*, 64(4), 228–241.
- Závodská, L., Kosorinova, E., Scerbakova, L., & Lesny, J. (2008). Environmental Chemistry of Uranium. *HV ISSN*, 1418–7108.
- Zhong, L., Szecsody, J. E., Truex, M. J., Williams, M. D., & Liu, Y. (2015). Ammonia gas transport and reactions in unsaturated sediments: Implications for use as an amendment to immobilize inorganic contaminants. *Journal of Hazardous Materials*, 289, 118–129.

CHAPTER II

Mineral Dissolution and Precipitation Processes under Highly Alkaline Conditions



This chapter was reproduced and adapted from Di Pietro, S.A., Emerson, H.P., Katsenovich, Y. Qafoku, N., and Szecsody, J. *Applied Clay Science*, **2020**, 189, 105520, <https://doi.org/10.1016/j.clay.2020.105520> with permission from Elsevier.

2 CHAPTER 2: MINERAL DISSOLUTION AND PRECIPITATION PROCESSES UNDER HIGHLY ALKALINE CONDITIONS

2.1 Abstract

The dissolution of phyllosilicate minerals exposed to high-pH environments was studied to quantify the influence of alkaline treatments and variable redox conditions on clay dissolution including incongruent dissolution phenomena. The objective of this research was to systematically quantify mineral dissolution with variable alkaline treatments and redox conditions for the first time. This study is focused on the dissolution of phyllosilicate minerals (illite, muscovite, and montmorillonite) under anaerobic and aerobic conditions using comparative solutions (sodium hydroxide and ammonium hydroxide) at similar hydroxide concentration. Batch data show that there is a rapid decrease in aluminum dissolution (< 240 h) and slow increase in silica dissolution over time (up to 1440 h). This trend was particularly evident for montmorillonite for which the greatest dissolution was observed with ammonium hydroxide treatment, likely due to intercalation of the polyatomic cation ammonium into the mineral's expandable layers. When comparing alkaline treatments, the strong base sodium hydroxide dissolved more of the mica minerals, illite and muscovite, likely due to ion-pairing between the silicate tetrahedra $[\text{SiO}_4]^{4-}$ and Na^+ cations in solution compared with weak base NH_4OH treatment. In addition, the decreasing redox changes in the absence of oxygen were similar, although the sodium hydroxide treatment had greater variability. For all investigated phyllosilicates, the calculated aqueous aluminum and silicon ratios over time were significantly different from the minerals' stoichiometric ratios. As a result, we conclude that incongruent dissolution occurred and suggest formation of secondary precipitates.

Understanding the potential for clay mineral alterations from interaction with alkaline solutions has implications for *in situ* remediation, mining operations, and waste interactions within the subsurface. This research shows that incongruent dissolution in phyllosilicate minerals occurs and will likely lead to secondary precipitation which may have long term physical and chemical impacts in the subsurface.

2.2 Introduction

Silicates and aluminosilicates comprise more than 75% of the Earth's continental crust (Dietrich & Skinner, 1979). Due to their abundance and specific properties (e.g. solubility and ion exchange capacity), clays present in the subsurface may be impacted by anthropogenic activities (Casey et al., 1993). In addition to alterations to clays naturally present, scientists may also place additional clay minerals into the subsurface for various purposes. For example, swelling clays, such as smectites, are used to seal wells and have been investigated for nuclear and hazardous waste repositories due to their swelling properties and sorption capacity (Bauer & Berger, 1998; Catalano & Brown Jr, 2005; Elert et al., 2015b; Gaucher & Blanc, 2006; Gautier et al., 2010; Joseph et al., 2017; Marsh et al., 2018a; West, 2008).

In the mining industry, waste in areas like Quebec, Canada and Redding, CA contain sulfide-rich minerals that generate acid mine drainage (AMD). When these highly reduced minerals encounter moisture and oxygen, mineral oxidation releases hydrogen cations and leads to a decrease in pH, releasing toxic metals and altering nearby minerals. A sustainable solution to AMD proposed by Doye and Duchesne is to neutralize the mine tailings with fine-grained alkaline materials, e.g. Ca-oxide and alumina cement, allowing for the pH to increase consequently adsorbing metals (Doye & Duchesne, 2003; Jönsson et al., 2005;

Song et al., 2018). For mineralized U deposits in Fernald, Ohio, ore extraction wastes are remediated via dilute solutions of oxidizers, e.g. ammonium bicarbonate and hydrogen peroxide. Further, alkaline leach methods are the primary technique for *in situ* U mining in the U.S. (Mason et al., 1997; Szecsody et al., 2013). Each of these operations may result in localized areas with highly alkaline porewaters, which may lead to significant alterations to local mineralogy.

In the case of legacy nuclear waste, former processing sites including Savannah River Site, Hanford Site, Idaho National Laboratory (formerly the National Reactor Testing Station), and Oak Ridge Reserve, aim to reduce transport of the major risk driving radionuclides (e.g., Pu, U, Np, Am, etc.) in the subsurface (Li & Kaplan, 2012). For example, the Hanford Site generated approximately 210,000 m³ of waste fluids with acidic co-contaminants, although some waste was over-neutralized to the alkaline range prior to disposal (Reynolds et al., 2018). In addition, ongoing remediation technologies may induce alkaline conditions in order to adsorb, co-precipitate, or coat heavy metals and radionuclides, e.g. ammonia (NH₃) gas in the vadose zone or sodium hydroxide (NaOH) injection to aquifers for U remediation (Emerson et al., 2017, 2018; Katsenovich et al., 2016, 2018; Qafoku, Ainsworth, Szecsody, & Qafoku, 2003; Szecsody et al., 2012, 2013). Injection of anhydrous NH₃ gas is also conducted for agricultural purposes as an effective source of nitrogen for crops as it is readily adsorbed by soil moisture (Shutske, 1996); however, it may also be utilized for pH manipulation of the subsurface for *in situ* remediation.

Due to both historic remedial actions and waste disposal, significant mineral alteration is found at legacy radioactive waste disposal sites and requires further investigation.

Therefore, the effects of prolonged exposure to alkaline solutions is the focus of this research. The U.S. DOE's Hanford Site in Washington State represents a valuable case study for dissolution and alteration of clay minerals due to waste release and potential remediation via alkaline injection. Uranium remediation via injection of NH_3 gas into vadose zone sediments has been considered previously (Szecsody et al., 2012), where dissolution of some aluminosilicates is induced, and subsequent precipitation of U silicates and aluminosilicate coatings on U surface phases may lead to decreased U mobility. Major aluminosilicate minerals in Hanford Site sediments include muscovite (9%), illite (2.8%), and montmorillonite (1.2%) (Qafoku et al., 2004; Serne et al., 2008). Although mica (e.g. illite and muscovite) and smectite (e.g. montmorillonite) minerals together constitute only 5-13% of the Hanford Site's total soil mass, they account for 40-60% of the total cation exchange capacity (CEC) of the bulk sediments (Serne et al., 2008).

The extent to which mineral dissolution occurs within the solid-liquid interface is dependent on exposure time and solution composition. Generally, dissolution occurs with an initial rapid rate, which gradually slows to reach steady state with respect to secondary reactions (Bibi et al., 2010; Szecsody et al., 2013; Youlton & Kinnaird, 2013). According to Crundwell's dissolution theory, phyllosilicates in alkaline solutions undergo dissolution in three steps: (1) aluminum atoms at the surface react with hydroxide ions, (2) silicate tetrahedra $[\text{SiO}_4]^{4-}$ detach from the solid surface, and products of steps one and two react with species in solution to form final products (Crundwell, 2014). The metal-oxygen bond detachment occurs in the first stage and is dependent on the bond strength. Because the bond dissociation energy of Si-O is $1.5\times$ stronger than Al-O, the breaking of the Si-O bond is considered the rate-limiting step in silicate dissolution (Lippert, 1960). For experiments

across an expanded range of solution pH (1.4 to 12.4), an initial Al release was confirmed with the previously mentioned theory, including at low temperatures (5- 20 °C) (Köhler et al., 2003).

Researchers reported incongruent dissolution of phyllosilicates under variable conditions (Lippert, 1960; Miranda-Trevino & Coles, 2003; Oelkers, 2001). For example, previous researchers have shown that incongruent dissolution and secondary phase formation of phyllosilicate minerals occurs in high pH environments (Elert et al., 2015b; Emerson et al., 2018; Mashal et al., 2004; Oda et al., 2014; Qafoku, Ainsworth, Szecsody, & Qafoku, 2003). However, few studies have compared alkaline conditions or treatments with relevance to contaminated sites such as the Hanford Site (Emerson et al., 2017, 2018; Galvan-Reyes et al., 2016; Panagiotopoulou et al., 2007; Qafoku, Ainsworth, Szecsody, & Qafoku, 2003). In sediments impacted by waste solutions released with high NaOH (Szecsody et al., 2012) or NaOH and NaNO₃ (Qafoku, Ainsworth, Szecsody, & Qafoku, 2003), significantly greater (i.e., three to eight times more) Si release to aqueous solutions occurred as compared to Al. Moreover, Köhler and team measured dissolution rates of illite and observed approximately 2:1 Si:Al release at pH greater than 11 with relatively low solid to solution ratios, which indicates that the solid to solution ratio is also important in these experiments (Köhler et al., 2003).

Previous studies also showed that the solid phase underwent geochemical changes (i.e., dissolution-precipitation reactions) under hyperalkaline conditions (Qafoku, Ainsworth, Szecsody, & Qafoku, 2003). For example hydrous silicate [e.g. Na-boltwoodite, Na₂(UO₂)SiO₄•1.5H₂O] precipitates formed in simplified conditions and in the presence of Hanford sediments (Katsenovich et al., 2016, 2018; Szecsody et al., 2013).

Similarly, Qafoku et al., observed feldspathoids in the cancrinite and sodalite groups upon SEM-EDS analysis as Al:Si molar ratios decreased from initial conditions with decreased aqueous Si after 200 days of reaction (Qafoku et al., 2004). Two different research teams also identified the aluminosilicate cancrinite $[\text{Na}_8\text{Al}_6\text{Si}_6\text{O}_{24}(\text{NO}_3)_2]$ from Hanford sediments extracted in the 200 East Area via SEM and XRD (Buck & McNamara, 2004; Qafoku et al., 2004; Szecsody et al., 2013; Wan et al., 2004). Studies confirmed similar aluminosilicate formation from zeolites (Kang & Egashira, 1997) and fly ash (Fernández-Jiménez et al., 2006) as well as alterations in sedimentary clays (e.g. Opalinus shale) (Chermak, 1992).

Select studies have also compared the effects of different alkaline treatments on mineral dissolution and alteration. For example, Panagiotopoulou et al. studied differences in aluminosilicate mineral leaching when reacted with highly concentrated alkali metal (KOH and NaOH) solutions for industrial applications at room temperature. These researchers found that metakaolin, a calcinated clay with slightly higher aluminum oxide (Al_2O_3) and quartz (SiO_2) content, dissolved 75.0 % of its Al and Si in NaOH while only 45.0 % in KOH solution in a 24 h contact-time (in 2.0 g/L batch solutions) (Panagiotopoulou et al., 2007). Duxson et al. noted similar trends for experiments when dissolving aluminosilicate geopolymers where NaOH liberated more Al and Si due to the $\text{Na}^+_{(\text{aq})}$ hydration shell, leading to “ion pairing” between the silicate anions coming from the phyllosilicates' tetrahedral layers and Na^+ cations from the alkaline treatment solution (Duxson et al., 2007). Furthermore, Emerson et al. observed that U removal increases along the alkaline trend $\text{NaOH} < \text{NH}_4\text{OH} < \text{NH}_3$ gas in batch experiments with U-spiked clay

minerals (5.0 g/L) and Hanford Site sediments (25 g/L) (Emerson et al., 2017, 2018; Szecsody et al., 2012).

Although previous research has shown that incongruent dissolution occurs under alkaline conditions for many minerals and sediments, there is a need to systematically compare the effects of different redox conditions and alkaline solutions on minerals. The objective of this research is to characterize the alterations (i.e., incongruent dissolution and formation of new precipitates) that occur as phyllosilicate clays undergo alkaline treatments representative of potential remediation options and historic waste disposal conditions including variable redox conditions for the first time. The present research aims to do so by comparing treatments with weak and strong base solutions and variable redox (aerobic to anaerobic) conditions on mineral dissolution. In this paper, results are presented for batch experiments conducted with similar free OH^- concentration (as 3.1 M NH_4OH and 0.01 M NaOH) exposed to illite, muscovite, or montmorillonite minerals. These experiments, conducted at room temperature and atmospheric pressure, were performed to closely monitor the release of cations (e.g. Al^{3+} , Si^{4+} , and $\text{Fe}^{2+/3+}$) into solution. These minerals are chosen due to their relevance to radionuclide remediation and representation of the weathering trend for phyllosilicate minerals (Hibbard, 2002; Qafoku, Ainsworth, Szecsody, & Qafoku, 2003; Szecsody et al., 2012).

2.3 Experimental Methodology

2.3.1 Materials

Experiments were conducted with three minerals: illite (IMt-2, Cambrian Hole, Silver Hill Mount, Clay Mineral Society), muscovite (Stoneham, Maine, Ward's Scientific), and montmorillonite (SWy-2, Crook County, Wyoming, Clay Mineral

Society). The minerals were washed prior to experiments via the following procedure. Suspensions (100 g/L) were mixed with 1.0 M NaCl prepared with ultrapure H₂O (with resistivity greater than 18 MΩ·cm, DIW), allowed to flocculate overnight, centrifuged at 4500 rpm in a benchtop centrifuge with a swing bucket rotor attachment (18,100 rcf, Thermo Scientific, Corvall ST 16R), then decanted and replaced with DIW. This process was repeated until the conductivity was less than 20 μS/cm to show that the majority of ions have been removed. Montmorillonite, however, was first suspended in 0.001 M HCl and then 0.5 mL of H₂O₂ to remove salts and limit redox active species (Boggs et al., 2015). Then, DIW was added to prior to conducting the same washing steps as illite and muscovite. After each step, the samples were centrifuged at 4500 rpm for 6 h for montmorillonite and 30 min for illite and muscovite and then the liquid was decanted. The longer centrifugation time was used for montmorillonite to aide in dewatering the expanding layers. Subsequently, minerals were dried for 6 days in an oven at 30 °C (LabNet International Inc.). In order to further dehydrate the expanding layers of montmorillonite, an additional drying step was conducted at 60 °C in a vacuum oven (Lindberg Blue M, ThermoScientific) at a pressure of 20 inches (in) Hg vacuum. After the 14-day drying period, the minerals were homogenized by crushing with a mortar and pestle as described previously (Emerson et al., 2018).

2.3.2 Mineral Characterization

2.3.2.1 Cation Exchange Capacity

The cation exchange capacity (CEC) was measured (Appendix, Table A.1) following the standard method developed by Lavkulich and Rhoades per ASTM D7503-10 (ASTM, 2010; Hendershot et al., 1993; Rhoades, 1983). Briefly, 0.4 g of air-dried

mineral was weighed and placed on a 2.5 μm ashless filter paper in a Büchner funnel and washed with four 30-mL portions of 1.0 M ammonium acetate and three 40-mL portions of isopropanol. A low suction (less than 10 kPa) was then applied to the filtering flask. It is important to note that each 40-mL portion was drained before the subsequent aliquot was added with all discarded at the end. Next, the isopropanol-washed soil was washed with four 50-mL portions of 1.0 M potassium chloride solution, again, allowing for drainage before continuing. The liquid phase recovered during this step was transferred into vials for analysis via an ammonia electrode (Orion 9512).

2.3.2.2 Average Particle Surface Area of Pure Minerals

The surface area of the minerals was determined from the corresponding nitrogen adsorption-desorption isotherms obtained at 77.35 K with a Micromeritics TriStar II (TriStar II 3020 V1.03) gas adsorption analyzer. Approximately 0.3 g of mineral was degassed at 383 K for 24 h with nitrogen gas. The specific surface area was determined using the Brunauer-Emmet-Teller (BET) methods (Brunauer et al., 1938) based upon the cross-sectional area of nitrogen (0.162 nm^2). Clay characterization for specific surface areas and CEC of pure minerals are given in the Appendix, Table A.1.

2.3.2.3 X-ray Diffraction (XRD) Analysis of Pure Minerals

Untreated illite, muscovite, and montmorillonite samples were analyzed by X-ray diffractometer (XRD) (Bruker GADD/D8 X-ray with Apex Smart CCD detector) at room temperature, humidity, and pressure. All peak positions were obtained by step-size goniometer scanning at 0.02 2θ intervals from $5^\circ - 38^\circ$ using $\text{CuK}\alpha$ x-rays at 40 kV. XRD chemical formulae and patterns are presented in Table A.1 and Figure A.1 in the Appendix, respectively.

2.3.2.4 Batch Dissolution Protocol

Previously washed minerals (33 g/L) were exposed to one of two solutions prepared in DIW: 1) 3.1 M NH_4OH (Fisher Chemical, 28 – 30% purity), and 2) 0.01 M NaOH (Fisher Chemical, 0.1 N \pm 0.5% purity). All three minerals were investigated under anaerobic and aerobic conditions in the presence of 0.01 M NaOH and 3.1 M NH_4OH solutions. The two alkaline solutions were used to target pH 12 in solutions (based on the dissociated OH^- concentration) to investigate potential impacts of basic remediation technologies on mineral dissolution. In addition, for each alkaline solution, a control was prepared (i.e., without minerals) to account for cation impurities in the base chemicals. Prior to contact time, the DIW was de-gassed with nitrogen gas or compressed air for 45 min for anaerobic and aerobic conditions, respectively. This step was conducted to remove oxygen and decrease dissolved CO_2 for anaerobic conditions and to equilibrate the DIW with gaseous oxygen and carbonate in air for aerobic conditions. Throughout experiments, vials were shaken at 40 rpm on an end-over rotator (Thermo Scientific Cel-Grow Tissue Culture and Fisher Scientific rotators for anaerobic and aerobic vials, respectively).

2.3.2.5 Sampling Protocol

Both pH (Thermo Scientific, 8175BNWP) and oxidation reduction potential (ORP, Mettler Toledo EM40-BNC, 30043106) were measured prior to removal of an aliquot for measurement of major cations. A three-point and a one-point calibration were completed prior to each set of measurements for the pH and ORP electrodes, respectively. Aliquots were extracted using a 1-mL Luer-lock syringe (Thermo Scientific) with a 0.20 μm polytetrafluoroethylene filter (PTFE, Tisch Scientific, Cat# SE4F13X03). Sampling was conducted at four different intervals: 24, 240, 745, and 1440 h. All samples were diluted in

a 1% HNO₃ solution for Si, Fe, and Al analysis by inductively couple plasma optical emission spectrometry (ICP-OES, Perkin Elmer 7300DV) or inductively coupled plasma mass spectrometry (ICP-MS, ThermoScientific iCAP RQ). During analysis, a scandium internal standard (High Purity Standards) was prepared (0.5 mg/L) for ICP-OES and injected simultaneously with the sample solutions. The instrument's minimum detectable concentration (MDC) for Si was 12 µg/L. Samples were also analyzed for Al and Fe on ICP-MS with a multi-element internal standard that included 1-10 µg/L of Sc, In, Y, Tb, Bi (High Purity Standards) with the following detection limits: Al 0.34 µg/L and Fe 0.71 µg/L.

2.4 Results

2.4.1 Mineral Dissolution Based on Aqueous Si

Figure 2.1 shows silicon (Si) dissolution from the investigated minerals as a function of time (24-, 240-, 745- and 1440-h) for both redox conditions and alkaline treatments (NaOH and NH₄OH) (see also Appendix, Figures A.3-7). With the exception of montmorillonite measuring significantly higher at the 24-h time point under anaerobic conditions with NH₄OH treatment, aqueous Si increased with time for all experimental conditions regardless of redox conditions or alkaline treatment. Because the aqueous Si concentrations continued to increase over the timescale of the experiments (60 days), these data suggest that equilibrium with respect to mineral dissolution was not reached. Although variable pH experiments were not conducted in this research, significant dissolution of Si was observed with this alkaline pH range (11.1 - 12.3). Further, previous investigations concluded that a larger amount of Si could be dissolved into alkaline solutions, up to 30

mmol/L in 24 h as compared to a maximum of 1.5 mmol/L in our experiments depending on the solid to solution ratio and equilibration time (Bauer & Berger, 1998; Jozefaciuk & Bowanko, 2002; Qafoku, Ainsworth, Szecsody, Qafoku, et al., 2003; Szecsody et al., 2012). Therefore, the observation of continuous and far from equilibrium dissolution shown in Figure 2.1 is consistent with previous work.

Silicon dissolution follows the trend montmorillonite > muscovite > illite under aerobic and anaerobic conditions based on the total Si measured in the aqueous phase over time for all conditions except for treatment with NaOH. For example, 155 ± 15 μmol of Si/g of mineral was measured in the aqueous phase after 60 days of montmorillonite reaction in NH_4OH solutions and aerobic conditions while only 53 ± 23 and 20 ± 3 μmol of Si/g of mineral was released from illite and muscovite, respectively, under equivalent conditions. This trend is similar throughout, although, for aerobic conditions in 0.01 M NaOH, montmorillonite dissolution was significantly lower than in NH_4OH (50 ± 4 versus 155 ± 15 μmol of Si/g of mineral) (Figure 2.1 and Appendix, Figure A.5.). However, a potential artifact of sampling for montmorillonite reacted with NaOH will be discussed in section 3.3 during comparison of treatment solutions. Regardless of treatment, muscovite and montmorillonite showed approximately twice as much dissolution after 745 h of alkaline exposure as compared to illite. A previous study presented similar observations where minor cation dissolution from illite occurred as compared to muscovite and montmorillonite minerals during a one-week treatment with ammonia gas (Szecsody et al., 2012). Such trends are also consistent with other dissolution studies (Jozefaciuk & Bowanko, 2002; Szecsody et al., 2013). For comparison, these data were fit with pseudo first and second order equations to estimate dissolution rates (Appendix, Tables A2-5) with

the best fits observed for first order models (R^2 of 0.44 to 0.94 for Si and 0.13 to 0.49 for Al). The fits of these models with experimental data are variable likely due to secondary precipitation as discussed in section 3.2, especially when considering the less soluble Al cation as fits showed significantly lower correlation (Appendix, Tables A4-A5). Therefore, only general discussion of trends with these fits will be included as they are not directly related to mechanistic reactions due to multiple phenomena likely simultaneously occurring (i.e., dissolution and precipitation). When comparing reaction constants, k , for the different treatments across minerals investigated, there is no clear trend for the first-order models though they provide better predictions. However, when comparing OH^- ion affinity between the alkaline treatments, NaOH shows similar k values, especially for mica minerals. Previous studies have confirmed the general trend that dissolution rates increase with increasing pH in similar systems (Carroll et al., 2016; Crundwell, 2014; Köhler et al., 2003; Langmuir, 1997; Rozalen et al., 2009). Walker suggests that the increased rate with pH is due to changes in the mineral surface charge with pH (Walther, 1996). It can also be related to the adsorption of OH^- ions as proposed for quartz and feldspar dissolution under alkaline conditions (Xiao & Lasaga, 1996).

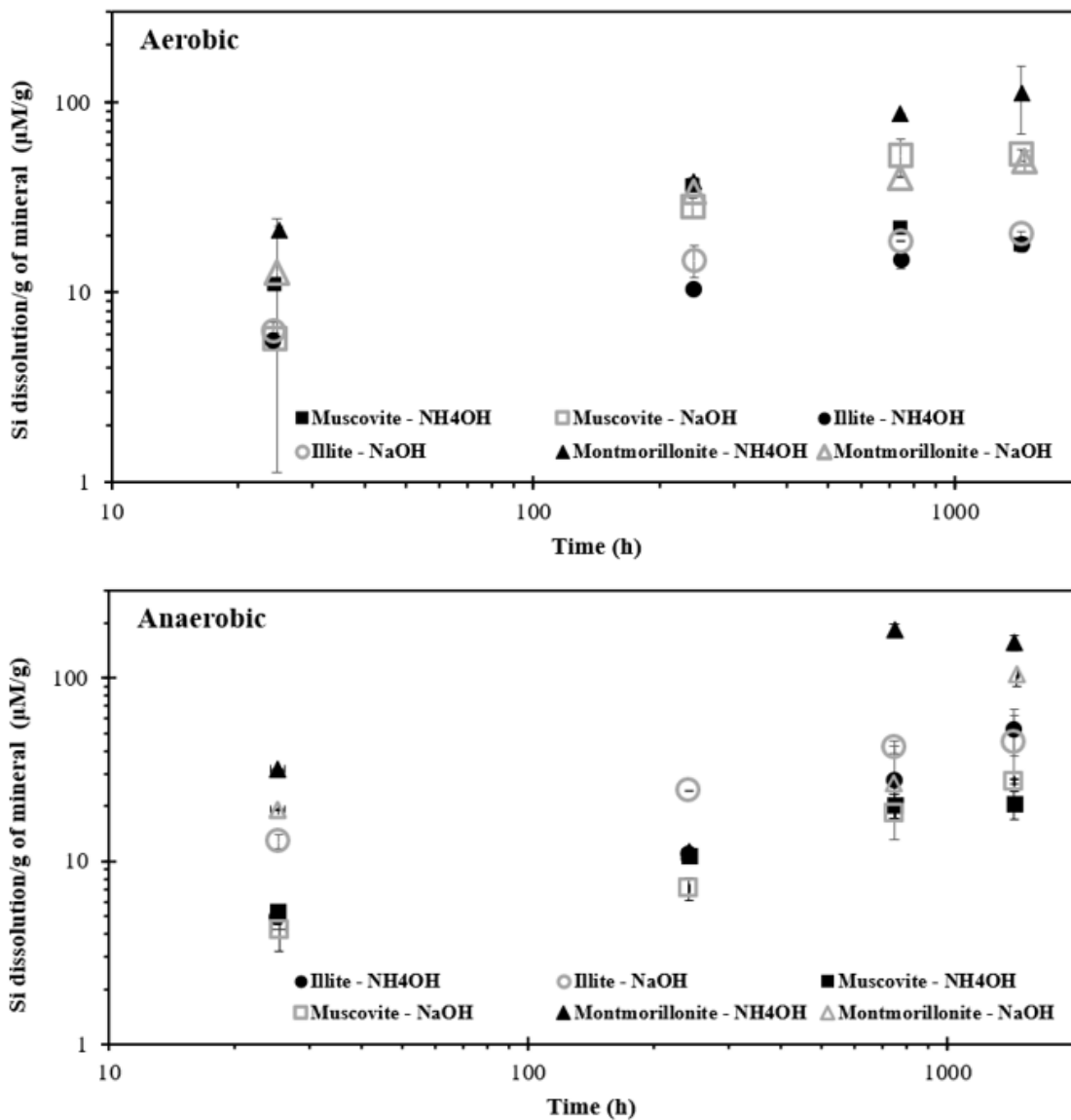


Figure 2.1. Aqueous Si, in $\mu\text{M/g}$, with time for batch experiments with 33 g/L minerals, including: montmorillonite (triangles), muscovite (squares), and illite (circles) with exposure to 3.1 M NH_4OH (closed black) and 0.01 M NaOH (open gray) under aerobic (top) and anaerobic (bottom) conditions. Note: error is based on analysis of triplicate samples.

Si solubility increases at pH values above the isoelectric point (\cong pH 9) due to silicate anion $[\text{SiO}(\text{OH})_3]^-$ formation (Alexander et al., 1954). This phenomenon occurs because, at elevated pH, the net negative charge from the solid phase and the high

proportion of the silicate ion in solution increases sharply. However, previous research also observed a correlation with surface area (Iler, 1979), although the low surface area muscovite (Appendix, Table A.1) does not represent a clear trend. Muscovite represented the lowest dissolution of the three minerals under aerobic conditions but greater dissolution than illite under anaerobic conditions. Further, dissolution rates are within an order of magnitude of those observed for montmorillonite and illite, although the surface area is more than two orders of magnitude lower.

Bauer and Berger compared smectite and kaolinite dissolution rates at 35 and 80 °C at various solid to liquid ratios for highly alkaline KOH solutions and noted differences amongst the minerals. For smectites [family of tetrahedral (T) - octahedral (O) - tetrahedral (T) layer aluminosilicate minerals including montmorillonite], dissolution was 1-2 orders of magnitude lower than kaolinite, a naturally occurring T-O aluminosilicate clay across both temperatures. The authors proposed that it was due to the difference in surface charge and mineral structure. While the rate limiting step for kaolinite is the O layer, in the case of smectites, it is the T layer. It is likely that the Al sites in the tetrahedral layer are more reactive than the inner Si-octahedral kaolinite layer (Bauer & Berger, 1998). As the OH⁻ ions are more accessible to the outer tetrahedral layer, Al detaches first from the surface. Dissolution is then followed by the silica tetrahedra and, as a result, increases the rate of dissolution. This mechanism confirms the theory proposed by Crundwell (Appendix, Figure A.2) and is expected to occur for phyllosilicate minerals investigated in this study contain two T layers (Crundwell, 2014). Further, the effect may also be impacted by surface area. Although Bauer and Berger (1998) did not observe changes in surface area with

dissolution and the surface area of montmorillonite was greater than kaolinite (64 vs. 11.7 m²/g) in other systems, the effect of available surface area may need to be considered.

2.4.2 Evidence for Incongruent Dissolution Under Alkaline Treatments

Figure 2.2 shows Al was removed under all conditions and minerals investigated while Figure 2.3 compares aluminum (Al) and silicon (Si) dissolution from investigated minerals as a function of time (24-, 240-, 745- and 1440-h) for both alkaline treatments (NaOH and NH₄OH) under anaerobic conditions with the results for aerobic conditions. The minerals analyzed showed similar trends across all conditions: aqueous Si concentrations increased with time and while aqueous Al was initially similar to or higher than Si, it quickly decreased as a function of time. Si and Al exhibited the greatest and lowest aqueous concentrations, respectively, after 60 days of reaction with approximately an order of magnitude difference. Similar trends were observed under aerobic conditions (Appendix, Figures A.4-5). When comparing aqueous Al measurements across sampling times, there is a significant decrease with time for all minerals Figure 2.2. This behavior is most evident after the first 24 h, while Si continues to increase across the experiments (up to 1440 h).

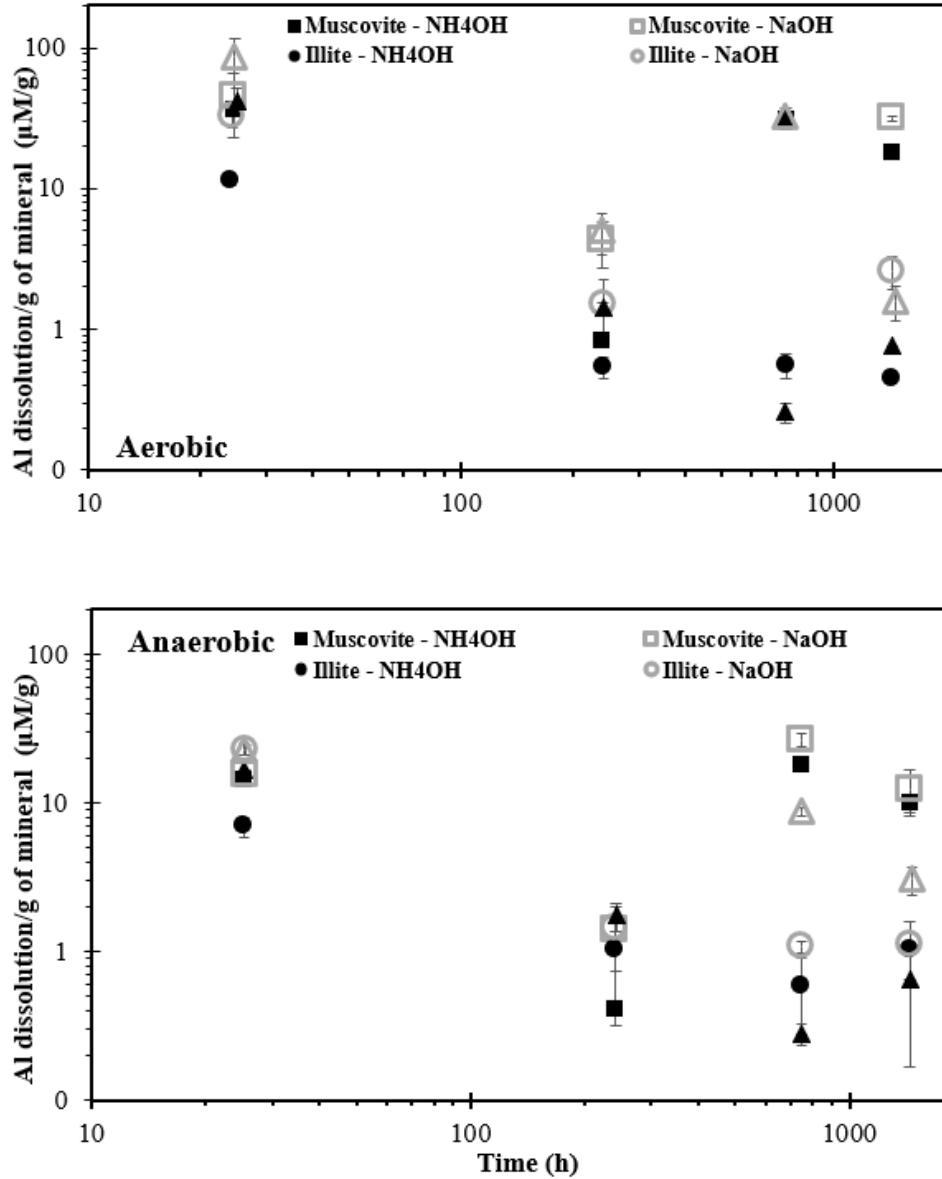


Figure 2.2. Aqueous Al, in $\mu\text{M/g}$, with time for batch experiments with 33 g/L minerals, including: montmorillonite (triangles), muscovite (squares), and illite (circles) with exposure to 3.1 M NH_4OH (closed black) and 0.01 M NaOH (open gray) under aerobic (top) and anaerobic (bottom) conditions. Note: error is based on analysis of triplicate samples.

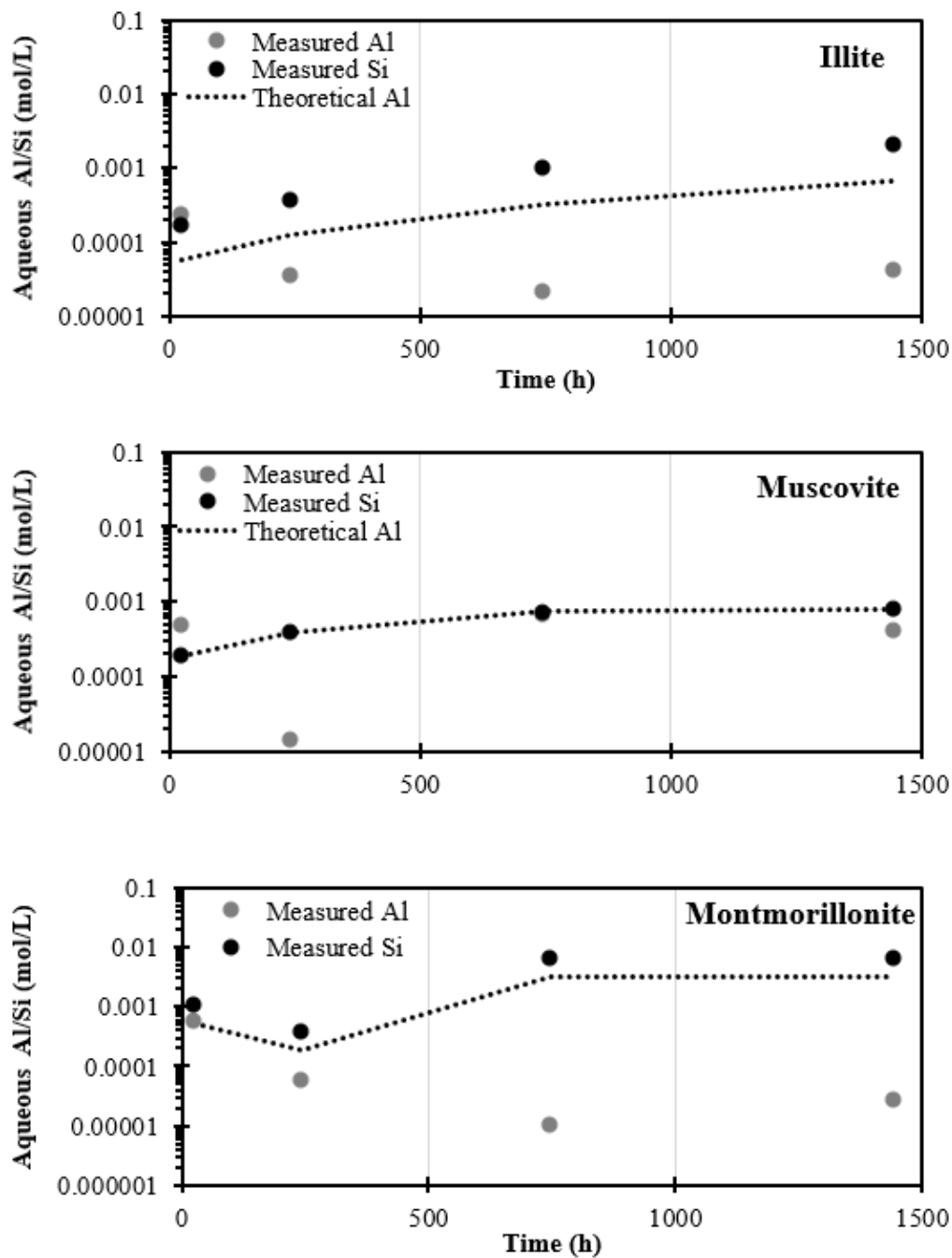


Figure 2.3. Aqueous Si (black) and Al (gray), in mol/L after reaction of 33 g/L suspension of minerals [illite (top), muscovite (middle) and montmorillonite (bottom)] over time (24-, 240-, 745- and 1440-h) with 3.1 M NH_4OH under anaerobic conditions, dashed lines represent congruent Al dissolution based on measured Si in the aqueous phase.

A focus of our experiments was to identify the extent of incongruent dissolution occurring in these systems based on a comparison of Al:Si ratios in the aqueous phase versus the theoretical ratio in the solid phase (Figure 2.3 and Appendix, Figures A.3-6). Figure 2.3 compares Al and Si measured in the aqueous phase with the theoretical amount of Al expected based on the mineral's chemical formula and measured aqueous Si (Appendix, Table A.1. Chemical Analysis (CEC and BET) and Theoretical Ratios for Minerals Table A.1). These values are calculated by dividing the measured aqueous Si concentration by the theoretical Si:Al ratio to estimate the theoretical Al. Figure 2.3 results show that significantly less Al is measured in the aqueous phase than expected likely due to secondary precipitation (Bibi et al., 2011; Emerson et al., 2018; Qafoku et al., 2003a). It should be noted that we cannot identify whether total aqueous Si is decreased due to secondary precipitation, although it is expected based on previous research at high pH and may remove Al as well as some other heavy metals (Iler, 1979). These data also support the theory that the poor fits for kinetics in the previous section are in part due to secondary precipitation which makes it impossible to resolve kinetic dissolution rates in this system.

The initial observation of aqueous Al at concentrations similar to or greater than Si at 24 h was likely due to the relative ease in cleavage of Al-O bonds compared to Si-O bonds at the initial stage of mineral dissolution (Appendix, Figure A.2a). Such bond cleavage causes Si to be the rate limiting step for Al dissolution over time (Appendix, Figure A.2b) (Bibi et al., 2011; Crundwell, 2014; Oelkers, 2001). Secondly, Al is removed from the surface and as a result of its relatively low solubility, secondary phase formation is likely to occur. Previous researchers have suggested similar phenomena (Emerson et al., 2017; Jozefaciuk & Bowanko, 2002; Qafoku, Ainsworth, Szecsody, Qafoku, et al., 2003;

Szecsody et al., 2013). For example, work done by Szecsody *et al.* noted a lesser dissolution of Al in comparison to Si in the alkaline pH range, particularly with NaOH treatment (Szecsody et al., 2013). Qafoku et al. conducted batch studies with Hanford sediments and also noted a significant dissolution rate increase for Si and a decrease for Al in the presence of NaOH (Qafoku et al., 2004), supporting our research in Figure 2.1 and 2.2. Although Qafoku and team's experiments were conducted at lower mineral concentration (10 g/L) and higher ionic strength (1.0 M) and pH (13.1-13.8), they noted that Al precipitated more than Si based on its lower solubility (Qafoku et al., 2003). These trends are similar to our results.

Numerous studies observed aluminosilicate secondary phase formation, such as sodalite, analcine, and cancrinite upon alkaline-treatment noting that stoichiometric dissolution is difficult due to secondary precipitation of Al (Buck & McNamara, 2004; Chermak, 1992; Fernández-Jiménez et al., 2006; Kang & Egashira, 1997; Qafoku et al., 2004; Rozalen et al., 2009; Szecsody et al., 2013; Wan et al., 2004). However, the comparison of both alkaline treatments presented in this research (NaOH and NH₄OH) have been limited in studies, except for the recent work of Emerson and Szecsody which was conducted for limited time points under aerobic conditions (Emerson et al., 2017; Szecsody et al., 2012). These authors predicted secondary phases including chrysotile, sepiolite, diaspore, and gibbsite based on aqueous ions measured after reaction of kaolinite with artificial groundwater and NaOH and NH₄OH with equilibrium, thermodynamic predictions using Geochemist Workbench (Emerson et al., 2018).

2.4.3 Effect of Alkaline Treatments

Figure 2.4 compares aqueous Si after mineral exposure to NaOH and NH₄OH alkaline treatments under aerobic conditions across all sampling events (24-, 240-, 745-, and 1440 h) (see Appendix, Figures A.4-5 for additional aerobic comparison and A.6-7 for anaerobic conditions). In general, the investigated minerals display no clear trend likely due to the complexity of interactions. While montmorillonite showed more dissolution with NH₄OH solution, illite and muscovite were generally lower throughout the 1440 h reaction time period with almost negligible differences between the two alkaline treatments. Figure 2.4 shows that muscovite and illite dissolved approximately six times less than montmorillonite in the presence of NH₄OH based on the final aqueous Si measurement. It is possible that the NH₄⁺ cation (1.43 Å atomic radius) leads to greater dissolution as previous work has shown that it may be readily intercalated in the interlayer basal spacing of montmorillonite (Bhiwankar & Weiss, 2006; Jorgensen & Weatherley, 2003). On the contrary, Na⁺ has an atomic radius of 0.95 Å (Tro et al., 2017). Although these radii may be similar, NH₄⁺ is ranked higher than Na⁺ in the replacement of ions for smectites (Gautier et al., 2010). Furthermore, smectites are commonly intercalated with quaternary ammonium salts to act as ion exchanging agents and to expand their interlayer basal spacing for X-ray diffraction. Increased flocculation due to the increased ionic strength from both alkaline solutions and mineral dissolution may also reduce dissolution with time due to less available surface area. When comparing alkaline treatments, Al concentrations in the aqueous phase were greater with NaOH versus NH₄OH solutions across all minerals, especially under aerobic conditions (Figure 2.2). Emerson et al. noted this effect when comparing similar alkaline treatments (i.e., NH₄OH vs. NaOH) with the phyllosilicate

mineral kaolinite for limited samples (Emerson et al., 2017). This is likely due to effects of molecular (NH_4OH becoming mostly NH_3 at elevated pH) versus ionic species (NaOH dissolving into Na^+ and OH^-) on solubility (Langmuir, 1997). Panagiotopoulou *et al.* also investigated the effect of alkali metals (i.e., K^+ and Na^+) in aluminosilicate minerals (2.0 g/L) at room temperature. These researchers found that metakaolin, a calcinated clay with slightly higher aluminum oxide (Al_2O_3) and quartz (SiO_2) content, had dissolved 75% of its Al and Si in NaOH while only 45% in KOH solution in a 24 h contact-time (Panagiotopoulou et al., 2007). Duxson *et al.* noted the same effect when comparing K^+ and Na^+ cations when dissolving aluminosilicate geopolymers and showed that NaOH liberates more Al and Si due to the $\text{Na}^+_{(\text{aq})}$ hydration shell leading to “ion pairing” between the silicate anions from the phyllosilicates' tetrahedral layers and Na^+ from the alkaline treatment solution (Duxson et al., 2007).

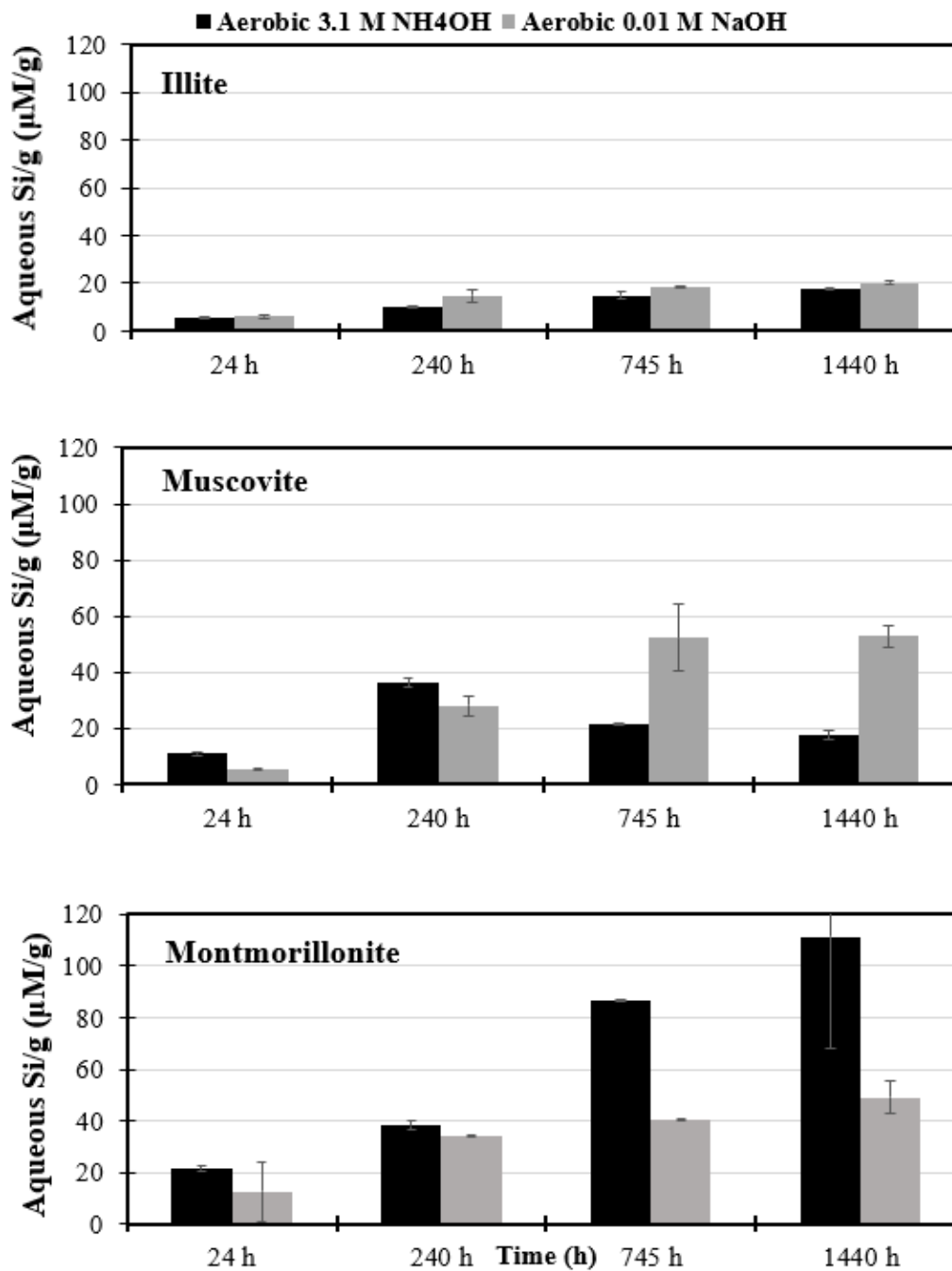


Figure 2.4. Comparison of Si removal during alkaline treatments (3.1 M NH₄OH - black and 0.01 M NaOH - gray) for minerals (33 g/L) illite (top), muscovite (middle) and montmorillonite (bottom) under aerobic condition. Note: error bars are based on analysis of triplicate samples.

Cations from the alkaline treatments (i.e., NH_4^+ and Na^+) can also have a significant influence on mineral dissolution processes. NH_4OH and NaOH have dissociation constants, K_b , of 1.76×10^{-5} and ~ 1 , respectively (Tro et al., 2017). Therefore, this study was designed to reach similar OH^- ion concentrations in solution for both alkaline treatments in order to reach similar pH. It was exceptionally difficult to filter the NaOH solution, especially for the expandable mineral montmorillonite. Due to both the nonpolar filter material (PTFE) and impacts of the solutions on mineral phases, the filterability of the solutions was decreased. Because NaOH is a strong base, its complete dissociation leads to polar Na^+ cations in solution or, at sampling time, in contact with the filter. The electrostatic repulsion between the $\text{Na}^+_{(\text{aq})}$ hydration shell and the PTFE filter likely led to difficulty in filtering and may explain the higher standard deviation. This cation polarity may also explain the high standard deviation observed in montmorillonite exposed to NH_4OH treatment as a similar concentration of NH_4^+ would be expected (although much higher concentration of the molecular species, NH_3) in solution as compared to NaOH due to a greater concentration of NH_4OH added to account for incomplete dissociation (Figure 2.4, bottom). In addition, the increased ionic strength will increase flocculation due to compression of the electrical double layer. For montmorillonite, flocculation may be further impacted by cations entering the interlayer basal spaces enhancing expansion of the interlayer. Based on the challenges during the initial 24-h sampling, longer centrifuge periods and multiple syringe filters were used to reduce error. Overall, these challenges did not significantly impact results based on the consistency in observed trends.

2.4.4 Effect of Redox and pH Conditions

Figure 2.5 shows ORP and pH measurements for investigated minerals as measured at the end of experiments. As expected, the systems prepared in the absence of oxygen reached reducing conditions based on negative ORP measurements. The opposite holds true for aerobic conditions. However, differences in ORP were also observed depending on the alkaline solution to which the mineral was exposed. In general, pH values were consistent throughout the experiments for both redox conditions (Appendix, Figure A.8). The standard deviation in pH was 0.72 and 1.1 units for anaerobic and aerobic conditions, respectively, across both treatments. It is possible that the greater range in pH for aerobic samples could be due to absorption of carbon dioxide from air. Further, the pH is generally greater for NH_4OH treatment indicating that slightly greater OH^- was added during adjustment as compared to NaOH . For aerobic conditions, ORP was approximately 100 mV higher in measurements for NaOH than in the NH_4OH solution. Emerson and team noted a similar trend in ORP between NaOH and NH_4OH alkaline treatment for several phyllosilicate minerals (Emerson et al., 2018). NH_3 gas application (as opposed to solutions) for remediation may enhance displacement of oxygen and carbon dioxide leading to more reducing conditions in the short term.

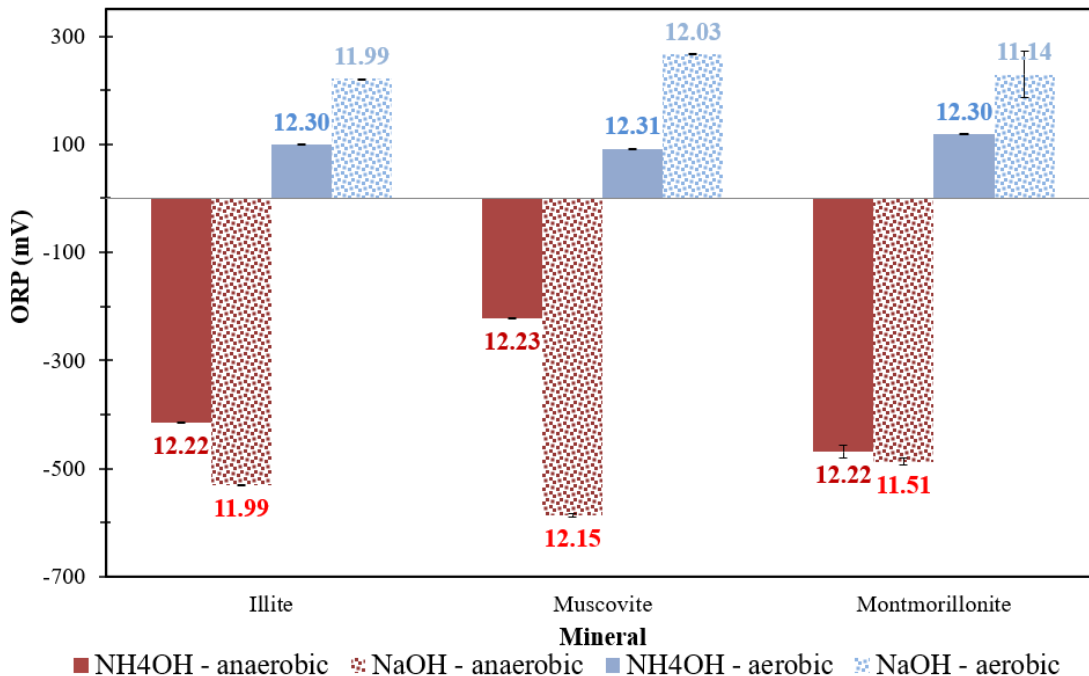


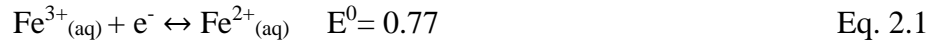
Figure 2.5. ORP, in mV, measurements for investigated minerals under anaerobic (red) and aerobic (light blue) conditions exposed to alkaline treatments (NaOH – pattern and NH₄OH – solid) after two months of reaction. Note: values printed above and below bars correspond to pH measurements and error bars are based on analysis of triplicate samples.

Trends in ORP for montmorillonite under aerobic and anaerobic conditions were similar. However, montmorillonite batch systems under anaerobic conditions fluctuated the least in ORP between the two alkaline treatments as compared to illite and muscovite which suggests it is influenced by redox sensitive Fe in the mineral. When comparing Fe dissolution across the phyllosilicate minerals, the trend follows montmorillonite>illite>muscovite (not shown as most measurements were below detection limits), as depicted in Figure 2.6. Both illite and montmorillonite minerals showed significant dissolution between 24- and 240-h contact-time for NaOH alkaline treatment with a decrease after 240 h potentially due to secondary precipitation. It is interesting to note that for montmorillonite Si dissolution was greater with NH₄OH treatment (likely due

to ammonium ion intercalation in the smectite's interlayer, section 2.4.3), Fe dissolution is greater with the strong base (NaOH) under anaerobic conditions. Research analyzing Hanford Site sediments under hyperalkaline (pH 13.4-14.0) conditions observed a relatively rapid (within four hours) Fe release to the aqueous phase in NaOH and NaNO₃ (Qafoku et al., 2003a; Qafoku et al., 2003b). In both studies, an ion-pairing effect between hydroxide ions from the solution and Fe from the phyllosilicate mineral structure likely caused dissolution under strong base alkaline treatment.

Because the dissolution of Fe was greater for anaerobic conditions, this suggests reduction of ferric, Fe³⁺, to more soluble ferrous, Fe²⁺, iron species (Figure 2.6). Work conducted by Schoonheydt and Johnston observed a reduction in solid phase Fe in anaerobic conditions, leading to an increase in CEC due to Fe reduction (Schoonheydt & Johnston, 2013). Further, according to our XRD characterization (Appendix, Figure A.1, top and bottom), illite and montmorillonite contain structural Fe³⁺. Because Fe is intrinsically present in its oxidized state, reducing conditions (i.e., anaerobic system) may enhance the solubility of Fe-oxides by reductive dissolution by up to four orders of magnitude as compared to acid/neutral pH ranges (Cornell & Schwertmann, 2003). The insignificant difference in ORP measurements for montmorillonite may suggest redox conditions moderated based on the formation of similar secondary Fe-oxides under both aerobic and anaerobic conditions. According to Eq. 2.1, the highly positive redox potential leads to Fe²⁺_(aq) species be in solution. Hydrolysis reactions (Eq. 2.2) eventually result in inorganic solid Fe(II) or Fe (III) hydroxide formation which may transform to different iron oxide and oxyhydroxides, where x represents each successive hydrolysis reaction

(Stumm & Morgan, 1991). As a result, such formation is particularly important for U-sequestration.



2.5 Discussion

The focus of this study was to identify differences in dissolution for phyllosilicate minerals following alkaline treatment under variable redox conditions. Removal of Al and Si to the aqueous phase upon treatment was used to observe mineral dissolution. Illite, muscovite, and montmorillonite demonstrated a steady increase in Si throughout the 60-day contact-time. Contrary to Si, there was a preferential release of Al over Si at the first sampling time followed by a decrease in aqueous Al. Both trends were generally observed throughout all experimental conditions, regardless of redox or alkaline condition. The significant change in dissolution of minerals at elevated pH and likely secondary mineral formation was observed in previous studies (Buck & McNamara, 2004; Chermak, 1992; Fernández-Jiménez et al., 2006; Kang & Egashira, 1997; Qafoku et al., 2004; Szecsody et al., 2013; Wan et al., 2004). This conclusion is also supported by the generally poor correlation of first and second order models with dissolution results.

As mentioned in section 2.4.2, all studied minerals present non-stoichiometric dissolution regardless of treatment or redox condition. However, Figure 2.3 distinctly displays incongruent behavior particularly for anaerobic conditions, although it is unclear if this is due to incongruent dissolution or secondary precipitation. Qafoku *et al.*, observed both dissolution and precipitation processes controlling the dissolution of Si and Fe after

1000 h (Qafoku et al., 2003a, b). Further, Rozalen et al. recognized the difficulty in stoichiometric ratios at and above neutral pH due to precipitation and/or sorption of Al and Fe secondary precipitates (Rozalen et al., 2009). The aqueous Fe concentration observed in our experiments likely lead to a steady state with respect to dissolution and precipitation processes over time.

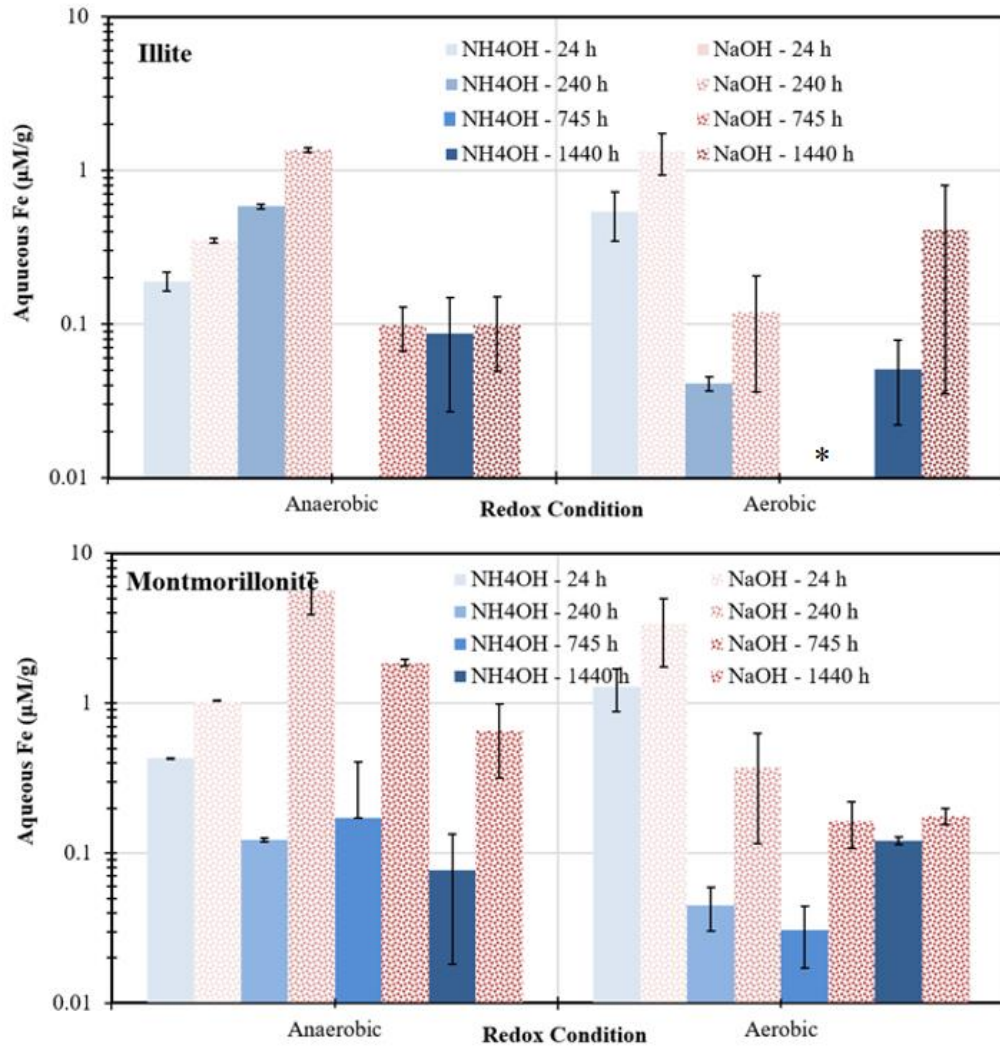


Figure 2.6. Total Fe dissolution with variable redox conditions for illite (top) and montmorillonite (below) across all sampling events (24-, 240-, 745-, 1440 h) for NH₄OH (solid) and NaOH (pattern) alkaline treatment with color darkening with time. Note*: missing measurements for illite mineral at 745 h sampling were below limit of detection; error based on analysis of triplicate samples.

When comparing alkaline treatments, the strong base NaOH dissolved more of the mica minerals, illite and muscovite. This is likely due to ion-pairing between Si tetrahedra and Na cations in solution. Montmorillonite, however, dissolved more with NH₄OH treatment. This is because of its interlayer basal spacing, which has been shown to intercalate the NH₄⁺ cation into the expandable layer causing greater dissolution due to greater available surface area interacting with solutions. ORP measurements were significantly different when compared by treatment, with a 100 mV higher measurement for NaOH than in NH₄OH solution. Although it is still unclear whether it is due to an unidentified interaction of solutions and mineral structures, it was noted that the ORP measurements of the alkaline solutions in contact with montmorillonite did not shift as significantly in anaerobic conditions. This suggests that removal is due from the redox sensitive element Fe as it increased in solution up to 240 h followed by a sharp decrease thereafter likely due to secondary precipitation. For all investigated phyllosilicate minerals, montmorillonite exhibited the most Al and Si dissolution at the first and last sampling event, respectively, confirming Crundwell's hypothesis that dissolution is due first to the weaker cleavage of Al-O bonds, followed by larger Si-O bond energy dissolution (Crundwell, 2014). On the contrary, illite dissolved the least, especially for aerobic conditions similar to previous observations (Jozefaciuk & Bowanko, 2002; Szecsody et al., 2012, 2013).

2.6 Conclusion

This unique study considered variable redox conditions and alkaline treatments in parallel for the first time for a series of phyllosilicate clay minerals. Results showed significant dissolution occurs upon exposure to highly alkaline (pH greater than 11)

solutions with slightly greater dissolution under anaerobic conditions. These observations suggest secondary precipitation may be an effective method for sequestration of contaminants within newly formed, low solubility aluminosilicate minerals. Previous researchers have shown that soluble contaminant cations, such as Cs, U, and Sr are likely to be sequestered and sorb to the newly formed minerals (Elert et al., 2015a; Mashal et al., 2004; Qafoku et al., 2003b). However, future work will focus on identification of secondary minerals by using thermodynamic predictions and determination of their ability to incorporate contaminants.

2.7 References

- Alexander, G. B., Heston, W. M., & Iler, R. K. (1954). The solubility of amorphous silica in water. *The Journal of Physical Chemistry*, 58(6), 453–455.
- ASTM. (2010). Standard test method for measuring the exchange complex and cation exchange capacity of inorganic fine-grained soils. *ASTM D7503-10*.
- Bauer, A., & Berger, G. (1998). Kaolinite and smectite dissolution rate in high molar KOH solutions at 35 and 80 C. *Applied Geochemistry*, 13(7), 905–916.
- Bhiwankar, N. N., & Weiss, R. A. (2006). Melt intercalation/exfoliation of polystyrene–sodium-montmorillonite nanocomposites using sulfonated polystyrene ionomer compatibilizers. *Polymer*, 47(19), 6684–6691.
- Bibi, I., Singh, B., & Silvester, E. (2011). Dissolution of illite in saline–acidic solutions at 25 C. *Geochimica et Cosmochimica Acta*, 75(11), 3237–3249.
- Bibi, I., Singh, B., & Silvester, E. (2010). Dissolution of phyllosilicates under saline acidic conditions. *19th World Congress of Soil Science, Soil Solutions for a Changing World*, 1(6).
- Brunauer, S., Emmett, P. H., & Teller, E. (1938). Adsorption of gases in multimolecular layers. *Journal of the American Chemical Society*, 60(2), 309–319.
- Buck, E. C., & McNamara, B. K. (2004). Precipitation of Nitrate–Cancrinite in Hanford Tank Sludge. *Environmental Science & Technology*, 38(16), 4432–4438.

- Carroll, S., Smith, M., & Lammers, K. (2016). *Chlorite, Biotite, Illite, Muscovite, and Feldspar Dissolution Kinetics at Variable pH and Temperatures up to 280 C*.
- Casey, W. H., Westrich, H. R., Banfield, J. F., Ferruzzi, G., & Arnold, G. W. (1993). Leaching and reconstruction at the surfaces of dissolving chain-silicate minerals. *Nature*, 366(6452), 253–256.
- Catalano, J. G., & Brown Jr, G. E. (2005). Uranyl adsorption onto montmorillonite: Evaluation of binding sites and carbonate complexation. *Geochimica et Cosmochimica Acta*, 69(12), 2995–3005.
- Chermak, J. A. (1992). Low temperature experimental investigation of the effect of high pH NaOH solutions on the Opalinus Shale, Switzerland. *Clays and Clay Minerals*, 40(6), 650–658.
- Cornell, R. M., & Schwertmann, U. (2003). *The iron oxides: structure, properties, reactions, occurrences and uses*. John Wiley & Sons.
- Crundwell, F. K. (2014). The mechanism of dissolution of minerals in acidic and alkaline solutions: Part II Application of a new theory to silicates, aluminosilicates and quartz. *Hydrometallurgy*, 149, 265–275.
- Dietrich, R. V., & Skinner, B. J. (1979). *Rocks and rock minerals*.
- Doye, I., & Duchesne, J. (2003). Neutralisation of acid mine drainage with alkaline industrial residues: laboratory investigation using batch-leaching tests. *Applied Geochemistry*, 18(8), 1197–1213.
- Duxson, P., Fernández-Jiménez, A., Provis, J. L., Lukey, G. C., Palomo, A., & van Deventer, J. S. J. (2007). Geopolymer technology: the current state of the art. *Journal of Materials Science*, 42(9), 2917–2933.
- Elert, K., Pardo, E. S., & Rodriguez-Navarro, C. (2015a). Alkaline activation as an alternative method for the consolidation of earthen architecture. *Journal of Cultural Heritage*, 16(4), 461–469.
- Elert, K., Pardo, E. S., & Rodriguez-Navarro, C. (2015b). Mineralogical evolution of di- and trioctahedral smectites in highly alkaline environments. *Clays and Clay Minerals*, 63(6), 414–431.
- Emerson, H. P., Di Pietro, S., Katsenovich, Y., & Szecsody, J. (2017). Effects of ammonium on uranium partitioning and kaolinite mineral dissolution. *Journal of Environmental Radioactivity*, 167.

- Emerson, H. P., Di Pietro, S., Katsenovich, Y., & Szecsody, J. (2018). Potential for U sequestration with select minerals and sediments via base treatment. *Journal of Environmental Management*, 223.
- Fernández-Jiménez, A., de la Torre, A. G., Palomo, A., López-Olmo, G., Alonso, M. M., & Aranda, M. A. G. (2006). Quantitative determination of phases in the alkaline activation of fly ash. Part II: Degree of reaction. *Fuel*, 85(14), 1960–1969.
- Gallucci, M. (2020). What to do with 177 giant tanks of radioactive sludge. *IEEE Spectrum*, 57(5), 24–33.
- Galvan-Reyes, C., Fuentes-Aceituno, J. C., & Salinas-Rodríguez, A. (2016). The role of alkalizing agent on the manganese phosphating of a high strength steel part 1: The individual effect of NaOH and NH₄OH. *Surface and Coatings Technology*, 291, 179–188.
- Gaucher, E. C., & Blanc, P. (2006). Cement/clay interactions – A review: Experiments, natural analogues, and modeling. *Waste Management*, 26(7), 776–788.
- Gautier, M., Muller, F., Le Forestier, L., Beny, J.-M., & Guegan, R. (2010). NH₄-smectite: Characterization, hydration properties and hydro mechanical behaviour. *Applied Clay Science*, 49(3), 247–254.
- Hendershot, W. H., Lalonde, H., & Duquette, M. (1993). Ion exchange and exchangeable cations. *Soil Sampling and Methods of Analysis*, 19, 167–176.
- Hibbard, M. J. (2002). *Mineralogy. A View Point of Geology*, McGraw-Hill.
- Iler, K. R. (1979). The chemistry of silica. *Solubility, Polymerization, Colloid and Surface Properties and Biochemistry of Silica*.
- Jönsson, J., Persson, P., Sjöberg, S., & Lövgren, L. (2005). Schwertmannite precipitated from acid mine drainage: phase transformation, sulphate release and surface properties. *Applied Geochemistry*, 20(1), 179–191.
- Jorgensen, T. C., & Weatherley, L. R. (2003). Ammonia removal from wastewater by ion exchange in the presence of organic contaminants. *Water Research*, 37(8), 1723–1728.
- Joseph, C., Mibus, J., Trepte, P., Müller, C., Brendler, V., Park, D. M., Jiao, Y., Kersting, A. B., & Zavarin, M. (2017). Long-term diffusion of U(VI) in bentonite: Dependence on density. *Science of the Total Environment*, 575, 207–218.

- Jozefaciuk, G., & Bowanko, G. (2002). Effect of acid and alkali treatments on surface areas and adsorption energies of selected minerals. *Clays and Clay Minerals*, 50(6), 771–783.
- Kang, S.-J., & Egashira, K. (1997). Modification of different grades of Korean natural zeolites for increasing cation exchange capacity. *Applied Clay Science*, 12(1–2), 131–144.
- Katsenovich, Y. P., Cardona, C., Lapierre, R., Szecsody, J., & Lagos, L. E. (2016). The effect of Si and Al concentrations on the removal of U(VI) in the alkaline conditions created by NH₃ gas. *Applied Geochemistry*, 73, 109–117.
- Katsenovich, Y. P., Cardona, C., Szecsody, J., Lagos, L. E., & Tang, W. (2018). Assessment of calcium addition on the removal of U(VI) in the alkaline conditions created by NH₃ gas. *Applied Geochemistry*, 92, 94–103.
- Köhler, S. J., Dufaud, F., & Oelkers, E. H. (2003). An experimental study of illite dissolution kinetics as a function of pH from 1.4 to 12.4 and temperature from 5 to 50°C. *Geochimica et Cosmochimica Acta*, 67(19), 3583–3594.
- Langmuir, D. (1997). Aqueous geochemistry of uranium. *Aqueous Environmental Chemistry*, 494–512.
- Li, D., & Kaplan, D. I. (2012). Sorption coefficients and molecular mechanisms of Pu, U, Np, Am & Tc to Fe(hydr)oxides: A review. *Journal of Hazardous Materials*, 243, 1–18.
- Lippert, E. (1960). The Strengths of Chemical Bonds, von TL Cottrell. Butterworths Publications Ltd., London 1958. *Angewandte Chemie*, 72(16), 602.
- Marsh, A., Heath, A., Patureau, P., Evernden, M., & Walker, P. (2018). Alkali activation behaviour of un-calcined montmorillonite and illite clay minerals. *Applied Clay Science*, 166, 250–261.
- Mashal, K., Harsh, J. B., Flury, M., Felmy, A. R., & Zhao, H. (2004). Colloid formation in Hanford sediments reacted with simulated tank waste. *Environmental Science & Technology*, 38(21), 5750–5756.
- Mason, C. F. V, Turney, W. R. J. R., Thomson, B. M., Lu, N., Longmire, P. A., & Chisholm-Brause, C. J. (1997). Carbonate Leaching of Uranium from Contaminated Soils. *Environmental Science & Technology*, 31(10), 2707–2711.
- Miranda-Trevino, J. C., & Coles, C. A. (2003). Kaolinite properties, structure and influence of metal retention on pH. *Applied Clay Science*, 23(1–4), 133–139.

- Oda, C., Walker, C., Chino, D., Ichige, S., Honda, A., Sato, T., & Yoneda, T. (2014). Na-montmorillonite dissolution rate determined by varying the Gibbs free energy of reaction in a dispersed system and its application to a coagulated system in 0.3 M NaOH solution at 70° C. *Applied Clay Science*, 93, 62–71.
- Oelkers, E. H. (2001). General kinetic description of multioxide silicate mineral and glass dissolution. *Geochimica et Cosmochimica Acta*, 65(21), 3703–3719.
- Panagiotopoulou, C., Kontori, E., Perraki, T., & Kakali, G. (2007). Dissolution of aluminosilicate minerals and by-products in alkaline media. *Journal of Materials Science*, 42(9), 2967–2973.
- Qafoku, Ainsworth, C. C., Szecsody, J. E., & Qafoku, O. S. (2003). Aluminum Effect on Dissolution and Precipitation under Hyperalkaline Conditions: I. Liquid Phase Transformations. *Journal of Environmental Quality*, 32(6), 2354–2363.
- Qafoku, Ainsworth, C. C., Szecsody, J., Qafoku, O. S., & Young, J. S. (2003). Aluminum Effect on Dissolution and Precipitation under Hyperalkaline Conditions: II. solid Phase Transformations. *Journal of Environmental Quality*, 32(6), 2364–2372.
- Qafoku, N. P., Ainsworth, C. C., Szecsody, J. E., & Qafoku, O. S. (2004). Transport-controlled kinetics of dissolution and precipitation in the sediments under alkaline and saline conditions. *Geochimica et Cosmochimica Acta*, 68(14), 2981–2995.
- Reynolds, J. G., Cooke, G. A., Page, J. S., & Warrant, R. W. (2018). Uranium-bearing phases in Hanford nuclear waste. *Journal of Radioanalytical and Nuclear Chemistry*, 316(1), 289–299.
- Rhoades, J. D. (1983). Cation exchange capacity. *Methods of Soil Analysis: Part 2 Chemical and Microbiological Properties*, 9, 149–157.
- Rozalen, M., Huertas, F. J., & Brady, P. V. (2009). Experimental study of the effect of pH and temperature on the kinetics of montmorillonite dissolution. *Geochimica et Cosmochimica Acta*, 73(13), 3752–3766.
- Schoonheydt, R. A., & Johnston, C. T. (2013). Surface and interface chemistry of clay minerals. In *Developments in clay science* (Vol. 5, pp. 139–172). Elsevier.
- Serne, Last, G. V., Gee, G. W., Schaef, H. T., Lanigan, D. C., Lindenmeier, C. W., Lindberg, M. J., Clayton, R. E., Legore, V. L., & Orr, R. D. (2008). *Characterization of vadose zone sediment: Borehole 299-E33-45 near BX-102 in the B-BX-BY waste management area*. Pacific Northwest National Lab.(PNNL), Richland, WA (United States).

- Shutske, J. M. (1996). *Using anhydrous ammonia safely on the farm*. Minnesota Extension Service, University of Minnesota.
- Song, Y., Wang, H., Yang, J., & Cao, Y. (2018). Influence of monovalent cations on the efficiency of ferrous ion oxidation, total iron precipitation, and adsorptive removal of Cr (VI) and As (III) in simulated acid mine drainage with inoculation of *Acidithiobacillus ferrooxidans*. *Metals*, 8(8), 596.
- Szecsody, Truex, M. J., Qafoku, N. P., Wellman, D. M., Resch, T., & Zhong, L. (2013). Influence of acidic and alkaline waste solution properties on uranium migration in subsurface sediments. *Journal of Contaminant Hydrology*, 151, 155–175.
- Szecsody, Truex, M. J., Zhong, L., Johnson, T. C., Qafoku, N. P., Williams, M. D., Greenwood, W. J., Wallin, E. L., Bargar, J. D., & Faurie, D. K. (2012). Geochemical and Geophysical Changes during Ammonia Gas Treatment of Vadose Zone Sediments for Uranium Remediation. *Vadose Zone Journal*, 11(4).
- Tro, N. J., Fridgen, T. D., Shaw, L., & Boikess, R. S. (2017). *Chemistry: A molecular approach*. Pearson Boston, MA.
- Walther, J. V. (1996). Relation between rates of aluminosilicate mineral dissolution, pH, temperature, and surface charge. *American Journal of Science*, 296(7), 693–728.
- Wan, J., Larsen, J. T., Tokunaga, T. K., & Zheng, Z. (2004). pH neutralization and zonation in alkaline-saline tank waste plumes. *Environmental Science & Technology*, 38(5), 1321–1329.
- West, D. N. (2008). US Department of the Interior. In *US Geological Survey*.
- Xiao, Y., & Lasaga, A. C. (1996). Ab initio quantum mechanical studies of the kinetics and mechanisms of quartz dissolution: OH⁻ catalysis. *Geochimica et Cosmochimica Acta*, 60(13), 2283–2295.
- Youlton, B. J., & Kinnaird, J. A. (2013). Gangue–reagent interactions during acid leaching of uranium. *Minerals Engineering*, 52, 62–73.
- Zachara, J., Brown, C., Christensen, J., Davis, J. A., Dresel, E., Kelly, S., Liu, C., McKinley, J., Serne, J., & Um, W. (2007). *A Site-Wide Perspective on Uranium Geochemistry at the Hanford Site*.

CHAPTER III

Characterization of Physicochemical Mineral Phase Alterations with Treatment

3 CHAPTER 3: CHARACTERIZATION OF PHYSICOCHEMICAL MINERAL PHASE ALTERATIONS WITH TREATMENT

3.1 Abstract

In situ remediation applications via ammonia (NH₃) gas are a potential treatment of deep vadose zone contamination. Ammonia gas injections increase mineral dissolution and formation of secondary precipitates as the pH is neutralized. However, there is a lack of fundamental understanding of clay alteration due to NH₃. In this batch study, pure phyllosilicate clay minerals (illite and montmorillonite) in synthetic groundwater were exposed to NH₃ gas and subsequent aeration (to mimic a return to natural conditions at circumneutral pH). Following treatment, solids were characterized using a variety of advanced characterization and spectroscopic techniques, including X-ray diffraction, N₂ adsorption-desorption analysis, FTIR spectroscopy, scanning electron microscope-energy dispersive spectroscopy, electron microscopy, and ²⁷Al and ²⁹Si MAS NMR methods to investigate physicochemical transformations. Results indicated that, at high pH, dioctahedral 2:1 clay minerals interact differently upon NH₃ gas treatment. While the montmorillonite interlayer collapsed due to NH₄⁺ cation intercalation, illite displays minimal alteration confirmed by FTIR analysis. Alteration of morphology and recrystallization was observed for both minerals following aeration upon microscopic (SEM and TEM) and surface area (BET) analysis. Further, local structural changes in the silicate tetrahedron [SiO₄]ⁿ⁻ and aluminol (Al-OH) groups were identified by MAS NMR. These observations are attributed to dissolution processes which break Si-O bonds with subsequent recrystallization of Al-OH in the phyllosilicate edges-sites as the pH is neutralized. This research has shown that mineral alteration and co-precipitation processes

initiated by NH₃ gas treatment may remove soluble contaminant cations from the aqueous phase through sorption and co-precipitation followed by coating with secondary phyllosilicate alteration products.

3.2 Introduction

The dissolution and alteration of minerals under alkaline solutions has been studied in different disciplines including geochemistry and materials science for the characterization of the materials and the remediation of contaminated sites. Alkaline technologies have been implemented for remediation of acidic plumes created by heap leach mining processes, sulfide-rich mine drainage, and acidic waste releases (Doye & Duchesne, 2003; Fernández et al., 2014; Mason et al., 1997) and alkaline technologies have been using for U leach mining (Mason et al., 1997). Remediation and treatment with ammonia (NH₃) gas, however, is a lesser- studied treatment option that requires further investigation (Zhong et al., 2015); the use of the gas phase is seldom explored as a natural material for remediation purposes, although it can be cost-effective, simpler to distribute, and less impactful to the vadose zone than aqueous methods. NH₃(g) quickly partitions into subsurface porewater due to its low Henry's constant ($K_H = 0.016$ atm/mol or a dimensionless value of $\sim 6.58 \times 10^{-4}$) (Tro et al., 2017) and prevents the addition of liquids that may increase contaminant mobility in unsaturated sediments. Moreover, more than 99% of the NH₃ mass is expected to partition to solution at 1.0% porewater content (Szecsody et al., 2012). NH₃ gas technology thus has the potential to sequester inorganic cations and radionuclides within solid phases in the subsurface. It has been shown to increase mineral dissolution and secondary precipitation reactions as the pH is neutralized,

potentially immobilizing contaminants within coatings and co-precipitates with relatively low solubility under natural conditions (Szecsody et al., 2012).

Due to its only recent proposal for vadose zone remediation, there have been only a limited number of studies quantifying the effects of NH₃-induced alkaline conditions on clay mineral alterations (Emerson et al., 2018; Katsenovich et al., 2016, 2018; Szecsody et al., 2012, 2020). Emerson *et al.*, noted that NH₃ gas treatment increased U removal more than aqueous (NaOH or NH₄OH) alkaline treatments and suggested that precipitation of secondary mineral phases from clay minerals occurred due to incongruent dissolution. Similarly, Katsenovich *et al.* (2016) and Szecsody *et al.* (2012) conducted different NH₃ gas treatment experiments to evaluate U removal from solution over time. While Szecsody's team used Hanford Site sediments (with 2 to 3% clays) for a one-year treatment (or 3 years as shown in the (Zhong et al., 2015) study), Katsenovich's batch solutions were spiked with U for a two-day contact time (Katsenovich et al., 2016; Szecsody et al., 2012). Both research groups found that hydrous U-silicates (e.g., sodium boltwoodite) were the predominant precipitates. These results were confirmed via geochemical speciation modeling. Via X-ray diffraction (XRD) analysis, Katsenovich and team also reported that uranyl carbonate phases were formed following NH₃ gas injection.

To date, however, research has not addressed the potential impact to clay mineralogy and the importance of ions dissolving from clays. It is likely that NH₃-induced pH changes affect clay minerals [both clay-mineral family and minerals sized (< 2 μm)] which are commonly present in the Earth's surface due to erosion, weathering, and diagenesis (Churchman & Lowe, 2012). Because clays are ubiquitous, they are an inexpensive tool

for remediation applications whether they are added to a system or already present (Dove, 1995). Aluminosilicate clays minerals contain two layers: Si-centered tetrahedral (T) layers and aluminum (Al)-centered octahedral (O) layers. These layers are held together by shared and electronically neutral basal oxygen atoms. In the simplest case for strongly weathered soils, the T-O layers are assembled in a 1:1 unit (Gualtieri et al., 2008). In moderately weathered soils, the T layers sandwich the O layer to build the T–O–T unit in a 2:1 ratio. Examples of 2:1 aluminosilicates are illite and montmorillonite clays, from the dioctahedral mica and smectite groups, respectively.

Aluminosilicates may undergo isomorphic substitutions affecting their T-O-T layers and, ultimately, their stoichiometry. Furthermore, there is a charge imbalance resulting in a permanent negative charge on the oxygen basal surfaces that leads to pH-independent cation adsorption defined as cation exchange capacity (CEC). The CEC is due to interactions between the T-O-T unit or the interlayer space (1.0 – 1.5 nm) (Brigatti et al., 2006). However, some pH-dependent cation adsorption is also expected on surfaces due to loss or gain of H^+ and OH^- on the surface. Whereas illite substitutions predominantly occur in the T layer with potassium (K^+) ions, montmorillonite can substitute in the O layer and host a wider range of interlayer cations, such as Na^+ , K^+ , Mg^{2+} , and Ca^{2+} (Grauer, 1994; Gualtieri et al., 2008). Moreover, the transformation of montmorillonite to illite occurs over time in the presence of K-rich groundwater (Marsh et al., 2018). Studies performed by Serne *et al.* concluded that the presence of illite is particularly important for contaminant sequestration, since it exhibits high adsorption capabilities and the potential for intercalation in between the TOT layer of its crystal structure (Serne et al., 2020).

Select studies have analyzed clay alterations post-alkaline treatment using complementary analytical techniques. For example, Chen *et al.* synthesized Zeolite Socony Mobil-5 (ZSM-5), a widely used aluminosilicate catalyst in the petroleum industry from illite mineral in 5.6 M NaOH solutions at 473 K (Chen et al., 2019). After Na₂O/SiO₂ molar ratio quantification and other characterization of morphology and mineralogy alteration, the team concluded that the high alkalinity (pH > 11) led to condensation of Si-O-Si bonds for the ZSM-5 formation after 24 h (Chen et al., 2019). Although the high temperature conditions of Chen and team's experiments are not relevant to environmental remediation conditions, these experiments can broadly inform on potential reactions and products. Moreover, Marsh *et al.* noted illite and montmorillonite alterations after just 24 h of exposure to NaOH solutions at 40 °C. For high Na:Al solution ratios, illite clay morphology was altered as shown by interlayer expansion during treatment curing, whereas montmorillonite formed a new geopolymer (eco-friendly binder) hydrosodalite {Na₈[AlSiO₄]₆(OH)₂} phase identified via ²⁷Al and ²⁷Si nuclear magnetic resonance (NMR), scanning electron microscopy with energy dispersive x-ray spectroscopy (SEM-EDS), Fourier transform infrared spectroscopy (FTIR), and XRD analysis (Marsh et al., 2018). Additional studies confirmed zeolite formation from montmorillonite and illite following NaOH exposure (1 – 14 M) at different temperatures (30 – 100 °C) via multiple analytical techniques (Belviso et al., 2017; El Hafid & Hajjaji, 2015; Kang & Egashira, 1997). Other researchers have also identified formation of secondary aluminosilicates in Hanford Site sediments interacted with simulated tank waste at pH > 13.5 in NaOH solution, such as cancrinite, zeolite, and sodalite (Barnes et al., 1999; Qafoku et al., 2004; Zhao et al., 2004).

However, unlike the aforementioned research, the present study proposes a gaseous alkaline treatment with NH_3 under environmental conditions. After NH_3 mass loss due to gas diffusion and reaction with porewaters and sediments, the pH is expected to return to natural soil conditions after approximately nine months of 10% NH_3 gas addition at 1.0% porewater content (Szecsody et al., 2020). As a consequence, we expect to observe changes in the solid phase due to both the dissolution and precipitation of secondary minerals. However, few works have investigated these conditions and most research characterizing sediments reacted under alkaline conditions was conducted with simulated tank waste (STW) solutions as opposed to gas treatments. Mashal and team noted that XRD diffraction patterns of aluminosilicates were altered due to dissolution upon interaction with STW solutions (Mashal et al., 2004). Using various analytical techniques (i.e., SEM-EDS, FTIR, and XRD) and saturation index calculations, the team concluded that dissolved Si and Al precipitated to form secondary minerals including cancrinite and sodalite (Mashal et al., 2004). Similarly, Wan *et al.*, tested Hanford Site sediments with STW solutions over a broad pH range (7 – 14) at room temperature (Wan et al., 2004). X-ray diffraction and SEM analysis confirmed cancrinite-zeolite precipitation and sodalite formation. The team suggested that secondary mineral formation was the result of hydroxide neutralization. Indeed, both batch-STW studies reported newly formed precipitation of secondary silicates minerals in Hanford sediments after the base was neutralized.

Although previous research demonstrates qualitative evidence of clay alteration due to reaction with alkaline solutions, there is a need to systematically measure alteration during NH_3 gas injection under environmental conditions as previous research has not been

reported that adequately addresses clay alteration under alkaline conditions relevant for environmental remediation of the subsurface with NH_3 gas. Indeed, pH manipulation needs to be better understood in order to (1) describe mineral alteration, (2) develop a conceptual model for contaminant interaction, and (3) predict the fate and transport of contaminants. The objective of the present research is to identify the major physicochemical changes of aluminosilicate minerals, illite and montmorillonite, following NH_3 gas and subsequent aeration treatments. This research conducted batch experiments to compare mineral solids at different stages of interaction with NH_3 gas with complementary characterization techniques. In this paper, results are presented for batch experiments conducted with exposure to 5% NH_3 /95% N_2 gas followed by aeration with ultrapure air for illite and montmorillonite minerals. These experiments provide a systematic investigation using Brunauer–Emmet–Teller (BET), X-ray diffraction (XRD), SEM-EDS, transmission electron microscopy (TEM), FTIR, and NMR spectroscopic techniques.

3.3 Experimental Methodology

3.3.1 Mineral Characterization

Characterization techniques were used to identify solid phase minerals prior to and post treatment, including XRD, Brunauer–Emmet–Teller (BET) surface area analysis, SEM-EDS, high resolution HR-TEM, and FTIR. This approach combined complementary techniques to determine mineral alterations upon pH manipulation based on comparison with control minerals. A concept map of the various solid phase characterization techniques shown in this chapter can be found in the Appendix, Figure A.9.

3.3.1.1 Cation Exchange Capacity

The cation exchange capacity (CEC) was measured following the standard method developed by Lavkulich and Rhoades per ASTM D7503-10 (ASTM, 2010; Hendershot et al., 1993; Rhoades, 1983). Briefly, 0.4 g of air-dried mineral was weighed and placed on a 2.5 μm ashless filter paper in a Büchner funnel and washed with four 30-mL portions of 1.0 M ammonium acetate and three 40-mL portions of isopropanol. A low suction (<10 kPa) was then applied to the filtering flask. It is important to note that each 40-mL portion was drained before the subsequent aliquot was added with all discarded at the end. Next, the isopropanol-washed soil was washed with four 50-mL portions of 1.0 M potassium chloride solution, again, allowing for drainage before continuing. The liquid phase recovered during this step was transferred into vials for total nitrogen analysis via an ammonia electrode (Orion 9512). Specific CEC for illite and montmorillonite minerals prior to treatment, along with chemical formulae and their respective theoretical ratios, are provided in Table 3.2. The CEC of a soil is expressed in centimol positive charge per kg of soil (cmol_c/kg).

3.3.1.2 X-ray Diffraction (XRD)

Untreated illite mineral samples were analyzed via Bruker GADD/D8 X-ray diffractometer with an Apex Smart Charge Coupled Device detector at room temperature, humidity, and pressure. All peak positions were obtained by step-size goniometer scanning at 0.02 2θ intervals from 5° to 40° using $\text{CuK}\alpha$ x-rays at 40 kV. Crystalline phase identification was performed via Match! powder pattern phase identification processing

software with the Powder Diffraction File (PDF) International Centre for Diffraction Data (ICDD®) database

3.3.1.3 Average Particle Surface Area via BET

The surface area of the illite mineral was determined in triplicates from the corresponding nitrogen adsorption-desorption isotherms obtained at 353 K with a gas adsorption analyzer (Micromeritics TriStar II 3020 V1.03). Approximately 0.30 g of mineral were degassed at 353 K for 24 h with nitrogen gas. The specific surface area was determined using the Brunauer–Emmet–Teller (BET) equation (Brunauer et al., 1938) based upon the cross-sectional area of monolayer adsorbed nitrogen (0.16 nm^2). Specific surface areas of illite mineral prior to treatment is provided in Table 3.2.

3.3.1.4 Scanning Electron Microscope with Energy Dispersive X-ray Spectroscopy (SEM-EDS)

Control (prior to treatments and post washing steps) and treated illite and montmorillonite mineral samples for microscopy analysis were prepared by attaching double-sided carbon conductive adhesive tape (12 mm in diameter and 260 μm in thickness, Electron Microscopy Sciences) to aluminum stubs and then sprinkling the dried mineral powder on the carbon tape. The uncoated specimen mounts were analyzed via SEM-EDS analysis. The analytical goal was to examine specimens for (1) morphology, (2) particle size, and (3) elemental composition. The chemical composition of pure (untreated) minerals are given in Table 3.3. Characterization was conducted via JEOL IT500Hr FE Scanning Electron Microscope (FE-SEM) equipped with the Bruker XFlash 6160 energy dispersive X-ray spectroscopy (EDS) with a 60 mm window silicon drift detector (SDD). EDS operating conditions were set at 15 keV accelerating voltage and a gun emission of

23 μA at 5.0×10^{-7} Pa vacuum pressure. The electron beam had an incident angle of 35° from the surface with ample signal of at least 40,000 counts per second for a 50-second duration. Collected data were quantified via the Bruker Esprit 2.2 software. SEM images were taken using the secondary detector at 3 keV and a working distance of approximately 10 mm.

3.3.1.5 High Resolution-Transmission Electron Microscope (HR-TEM) Analysis

High resolution transmission electron microscopy (HR-TEM) was carried out with a Phillips CM200 FEG microscope operating at 200 kV attached to a Tungsten light. Ammonia-treated pure minerals were previously sonicated for four hours in an ethanol suspension. The particles were then collected directly onto 300 mesh copper (Cu) grids (Electron Microscopy Sciences, EMS). TEM specimens were viewed under a magnification of 80,000 - 500,000 with images recorded on a Kodak camera with a 1024 x 1024 cooled Gatan CCD. A concept map identifying the differences between SEM and TEM can be found in the Appendix, Figure A.10.

3.3.1.6 Fourier Transposed Infrared Spectroscopy (FTIR) Analysis

The illite and montmorillonite mineral samples were characterized via transmissive infrared spectroscopy using a variant of the KBr pellet method. Pellets were prepared quantitatively using a two-step serial dilution: IR-grade KBr (Pike Technologies) was ground in stainless steel canisters for 60 s in a Pike ShakIR amalgamator, then filtered through a #60 mesh (250 μm) sieve to remove large particles. Illite and montmorillonite were grounded using an agate mortar and pestle. In the first step, ~100 mg of analyte mineral was mixed with ~900 mg KBr and mixed/shaken in a stainless canister with ball

and mixed thoroughly. From this mix, 25 mg were withdrawn, mixed with 975 mg fresh KBr, thus further diluted to obtain a ~0.25% mixture by mass. At each step, solid mixtures were ground in the amalgamator for 15 s followed by scraping the canister edges to loosen clumped sample; mixing/scraping steps were repeated 3 times. Pellets were pressed under vacuum using a Carver Mini-C 12-ton hydraulic press. Spectra were baseline corrected using the OPUS software which also removed vapor-phase CO₂ and H₂O interferents.

Infrared data were recorded using double-sided forward-backward interferograms on a previously described Bruker Tensor 37 Fourier transform instrument (Myers et al., 2018; Rettie et al., 2016). Spectra were recorded using a silicon carbide (SiC) source, an extended range Ge/KBr beamsplitter (better signal at higher frequency), and a deuterated tri-glycine sulfate (DTGS) detector. Interferograms were phase-corrected using Mertz's method (Mertz, 1967), zero filled 4x prior to transformation to produce single-beam spectra from 370 to 7500 cm⁻¹ (Sweet et al., 2013). Data were recorded at 2.0 cm⁻¹ resolution to provide greater precision for peak positions. For the reference (I₀) spectrum 2048 scans were typically recorded with 1024 scans for the mineral analyte (I sample) spectrum. Absorbance spectra were generated in the typical $-\log(I/I_0)$ manner with KBr pellet "blanks" recorded as separate spectra and subtracted from the analyte spectrum, largely to remove O-H bending and stretching band peaks in the 1600 and 3400 cm⁻¹ ranges, respectively, arising due to trace water in the KBr. After subtraction, the analyte spectrum was scaled from 0.0 to 2.0 absorbance (ABS) units. Finally, high wavenumber regions were smoothed using a Savitzky-Golay algorithm and a 9-point running average using OPUS software.

3.3.1.7 Solid-State Nuclear Magnetic Resonance (NMR)

3.3.1.7.1 ²⁷Al NMR-Magic-Angle Spinning (MAS) and Multiple-Quantum Magic-Angle Spinning (MQMAS)

²⁷Al MAS NMR experiments were carried out on a 400 MHz (9.4 T) Bruker AVANCE Neo spectrometer operating at a 104.25 MHz. Experiments were conducted using a 1.6 mm Phoenix H/FX MAS probe while spinning at 35 kHz. Single pulse spectra were collected using a 17° pulse (0.25 μs) (RF field strength of 174 kHz), a recycle delay of 1 s, and without high-powered proton decoupling. ²⁷Al MQMAS NMR experiments were collected using a RF field strength of 174 kHz for the excitation and conversion pulses (2.75 and 1.2 μs, respectively). A RF field strength of ~28 kHz was used for the 90° selective pulse (9 μs). For 2D acquisition, the rotor synchronized sequence was incremented through 32 t₁ steps collecting 1548 transients per t₁ increment with a recycle delay of 3 s. The ²⁷Al chemical shift scale was externally referenced to 0.1 M solution of AlCl₃ at 0.0 ppm.

3.3.1.7.2 ²⁹Si Nuclear Magnetic Resonance

²⁹Si MAS NMR experiments were carried out on a 300 MHz (7.1 T) Tecmag Apollo with a 7.5 mm Chemagnetics CPMAS probe tuned to 59.8 MHz. A 30° tip angle of 3 μs was applied, followed by data acquisition without high-powered proton decoupling. Samples were packed into 7.5 mm zirconia rotors with spinning speeds from 4 – 4.5 kHz and the experimental delay was set to 900 s. Chemical shifts were referenced externally to kaolinite at -91.5 ppm.

Table 3.1. PH readings post 5% NH₃/95% N₂ injection (~30 d) and post aeration step (24 h). Note: standard deviations are based on triplicate measurements

Mineral	pH initial	pH aeration
Illite	11.24 ± 0.06	8.58 ± 0.08
Montmorillonite	11.22 ± 0.05	8.51 ± 0.22

Table 3.2. Theoretical Ratios and Cation Exchange Capacity (CEC) for Pure Minerals
Illite and Montmorillonite Pure Minerals

Mineral	Chemical Formulae	Theoretical Al:Si	CEC (cmol/kg)
Illite	K(Mg,Fe) ₃ (Al, Fe)Si ₃ O ₁₀](OH) ₂	0.33	17.6
Montmorillonite	Ca _{0.2} (Al,Mg,Fe) ₂ (Si ₄ O ₁₀)(OH) ₂ · nH ₂ O	0.50	9.73

Table 3.3. Chemical Composition of illite (SWy-1, Clay Minerals Society, Cambrian Hole, Silver Hill Mount) and montmorillonite (Clay Mineral Society, Crook County, Wyoming) used, in oxide % wt based on SEM-EDS analyses of minerals prior to treatments. Note: standard deviations are based on the average composition of nine data points

Oxide	SiO ₂	Al ₂ O ₃	FeO/Fe ₂ O ₃	K ₂ O	MgO	TiO ₂	CaO	Na ₂ O	Total
Illite	55.7±8.6	24.6±2.5	6.7±3.6	7.8±1.3	2.5±0.3	0.90±0.5	0.1±0.1	0.2±0.2	100
Montmorillonite	66.6±6.2	19.6±3.1	7.8±5.3	0.2±0.1	2.3±0.6	2.3±0.6	0.7±0.2	0.7±0.2	98.3*

*detected trace impurities such as Mn and Cr are not included in the sum total

3.3.2 Materials

Experiments were conducted using two minerals: illite (Clay Minerals Society, Cambrian Hole, Silver Hill Mount) and montmorillonite (SWy-1, Clay Mineral Society, Crook County, Wyoming). The minerals were washed prior to experiments following the procedure described in Di Pietro *et al.*, 2020 based on previous research (Baeyens & Bradbury, 2004; Boggs et al., 2015; Di Pietro et al., 2020). Briefly, suspensions (100 g/L) were mixed with 1.0 M NaCl prepared with ultrapure H₂O [resistivity greater than 18 M Ω ·cm, deionized water (DIW)], allowed to flocculate overnight, centrifuged at 4500 rpm (18,100 rcf) in a benchtop centrifuge with a swing bucket rotor attachment (Thermo Scientific, Corvall ST 16R). Supernatant was then decanted and replaced with DIW. This process was repeated until the conductivity was less than 20 μ S/cm to show that most ions had been removed. Montmorillonite (6.0 g), however, was first mixed with 60 mL of 0.001 M HCl and 0.5 mL of H₂O₂ to remove salts and limit redox active species (Boggs et al., 2015) followed by a DIW wash. After each step, the samples were centrifuged at 4500 rpm for 6 h for montmorillonite and 30 minutes for illite, after which the liquid was decanted. The longer centrifugation time was used for montmorillonite to aide in dewatering the expanding layers. Subsequently, minerals were dried for 6 days in an oven at 30 °C prior to use in experiments (LabNet International Inc.).

3.3.3 Batch Protocol

Previously washed minerals were suspended (70 g/L) in SGW (Appendix Table A.5, 7.2 mM total ionic strength). The simplified SGW in Table A.5 is based on previous work (Emerson et al., 2017, 2018; Szecsody et al., 1998; Truex et al., 2017). Duplicate

suspensions were exposed to 5% NH₃ (anhydrous UN1007RQ, Airgas)/95% N₂ (UHP300, Airgas) inside a plastic glovebag (GlasCol, 27 x 27 x 15 inch). Samples inside were uncapped for 12-16 h to equilibrate with the gas phase. Samples were then re-capped, covered with parafilm, and set to equilibrate on an end-over-end tube revolver at 40 rpm (Thermo Scientific) for approximately one month. Because there is a need to investigate secondary precipitation under circumneutral pH conditions reached after re-equilibration of minerals and solutions with air, a second set of suspensions underwent aeration treatment after the one-month equilibration with NH₃. The aeration step consisted of a 10 psi flow rate (5.68 mL/min) of ultrapure air split into three tubing lines to allow for simultaneous treatment of three samples per tank. Then, pH measurements (Thermo Scientific Orion VersaStar, 8175BNWP) were taken both prior to and following the aforementioned steps to confirm alkaline (pH 12) and aeration (pH 8) treatments, respectively, with a three-point calibration (pH 4.01, 7.00, and 10.01 Buffers, Thermo Scientific). Table 3.1 lists the recorded pH measurements taken 30 days post 5% NH₃/95% N₂ injection and 24 h of aeration treatment.

3.4 Results and Discussion

3.4.1 Characterization of Illite Prior to Treatment

The X-ray diffraction pattern of unreacted (control) illite is seen in Figure 3.1. The XRD matching analysis (PDF# 00-058-2015) revealed that it contained primarily illite with $55.7 \pm 8.6\%$ quartz (as identified by the sharp peak at $2\theta = 26.6$ at 3.34 \AA) and minor amounts of calcite, kaolinite, and microcline. The XRD pattern characteristic of illite was shown at $2\theta = 9.01$ (9.80 \AA), 17.9 (4.93 \AA), 19.7 (4.51 \AA), and 35.9 (2.49 \AA). The interlayer

basal₀₀₁ feature indicative of illite can be easily detected by the pattern's broadest peak found at $2\theta = 9.01$ (9.80 \AA). Previous studies on this clay identified it to be composed of >90% illite mostly of the 1M/1M_d polytype (Gailhanou et al., 2007). The BET surface area of the untreated illite was found to be $20.4 \pm 0.1 \text{ m}^2/\text{g}$ (Table 3.4). Further, the CEC of pure illite (Clay Minerals Society, Cambrian Hole, Silver Hill Mount) was estimated to be 17.6 cmol/kg. Other values for the CEC reported in the literature for the illite range from an intermediate CEC value of 10 – 40 cmol/kg (O'Loughlin et al., 2000).

Elemental analysis results (expressed in weight percent, wt%, of oxides) are presented in Table 3.3. The main constituents for illite are silicate (55.7%), alumina (24.6%), and potassium (7.83%) and are consistent with literature (He et al., 1995; Konan et al., 2012; Nieto et al., 2010; Środoń & MaCarty, 2008). The Al/Si ratio can also provide useful information. Based on SEM-EDS results, this ratio was calculated to be 0.50 ± 0.07 (n=9). The SEM-EDS is a surface sensitive technique, having the electron beam penetrating a maximum depth of 1.0 μm depending on the beam energy during analysis. According to the best illite phase match from XRD analysis, the Al/Si theoretical ratio is 0.33 (Table 3.2). However, discrepancies may be explained by the intrinsic nature of the mineral, as illite minerals have a range of ratios rather than a fixed stoichiometry due to isomorphic substitutions (Marsh et al., 2018).

In addition, an FTIR spectrum of untreated illite is shown in Figure 3.2. Absorption bands between 4000 and 600 cm^{-1} from literature are assigned in the Appendix, Figure A.11. Briefly, the characteristic vibration bands of aluminosilicate phases and quartz can be identified in the FTIR spectra in the 420-550 cm^{-1} and 900-1200 cm^{-1} regions,

respectively (Jiang et al., 2008; Mezni et al., 2011; Sedmale et al., 2017). The band at 981 cm^{-1} is stretching vibrations of the Si–O bond, and the shoulder at 906 cm^{-1} to the Al–Al–OH bending mode (Öztop & Shahwan, 2006). Bands in the region 3700 and 1600 cm^{-1} domains are assigned to water. The 1650 cm^{-1} band is attributed to physically adsorbed water molecules bending on the illite surface. However, in the case of the 3620 cm^{-1} band, the O–H stretching mode is attributed to the internal hydroxyl groups from the mineral structure, lying between the tetrahedral and octahedral layers (Konan et al., 2012). The variations in these bands upon alkaline treatment, along with other phase characterization modifications, are discussed later in this text. However, it is important to note that prior to NH_3 gas treatment the natural pH of the clay mineral suspension in the SGW solution was 7.61 ± 0.15 , consistent with the pH of a relatively pure illite suspension (Konan et al., 2007).

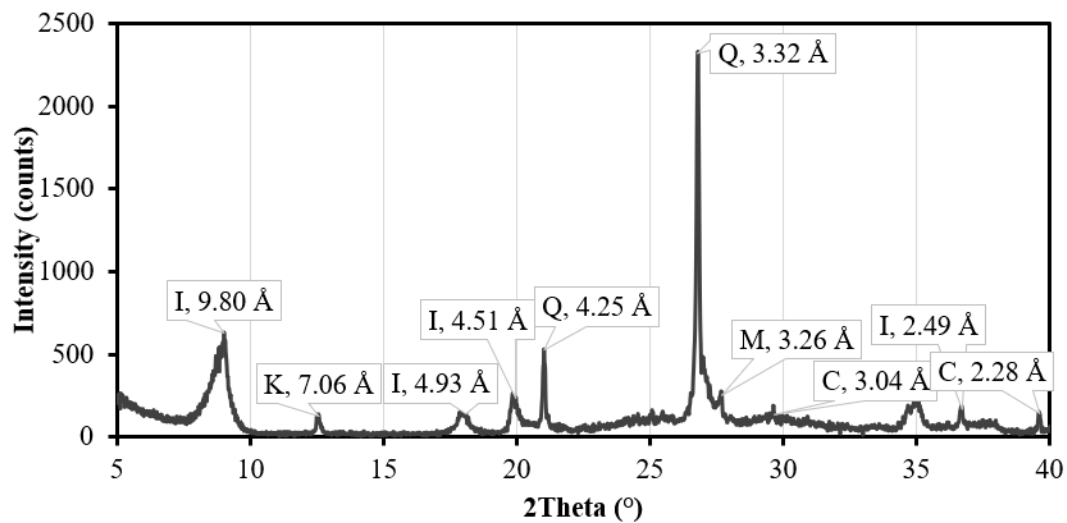


Figure 3.1. X-ray diffraction pattern of illite clay. I, illite; K, kaolinite; Q, quartz; M, microcline; C, calcite.

Table 3.4. BET surface area measurements (average and standard deviation based on triplicate measurements) for illite mineral exposed to ammonia (pH 12) and aeration (pH 8) treatments

Mineral	BET Surface Area (m ² /g)		
	Untreated	pH 12	pH 8
Illite	20.4 ± 0.1	11.9 ± 0.1	21.2 ± 0.6

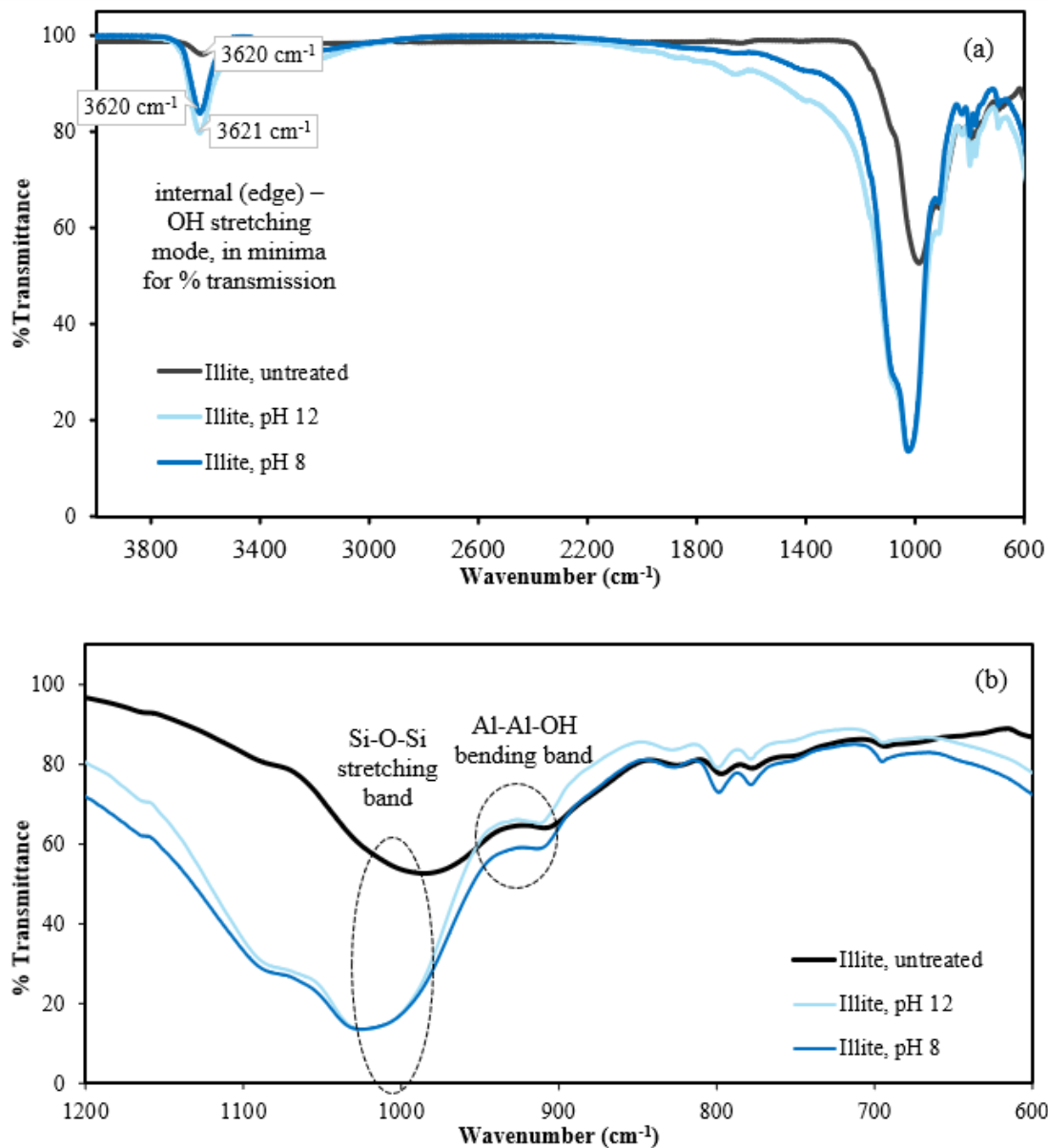


Figure 3.2. Infrared spectra of illite mineral (untreated in black) (a) prior to 95% N₂/5% NH₃ gas treatment, during gas treatment at pH 12 (light blue) and post treatment (darker blue) for 30-day contact time in SGW solution (7.2 mM) at pH 8 and (b) during 95% N₂/5% NH₃ gas treatment at pH 12 (dark blue) and aerated treated at pH 8 (light blue) in comparison with untreated illite (black) showing the Si-O-Si and Al-Al-OH bands at ~ 1000 and ~ 915 cm⁻¹ (dotted circle).

3.4.2 Illite Physical Alterations

Characterization was performed on illite following the two steps of treatment to identify physicochemical changes following NH₃ gas and subsequent aeration treatments. The specific surface area (BET) was measured using the standard nitrogen adsorption-desorption isotherm technique (Brunauer et al., 1938) performed on illite-treated samples. In both cases, three measurements were made for each sample and the results were averaged (Table 3.4). The technique measures (in m²/g) the maximum surface area accessible to water molecules, exchangeable cations, as well as internal surfaces of the minerals (Środoń & MaCarty, 2008). As listed in Table 3.4, the specific surface area decreased drastically upon NH₃ gas treatment from 20.4 ± 0.1 to 11.9 ± 0.1 m²/g or a 58% decrease, potentially due to dissolution of smaller particles with a larger surface area followed by agglomeration of secondary precipitates.

Although previous studies have not investigated NH₃ gas effects on illite at ambient temperatures, two studies reached similar conclusions as to the effects of alkaline treatment of illite at elevated temperature with Ca(OH)₂ and NaOH, respectively. The investigation on illite (Silver Hill) reactions with Ca(OH)₂ at elevated temperatures from 20 to 650 °C conducted by He *et al.* showed that there was a 43.0 % decrease in specific surface area from the untreated illite (He et al., 1995). These authors argue that the decrease is due to an increase in agglomeration of illite particles and closing of pores upon treatment and higher temperature. Similarly, Ruiz *et al.*, found a 53.0 % decrease with BET measurements when bentonite mineral suspensions, containing 82.0 % montmorillonite were exposed to 3.75 M NaOH (Ruiz et al., 1997).

The increase in pH caused by treatment with NaOH is expected to be similar for NH₃ gas treatment as shown by Eq. 1.7, confirming that a similar phenomenon may be observed with NH₃ gas treatment. According Köhler *et al.*, it is important to understand the surface area changes in minerals because they affect chemical and physical processes in soils and groundwater, including contaminant sorption processes (Köhler et al., 2005). Moreover, the moderate CEC and specific surface area of illite highlight its potential as an adsorbent for various contaminants including for environmental remediation (Zhen et al., 2017).

Insight into micro-structural alterations can also be supported with particle size and surface area analysis. Figure 3.3 includes micrographs which depict morphology changes of the measured particles by SEM following NH₃ gas and aeration treatments at zoom magnification 1000x. For further SEM micrographs at various magnifications, see Appendix, Figure A.12. For the untreated illite, SEM micrographs (Figure 3.3a) appear as mostly plate-like (i.e., common feature of phyllosilicate minerals), irregular particles with sizes ranging from approximately 0.5 to 15 µm. After ammonia treatment (Figure 3.3b), SEM micrographs reflect agglomeration of smaller particles. For the aerated samples (Figure 3.3c), SEM micrographs show particles occur mostly in clusters slightly larger than following only ammonia treatment. The particle range for ammonia (pH 12) and aerated (pH 8) treatments ranges from 9.1 – 21.9 µm and 15.1 – 24.9 µm, respectively. In order to corroborate that the particle size is different between both treatments, two-factor replication statistical analysis was conducted for particle sizes estimated at 1000x magnification. Table 3.5 shows the calculated average particle size (in µm) for 33 data points and *p*-value for the Between-Subjects-Effects test (for further details, see Appendix,

Table C.3). Because p -value is ≤ 0.05 ($p=0.0003$), it was concluded that there is a statistically significant difference between NH_3 (pH 12) and aerated (pH 8) treatments.

In the late 1980's, there was great interest to develop high-silica (SiO_2) content zeolites. The "new-generation zeolites", such as ZSM-5, provided a way to include more Al into the mineral's framework, which in turn led to favorable effects in catalytic reactions and isomer separation. The methodology behind this preparation was alkaline media. However, a significant factor was understanding morphology change during the transformation. Researchers Mostowicz and Beraz (1989) proposed several parameters leading to the zeolite alterations. According to their summary, the morphology of the products formed upon treatment is related to the SiO_2 content of the original material, the alkalinity of the solution, and the presence of other cations or non-reactive compounds (Mostowicz & Berak, 1989). In the study conducted by Ruiz *et al.*, authors concluded that the spherical units formed are due to the NaOH treatment controlling the crystalline phases, while the unit size of particle depends on the characteristics of the medium used (i.e., charged ions or uncharged compounds) (Ruiz et al., 1997). For their study, the presence of ions in the pH 12 solution results in smaller units (15.0 ± 4.9 , $n=33$). Similarly to the investigated pH 12 treatment, not only do samples contain the ionic constituents from the SGW composition (Appendix, Table A.5) but also charged ions (NH_4^+) and molecular species (NH_3) from aqueous partitioning from NH_3 gas (Eq. 1.7). Consequently, an increase in average particle size at pH 8 suggests secondary precipitation. This is in good agreement with the research of Ruiz *et al.* and confirms Mostowicz and Beraz's theory. In fact, recent work from geochemical equilibrium simulations at high pH also in similar SGW solution

predict formation of diaspore, α -AlO(OH), correlating to the potential change in crystalline phases during NH₃ gas and subsequent aeration treatments (Emerson et al., 2017; Szecsody et al., 2012). Moreover, the particle size decrease and increase during NH₃ gas and aeration treatments, respectively, would explain the higher specific surface area of illite treated samples shown in Table 3.4.

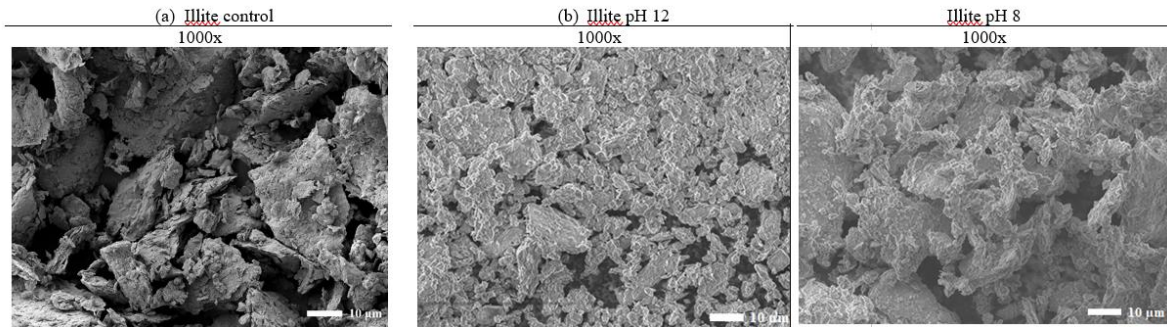


Figure 3.3. SEM images of (a) control untreated illite mineral taken in backscatter mode, (b) illite treated with 95% N₂/5% NH₃ gas treatment at pH 12, and (c) post treatment in secondary mode for 30-day contact time in SGW solution (7.2 mM).

Table 3.5. Descriptive statistics (ANOVA: two-factor with replication) and particle size measurements of illite ammonia- and aerated- treated samples taken from magnification 1000x SEM images

pH – Treatment	Average Particle Size (µm)	Data Points	Significance <i>p</i> value ^a (≤ 0.05)
12 – Ammonia	15.0 ± 4.9	n = 33	0.0003
8 – Aerated	18.4 ± 3.0	n = 33	

^a ‘Tests of Between-Subjects Effects’ with significant $p \leq 0.05$

3.4.3 Effect of Ammonia Intercalation into Mineral's Interlayer

The FTIR spectra for aluminosilicate minerals illite and montmorillonite show NH_4^+ intercalation in Figure 3.4, presumably from the $\text{NH}_3(\text{g})$ reacting with water to form NH_4^+ and OH^- ions in the void spaces. The X-ray pattern and FTIR band attributions of unreacted montmorillonite are given in the Appendix, Figure A.13 and Table A.12, respectively. Although both minerals have a similar 2:1 type structure, their exchangeable cations in the interlayers behave differently by ion-exchange reactions due to isomorphic substitution. In order to understand the cation intercalation, it is imperative to differentiate the mineral's layer charge, defined by χ . A common feature of phyllosilicates is their negative layer charge, which is electrically balanced by the charge of exchangeable cations located primarily between the T layers (Brigatti et al., 2006; Chiou & Rutherford, 1997). While the smectite group has a layer charge of $\chi = 0.25\text{-}0.50$ (Laird, 1987), the dioctahedral mica, particularly illite, ranges from 0.50-1.0 (Środoń et al., 1986). In general, the greater the χ , the greater the cation fixation (Sawhney, 1972). Therefore, montmorillonite can host a wider range of interlayer cations, whereas illite can only position K^+ cations and not is readily exchangeable (Marsh et al., 2018; Zhen et al., 2017). According to Sawhney, the layer charge also affects the basal d_{001} spacing or interlayer collapse (Sawhney, 1972). This difference can be demonstrated by XRD interlayer measurements (illite $d_{001} = 9.80 \text{ \AA}$, Figure 3.1; montmorillonite $d_{001} = 14.1 \text{ \AA}$, Figure A.13). As a result, it is expected that the intercalation of NH_4^+ is more prominent in phyllosilicates with a greater χ value.

Figure 3.4a compares NH_4^+ intercalation for untreated and alkaline treated aluminosilicate minerals. The montmorillonite-treated spectrum shows a broad infrared

absorption feature in the 3170 - 3340 domain, indicative of N-H stretching modes of the NH_4^+ cation (3300-2840 cm^{-1}) (Johnson et al., 2020; Pankewitz et al., 2007; Petit et al., 1998; Socrates, 1995). Although the NH_4^+ deformation band (bending mode) of the N-H bonds, at 1385-1430 cm^{-1} is observed for both minerals, it is significantly more pronounced for montmorillonite (Navratilova et al., 2007; Petit et al., 1998).

The intercalation of the NH_4^+ cation suggests a disruption or collapse of the interlayer and, hence, the degree of cation fixation. Numerous reports studied the fixation in both expandable and non-expandable layers (Sawhney, 1972). Ultimately, it is the nature of the cation which dictates the selective sorption in the interlayer. Rajec *et al.*, explains that the preferential sorption of cations to clays is predominantly related to their low hydration level. Cations with low hydration level, such as K^+ , Cs^+ , Rb^+ , and NH_4^+ cause low χ clays to dehydrate and collapse with the cations remaining fixed in the interlayer space. Conversely, cations with a high hydration level, such as Ca^{2+} , Mg^{2+} , and Sr^{2+} , produce expanded interlayers and are not fixed (Rajec et al., 1999; Sawhney, 1972). This is the case for montmorillonite, for which the clay readily sorbs water and polar molecules, resulting in interlayer expansion (Barton, 2002; Chiou & Rutherford, 1997; Laird, 1987; Nadeau, 1985). Zhen *et al.*, on the contrary, explain that intercalation in illite is less common because the interlayer is already collapsed and bound tightly (Zhen et al., 2017). Lastly, Pironon *et al.*, concluded that K^+ and NH_4^+ have similar radii (K^+ , $r = 1.37 \text{ \AA}$; NH_4^+ , $r = 1.43 \text{ \AA}$) allowing the polyatomic ion to substitute for K^+ in minerals, explaining why there is a broader adsorption band for treated illite in Figure 3.4b (Lumen Learning, 2019; Pironon et al., 2003).

Selected area electron diffraction (SAED) patterns and TEM images at 100 and 200 nm resolution show the lattice-fringe of the minerals in Figure 3.5. The features observed for untreated minerals (Figure 3.5a and in Figure 3.5d) are similar to images presented in literature, showing multiple rings representative of polymorphism for the SAED patterns and layer-stacking sequences for the TEM micrographs characteristic of phyllosilicate minerals (Bauluz et al., 2002; Dağ et al., 2019; Nadeau, 1985; Nieto et al., 2010; Xiang et al., 2019). After the minerals were exposed to NH_3 gas for 30 days, the SAED patterns have less pronounced polymorphic rings (Figure 3.5b and Figure 3.5e), indicative of less crystalline and more disordered phases. While it is difficult to demonstrate NH_4^+ ion intercalation within the patterns, TEM micrographs show some corrosion traces on the edges of the minerals. The long, parallel and undulated darker zones on the edge of the mineral could be frayed due to alkaline-induced dissolution, potentially demonstrating the intercalation of the polyatomic cation (Inset Figure 3.5b and Figure 3.5e and Appendix, Figure A.14b and Figure A.14e). These micrograph images correlate to Dağ *et al.*, studies, in which the team observed interlayer expansion of montmorillonite via SEM, TEM, and XRD analysis after a polymerization (styrene monomer) alteration at 85°C for 2 h.

Although the aforementioned synthesis procedure is divergent from the present treatment, literature suggests that the edges are the most pH-dependent and reactive sites for clays (Köhler et al., 2005; Kriaa et al., 2009; Kuwahara, 2008; Missana et al., 2008; Yokoyama et al., 2005). Even though the edges of clay minerals account for only ~20% of the total surface area of illite minerals (Konan et al., 2012), the OH^- available on the periphery of the clay mineral (i.e., edge) is the most reactive surface functional group

(Kriaa et al., 2009). For example, Missana *et al.*, suggests that the sorption of strontium onto illite-smectite mixed clays via surface complexation may take place on the edge site. Moreover, De Koning and Comans affirm that the edges of illite collapsed after being exposed to high (several mmol/L) NH_4^+ concentration in the porewaters during batch desorption experiments. The consequent result of the illite interlayer collapse, the authors suggest, allows for the radioactive isotope cesium to be selectively adsorbed (De Koning & Comans, 2004). Dissolution rate measurements on illite under acid and alkaline conditions further confirm that the edges (O layer) of the clay dissolve faster than the basal planes (T layers), changing the clay morphology and decreasing the percentage of the reactive edge sites (Köhler et al., 2005). Similarly, independent studies on muscovite (Kuwahara, 2008) and montmorillonite (Yokoyama et al., 2005) dissolution under highly alkaline conditions ($\text{pH} > 11.2$) confirm via atomic force microscopy that dissolution solely occurs at particle edges, with negligible dissolution on the basal planes.

Upon aeration, illite and montmorillonite SAED patterns (Figure 3.5b and 3.5f) have more pronounced polymorphic rings than those of the ammonia-treated patterns, indicative of more crystalline phases. It is interesting to note that the untreated SAED images (Figures 3.5a and 3.5d) are analogous to the diffraction bands of the aerated, pH 8 SAED images. This suggests that during the process of aeration, the minerals recrystallized following dissolution at high pH and secondary precipitation. While the morphology alteration is difficult to discern via SAED patterns, the reader is suggested to note the difference in ammonia and aerated illite particles via SEM analysis (Appendix, Figure A.12).

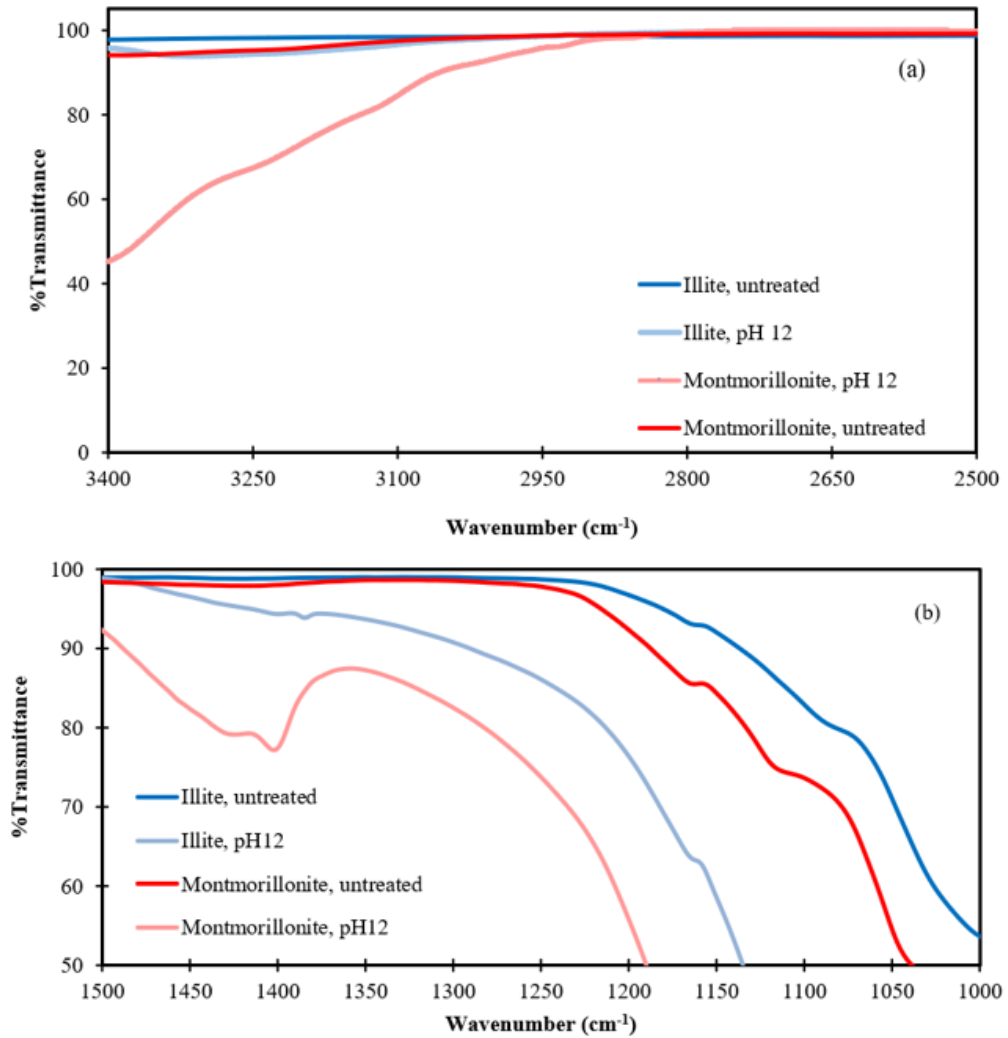


Figure 3.4. Infrared spectra of aluminosilicate minerals (illite-blue and montmorillonite-red) showing (a) the effect of ammonium intercalation as evidenced by the stretching vibrations of N-H groups at $\sim 3100 \text{ cm}^{-1}$ and (b) the bending vibrational modes of N-H groups at $\sim 1404 \text{ cm}^{-1}$ prior to 95% $\text{N}_2/5\% \text{NH}_3$ gas treatment (control, darker) and post treatment (lighter) for 30-day contact time in SGW solution (7.2 mM) at pH 12.

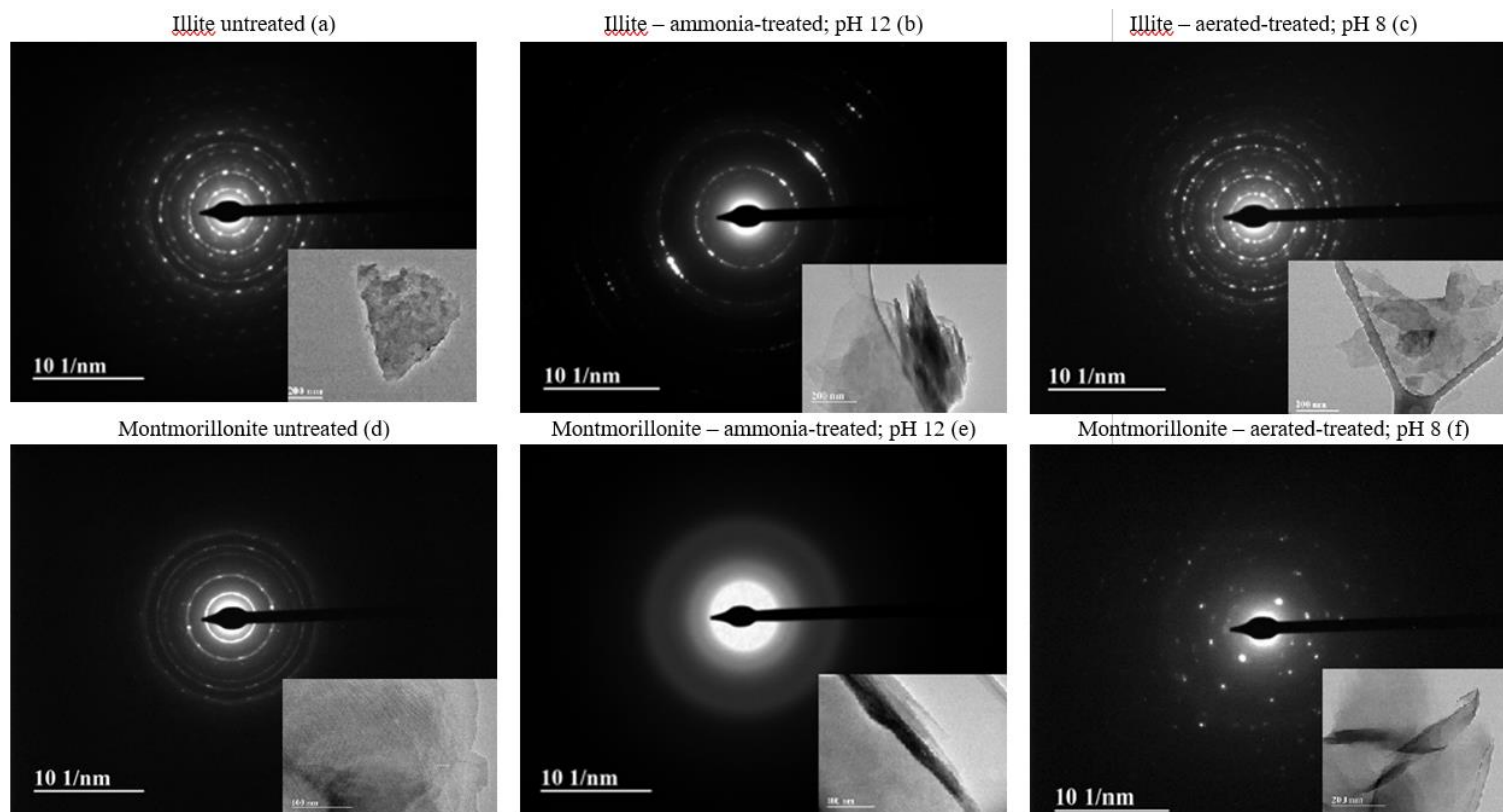


Figure 3.5. Selected area electron diffraction (SAED) image patterns of the crystalline aluminosilicate minerals (illite, top; montmorillonite, bottom) for untreated minerals (a and d), treated with 95% N₂/5% NH₃ gas for 30-day contact time in SGW solution (7.2 mM) at pH 12 (b and e) and aerated-treated at pH 8 (c and f). Bottom right show inset micrographs of Transmission Electron Microscope (TEM) images at 100 and 200 nm resolution

3.4.4 Evidence of Incongruent Dissolution Phenomena

Previous research has suggested incongruent dissolution was occurring in a similar system based on analysis of the aqueous phase ions (Di Pietro et al., 2020; Emerson et al., 2018); however, the solid phase had not yet been adequately characterized to prove incongruent dissolution. In general, under alkaline conditions, the OH⁻ ions first react with the metal atom found at the edge surface (Crundwell, 2014), especially the Al atom as its bond dissociation energy is approximately 1.5x less than that of the Si-O bond (Lippert, 1960). Subsequently, the OH⁻ ions attack the bridging oxygen bonds between the Al and Si atoms (O layer) acting as electron acceptor sites (Lewis acid), also from the existing edge illite surface. From this mechanism, the catalyzed aluminol (Al-OH), and later silanol (Si-OH), sites are detached from the edge site (Kuwahara, 2008). According to Yokoyama *et al.*, these bonds are the most important reactive sites in the dissolution reaction of dioctahedral (Si-O-Al) phyllosilicates (Yokoyama et al., 2005). These could thus provide valuable insight towards incongruent dissolution phenomenon and potential secondary mineral transformation. Referring to Figure 3.2a, ammonia-treated and subsequently aerated illite have sharp infrared peaks at 3621 and 3620 cm⁻¹, respectively. This absorption band corresponds to the stretching of OH groups of Al-OH bonds at the edge (O layer) of illite and is in agreement with the literature (Jiang et al., 2008; Konan et al., 2012; Sedmale et al., 2017; Wanyika, 2014). It is interesting to note that a recent study by Chen *et al.*, found these particular OH groups, perpendicular to the surface (001), had the highest sorption capacity at the edge surface of the O layer in kaolinite mineral (Cheng et al., 2020). This discovery suggests that NH₄⁺ adsorption is most stable between the three active O atoms position, confirmed by the -OH stretching modes in the FTIR spectrum. Similarly,

Kubicki *et al.*, concludes that salicylic acid also sorbs on the edges of the illite grains, predominantly on the Al atoms of the O layer under acidic and neutral conditions (Kubicki *et al.*, 1997). Thus, we can then infer that, whether polyatomic or organic species, sorption is highly likely to occur on the edges of the clay minerals, regardless of pH conditions. However, more studies would need to be conducted and that is beyond the scope of the present paper.

As an aluminosilicate, it is expected that illite shows alumino-silicate structural absorption bands in its FTIR spectrum. Figure 3.2 shows both the typical Al-Al-OH and Si-O-Si stretching vibrations at 913 and 1022 cm^{-1} , respectively (Socrates, 1995). While there are differences in transmittance percentages and shifts between untreated and treated illite samples mostly like due to dissolution mechanisms explained previously; there is, however, negligible difference between pH treatments. The Si-O-Si stretching band at 1022 cm^{-1} is especially notable as it displays no significant change upon treatment. Thus, these results indicate that the T layer framework structure of illite is still intact after alkaline treatment, confirming the theory that basal surfaces are relatively unreactive during short-term (<30 days) dissolution (Bickmore *et al.*, 2001; Kuwahara, 2008; Yokoyama *et al.*, 2005). This is expected as the basal surfaces (T layers) are highly stable and charge-satisfied siloxane bonds, whereas the edge surfaces have a tendency to form inner-sphere complexes with protons and cations as per the examples described above by Chen *et al.*, and Kubicki *et al.*, studies (Bickmore *et al.*, 2001) and as illustrated for NH_4^+ in Figure 3.2.

Because Al is removed from the illite surface first and exhibits relatively low solubility, secondary mineral phase formation is likely to occur. To consider such

formation, ratios of the percent transmission maxima of the most important aluminol and silicate structural functions were calculated as shown in Table 3.6. With a reference of 1.22 as the untreated illite control, peak height ratios from NH_3 treated to aeration-treated increased 4.6 times. This is indicative that secondary phase precipitation is forming since there is a significant change in the surface-sensitive peak ratios. However, the increase in the ratios suggests that the signal from Al-Al-OH is decreasing (increasing transmittance, decreasing absorption). Therefore, this suggests that the increase in ratios from the control to ammonia gas treatment is indicative of incongruent dissolution while the more significant increase from ammonia gas treatment to aeration is indicative of co-precipitation of Al within Si precipitates.

To augment the FTIR studies, SEM-EDS elemental composition analysis was conducted by calculating Al/Si ratios during NH_3 and aeration treatments. Table 3.7 shows the average, variable, number of observation data points, and p value of the t -test performed. Results demonstrate a decrease in the average Al/Si ratio ($n=9$) after a pH decrease. As in the FTIR peak height ratios for pH 8-aerated samples, this decrease suggests that the aqueous Al is decreasing in solubility at a higher rate than Si, and thus, forming secondary mineral phase formation. This is in accordance with recent studies where authors predict aluminosilicate re-precipitation of various silica and aluminosilicate solid phases (Di Pietro et al., 2020; Emerson et al., 2018; Mashal et al., 2004; Qafoku, Ainsworth, Szecsody, Qafoku, et al., 2003; Zhong et al., 2015). To compare the two Al/Si ratios, a t -test was conducted. The p -value is ≤ 0.05 ($p = 0.024$), suggesting that both treatments are comparable, and thus statistically different.

Table 3.6. FTIR % transmission ratios of Al-Al-OH/Si-O-Si peak heights (at 913 cm⁻¹ and 1022 cm⁻¹, respectively) for illite mineral

Treatment	Al-Al-OH/Si-O-Si	Si transmission (%)	Al transmission (%)
Untreated	1.22	52.6	64.0
Ammonia, pH 12	6.63	9.83	65.2
Aerated, pH 8	30.4	1.62	49.3

Table 3.7. *t*-Test (average, variance, observation number and *p* value) for Al/Si illite ratios (pH 12 and 8) assuming unequal variances

	pH 12	pH 8
Average	0.475	0.374
Variance	0.002	0.011
Observations spots	9	9
<i>p</i> (≤ 0.05 or $>$)	0.024	
<i>p</i> = 0.024 is ≤ 0.05 , therefore the data set is statistically different		

3.4.5 Characterization of Mineral Transformations

The local structural transformations induced by the ammonia and aeration treatments are investigated with solid-state ²⁹Si NMR. The ²⁹Si MAS NMR spectra of the untreated (control), ammonia-treated, and aerated illite samples are shown in Figure 3.5. In most naturally occurring silicates, Si is tetrahedrally coordinated by oxygen and have chemical shifts (δ) in the range of -60 to -120 ppm (Kirkpatrick et al., 1985). For the untreated sample, the resolved peak appeared within range at ~ -111 ppm. According to comparative ²⁹Si MAS NMR illite studies, this chemical shift is representative of low-cristobalite, a mineral polymorph within the quartz group (Thompson, 1984). Preliminary characterization studies indicate that illite contains a large percentage of SiO₂ (55.7 ± 8.6 wt%, Table 3.3) and a prominent sharp quartz peak (Figure 3.1), consistent with the

presented SEM-EDS and XRD analysis, respectively. The small shoulder at ~ -101 ppm is attributed to illite, correspondent to the framework aluminosilicates $Q^4(0Al)$ coordination due to the $[SiO_4]^{n-}$ groups crosslinked in the tetrahedral sheets with no Al in the neighboring (Alver et al., 2016; Kirkpatrick et al., 1985). It is important to note that the usual notation to describe the extent of Si polymerization and the number of Al is given by $Q^m(nAl)$, where m is the number of bridging oxygens to which the Si is coordinated to and n is the number of Al (Kirkpatrick et al., 1985).

As the samples are treated, the peak at ~ -111 ppm is still present; it is, however, slightly deshielded (i.e., less negative chemical shift), indicating that the tectosilicate phases remain after treatments in the investigated illite samples. The strong paramagnetic influence may be caused by the: (1) Fe content and/or (2) different local structure, potentially due to Si substitution. ^{29}Si MAS NMR studies have previously provided evidence that samples containing Fe in the octahedral sheet had intensity lines considerably broadened by paramagnetic interaction (Carroll et al., 2005; Roch et al., 1998; Sanz & Serratos, 1984). We can be certain that a significant percentage of Fe is found in our illite samples as chemical analysis detected 6.7 ± 3.6 wt% in Fe-content, a value within the range suggested by Carroll *et al.* (4.8-7.1 wt%) (Carroll et al., 2005) and verified by Roch *et al.* studies (6.3 wt%) (Roch et al., 1998). These distorted lineshapes display a deshielded chemical shift between $\delta = -93$ and -83 , in accordance to $Q^{2-3}(0-3Al)$ phyllosilicate coordination (Figure 3.6) (Barnes et al., 1986; Kirkpatrick et al., 1985; Lippmaa et al., 1980; Thompson, 1984). The observed shift in local structure around the Si atoms is likely due to the incorporated cations for octahedral sites, typically being Al,

Mg and Fe ions (Barnes et al., 1986). In a recent alkaline comparative treatment with illite mineral, formation of secondary Fe-oxides via oxidation-reduction potential (ORP) measurements have been suggested (Di Pietro et al., 2020). The effect in reduction (i.e., ammonia treatment) and subsequent oxidation (i.e., aeration treatment) could explain the shift in resonance, leading to secondary formation and supporting incongruent dissolution phenomena.

Further, a quantitative examination was conducted on the extent of Si polymerization according to Q orientation. As shown in Figure 3.7, both treated illite samples increase in their Q² (bridging groups) abundance (78.5%, pH 12; 75.8%, pH 8) in comparison to the untreated control (11.2%) sample. According to Lippmaa *et al.*, a regular paramagnetic shift accompanies increasing substitution of Si by Al in the Q⁴ coordination units (Lippmaa et al., 1980). It is important to note that, although untreated illite sample contained 52.5% Q³ (phyllosilicate) orientation abundance, quantitative examination determined 36.3%, a lower yet substantial Q⁴ (framework silicate structure) abundance. Therefore, the Q² orientation increase is mostly likely due to Al substitution. Such hypothesis is in accordance to the general ²⁹Si MAS NMR rule that the effect of octahedral Al increases as the polymerization of the material decreases (Kirkpatrick et al., 1985). As previously stated in sections 3.4.3 and 3.4.4, the edge sites (O layer) of clays are the most reactive surface functional group due to its Lewis acid behavior (electron acceptor). Several studies conclude that Si replaced by Al substitution is more likely to occur in the O layer, with lower percentages, ~12.0% (Bibi et al., 2011), 14.8% (Mankin & Dodd, 1961) and 16.7% (Grim, 1953), resulting in the T layer. Therefore, it can be concluded that the chemical

shifts in treated samples shown in Figure 3.6 are likely due to Al substitution in the O layer, and to a lesser extent Fe paramagnetic perturbation, as supported by TEM micrographs (Figure 3.5) and decrease in Al:Si ratios (Table 3.6).

In order to support the T and O layer transformations around the Si atoms and to quantify the incorporation of Al into edge sites, ^{27}Al MAS NMR (Figure 3.8) was conducted. All three samples show the same 3 peaks at ~ 65 , ~ 53 , and ~ -0.4 ppm, with slight changes in intensity of the 53 ppm peak depending on treatment. The higher frequency peaks, 65 and 53 ppm, correspond to tetrahedrally coordinated Al(IV) and the peak at -0.4 ppm corresponds to octahedrally coordinated Al, Al(VI). According to Pardal *et al.*, Al tetrahedral positions are Q^2 (bridging or pairing groups) and Q^3 (phyllosilicates). These positions are in accordance to Figure 3.6, particularly for Q^2 in ammonia-treated and subsequently aerated- samples, as they exhibit $> 75.8\%$ local structure to Si. Sun *et al.* proposed that the Al(IV) coordination corresponded to Al located in either Q^3 positions or Q^2 bridging positions charge-balanced by Ca^{2+} (Sun *et al.*, 2006). While our SGW solution does contain Ca^{2+} ions, the Al(IV) coordination was primarily charge-balanced by NH_4^+ ions during ammonia-treatment. Although the interaction with NH_4^+ ions occurred for the ammonia-treated sample, Figure 3.7 shows very similar trends to the untreated control illite sample. Further, it is well-known that the presence of Al instead of adjacent Si for any Si atom site produces a higher frequency shift of $\sim 3\text{-}5$ ppm, supporting the hypothesis previously stated on Si replacement by Al substitution occurring in the O layer and Al incorporation on the edge-sites (Duxson *et al.*, 2005; Engelhardt & Michel, 1987; Pardal *et al.*, 2012).

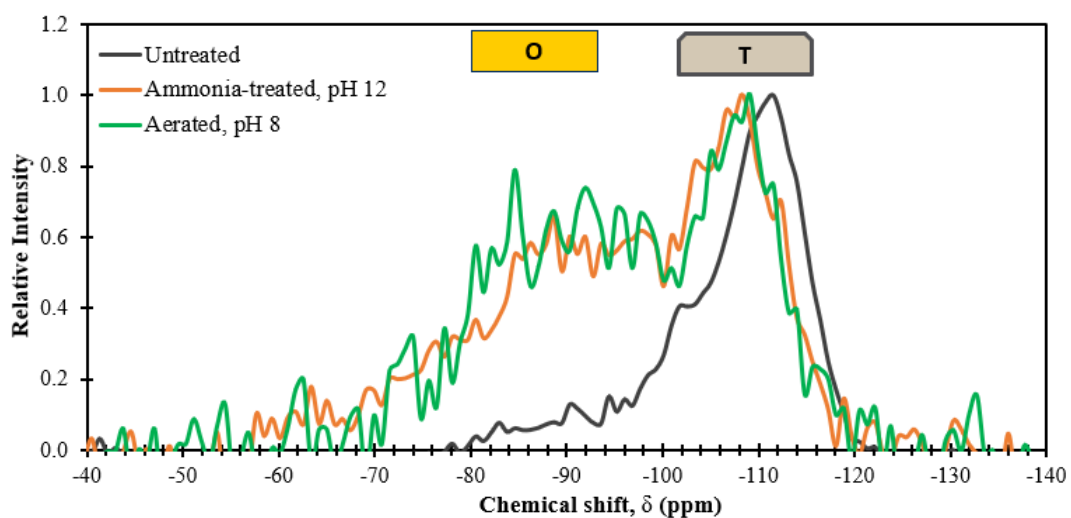


Figure 3.6. ^{29}Si NMR for illite control (black), ammonia-treated (orange), and aerated (green). Shapes above spectra represent where within the illite phyllosilicate structure are splitting and shifting (ppm). Note: “T” and “O” are representative of tetrahedral and octahedral layers, respectively.

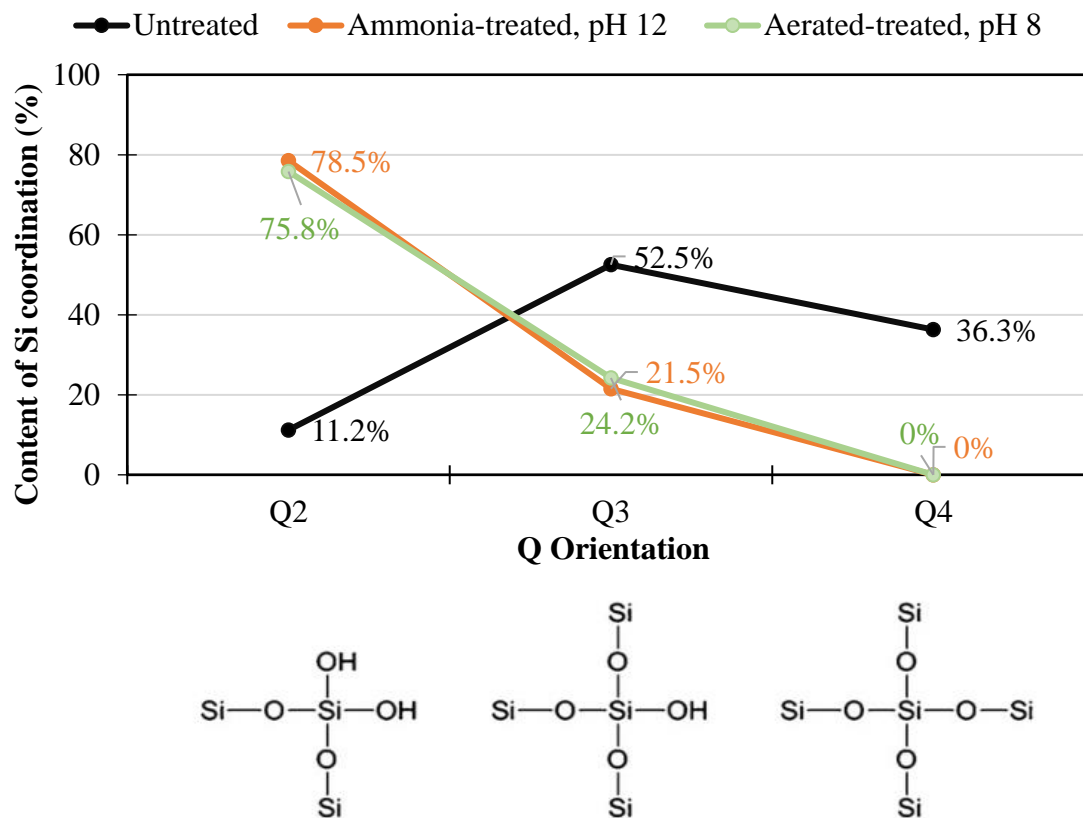


Figure 3.7. Plot of the Q2, Q3, and Q4 content (in %) according to ^{29}Si NMR spectroscopy for illite (untreated), ammonia-treated (orange), and aerated (green). Note: the bottom image shows the extent to Si polymerization according to Q orientation.

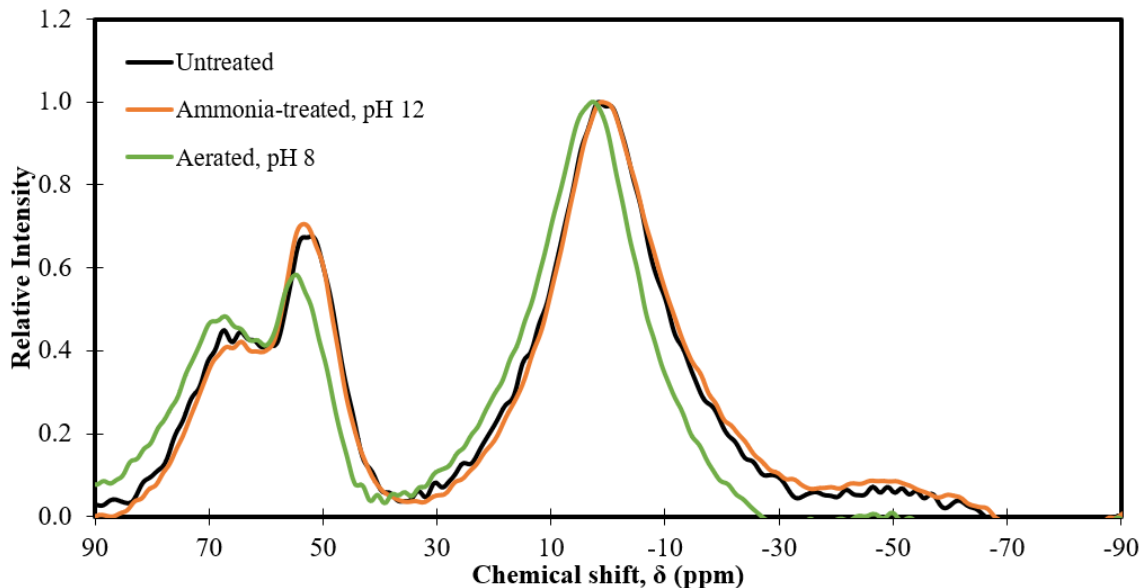


Figure 3.8. ^{27}Al MAS (y-axis) NMR for illite control (black), ammonia-treated (orange), and aerated (green).

3.5 Conclusion

This study has identified the major physicochemical changes of aluminosilicate minerals following NH_3 gas treatment and subsequent aeration. This systematic investigation used a range of characterization and spectroscopic techniques. Even though illite and montmorillonite are both dioctahedral 2:1 clay minerals, their interaction with NH_3 gas is different. The low hydration level of the NH_4^+ cation allows for interlayer collapse in the montmorillonite clay, yet not as pronounced in the illite mineral as demonstrated by FTIR. However, both minerals demonstrate an alteration in morphology and recrystallization following aeration upon microscopic (SEM and TEM) and surface area (BET) analysis. These physical changes were further supported by MAS NMR analysis, where edge-site Al and $[\text{SiO}_4]^{n-}$ groups display changes in local structure for ammonia- and aerated-treated samples.

The results highlight the importance of mineral alteration upon *in situ* remediation with NH₃ gas, particularly following treatment as NH₃ is removed from the aqueous phase by adsorption to sediments and diffusion through gas phases as pH returns to natural soil conditions. At pH ~ 8.5, mineral samples exhibited larger particle size, pronounced polymorphic rings, incongruent dissolution phenomena, and higher Al content in the O layer, indicative of secondary phase formation due to relatively low solubility at circumneutral conditions. For the environmental remediation application, these mineral alteration and co-precipitation processes could remove soluble contaminant cations from the aqueous phase and coat minerals with adsorbed contaminants on the surface such as illite and montmorillonite. Future research will be necessary to understand the complex reactions induced by alkaline remediation techniques on heterogeneous sediment samples to determine whether they will exhibit the same physicochemical changes. Overall, injection of NH₃ gas treatment of aluminosilicate minerals demonstrates potential contaminant sequestration through mineral alterations discussed in this research.

3.6 References

- Alver, B. E., Dikmen, G., & Alver, Ö. (2016). Investigation of the influence of heat treatment on the structural properties of illite-rich clay mineral using FT-IR, ²⁹Si MAS NMR, TG and DTA methods. *Anadolu University*, 17(5), 823–829.
- ASTM. (2010). Standard test method for measuring the exchange complex and cation exchange capacity of inorganic fine-grained soils. *ASTM D7503-10*.
- Baeyens, B., & Bradbury, M. H. (2004). Cation exchange capacity measurements on illite using the sodium and cesium isotope dilution technique: effects of the index cation, electrolyte concentration and competition: modeling. *Clays and Clay Minerals*, 52(4), 421–431.

- Barnes, Clague, A. D. H., Clayden, N. J., Dobson, C. M., & Jones, R. B. (1986). The application of ^{29}Si and ^{27}Al solid state n.m.r. spectroscopy to characterising minerals in coals. *Fuel*, 65(3), 437–441.
- Barnes, M. C., Addai-Mensah, J., & Gerson, A. R. (1999). The solubility of sodalite and cancrinite in synthetic spent Bayer liquor. *Colloids and Surfaces A: Physicochemical and Engineering Aspects*, 157(1–3), 101–116.
- Barton, C. D. (2002). Clay minerals. In: Rattan Lal, Comp., Ed. *Encyclopedia of Soil Science*. New York, New York: Marcel Dekker: 187-192.
- Bauluz, B., Peacor, D. R., & Ylagan, R. F. (2002). Transmission electron microscopy study of smectite illitization during hydrothermal alteration of a rhyolitic hyaloclastite from Ponza, Italy. *Clays and Clay Minerals*, 50(2), 157–173.
- Belviso, C., Cavalcante, F., Niceforo, G., & Lettino, A. (2017). Sodalite, faujasite and A-type zeolite from 2: 1 dioctahedral and 2: 1: 1 trioctahedral clay minerals. A singular review of synthesis methods through laboratory trials at a low incubation temperature. *Powder Technology*, 320, 483–497.
- Bibi, I., Singh, B., & Silvester, E. (2011). Dissolution of illite in saline–acidic solutions at 25 C. *Geochimica et Cosmochimica Acta*, 75(11), 3237–3249.
- Bickmore, B. R., Bosbach, D., Hochella, M. F., Charlet, L., & Rufe, E. (2001). In situ atomic microscopy study of hectorite and nontronite dissolution: Implications for phyllosilicate edge surface structures and dissolution mechanisms. *American Mineralogist*, 86(4), 411–423.
- Boggs, M. A., Dai, Z., Kersting, A. B., & Zavarin, M. (2015). Plutonium (IV) sorption to montmorillonite in the presence of organic matter. *Journal of Environmental Radioactivity*, 141, 90–96.
- Brigatti, M. F., Galan, E., & Theng, B. K. G. (2006). Structures and mineralogy of clay minerals. *Developments in Clay Science*, 1, 19–86.
- Brunauer, S., Emmett, P. H., & Teller, E. (1938). Adsorption of gases in multimolecular layers. *Journal of the American Chemical Society*, 60(2), 309–319.
- Carroll, Kemp, T. F., Bastow, T. J., & Smith, M. E. (2005). Solid-state NMR characterisation of the thermal transformation of a Hungarian white illite. *Solid State Nuclear Magnetic Resonance*, 28(1), 31–43.
- Chen, S., Guan, D., Zhang, Y., Wang, Z., & Jiang, N. (2019). Composition and kinetic study on template- and solvent-free synthesis of ZSM-5 using leached illite clay. *Microporous and Mesoporous Materials*, 285, 170–177.

- Cheng, Q., Li, Y., Qiao, X., Guo, Y., Zhao, Y., Zhang, Q., Ju, Y., & Shi, Y. (2020). Molecular Modeling of Ammonia Gas Adsorption onto the Kaolinite Surface with DFT Study. *Minerals*, 10(1), 46.
- Chiou, C. T., & Rutherford, D. W. (1997). Effects of exchanged cation and layer charge on the sorption of water and EGME vapors on montmorillonite clays. *Clays and Clay Minerals*, 45(6), 867–880.
- Churchman, G. J., & Lowe, D. J. (2012). *Alteration, formation, and occurrence of minerals in soils*. CRC press.
- Crundwell, F. K. (2014). The mechanism of dissolution of minerals in acidic and alkaline solutions: Part II Application of a new theory to silicates, aluminosilicates and quartz. *Hydrometallurgy*, 149, 265–275.
- Dağ, S. E., Bozkurt, P. A., Eroğlu, F., & Çelik, M. (2019). Preparation, characterization, and properties of polystyrene/Na-montmorillonite composites. *Journal of Thermoplastic Composite Materials*, 32(8), 1078–1091.
- De Koning, A., & Comans, R. N. J. (2004). Reversibility of radiocaesium sorption on illite. *Geochimica et Cosmochimica Acta*, 68(13), 2815–2823.
- Di Pietro, S. A., Emerson, H. P., Katsenovich, Y., Qafoku, N. P., & Szecsody, J. E. (2020). Phyllosilicate mineral dissolution upon alkaline treatment under aerobic and anaerobic conditions. *Applied Clay Science*, 189.
- Dove, P. M. (1995). Kinetic and thermodynamic controls on silica reactivity in weathering environments. *Chemical Weathering Rates of Silicate Minerals*, 235–290.
- Doye, I., & Duchesne, J. (2003). Neutralisation of acid mine drainage with alkaline industrial residues: laboratory investigation using batch-leaching tests. *Applied Geochemistry*, 18(8), 1197–1213.
- Duxson, P., Provis, J. L., Lukey, G. C., Separovic, F., & van Deventer, J. S. J. (2005). ²⁹Si NMR study of structural ordering in aluminosilicate geopolymer gels. *Langmuir*, 21(7), 3028–3036.
- El Hafid, K., & Hajjaji, M. (2015). Effects of the experimental factors on the microstructure and the properties of cured alkali-activated heated clay. *Applied Clay Science*, 116, 202–210.
- Emerson, H. P., Di Pietro, S., Katsenovich, Y., & Szecsody, J. (2017). Effects of ammonium on uranium partitioning and kaolinite mineral dissolution. *Journal of Environmental Radioactivity*, 167.

- Emerson, H. P., Di Pietro, S., Katsenovich, Y., & Szecsody, J. (2018). Potential for U sequestration with select minerals and sediments via base treatment. *Journal of Environmental Management*, 223.
- Engelhardt, G., & Michel, D. (1987). *High-resolution solid-state NMR of silicates and zeolites*.
- Fernández, R., Ruiz, A. I., & Cuevas, J. (2014). The role of smectite composition on the hyperalkaline alteration of bentonite. *Applied Clay Science*, 95, 83–94.
- Gailhanou, H., Van Miltenburg, J. C., Rogez, J., Olives, J., Amouric, M., Gaucher, E. C., & Blanc, P. (2007). Thermodynamic properties of anhydrous smectite MX-80, illite IMt-2 and mixed-layer illite–smectite ISCz-1 as determined by calorimetric methods. Part I: Heat capacities, heat contents and entropies. *Geochimica et Cosmochimica Acta*, 71(22), 5463–5473.
- Grauer, R. (1994). Bentonite as a backfill material in a high-level waste repository. *MRS Bulletin*, 19(12), 43–46.
- Grim, R. E. (1953). *Clay mineralogy* (Vol. 76, Issue 4). LWW.
- Gualtieri, A. F., Ferrari, S., Leoni, M., Grathoff, G., Hugo, R., Shatnawi, M., Paglia, G., & Billinge, S. (2008). Structural characterization of the clay mineral illite-1M. *Journal of Applied Crystallography*, 41(2), 402–415.
- He, C., Makovicky, E., & Øsbæck, B. (1995). Thermal stability and pozzolanic activity of calcined illite. *Applied Clay Science*, 9(5), 337–354.
- Hendershot, W. H., Lalonde, H., & Duquette, M. (1993). Ion exchange and exchangeable cations. *Soil Sampling and Methods of Analysis*, 19, 167–176.
- Jiang, T., Li, G., Qiu, G., Fan, X., & Huang, Z. (2008). Thermal activation and alkali dissolution of silicon from illite. *Applied Clay Science*, 40(1), 81–89.
- Johnson, T. J., Diaz, E., Hughey, K. D., Myers, T. L., Blake, T. A., Dohnalkova, A. C., & Burton, S. D. (2020). Infrared Optical Constants from Pressed Pellets of Powders: I. Improved n and k Values of (NH₄)₂SO₄ from Single-Angle Reflectance. *Applied Spectroscopy*, 74(8), 851–867.
- Kang, S.-J., & Egashira, K. (1997). Modification of different grades of Korean natural zeolites for increasing cation exchange capacity. *Applied Clay Science*, 12(1–2), 131–144.

- Katsenovich, Y. P., Cardona, C., Lapiere, R., Szecsody, J., & Lagos, L. E. (2016). The effect of Si and Al concentrations on the removal of U(VI) in the alkaline conditions created by NH₃ gas. *Applied Geochemistry*, 73, 109–117.
- Katsenovich, Y. P., Cardona, C., Szecsody, J., Lagos, L. E., & Tang, W. (2018). Assessment of calcium addition on the removal of U(VI) in the alkaline conditions created by NH₃ gas. *Applied Geochemistry*, 92, 94–103.
- Kirkpatrick, R. J., Smith, K. A., Schramm, S., Turner, G., & Yang, W.-H. (1985). Solid-state nuclear magnetic resonance spectroscopy of minerals. *Annual Review of Earth and Planetary Sciences*, 13(1), 29–47.
- Köhler, S. J., Bosbach, D., & Oelkers, E. H. (2005). Do clay mineral dissolution rates reach steady state? *Geochimica et Cosmochimica Acta*, 69(8), 1997–2006.
- Konan, Peyratout, C., Bonnet, J.-P., Smith, A., Jacquet, A., Magnoux, P., & Ayrault, P. (2007). Surface properties of kaolin and illite suspensions in concentrated calcium hydroxide medium. *Journal of Colloid and Interface Science*, 307(1), 101–108.
- Konan, Peyratout, C., Smith, A., Bonnet, J.-P., Magnoux, P., & Ayrault, P. (2012). Surface modifications of illite in concentrated lime solutions investigated by pyridine adsorption. *Journal of Colloid and Interface Science*, 382(1), 17–21.
- Kriaa, A., Hamdi, N., & Srasra, E. (2009). Proton adsorption and acid-base properties of Tunisian illites in aqueous solution. *Journal of Structural Chemistry*, 50(2), 273–287.
- Kubicki, J. D., Itoh, M. J., Schroeter, L. M., & Apitz, S. E. (1997). Bonding mechanisms of salicylic acid adsorbed onto illite clay: an ATR–FTIR and molecular orbital study. *Environmental Science & Technology*, 31(4), 1151–1156.
- Kuwahara, Y. (2008). In situ observations of muscovite dissolution under alkaline conditions at 25–50 °C by AFM with an air/fluid heater system. *American Mineralogist*, 93(7), 1028–1033.
- Laird, D. A. (1987). *Layer charge and crystalline swelling of expanding 2: 1 phyllosilicates*. University Microfilms International.
- Lippmaa, Maegi, M. ., Samoson, A., Engelhardt, G., & Grimmer, A. R. (1980). Structural studies of silicates by solid-state high-resolution silicon-29 NMR. *Journal of the American Chemical Society*, 102(15), 4889–4893.
- Lumen Learning. (2019). *Silicate Minerals*.
<https://courses.lumenlearning.com/physicalgeology/chapter/2-4-silicate-minerals/>

- Mankin, C. J., & Dodd, C. G. (1961). Proposed reference illite from the Ouachita Mountains of southeastern Oklahoma. *Clays and Clay Minerals*, 10(1), 372–379.
- Marsh, A., Heath, A., Patureau, P., Evernden, M., & Walker, P. (2018). Alkali activation behaviour of un-calcined montmorillonite and illite clay minerals. In *Applied Clay Science* (Vol. 166, pp. 250–261).
- Mashal, K., Harsh, J. B., Flury, M., Felmy, A. R., & Zhao, H. (2004). Colloid formation in Hanford sediments reacted with simulated tank waste. *Environmental Science & Technology*, 38(21), 5750–5756.
- Mason, C. F. V, Turney, W. R. J. R., Thomson, B. M., Lu, N., Longmire, P. A., & Chisholm-Brause, C. J. (1997). Carbonate Leaching of Uranium from Contaminated Soils. *Environmental Science & Technology*, 31(10), 2707–2711.
- Mertz, L. (1967). Auxiliary computation for Fourier spectrometry. *Infrared Physics*, 7(1), 17–23.
- Mezni, M., Hamzaoui, A., Hamdi, N., & Srasra, E. (2011). Synthesis of zeolites from the low-grade Tunisian natural illite by two different methods. *Applied Clay Science*, 52(3), 209–218.
- Missana, T., Garcia-Gutierrez, M., & Alonso, U. (2008). Sorption of strontium onto illite/smectite mixed clays. *Physics and Chemistry of the Earth*, 33(SUPPL. 1).
- Mostowicz, R., & Berak, J. M. (1989). Morphology of Zeolites, Primarily Pentasils, and Its Significance for Catalysis. *Catalysis on Zeolites*, 20(17), 187–203.
- Myers, T. L., Tonkyn, R. G., Danby, T. O., Taubman, M. S., Bernacki, B. E., Birnbaum, J. C., Sharpe, S. W., & Johnson, T. J. (2018). Accurate measurement of the optical constants n and k for a series of 57 inorganic and organic liquids for optical modeling and detection. *Applied Spectroscopy*, 72(4), 535–550.
- Nadeau, P. H. (1985). The physical dimensions of fundamental clay particles. *Clay Minerals*, 20(4), 499–514.
- Navratilova, Z., Wojtowicz, P., Vaculikova, L., & Sugarkova, V. (2007). Sorption of alkylammonium cations on montmorillonite. *Acta Geodynamica et Geomaterialia*, 4(3), 59.
- Nieto, Mellini, M., & Abad, I. (2010). The role of H_3O^+ in the crystal structure of illite. *Clays and Clay Minerals*, 58(2), 238–246.
- O’Loughlin, E. J., Traina, S. J., & Sims, G. K. (2000). Effects of sorption on the biodegradation of 2-methylpyridine in aqueous suspensions of reference clay

- minerals. *Environmental Toxicology and Chemistry: An International Journal*, 19(9), 2168–2174.
- Öztop, B., & Shahwan, T. (2006). Modification of a montmorillonite–illite clay using alkaline hydrothermal treatment and its application for the removal of aqueous Cs⁺ ions. *Journal of Colloid and Interface Science*, 295(2), 303–309.
- Pankewitz, T., Lagutschenkov, A., Niedner-Schatteburg, G., Xantheas, S. S., & Lee, Y.-T. (2007). Infrared spectrum of NH₄⁺(H₂O): Evidence for mode specific fragmentation. *The Journal of Chemical Physics*, 126(7), 74307.
- Pardal, X., Brunet, F., Charpentier, T., Pochard, I., & Nonat, A. (2012). ²⁷Al and ²⁹Si solid-state NMR characterization of calcium-aluminosilicate-hydrate. *Inorganic Chemistry*, 51(3), 1827–1836.
- Petit, S., Righi, D., Madejová, J., & Decarreau, A. (1998). Layer charge estimation of smectites using infrared spectroscopy. *Clay Minerals*, 33(4), 579–591.
- Pironon, J., Pelletier, M., De Donato, P., & Mosser-Ruck, R. (2003). Characterization of smectite and illite by FTIR spectroscopy of interlayer NH₄⁺ cations. *Clay Minerals*, 38(2), 201–211.
- Qafoku, Ainsworth, C. C., Szecsody, J., Qafoku, O. S., & Young, J. S. (2003). Aluminum Effect on Dissolution and Precipitation under Hyperalkaline Conditions: II. solid Phase Transformations. *Journal of Environmental Quality*, 32(6), 2364–2372.
- Qafoku, N. P., Ainsworth, C. C., Szecsody, J. E., & Qafoku, O. S. (2004). Transport-controlled kinetics of dissolution and precipitation in the sediments under alkaline and saline conditions. *Geochimica et Cosmochimica Acta*, 68(14), 2981–2995.
- Rajec, P., Šucha, V., Eberl, D. D., Środoń, J., & Elsass, F. (1999). Effect of illite particle shape on cesium sorption. *Clays and Clay Minerals*, 47(6), 755–760.
- Rettie, A. J. E., Chemelewski, W. D., Wygant, B. R., Lindemuth, J., Lin, J.-F., Eisenberg, D., Brauer, C. S., Johnson, T. J., Beiswenger, T. N., & Ash, R. D. (2016). Synthesis, electronic transport and optical properties of Si: α-Fe₂O₃ single crystals. *Journal of Materials Chemistry C*, 4(3), 559–567.
- Rhoades, J. D. (1983). Cation exchange capacity. *Methods of Soil Analysis: Part 2 Chemical and Microbiological Properties*, 9, 149–157.
- Roch, G. E., Smiths, M. E., & Drachman, S. R. (1998). Solid state NMR characterization of the thermal transformation of an illite-rich clay. *Clays and Clay Minerals*, 46(6), 694–704.

- Ruiz, Blanco, C., Pesquera, C., Gonzalez, F., Benito, I., & Lopez, J. L. (1997). Zeolitization of a bentonite and its application to the removal of ammonium ion from waste water. *Applied Clay Science*, 12(1–2), 73–83.
- Sanz, J., & Serratosa, J. M. (1984). Silicon-29 and aluminum-27 high-resolution MAS-NMR spectra of phyllosilicates. *Journal of the American Chemical Society*, 106(17), 4790–4793.
- Sawhney, B. L. (1972). Selective Sorption and Fixation of Cations by Clay Minerals: A Review. In *Clays and Clay Minerals* (Vol. 20). Pergamon Press.
- Sedmale, G., Randers, M., Rundans, M., & Seglins, V. (2017). Application of differently treated illite and illite clay samples for the development of ceramics. *Applied Clay Science*, 146(January), 397–403.
- Serne, R., Qafoku, N., Szecsody, J. E., & Truex, M. (2020). *Sediment Mineralogy Data Review for the Hanford Central Plateau*.
- Socrates, G. (1995). Infrared characteristic group frequencies, Tables and charts. *Journal of the American Chemical Society*, 117(5), 1671.
- Środoń, J., Morgan, D. J., Eslinger, E. V., Eberl, D. D., & Karlinger, M. R. (1986). Chemistry of illite/smectite and end-member illite. *Clays and Clay Minerals*, 34(4), 368–378.
- Środoń, & MaCarty, D. K. (2008). Surface area and layer charge of smectite from CEC and EGME/H₂O-retention measurements. *Clays and Clay Minerals*, 56(2), 155–174.
- Sun, G. K., Young, J. F., & Kirkpatrick, R. J. (2006). The role of Al in C–S–H: NMR, XRD, and compositional results for precipitated samples. *Cement and Concrete Research*, 36(1), 18–29.
- Sweet, L. E., Blake, T. A., Henager, C. H., Hu, S., Johnson, T. J., Meier, D. E., Peper, S. M., & Schwantes, J. M. (2013). Investigation of the polymorphs and hydrolysis of uranium trioxide. *Journal of Radioanalytical and Nuclear Chemistry*, 296(1), 105–110.
- Szecsody, Bagwell, C., Mackley, R., & Hoyle, S. (2020). *Evaluation of Ammonia Discharge into PUREX Crib 216-A-37-1 and Nitrogen Species Fate in the Subsurface*.

- Szecsody, J. E., Krupka, K. M., Williams, M. D., Cantrell, K. J., Resch, C. T., & Fruchter, J. S. (1998). *Uranium mobility during in situ redox manipulation of the 100 areas of the hanford site*. Pacific Northwest National Lab.(PNNL), Richland, WA (United States).
- Szecsody, Truex, M. J., Zhong, L., Johnson, T. C., Qafoku, N. P., Williams, M. D., Greenwood, W. J., Wallin, E. L., Bargar, J. D., & Faurie, D. K. (2012). Geochemical and Geophysical Changes during Ammonia Gas Treatment of Vadose Zone Sediments for Uranium Remediation. *Vadose Zone Journal*, 11(4).
- Thompson, J. G. (1984). ^{29}Si and ^{27}Al nuclear magnetic resonance spectroscopy of 2:1 clay minerals. *Clay Minerals*, 19(2), 229–236.
- Tro, N. J., Fridgen, T. D., Shaw, L., & Boikess, R. S. (2017). *Chemistry: A molecular approach*. Pearson Boston, MA.
- Truex, M. J., Demirkanli, D. I., Szecsody, J. E., Snyder, M. M., Moran, J. J., Nims, M. K., Lawter, A. R., Resch, C. T., Saunders, D. L., & Qafoku, N. P. (2017). *Contaminant Attenuation and Transport Characterization of 200-DV-1 Operable Unit Sediment Samples from Boreholes C9497, C9498, C9603, C9488, and C9513*. Pacific Northwest National Lab.(PNNL), Richland, WA (United States).
- Wan, J., Larsen, J. T., Tokunaga, T. K., & Zheng, Z. (2004). pH neutralization and zonation in alkaline-saline tank waste plumes. *Environmental Science & Technology*, 38(5), 1321–1329.
- Wanyika, H. (2014). Controlled release of agrochemicals intercalated into montmorillonite interlayer space. *The Scientific World Journal*, 2014.
- Xiang, G., Ye, W., Yu, F., Wang, Y., & Fang, Y. (2019). Surface fractal dimension of bentonite affected by long-term corrosion in alkaline solution. *Applied Clay Science*, 175, 94–101. <http://www.sciencedirect.com/science/article/pii/S0169131719301358>
- Yokoyama, S., Kuroda, M., & Sato, T. (2005). Atomic force microscopy study of montmorillonite dissolution under highly alkaline conditions. *Clays and Clay Minerals*, 53(2), 147–154.
- Zhao, H., Deng, Y., Harsh, J. B., Flury, M., & Boyle, J. S. (2004). Alteration of kaolinite to cancrinite and sodalite by simulated Hanford tank waste and its impact on cesium retention. *Clays and Clay Minerals*, 52(1), 1–13.
- Zhen, R., Jiang, Y. S., Li, F. F., & Xue, B. (2017). A study on the intercalation and exfoliation of illite. *Research on Chemical Intermediates*, 43(2), 679–692.

Zhong, L., Szecsody, J. E., Truex, M. J., Williams, M. D., & Liu, Y. (2015). Ammonia gas transport and reactions in unsaturated sediments: Implications for use as an amendment to immobilize inorganic contaminants. *Journal of Hazardous Materials*, 289, 118–129.

CHAPTER IV

Determination of Solid Phases Speciation and Mobility of Uranium

4 CHAPTER 4: DETERMINATION OF SOLID PHASES SPECIATION AND MOBILITY OF URANIUM

4.1 Abstract

Uranium (U) sorption and partitioning was evaluated in SGW of phyllosilicate minerals and Hanford Site sediments using traditional batch experiments to evaluate the association of mobile and immobile U species to the solid phase. The reactivity of the U species was dependent on several factors, such as contact time (short and long-term periods), remediation treatment, and surface characteristics. The objective of this study was to determine whether the application of the reactive gas, ammonia (NH₃), could be effective for sequestration of U in vadose zone conditions such as those at the Hanford Site in Washington State, U.S. Results of this investigation demonstrate U removal upon calcite formation and secondary coatings, such as Fe-oxides and aluminosilicates, upon NH₃ leaving the system. In addition, extensive solid phase characterization techniques were employed to understand the mineral transformations and U behavior upon the reactive gas remedy. For example, absorption spectroscopy X-ray absorption near edge structure (XANES) analysis showed a significant fraction of U (26±11%) in the reduced U form for the phyllosilicate illite mineral investigated during the short-term contact time batch experiment. In addition, geochemical speciation modeling provided a way to predict U species and secondary mineral phases upon treatment. Overall, this promising technology may be capable of immobilizing U in solid phases as these secondary phases may remove the contaminant via adsorption, precipitation, and co-precipitation processes and may coat uranium phases with low solubility minerals as the pH returns to Hanford Site's natural conditions.

4.2 Introduction

Uranium (U) is a significant contaminant of concern in the subsurface at nuclear materials production and disposal sites (Harvey, 2000; Qafoku et al., 2005; Reynolds et al., 2018; Silva & Nitsche, 1995; Walls et al., 2011; Zachara et al., 2007). U mobility is controlled by interactions with the mineral-water interface which requires an understanding of fundamental processes such as surface precipitation, sorption, and U complexation as it is crucial for remediation of contaminated soils and sediments (Silva & Nitsche, 1995).

U from underground tanks, such as those at the U.S. Department of Energy's (DOE) Hanford Site in Washington State, USA, or underground geological disposal of transuranic wastes disposals, such as the Waste Isolation Pilot Plant (WIPP) in New Mexico, USA, has been released primarily as the uranyl (UO_2^{2+}) ion, a dominant and stable aqueous species (Chapman & Hooper, 2012; Qafoku, Ainsworth, Szecsody, & Qafoku, 2003; Reeder et al., 2000). Although U exists in four potential oxidation states (+3, +4, +5, +6), only the +4 and +6 oxidation states are found in significant amounts in the natural environment (Bethke, 2008; Grenthe et al., 1992). The two oxidation states, tetravalent U (+4) and hexavalent UO_2^{2+} (+6), are strongly dependent on their oxidation reduction (redox) conditions, and as a result, contaminant mobility. Due to its stability in aquatic environments, the mobility of the ion is even higher upon formation of uranyl carbonate (CO_3^{2-}) complexes, including $[\text{UO}_2(\text{CO}_3)_2]^{2-}$ and $[\text{UO}_2(\text{CO}_3)_3]^{4-}$, under neutral to alkaline conditions (Abdelouas, 2006). These uranyl carbonate species are particularly dominant in high-pH tank waste disposals. Researchers Qafoku and Icenhower found that the solid

phase speciation of U is complex with different processes dominating as the pH of waste released to the subsurface is neutralized (Qafoku & Icenhower, 2008).

Furthermore, the UO_2^{2+} ion has a strong tendency to be sorbed by fine-grained mineral phases ($< 2 \mu\text{m}$) in the absence of carbonate. Several conducted studies have focused on sorption affinities of iron oxides (Duff et al., 2002; Hsi & Langmuir, 1985; Sato et al., 1997; Waite et al., 1994) and phyllosilicate clay minerals (Catalano & Brown, 2005; Davis et al., 2004; Křepelová et al., 2006; Liao et al., 2020; Moyes et al., 2000) and results demonstrate that these solid phases attain U^{+6} uptake, most commonly achieved by adsorption, and thus decreasing the contaminant mobility (Reeder et al., 2000). However, adsorption capabilities are dependent on total U concentration, pH, mass loading, and redox conditions. Most pertinent to the latter dependency, U^{4+} precipitates as a highly insoluble UO_2 phase under reducing conditions (Edelstein et al., 2011). As previously stated in section 1.2.1, tetravalent U precipitates predominate over hexavalent U complexes under most conditions. However, when reducing conditions are not significant for prolonged periods of time, neutrally charged uranyl carbonate and uranyl-hydroxide species (refer to Figure 1.4) may precipitate when their concentrations reach solubility limits. This process may allow for coating of co-precipitated U.

Previous studies have shown that low solubility mineral, such as cancrinite, sodalite, hydrobiotite, brucite and goethite, may form as secondary coatings in alkaline simulated nuclear waste solution (Bickmore, Nagy, et al., 2001; Mashal et al., 2005; Qafoku et al., 2004; Qafoku & Icenhower, 2008; Zhao et al., 2004). For example, Qafoku *et al.* identified secondary mineral cancrinite on the surface of contaminated soil particles in a column

experiment via scanning electron microscopy (SEM) micrographs (Qafoku et al., 2004). The subsequent and newly formed cancrinite may be an important factor into determining the fate of U, potentially resulting in U-sequestration. More recently, concerns about the mobility of U in liquid–solid interfaces have focused attention on its potential uptake by carbonate minerals, such as CaCO_3 , which are among the most common secondary phases forming in near-surface environments (Reeder et al., 2000). Results demonstrated that the incorporation of U into CaCO_3 controlled its mobility behavior (Dong et al., 2005; Liao et al., 2020; Ma et al., 2014; Nicolas et al., 2019).

However, to the best of our knowledge, the retention properties of the dominant and stable UO_2^{2+} radionuclide ion as a result of ammonia (NH_3) gas injection have not yet been addressed. A promising technology capable of altering redox and oxidation state, and thus, the mobility of U is NH_3 gas injection. The *in situ* injection of the alkaline gas is designed to temporarily raise the pH of the aqueous phase to dissolve mineral phases found in commonplace U leakage sites. When the system returns to a circumneutral pH as the gas dissipates from the system, it is hypothesized that three removal mechanisms will simultaneously occur for U: (1) adsorption to mineral phases, (2) precipitation of U phases, and (3) co-precipitation as the aqueous phase is saturated with Si, Al, and similar ions followed by (4) coating of adsorbed and co-precipitated U phases with low solubility precipitates (Emerson et al., 2018). For the purpose of the presented study, we will focus on mechanism pathways (3) and (4).

Indeed, pH manipulation needs to be understood in order to convert mobile and soluble U species to low solubility precipitates that are stable in the natural environment.

During the treatment, it is unknown how much U will be removed during the following phases (1) the initial ammonia gas treatment and pH increase, (2) the transient phase characterized by significant variability in pH, and (3) following return to natural conditions. This research conducted batch experiments of Hanford Site sediments and phyllosilicate minerals, illite, muscovite, and montmorillonite to determine secondary phase formation at the latter stage (i.e., circumneutral pH) of interaction with NH₃ gas with complementary characterization techniques. In this paper, results are presented for batch experiments conducted with exposure to 5% NH₃/95% N₂ gas followed by aeration with ultrapure air for sediments and minerals. These experiments provide a systematic investigation using X-ray diffraction (XRD), Scanning Electron Microscope with Energy Dispersive X-ray Spectroscopy (SEM-EDS), electron microprobe (EMPA), and X-ray absorption near edge spectroscopy (XANES) analytical techniques.

4.3 Experimental Methodology

4.3.1 Materials

U-spiked batch experiments were conducted using Hanford sediments obtained in Pasco, WA (< 2 mm size fraction) and three minerals: illite (Clay Minerals Society, Cambrian Hole, Silver Hill Mount), muscovite (Ward's Natural Science Establishment, Inc., Stoneham, Maine), and montmorillonite (Clay Mineral Society, Crook County, Wyoming). A wash methodology step to the four types of solid phases was conducted prior to experiments. The step was based on previous research (Baeyens & Bradbury, 2004; Boggs et al., 2015; Di Pietro et al., 2020). Briefly, suspensions (100 g/L) were mixed with 1.0 M NaCl prepared with ultrapure H₂O (resistivity greater than 18 MΩ·cm, DIW),

allowed to flocculate overnight, centrifuged at 4500 rpm (18,100 rcf) in a benchtop centrifuge with a swing bucket rotor attachment (Thermo Scientific, Corvall ST 16R). Supernatant was then decanted and replaced with DIW. This process was repeated until the conductivity was less than 20 $\mu\text{S}/\text{cm}$ to show that most ions had been removed. Montmorillonite (6.0 g), however, was first suspended in 60 mL of 0.001 M HCl, then 0.5 mL of H_2O_2 were added to remove salts and limit redox active species (Boggs et al., 2015), and finally a DIW wash. After each step, the samples were centrifuged at 4500 rpm for 6 h for montmorillonite and 30 minutes for illite and muscovite, after which the liquid was decanted. A longer centrifugation time was used for montmorillonite to aide in dewatering the expanding layers. Subsequently, minerals were dried for 6 days in an oven at 30°C prior to use in experiments (LabNet International Inc.).

4.3.2 Batch Protocol

4.3.2.1 Experiment 1: Short-Term Illite Clay Mineral

Previously washed illite mineral (0.1 g) was suspended in a 500-mL bottle (Nalgene) in SGW solution of ~ 125 mL (Table 4.1). For the purpose of this short term (three-day) experiment, three samples were prepared: 1) calcite co-precipitates from SGW, 2) illite exposed to U and treated with NH_3 gas, and 3) illite exposed to U and treated with NH_3 gas with aeration to return to neutral pH conditions. All NH_3 gas treatments were conducted in a glovebag (GlasCol) with approximately 5% $\text{NH}_3/95\%$ N_2 with the samples uncapped for 12-16 hours to equilibrate with the gas phase at atmospheric pressure. The initial concentration of 500 ppb of U(VI) (plasma standard, Assurance 1000 ppm) in the aqueous phase in these experiments is similar to that expected in the subsurface based on

previous leaching experiments from contaminated sediments removed from the Hanford Site (Szecsody et al., 2010). Approximately two liters of SGW with 500 ppb U were treated in order to recover 100 milligrams of solid. Table 4.2 summarizes the batch conditions for this experiment.

In order to increase the loading of U without precipitating at neutral pH conditions (i.e., before alkaline treatment), sequential treatments were conducted with illite at a concentration of 0.8 g/L with 500 ppb of U in SGW. Table 4.3 summarizes the U loadings ($\mu\text{g/g}$) for both treatments. After each step, the samples were centrifuged and the aqueous phase was decanted, except an aliquot (~ 0.30 mL) sample was set aside for U analysis. The aliquots were acidified in 1% HNO_3 (Fisher, ACS Plus) for analysis by kinetic phosphorescence analyzer (KPA-11, Chemchek). After the supernatant was discarded, a fresh solution was added with U for NH_3 gas treatment. Samples for illite exposed to U and treated with NH_3 gas were loaded and treated twice in series to reach an appropriate loading, but the aerated samples were sequentially loaded three times as some U was expected to be lost during aeration and washing. Following the loading steps, the samples were washed twice with pH-adjusted DIW. The solid phases were recovered and dried at 40°C (LabNet International Inc).

Table 4.1. SGW composition for aging of mica minerals and Hanford Site sediments batch protocol (7.2 mM total ionic strength).

Element	(mmol/L)
Na ⁺	1.3
Ca ²⁺	1.9
HCO ₃ ⁻	1.3
Cl ⁻	3.8

Table 4.2. Summary of batch initial conditions for Experiments 1, 2, and 3

Experiment Description	Contact Time	U concentration (ppb)	Solid:liquid (g/L)	Solid Phase
Experiment 1 – Short-Term	3-day	545	0.80	Illite
Experiment 2 – One-Month	60-day	1128	25	phyllosilicates minerals and Hanford sediments
Experiment 3 – Short and Long Term	3-day	1080	0.63	phyllosilicates minerals and Hanford sediments
	6-month and 6 days*			

Note*: Experiment 3 Long-Term for montmorillonite was a 5-month and 21-day contact time

Table 4.3. Summary of U loading ($\mu\text{g/g}$) for Experiments 1, 2, and 3 for all investigated solid phases at both ammonia and aerated treatments

Mineral	Experiment 1 – Short-Term		Experiment 2 – One-Month	Experiment 3			
	Ammonia – pH 12 ($\mu\text{g/g}$)	Aerated – pH 8 ($\mu\text{g/g}$)	Aerated – pH 8 ($\mu\text{g/g}$)	Short Term		Long-Term	
				Ammonia – pH 12 ($\mu\text{g/g}$)	Aerated – pH 8 ($\mu\text{g/g}$)	Ammonia – pH 12 ($\mu\text{g/g}$)	Aerated – pH 8 ($\mu\text{g/g}$)
Illite	1510 \pm 44	270 \pm 77	151.1 \pm 1.6	*	1398 \pm 45	1292 \pm 14	118 \pm 4.0
Muscovite	N/A	N/A	163.9 \pm 5.0	1080 \pm 35	962 \pm 31	1154 \pm 18	106 \pm 5.0
Montmorillonite	N/A	N/A	199.6 \pm 2.5	597 \pm 22	863 \pm 31	798 \pm 79.3	178 \pm 3.9
Hanford sediments	N/A	N/A	147.8 \pm 1.3	911 \pm 29	1024 \pm 33	1356 \pm 15	358 \pm 11

Note*: there was no measurement recorded for illite short-term, ammonia treatment

4.3.2.2 Experiment 2: One-Month Phyllosilicate Minerals and Hanford Site Sediments

Approximately 5.5 g of previously washed minerals (illite, muscovite, and montmorillonite) and Hanford sediments (see section 2.3.1) were suspended in 220 mL of SGW solution (25 g/L) and equilibrated with a 5% NH₃/95% N₂ atmosphere, as described in Table 4.2. The goal for experiment 2 was to help promote precipitation of U with the dissolved ions from the clays as the pH was decreasing; therefore, the solid phase and SGW volume were increased and decreased, respectively (Appendix, Table A.9). Samples were then mixed on a platform shaker at 40 rpm (Thermo Scientific) for approximately one month. Once this aging period was complete, the samples were centrifuged and 1.0 mL of each supernatant was diluted with 9.0 mL of a 1% HNO₃ solution. The dilution was analyzed for total dissolved Al and Si by inductively coupled plasma optical emission spectroscopy (ICP-OES, Perkin Elmer, Optima 7300 DV). After ICP-OES analysis, the remaining aqueous phase was decanted, transferred to a separate 50-mL centrifuge tube, spiked to 1000 ppb U (plasma standard, Assurance 1000 ppm), and statically equilibrated on the benchtop for four days. After mixing, half of these samples were centrifuged and analyzed for total dissolved U dissolved U by inductively coupled plasma mass spectrometry (ICP-MS, Thermo Scientific iCAP RQ). Table 4.3 summarizes the U loadings (μg/g) for the aerated treatment after ICP-MS analysis. The other half of the samples were aerated as described in section 3.3.3, and then centrifuged and analyzed for total dissolved U. Lastly, solids were dried in an oven at 28°C (LabNet International Inc.) for 15 days. Table A.9 in the Appendix lists the oxidation-reduction potential (ORP, Mettler Toledo EM40-BNC, 30043106) and pH of each suspension measured before and after aeration treatment.

4.3.2.3 Experiment 3: Short- and Long-Term U Aging of Phyllosilicate Minerals and Hanford Site Sediments

Previously washed minerals (0.5 g) were suspended in a 1-L bottle (Nalgene) in SGW solution of ~800 mL (0.65 g/L, Table 4.2). Duplicate suspensions were equilibrated for 12–16 hours with a 5% NH₃ (anhydrous, Airgas)/95% N₂ (UHP300, Airgas) atmosphere inside a plastic glovebag (GlasCol, 27 x 27 x 15 inch) inside a fumehood. Then, samples were capped, covered with parafilm, and mixed on a platform shaker at 40 rpm (Thermo Scientific) for six months and six days. This extended mixing period facilitated aging and alteration of the minerals at high pH (~11.5). Once the aging period was complete, the samples were centrifuged at 5000 rpm for 30 min (4704 rcf, Thermo Scientific, Sorvall ST 16R centrifuge) to remove particles >100 nm based on Stoke's law (Jackson, 2005). After centrifuging, 0.30 mL of the supernatant was diluted with 1.0 mL of a 1% HNO₃ solution (Fisher, ACS Plus) and analyzed for U by ICP-MS, and Si and Al by ICP-OES.

To investigate secondary mineral precipitation at circumneutral pH, a second set of suspensions were aerated, after the six-month aging period, to lower the suspension pH to ~8. This was achieved by simultaneously purging each suspension with ultrapure air at 5.68 mL/min for three days. After the aeration treatment, the samples were centrifuged as described in the previous paragraph, analyzed for U, Si, and Al, then washed with pH-adjusted water (pH 7.5 – 8), and the solid phase was dried in an oven at 28°C (LabNet International Inc.) for 15 days. The pH was measured before and after aeration using a Ross combination electrode (Thermo Sci. Orion 8175BNWP) calibrated with three NIST standard buffer solutions (pH 4.01, 7.00, and 10.01, Thermo Scientific). The U loading (in µg/g) for both contact times and treatments is listed in Table 4.3.

4.3.3 Mineral Characterization

4.3.3.1 Scanning Electron Microscope with Energy Dispersive X-ray Spectroscopy (SEM-EDS) Analysis of Phyllosilicate Minerals

Control (washed without gas treatment) and treated illite, muscovite, and montmorillonite mineral samples for microscopy analysis were prepared by attaching double-sided carbon conductive adhesive tape (12 mm in diameter and 260 μm in thickness, Electron Microscopy Sciences) to aluminum stubs and then sprinkling the dried mineral powder on the carbon tape. The uncoated mounts were analyzed on scanning electron microscope with energy dispersive spectroscopy (SEM-EDS) analysis (JEOL IT500Hr FE Scanning Electron Microscope equipped with the Bruker XFlash 6160 EDS with a 60 mm window silicon drift detector). EDS operating conditions were set at 15 keV accelerating voltage and a gun emission of 23 μamps at 5.0×10^{-7} Pa vacuum pressure. The electron beam had an incident angle of 35° from the surface with ample signal of at least 40,000 counts per second for a 50-second duration. Collected data were quantified via the Bruker Esprit 2.2 software. SEM images were taken using the secondary detector at 3 keV and a working distance of approximately 10 mm.

4.3.3.2 Uranium Mapping by Electron Micro Probe Analysis (EMPA) with Wavelength-Dispersive Spectrometry (WDS) detector

4.3.3.2.1 Electron Micro Probe Analysis (EMPA) Sample Preparation

Prior to electron microprobe X-ray analysis (EMPA), the U-spiked and ammonia-treated illite mineral was prepared in epoxy and polished. Epoxy was mixed from two parts by volume of EpoThin 2 epoxy (Buehler Inc., Lake Bluff, Illinois, resin CAT #20-3440-032) to one part by volume EpoThin 2 hardener (CAT #20-3442-016). After a two-minute hand mixing, approximately 24 mg of the mineral was inserted into the mixture. Then,

approximately 3 mL of mixed epoxy was decanted into a 1” round plastic cup. The round cup was left overnight inside the airlock vacuum chamber at 25 in Hg to eliminate any air bubbles that may have formed during mixing. The sample was polished with two grit-size polishing papers: 400 and 600 (Ted Pella, Inc., #817-105; #817-106), and then 600 grit (Ted Pella, Inc., #817-106) polishing papers. To conclude the polishing method, the sample was polished with a Nylon polishing cloth (Ted Pella, Inc., #816-63) that contained a one-micron diamond polish paste to smooth the surface of the mount epoxy (Metadi II, Buehler cat #40-6244). The polished sample surface was cleaned with methanol between each grit size.

4.3.3.2.2 EMPA of Illite Samples

Prior to electron microprobe X-ray analysis (EMPA), U-spiked and ammonia-treated illite mineral was prepared in epoxy and polished. Epoxy was mixed from two parts by volume of EpoThin 2 epoxy (Buehler Inc., Lake Bluff, Illinois, resin CAT #20-3440-032) to one part by volume EpoThin 2 hardener (CAT #20-3442-016). After a two-minute hand mixing, approximately 24 milligrams of the mineral were inserted into the mixture. Then, approximately 3 mL of epoxy was decanted into a 1” round plastic cylinder. The round cylinder was left overnight inside the airlock vacuum chamber at 3.33 kPa to eliminate any air bubbles that may have formed during mixing. The sample was polished with two grit-size polishing papers: 400 and 600 (Ted Pella, Inc., #817-105; #817-106). To refine, the sample was then polished with a Nylon polishing cloth (Ted Pella, Inc., #816-63) with a one-micron diamond polish paste to smooth the surface of the mount epoxy (Metadi II, Buehler cat #40-6244). The polished sample surface was cleaned with methanol between each grit size. A JEOL 8900R Superprobe equipped with five two-crystal wave-

length dispersive spectrometers (WDS) and a single EDS detector was used to analyze the prepared samples from section 1.3.2.3, Experiment 3 – Short and Long-Term. The two-crystal spectrometers (TAP and PET/LiF) were set up to simultaneously detect multiple elements (i.e., Ca, Al, Si, Fe, etc.) as the beam rastered across the sample surface. The instrument had an accelerating voltage of 25.0 kV with 512 μm spot size, and 40 ms dwell time.

4.3.3.3 X-ray Fluorescence (XRF) Analysis of Hanford Site Sediments

As Table 4.2 describes, Experiment 2 – One-Month and Experiment 3 – Short-Term Hanford Sediments were analyzed via XRF technique. Once the Hanford sediment specimen was loaded onto the studs (Electron Microscopy Sciences) and placed into the holder, the specimen was inserted into the SEM chamber and evacuated to high vacuum ($1.33 \times 10^{-7-8}$ Pa). Using a secondary detector, material particles designated for XRF analysis were located and examined at three different locations. The XRF (X-Trace) source, with a rhodium filament operating at 50 kV, was turned on at the beginning of the event when the sample holder was inserted into the SEM (JEOL IT500hr FE). When the SEM reached full vacuum, the beam was energized to 2.3 kV for standard imaging and scanned by the EDS. The Energy Dispersive Spectrometer system was a Bruker Quantax 400 using the Esprit 2.0 software SDD (Silicon Drifted Detector) with a 60 mm window performing at -45 °C. Ten spots were selected per specimen and collected at 400 seconds per spot. Hanford sediment particles were analyzed at a magnification of 180x (particle size approximately 250 μm in width) with U detection.

4.3.3.4 Electron Microscopy (EM) with Energy-Dispersive X-ray (EDX) spectrometer detector Sample Preparation and Analysis

Approximately 50 milligrams of each of the dried aerated (pH ~ 8) Hanford sediments and phyllosilicate mineral solid phases from Experiment 2 – One-Month samples were suspended in ethanol (95.0%, CAS#64-17-5) in 7 mL flat-bottom glass vials. For the Hanford sediment samples, duplicate suspensions were prepared in 1, 2, and 5 mL of ethanol. For the phyllosilicate minerals, duplicate suspensions in 1 and 5 mL of ethanol were prepared. After sonicating (FS20, Fisher Scientific) the suspensions for ~2 minutes, the vials were placed on a flat surface and allowed to settle for ~10 minutes to remove larger particles. Then, a drop of each suspension was pipetted onto the dark side of individual TEM grids (200 mesh carbon-type B, TED Pella Inc.). Excess liquid on the TEM grids was gently removed after ~5 – 10 minutes with a lint-free tissue and each grid was then transferred into a TEM grid box and dried in a desiccator overnight.

Mounted samples were analyzed by Drs. Shanna L. Estes and Brian A. Powell at the Clemson University Electron Microscopy Facility (EMF) using a Hitachi HD-2000 scanning transmission electron microscope (STEM). Multiple secondary electron (SE) micrographs and energy-dispersive X-ray (EDX) spectra were collected for all analyzed samples. Elemental analyses from the EDX spectra were used to approximate compositions of the imaged solids. The two peaks at approximately 8–9 keV in the EDX spectra are Cu X-ray emission lines arising from the TEM grids, which are composed of Cu and carbon. Because X-ray emissions from the Cu and C of the TEM grids overwhelms any emission from Cu and C within the samples, these elements were removed from the quantitative

elemental analyses. For some micrographs, more than one area on the image was selected for EDX analysis.

4.3.3.5 X-Ray Diffraction (XRD) Analysis of Illite Mineral

Experiment 3 – Short- and Long-Term U-spiked phyllosilicate minerals (illite, muscovite, and montmorillonite) samples were analyzed (Bruker D2 PHASER X-ray diffractometer equipped with built-in chiller, LYNXEYEXET, 1D mode, detector) at room temperature, humidity, and pressure (Table 4.2). Due to samples being radioactive, caution was taken when transferring ~ 1.0 g of the solid sample onto the XRD sample holder with zero diffraction plates (\varnothing 24.6 mm \times 1.0 mm thickness with cavity \varnothing 10 mm \times 0.2 mm depth, MTI Corporation). All peak positions were obtained by step-size goniometer scanning at 0.02 2θ intervals from 5° to 40° using CuK α x-rays at 40 kV. Crystalline phase identification was performed via DIFFRAC.EVA. V5.1 powder pattern phase identification processing software with the Powder Diffraction File (PDF) International Centre for Diffraction Data (ICDD[®]) database.

4.3.3.6 X-ray Absorption Near Edge Structure (XANES) Analysis of Illite Mineral

Data were collected at the Advanced Photon Source (APS), a DOE Office of Science User Facility operated for the DOE Office of Science by Argonne National Laboratory, beamline 12-BM-B at the U L_{III} edge (17166 eV) at room temperature by Dr. Sarah Saslow (PNNL staff scientist). The standards and samples (~100 milligrams) were pressed into polytetrafluoroethylene (PTFE) windows sealed with Kapton tape on both sides and at the edges. Samples were packed into the PTFE windows with dilution whereas the standards were diluted and homogenized in cellulose (15% standard, 85% cellulose) before packing. XANES data were collected from 200 eV below the edge to 854 eV above the edge; the

data from 20 eV below the edge to 50 eV above the edge was obtained with 0.40 eV spacing. The remaining data above the edge was obtained with a k-spacing of 0.05, and the collection time was collected with a 0.5 exponent. Transmission standard data was obtained using argon (Ar) filled ion chambers, with its spectra provided in (Appendix, Figure A.15). Fluorescence sample data was collected in triplicates using a 13 element Ge detector and normalized to I_0 to correct for dead time. Spectra were normalized and fit using standard spectra in *Athena* software. XANES spectra were carefully energy calibrated using zirconium (Zr) foil as an energy reference. The sample XANES spectra were allowed to vary in energy during linear combination analysis (LCA) fitting in *Athena*. LCA fitting for U speciation was performed using collected fluorescence spectra for the samples and transmission spectra collected for the standards. Minimal shift in the Zr foil absorption energy edge was observed throughout the experiment.

4.3.4 Geochemical Speciation Modeling

Speciation modeling to predict the formation of uranium solid phases likely to be present in this system was conducted using the Geochemist Workbench[®] (GWB) version 12.0 with the Visual *MINTEQ* database (thermo-minteq) formatted by Jon Petter Gustafsson (KTH Royal Institute of Technology). The database was previously manually updated with the most recently published thermodynamic equilibrium constants for aqueous complexation reactions for relevant uranyl species. The equilibrium constants for ternary complexes of uranyl carbonate, $\text{Ca}_2\text{UO}_2(\text{CO}_3)_{3(\text{aq})}$ and $\text{CaUO}_2(\text{CO}_3)_3^{2-}$, and polynuclear U(VI) hydroxide-carbonate complexes were updated based on the recommendations from OECD's NEA TDB (Emerson et al., 2017; Katsenovich et al., 2018). Concentrations of Al, U, and Si were kept constant in all modeling simulations at

0.185 mM, 0.02 mM, and 1.50 mM, respectively. Dissolved oxygen was set at 8.4 mg/L at a constant temperature of 25 °C based on saturation with air. The simulations were repeated by sliding pH from 8 to 12, imitating the pH values reached after the injection of 5% of NH₃ [5% NH₃/95% N₂; 3.1 mol/L of NH_{3(aq)}]. The modeling of the treated solid samples with NH₃ gas was assumed to be closed from the atmosphere, applicable to the core of the gas injection in the field in the short term.

4.4 Results and Discussion

4.4.1 Mineral Transformation and U Interaction Mechanism

4.4.1.1 Iron Interaction Mechanisms

As stated in section 1.2.3, Fe may also sequester U from contaminated groundwater. Figure 1.7c and 1.7d show that Fe impurities are present in clays which may influence U(VI) adsorption, reduction, and co-precipitation processes. To verify these sequestration pathways, as the NH₃-treated solid phase was decreasing in pH, elemental mapping via EMPA and STEM as well as bulk XRD were conducted.

Characterization techniques such as XRD (Figure A.1, top) identified Fe in the untreated illite mineral. In addition, SEM-EDS analysis also identified Ti impurities (Table 3.3) in the same mineral. Researchers Payne *et al.*, propose that trace impurities, such as Ti/Fe-rich phases (e.g., titanomagnetites), and mineral coatings, such as Fe-oxide ferrihydrite, can play a dominant role in the uranyl sorption (Payne et al., 1998). In addition, synthesis studies of U-Fe oxides indicated that stable uranyl ion was incorporated into the Fe oxides, rather than substituted due to the radioactive ion being almost three times the size of Fe³⁺ (Duff et al., 2002). On a molecular level, the surface of the Fe oxide is both polar and charged, offering an ideal reactive site for uranyl ion sorption.

EMPA maps show U with associated stable element Fe, in a single grain (Figure 4.1, top) and various particles (Figure 4.1, bottom) obtained from the illite NH₃- and aerated-treated samples in Experiment 3. The elemental distribution maps for Fe showed a sparse but distinct association with U in all samples (Figure 4.1, red lines and Figure A.16). The relationship could signify the presence of U adsorbed to or co-precipitated with Fe-oxide species. According to Qafoku and Icenhower and citations wherein, high specific surface area Fe-oxides show great affinity for aqueous U(VI) under circumneutral and slightly alkaline conditions (Qafoku & Icenhower, 2008). This pH range was investigated for illite mineral in Experiment 3. This Fe-oxide-U proposed pathway supports our EMPA correlation study (Figure 4.1 and Figure A.16).

Furthermore, U(VI) has been shown to be concentrated with Fe-oxide coatings on Si-phases, such as quartz (Read et al., 1993). Work conducted by Abarca Betancourt concluded that Si concentrations of 25 mmol/L resulted in high U removal efficiencies when the solid samples were spiked with 5 mmol/L of Fe (Abarca Betancourt, 2017). Additional research suggests that elevated Si concentrations may play a role in the removal of U in the presence of Fe, possibly due to (1) impacts on Fe mineral transformations and (2) larger surface area of Si precipitates enhancing collection Fe oxides on surfaces (Boglaienko et al., 2021). Although EMPA does not quantitatively measure its content during mapping, Si (55.7±8.6 wt. % via SEM-EDS) is prominent throughout the illite particles during EMPA analysis. Although the highest Si zones shown in Figures 4.1 and A.17-18 align with Fe, supporting the Fe-oxide mechanism and Abarca Betancourt's recent studies.

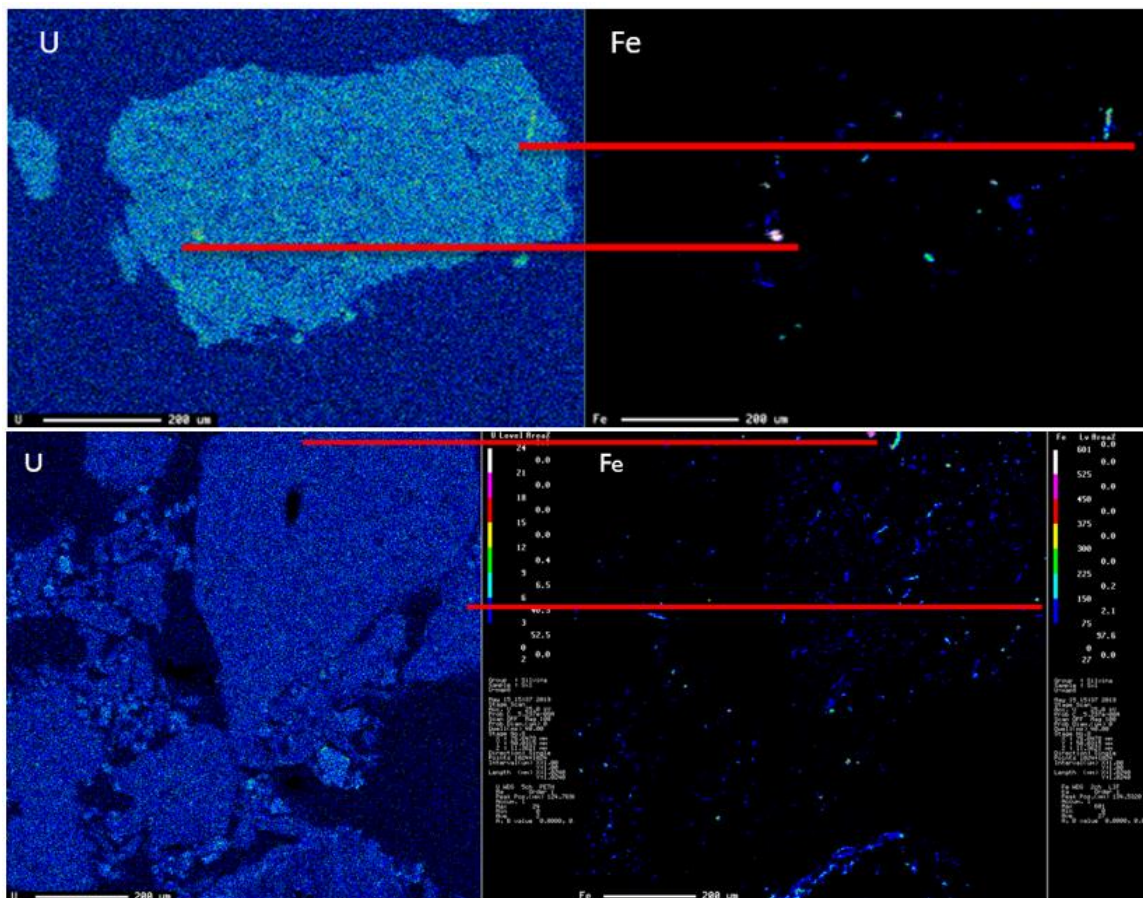


Figure 4.1. EMPA micrographs and corresponding elemental maps for U and Fe showing a correlation on illite particle (top) and particles (bottom) post-ammonia (5% NH₃/95% N₂) and aerated treatments in Experiment 3.

4.4.1.2 Redox Impacts on Uranium Speciation

Extensive literature has shown that the fate and transport of U in the natural environment is greatly affected by redox transformations between U(VI) and U(IV) (Chen et al., 2017). This is due to the profoundly different solubility, sorption, and complexation affinities of the two primary oxidation states (Langmuir, 1997). Because U(IV) is more likely to precipitate, recent studies have proposed reducing soluble U(VI) to the less soluble U(IV) to immobilize U at contaminated sites (Chen et al., 2017; Duff et al., 2002; Ling & Zhang, 2015; Sheng & Fein, 2014; Tsarev et al., 2017; Yuan, 2015). In this research,

reducing conditions may be achieved by the displacement of atmospheric air during injection of the NH_3/N_2 gas mixture.

As shown in section 2.4.4, the system conditions became highly anaerobic at -500 mV (Figure 2.5). As in the work conducted by Schoonheydt and Johnston, a reduction of Fe-containing illite was observed with Fe dissolution in oxygen-deprived conditions (Schoonheydt & Johnston, 2013). Consequently, after the illite mineral was aerated, the subsequent decrease in pH and increase in Fe oxidation likely led to surface precipitation of Fe-oxides, which may incorporate or adsorb U, as explained in section 4.4.1.1. Although U was not present in Chapter 2 experiments, previous data shows that conditions are much more reducing following treatment with NH_3 gas (5% NH_3 /95% N_2) as compared to natural subsurface conditions based on ORP measurements, 530 ± 50 mV versus 150 ± 15 mV before and after gas treatment, respectively (Emerson et al., 2018). Although these are sub-oxic and not reducing conditions (at 150 mV), it is possible that reduction of U occurred as previous research suggests that reduction of U can occur below 250 mV (McKinley et al., 2007).

Experiment 1 was conducted to study U(VI) reduction via XANES analysis of oxidation states. U-XANES spectra for Experiment 1 are provided in Figure 4.2a-c. Illite- NH_3 (Figure 4.2a) and illite-aerated samples were both exposed to U and treated with NH_3 gas, while the illite-aerated (Figure 4.2b) sample was aerated following treatment to return to neutral pH conditions. As shown in Table 4.3, the estimated U solid loadings from KPA measurements of the aqueous phase were 1510 and 270 $\mu\text{g/g}$, respectively.

For both illite samples analyzed, +6 is the dominant U oxidation state with an estimated >74% (Table 4.4). However, there is a significant fraction of U in the +4 oxidation state (up to 26%). A similar fraction was also observed for U co-precipitated in CaCO₃ from SGW in the absence of illite. For the aerated sample (Figure 4.2b), efforts were not made to keep it under reducing conditions as they were aerated, washed, and dried in the presence of air. Therefore, it is notable that a significant fraction of U(IV) persists in the solid phase. It is suggested that a fraction of U(IV) remains due to incorporation into the mineral phase during treatment (Emerson et al., 2018; Katsenovich et al., 2018; Meece & Benninger, 1993; Szecsody et al., 2012). Furthermore, such significance is differentiated from XANES studies conducted by Catalano *et al.* and McKinley *et al.* whose analyses indicated that Hanford Site sediments at natural conditions contained U in +6 valence state exclusively (Catalano et al., 2004; McKinley et al., 2002). It is notable that 91% of the U is in the +6 oxidation state immediately after treatment with the total U(VI) decreasing after aeration (Table 4.4). This suggests that release of U(VI) is adsorbed to the surface into solution with co-precipitated U(IV/VI) phases remaining after aeration due to coating of low solubility phases at neutral pH. Consequently, this result is consistent with U(VI) being relatively soluble at neutral pH in the presence of atmospheric carbonate and with the ultimate loadings before and after aeration.

Furthermore, it must be noted that the spectra for U associated with illite following NH₃ gas treatment (Figure 4.2a) and NH₃ gas treatment with subsequent aeration (Figure 4.2b) are not as smooth as the spectra of U co-precipitated with calcite (Figure 4.2c) due to the significantly lower concentration of U present, with 850 and 350 ppm, respectively.

The estimated U loading in calcite from aqueous phase KPA measurements, contrarily, were 3300 ppm. The XANES spectra difference shown in black lines in Figure 4.2 led to greater error in the fitting for illite solids as the samples were near detection limits. Explained in the upcoming section, U may be more likely to co-precipitate with CaCO_3 than to associate with illite under these pseudo-reducing, high pH conditions of Experiment 1.

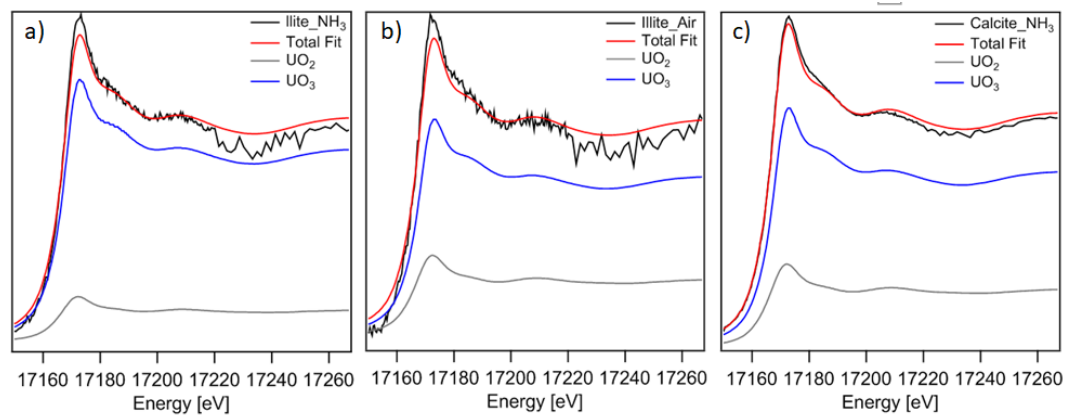


Figure 4.2. Uranium L_{III} -edge XANES spectra shown in black for (a) Illite- NH_3 at pH 12, (b) Illite-aerated, and (c) calcite- NH_3 at pH 8 in Experiment 1. Fraction-adjusted standards contributing to total fit shown for UO_2 (gray) and UO_3 (blue), and total U fit (red).

Table 4.4. XANES U L_{III} -Edge Linear Combination Analysis (LCA) Results in Percentages for Calcite NH_3 -gas, Illite NH_3 -gas, and Illite-aerated treated samples sent to Argonne National Laboratory

Sample	Valence State	Calcite NH_3 , pH 12	Illite NH_3 , pH 12	Illite Aerated, pH 8
UO_2 Fraction	U(IV)	$26 \pm 4\%$	$15 \pm 8\%$	$26 \pm 11\%$
UO_3 Fraction	U(VI)	$77 \pm 4\%$	$91 \pm 8\%$	$74 \pm 11\%$

4.4.1.3 Secondary Calcite Formation

Due to the high abundance of calcite (up to 32% wt.) in Hanford Site sediments (Dong et al., 2005; Qafoku & Icenhower, 2008), it is imperative to understand its interaction with U. As Figure 1.13 shows, a significant percentage (73-83%) of the U in contaminated sediments from the Hanford Site has been detected as co-precipitated U-calcite. To a lesser extent, aqueous or adsorbed U-carbonate complexes (1-7% and 2-51%, respectively) are found at the Site. Aqueous U-carbonate species are of significant concern due to their high mobility and low sorption. However, under natural Hanford Site conditions, carbonate coatings are commonly found among other phases, such as Fe-oxides and aluminosilicates. Therefore, it is common for stable and mobile UO_2^{2+} ions to adsorb and interact with calcite rather than other phases (Dong et al., 2005). The following two characterization studies (XANES and XRD) aim to provide a better understanding of calcite formation and U-sequestration mechanisms.

U-XANES spectra for ammonia- and aerated-treated illite samples are provided in Figure 4.2b-c. As a by-product during Experiment 1, precipitates formed following NH_3 gas treatment in SGW with 500 ppb U and consisted mainly of calcite (Figure 4.2c). As in Emerson *et al.* work, the SGW background used in this study was composed of CaCl_2 and NaHCO_3 salts (Table 4.1) and then dissolved into Na^+ , Ca^{2+} , and CO_3^{2-} ions. Their work found that solutions were saturated at elevated pH during treatments and likely formed calcite as shown by speciation modeling (Zheng et al., 2008). It is important to note; however, that Ca^{2+} has been reported to block access for other ions, such as Na^+ and Cs^+ , during mineral sorption (Dong et al., 2005; Wan et al., 2004). This higher sorption affinity

allows for Ca^{2+} co-precipitation processes to dictate over cation exchange, allowing for CaO_3 coating on the mineral surface. Observable in Figure 4.2 and Table 4.4, CaO_3 forms and likely incorporates U. Subsequently, incongruent dissolution phenomenon for aluminosilicates (sections 2.4.2 and 3.4.4) will likely lead to the coating of calcite-U phases. Therefore, this mechanism is of utmost importance as it can reduce re-mobilization in the long-term due to (1) low solubility of CaO_3 at high pH and (2) saturation under natural Hanford Site conditions.

To identify potential phases that could be forming *in situ* and incorporation U, phyllosilicate minerals illite, muscovite, and montmorillonite (section 4.3.2.3) were analyzed via XRD analysis after a long-term aging process in the presence of U. Via DIFFRAC.EVA. V5.1 software matching, the XRD patterns of the untreated (control) and treated (NH_3 and aerated treatments) illite, muscovite, and montmorillonite minerals are shown in Figure 4.3. Table A.11 and Table A.12 in the Appendix show the 2θ values with its respective *d*-spacing measurement (in Å) based on Bragg's Law, Eq. 4.1 (Cole, 1970).

$$n\lambda = 2d\sin\theta \quad \text{Eq. 4.1}$$

The XRD pattern for the illite control sample (Figure 4.3a) contained illite as the major phase, with quartz, microcline, and kaolinite present as minor phases (Table A.11). The montmorillonite control pattern contained montmorillonite, muscovite, quartz and minor amounts of feldspar (microcline) (Table A.12). It is worth mentioning that the major peaks do not shift significantly (*d*-spacing) when comparing control and treatment minerals with the exception of montmorillonite as its interlayer basal₀₀₁ *d*-spacing was shifted 0.48 Å from theoretical measurements (Chipera & Bish, 2001). No other peak comparison

resulted in such significant difference, and as explained in section 3.4.3, shifts are primarily due to NH₃ gas intercalation.

Additionally, it is important to note that muscovite was not included in the table description. Unlike the illite and montmorillonite patterns, there were no significant changes in the muscovite patterns. The only exception is at approximately 29° 2θ where two small peaks were observed in both the NH₃ and aerated treated patterns (Figure 4.3b). This lattice parameter is representative of calcite (Falini et al., 1998).

When comparing the interlayer (or basal d₀₀₁ spacing) of illite and montmorillonite minerals, some differences arise. While illite's *d*-spacing remain constant throughout experimental and theoretical measurements, montmorillonite's changes. This is due to montmorillonite expanding and swelling interlayer ability largely dependent on charge (Meier & Nüesch, 1999). Fusová found that smectites decrease in *d*-spacing size when heated and increase when treated with ethylene glycol (Fusová, 2009). While both of the aforementioned treatments are not applicable to the current experiment protocol, montmorillonite increased from 14.14 Å to 14.52 Å (at pH 12) to 14.70 Å (at pH 8) (Table A.12). This is probably due to NH₃/NH₄⁺ ion intercalation into montmorillonite interlayer, as mentioned in (section 3.4.3) (Di Pietro et al., 2020).

When comparing peak intensities, new emergent peaks are reflected at 23.1°, 29.5°, 36.0°, & 39.7° and 23.1°, 29.5° & 31.5 2θ for illite and montmorillonite, respectively (shown in blue circles, Figure 4.3). Because the seemingly increase in intensity for aeration treatment at pH 8 (purple, Figure 4.3) in comparison to NH₃ treatment at pH 12 (orange, Figure 4.3), it suggests that CaCO₃ is more prominent at aeration treatment. Thus, XRD

analysis is supportive of previous studies, including that of XANES data, that calcite could potentially incorporate U and bind into phyllosilicate minerals phase.

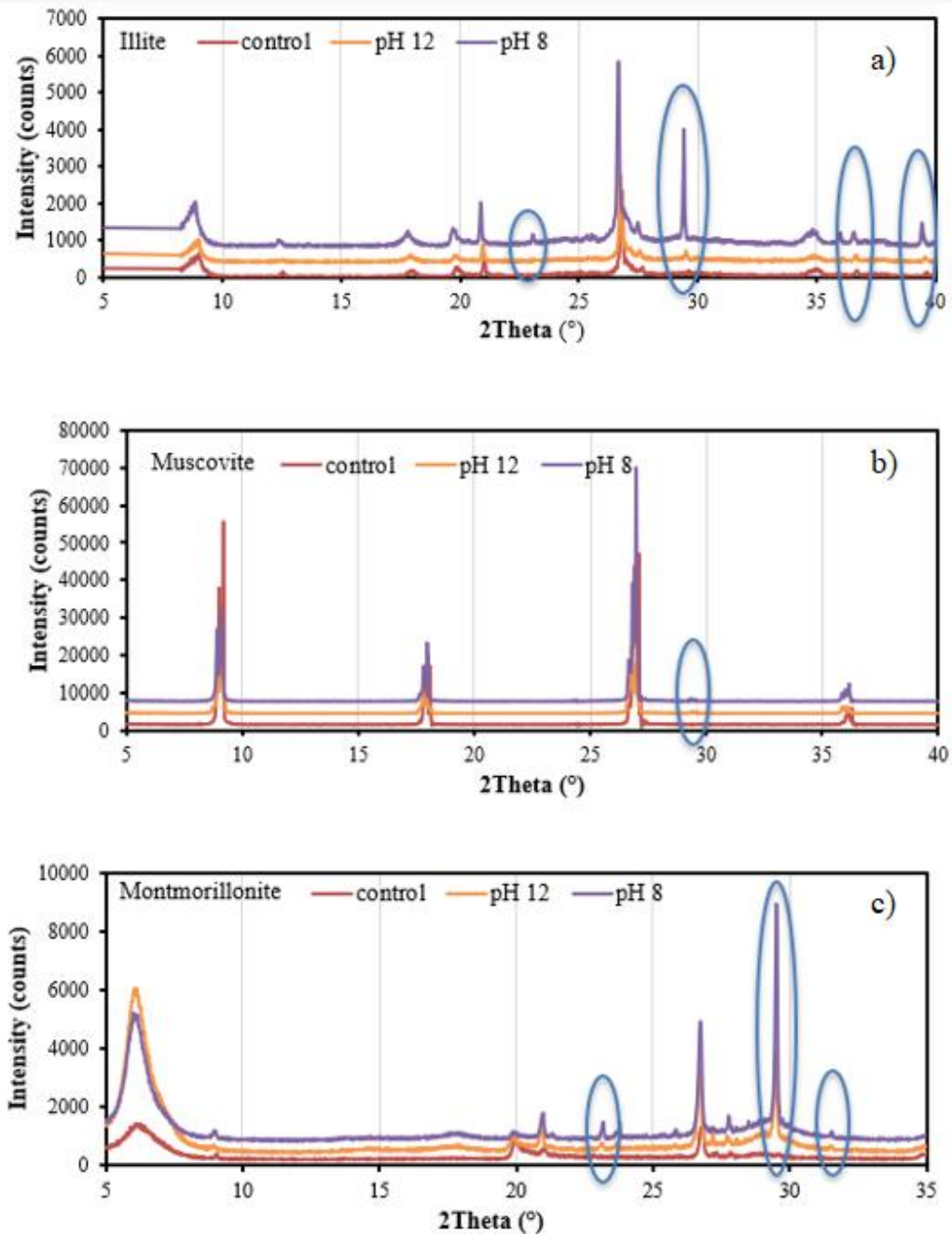


Figure 4.3. XRD patterns for (a) illite, (b) muscovite, and (c) montmorillonite showing (blue circle) calcite (CaCO_3) formation peaks during ammonia (orange) and aeration (purple) treatments

4.4.1.4 Incongruent Dissolution of Phyllosilicate Clay Minerals

New minerals are likely to form from natural mineral dissolution and precipitation processes during their complex interactions with waste constituents, especially from Al and Si phases like newly precipitated cancrinite and sodalite (Bickmore, Nagy, et al., 2001; Buck & McNamara, 2004; Di Pietro et al., 2020; Mashal et al., 2004; Stumm & Morgan, 1991). These may adsorb, co-precipitate, or coat contaminant-laden solids. Indeed, these pathways alter the minerals, potentially incorporating mobile contaminants. One possible alteration is via incongruent dissolution phenomenon.

The previous chapters evidenced incongruent dissolution phenomenon; however, the aluminosilicate minerals investigated were not exposed to U in SGW solutions. Table 4.5 summarizes the Al/Si ratios of phyllosilicate minerals illite, muscovite, and montmorillonite during treatment (NH₃ and aerated) and controlled conditions (representative of natural groundwater) for two sets of contact-times (one-month and six-month). For Experiment 3, the six-month contact time showed a decrease in the calculated Al/Si from untreated (0.50 ± 0.07) to NH₃ (0.35 ± 0.01) to aerated (0.24 ± 0.02) treatments via SEM-EDS analysis on the surface of illite. These data support dissolution experiments from Figure 2.3 and ratios in Table 3.6. However, for Experiment 2, the Al/Si ratios increased from untreated to aerated treatment at pH 8. Note that, with the exception of muscovite, the pH 8 Al/Si ratios are similar to those calculated for Hanford sediments via SEM-XRF analysis (Appendix, Table A.10). There may be four valid hypotheses for the increasing ratio in Experiment 3 vs. 2: (1) a shorter contact-time, preventing Al dissolution from the surface, (2) differences in solid to solution ratios, producing a different saturation

in the aqueous phase, (3) variability in data points, and (4) variability between two different EDS detectors.

Although literature is limited on Al/Si ratios during NH₃ treatment, recent studies with NH₃-treated batch experiments showed that U(VI) removal from solution (containing the same background electrolytes as Table 4.1) increased as the Al/Si ratios decreased when the U concentration was 2.0 ppm (Emerson et al., 2017, 2018; Katsenovich et al., 2018). Their experiments combined with our results in Table 4.5 support incongruent dissolution as a valid phenomenon for the immobilization of contaminants, particularly U.

Moreover, though the Al distribution maps show trends and associations with Si, none were definitive with U (Figure A.17 and Figure A.18). Crystalline aluminum hydroxide, [Al(OH)₃], precipitates at circumneutral pH due to its point of zero charge (PZC = ~8.7, where the sum of the positive and negative charges on the solid's surface is zero) (Tombacz et al., 2000). Interestingly, this pH is an approximate value of Hanford's groundwater (pH ~8.5) (Wellman et al., 2008). Geochemical modeling simulations specific for Hanford Site conditions predicted Fe- (hematite, Fe₂O₃) and Al- [diaspore, Al(OH)₃] containing minerals (Szecsody et al., 2012). Studies conducted by Su and Suarez proposed that Al is more likely to interact with HCO₃⁻ and CO₃²⁻ ions rather than U via ligand exchange reactions, resulting in limited U adsorption on the surface of Al(OH)₃ (Su & Suarez, 1997).

Table 4.5. Summary SEM-EDS showing Al/Si ratios for U-spiked, ammonia and aerated sample experiments

Experiment	Mineral-Treatment pH	Al/Si Weight %	Data Point
Experiment 2 – One-Month	Illite-untreated	0.50 ± 0.07	n=9
	Illite-8	0.56 ± 0.01	n=4
	Muscovite- untreated	0.78 ± 0.03	n=10
	Muscovite-8	0.84 ± 0.02	n=5
	Montmorillonite- untreated	0.33 ± 0.06	n=10
	Montmorillonite-8	0.42 ± 0.05	n=5
Experiment 3 – Long-Term	Illite-untreated	0.50 ± 0.07	n=9
	Illite-12	0.35 ± 0.01	n=9

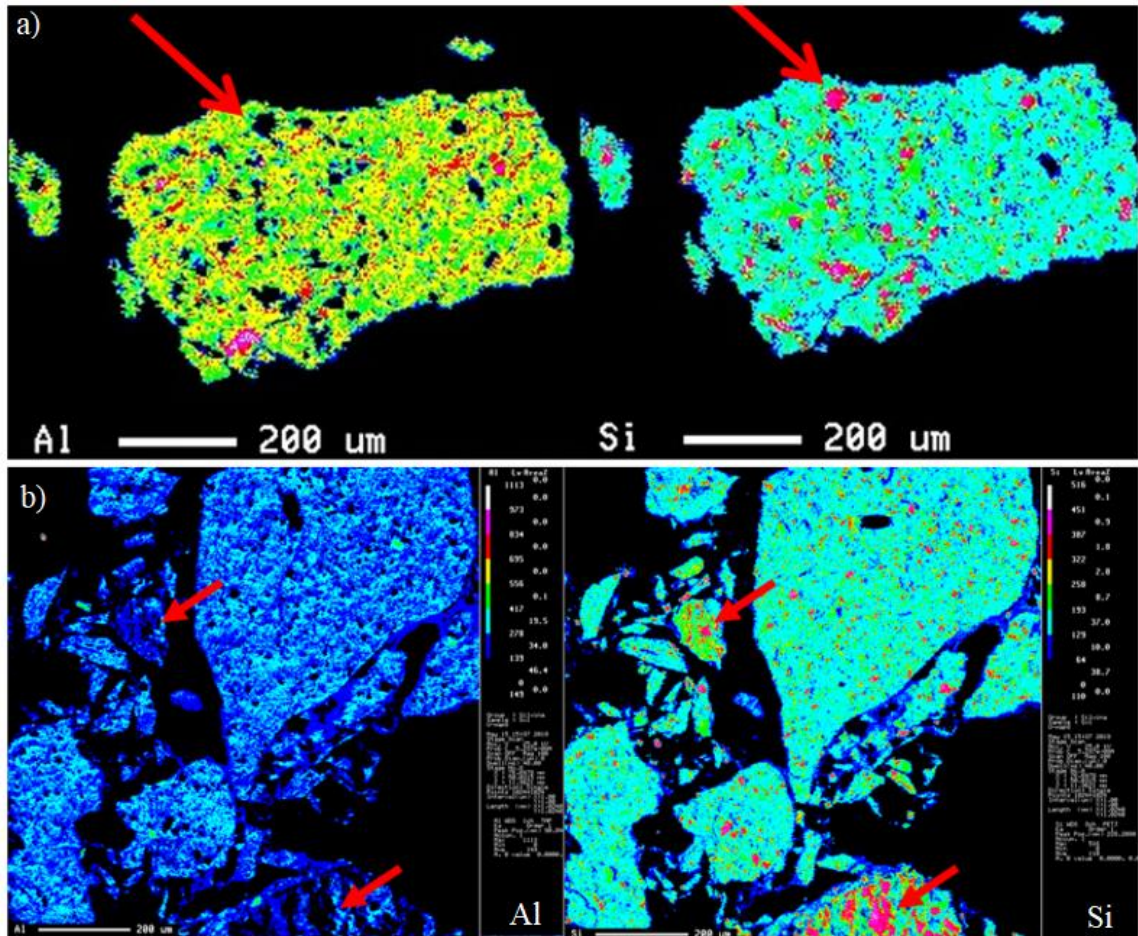


Figure 4.4. EMPA micrographs and corresponding elemental maps for Al and Si showing a correlation on illite particle (top) and particles (bottom) post-ammonia (5% $\text{NH}_3/95\% \text{N}_2$) and aerated treatments in Experiment 3.

4.4.1.5 Discussion of Potential U Sequestration Mechanisms

As mentioned at the beginning of section 4.4.1.4, precipitated aluminosilicates such as cancrinite and sodalite may potentially incorporating mobile contaminants. However, Fe-oxides may be a promising approach for U removal due to their high reactivities and electron transfer reactions. With the presence of Fe-oxides, such as ferrihydrite, and the occurrence of Fe(II)-bearing minerals, such as biotite (mica mineral) and magnetite, along with aluminosilicates at the Hanford Site sediments, the association between Al, Si, and Fe highlights their potential for dissolution and re-precipitation with U at high pH and secondary coating of U species with silicates and Fe-oxides.

Furthermore, formation of CaCO_3 phases shown in section 4.4.1.3 likely occurs prior to or during incongruent dissolution phenomenon potentially allowing for Al-Si precipitates to coat carbonate phases, reducing their dissolution upon return to neutral pH. This may aid in reducing contaminant mobility in the long-term due to their low solubility.

4.4.2 Uranium K_d Values for Phyllosilicate Minerals and Hanford Site Sediments

In order to estimate the migration potential of U, batch experiments with phyllosilicate minerals and Hanford Site sediments were used to describe the distribution of the contaminant between the solid and liquid phase. The U loadings (in $\mu\text{g/g}$) are listed in Table 4.3 for the solid phases investigated after NH_3 gas and aeration treatments during short- and long-term contact times in Experiment 3 (visual representation in the Appendix, Figure A.20). Except for muscovite, the U loading was higher during the three-day aeration treatment than the six-month treatments. When comparing U-loading between treatments during the six-month term, there is a minimum of $600 \mu\text{g/g}$ difference for all investigated

solid phases. The decrease in U loading may potentially be due to the significant U desorption that occurs with aeration (i.e., agitation of air bubbles within the Nalgene bottle). The solid is likely to transform into different, more soluble solid phase with longer term aging. The partitioning of U is estimated between the solid and liquid phases with a higher K_d being representative of greater retardation or slower transport through the aqueous phase.

As explained in section 1.2.3, the partitioning coefficients for U in this work are presented as an interaction of several processes (sorption, complexation, and precipitation, among others) happening simultaneously. The apparent partitioning coefficient (K_d) is shown in Eq. 1.5 and represents an estimation of the U concentrations in the solid and aqueous phases based on adsorption and co-precipitation processes (section 1.2.3). Figure 4.5 and Figure 4.6 compare the apparent K_d 's (in mL/g) for the partitioning of 1000 ppb U in the presence of 0.6 g/L phyllosilicate minerals and Hanford Site sediments after three-day and six-month of equilibration (Experiment 3). K_d values ranged from high (up to 3.2×10^4 mL/g) where U would be virtually immobile, to lower values (107 mL/g) where retarded mobility would occur. Although the K_d could vary significantly with solid to solution ratio since dissolved U is dependent on the solution, here the ratio was set to be constant for all minerals and sediments. It is important to note that while our batch experiments were performed at 0.6 g/L, much larger solid to solution ratios exist at the Hanford Site's vadose zone mobility (Liu et al., 2004) and thus, higher potential for co-precipitation due to secondary precipitation and incongruent dissolution is expected, consequently resulting in larger U incorporation and lower long-term mobility.

When comparing the effect of aging time for each solid phase (Figure 4.5), apparent K_d 's show similar trends between treatments. The similarity of the results provides broad evidence that equilibrium for adsorption was reached in both sets of aging samples. For Experiment 3 – Short-term (three-day) samples, apparent K_d 's do not vary greatly. However, for the long-term (six-month) samples, apparent K_d 's increases by more than two orders of magnitude after aeration treatment (Figure 4.6). The increase in K_d value shows more U is retained in the solid phase during NH_3 treatment followed by release during aeration.

Moreover, the decrease in U mobility could potentially be due to (1) incorporation and precipitation into minerals with low solubility at neutral pH and (2) adsorption to minerals' surface (Duff et al., 2002; Emerson et al., 2018; Liu et al., 2004; Qafoku & Icenhower, 2008), as evidenced by previous studies, and (3) aluminosilicate coating processes with low solubility precipitates (Qafoku & Icenhower, 2008; Szecsody et al., 2012). It is worth noting that even though the apparent K_d 's values decreased after aeration treatment (i.e., less U in the solid phase likely due to U release to the aqueous phase as mentioned previously), U removal is still significantly greater ($K_d < 8.0 \text{ mL/g}$) than natural conditions currently existing at the Hanford Site (Liu et al., 2004; Serne et al., 2008; Szecsody et al., 2013; Zachara et al., 2007).

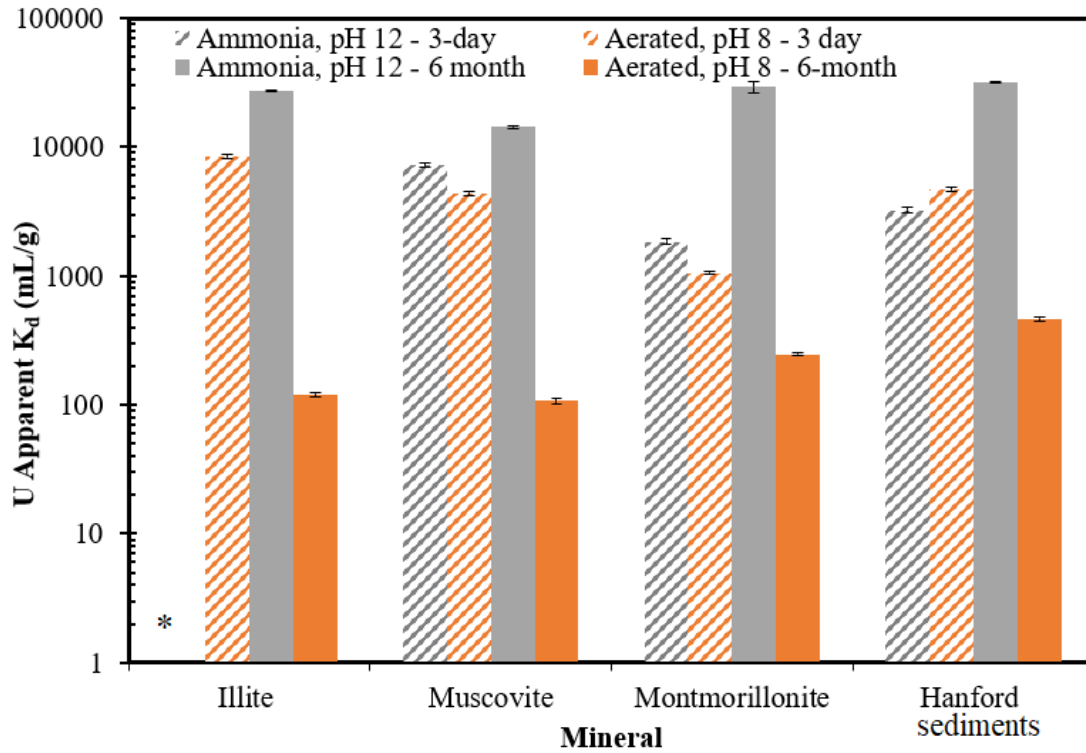


Figure 4.5. Partitioning coefficient K_d (mL/g) U measurements of phyllosilicate minerals and Hanford Site sediments upon ammonia (gray) or aerated (orange) treatment during three-day (pattern) or six-month (solid) contact time for Experiment 3. Note*: there was no measurement recorded for illite 3-day, ammonia treatment.

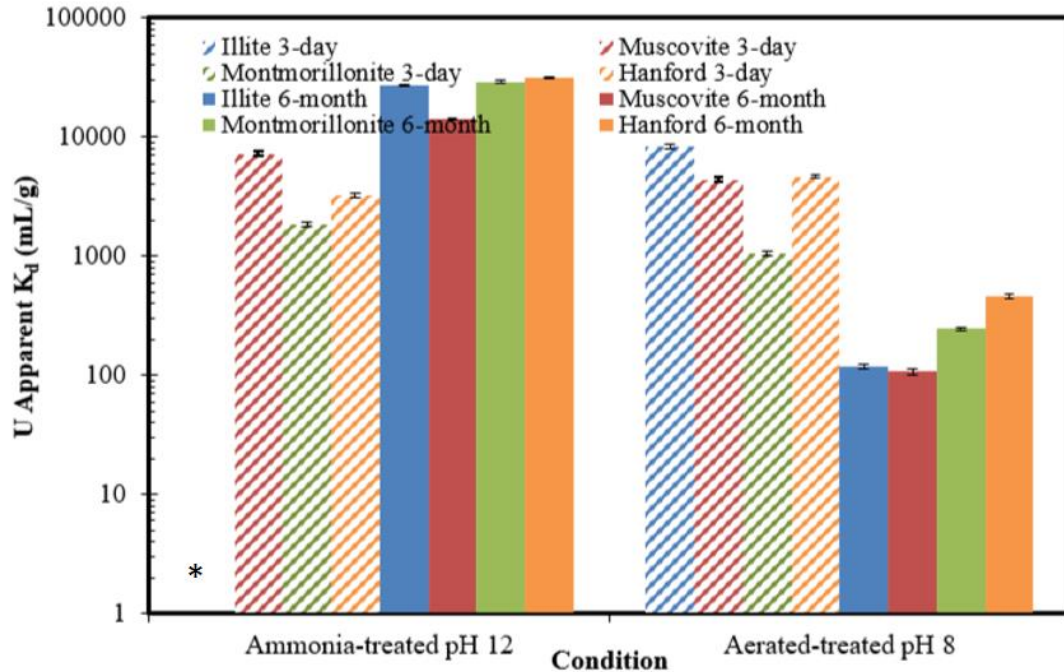


Figure 4.6. Partitioning coefficient K_d (mL/g) U measurements of illite (blue), muscovite (red), montmorillonite (green) and Hanford Site sediment (orange) minerals upon ammonia (left) or aerated (right) treatment during three-day (pattern) or six-month (solid) contact time for Experiment 3. Note*: there was no measurement recorded for illite 3-day, ammonia treatment.

4.4.3 Predicting Solid Phases upon Ammonia Gas Technology using Geochemist Workbench Modeling

Geochemist Workbench® (GWB) thermodynamic equilibrium modeling was used to calculate mineral saturation indices and to identify U-solid phases potentially in equilibrium with the SGW compositions and NH_3 gas application, simulating Hanford Site conditions. These modeling results do not predict adsorption, incorporation, or coating processes but can be used to identify important mineral phases with and without U that are predicted to form based on the solution phase species measured in these experiments. The saturation index (SI or Ω) is used to quantify the distance a system is from equilibrium

(Schott et al., 2009). Defined by Eq. 4.2, Q stands for the activity product and K_{sp} is the mineral solubility product at equilibrium at the temperature of interest.

$$\Omega = (Q/K_{sp}) \quad \text{Eq. 4.2}$$

Ω is dimensionless and, as in standard thermodynamics, a value of 1 represents equilibrium. With a quotient less than 1, reactants are undersaturated with respect to the solution composition and the reaction will tend to go towards the product side. When Ω is greater than 1, the reactants are supersaturated, and the reaction will tend towards the reactants or solid phase precipitates in this discussion (Cantrell et al., 2011; Schott et al., 2009). The GWB speciation modeling predicted that the SGW solution was saturated (i.e., $\Omega > 1$) with respect to five major minerals at pH ~10.8 (Appendix, Table A.9) as shown by Figure 4.7. Table 4.6 lists the relevant U-bearing mineral phases and their structural formula predicted by the GWB software. Consistent with literature, the speciation modeling identified the formation of Na-boltwoodite and uranophane, the most common uranyl silicate solid phases found in the vadose zone environment at the Hanford Site (Liu et al., 2004; Szecsody et al., 2012; Um et al., 2009; Zachara et al., 2007). Further, detailed spectroscopic studies on U(VI)-contaminated Hanford sediments indicated that the precipitates were uranophane, K-boltwoodite (Z. Wang et al., 2005), and Na-boltwoodite (Catalano et al., 2004). In the case of Na-boltwoodite, its formation was expected in some areas of the Hanford Site as the local porewater reached U concentrations in the range of $10^{-4} - 10^{-3}$ M, near saturation with respect to the uranyl silicate (Catalano et al., 2004). It is important to note that this concentration range is two orders of magnitude higher than the added U the presented experiments.

As mentioned in section 1.2.1, when free uranyl ions are present in alkaline environments, anionic aqueous species such as $\text{UO}_2(\text{CO}_3)_2^{2-}$ and $\text{UO}_2(\text{CO}_3)_3^{4-}$ are formed (Figure 1.4). According to Liu *et. al.*, the latter aqueous species accounted for greater than 78% of the dissolved U in all of Hanford Site porewater, with the remainder occurring as $\text{Ca}_2\text{UO}_2(\text{CO}_3)_3$ and $(\text{UO}_2)(\text{CO}_3)_2^{2-}$ (Liu et al., 2004). Such stable and water-soluble uranyl species tend to co-precipitate with the CaCO_3 formed at circumneutral pH. Thus, it is expected to form CaCO_3 polymorphs (e.g., vaterite, aragonite, calcite) and uranyl carbonates, such as liebigite, as shown in the GWB speciation diagrams in Figure 4.7 and Figure 4.8.

Lastly, a recent study proved U retardation on comparative alkaline treatments in the presence of various minerals and natural Hanford sediments. Results suggest that U removal from the aqueous phase increases from $\text{NaOH} < \text{NH}_4\text{OH} < \text{NH}_3$ gas in the SGW solution (Emerson et al., 2018). These results are of relevance to the presented study as the background electrolytes in the SGW solution are equal in composition (i.e., Na^+ , Ca^{2+} , HCO_3^- , etc.) and both at elevated pH (~11.5). The researchers state that under these conditions, the SGW solution is saturated with respect to calcite. Thus, we can conclude that the U co-precipitation with calcite phenomena presented in their work is highly likely to occur in our batch experiments, supporting section 4.4.1.3 on calcite formation.

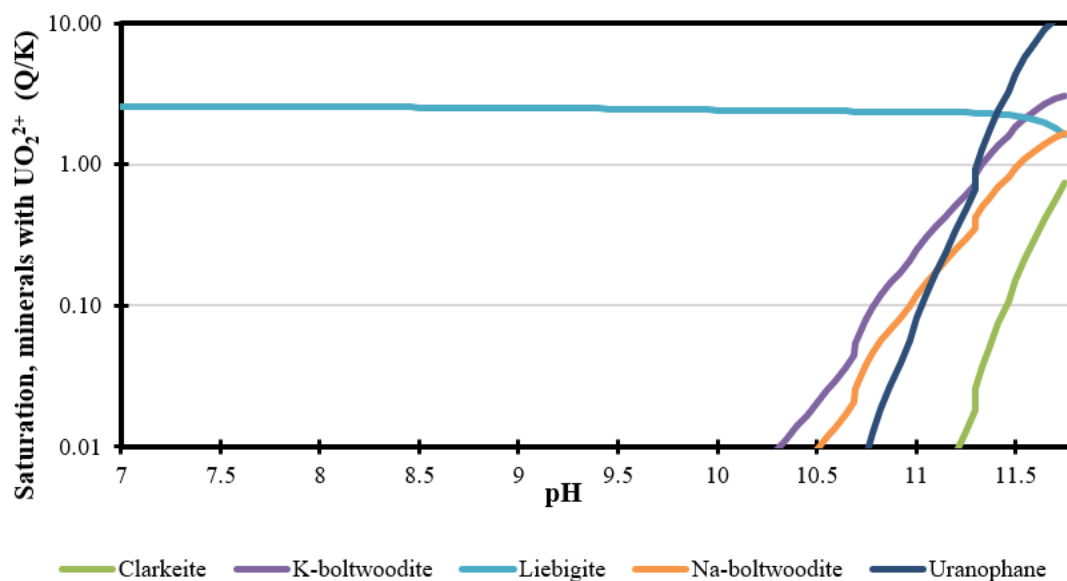


Figure 4.7. Saturation index of U-bearing mineral phases diagram plotted as a function of pH for 5.0% of NH_3 [3.1 mol/L $\text{NH}_3(\text{aq})$] in SGW.

Table 4.6. Uranyl mineral phases used in the Geochemist Workbench[®] speciation modeling

Mineral Phase	Structural Formula
<i>Uranyl Carbonates</i>	
Liebigite	$\text{Ca}_2\text{UO}_2(\text{CO}_3)_3 \cdot 10\text{H}_2\text{O}$
<i>Uranyl hydroxides</i>	
Clarkeite	$\text{Na}(\text{UO}_2)\text{O}(\text{OH})$
<i>Uranyl Silicates</i>	
K-Boltwoodite	$\text{KH}_4\text{SiO}_4 \text{UO}_2 \cdot 1.5\text{H}_2\text{O}$
Na-Boltwoodite	$\text{NaHSiO}_4 \text{UO}_2 \cdot 1.5\text{H}_2\text{O}$
Uranophane	$\text{Ca}(\text{UO}_2)_2(\text{HSiO}_4)_2 \cdot 5\text{H}_2\text{O}$

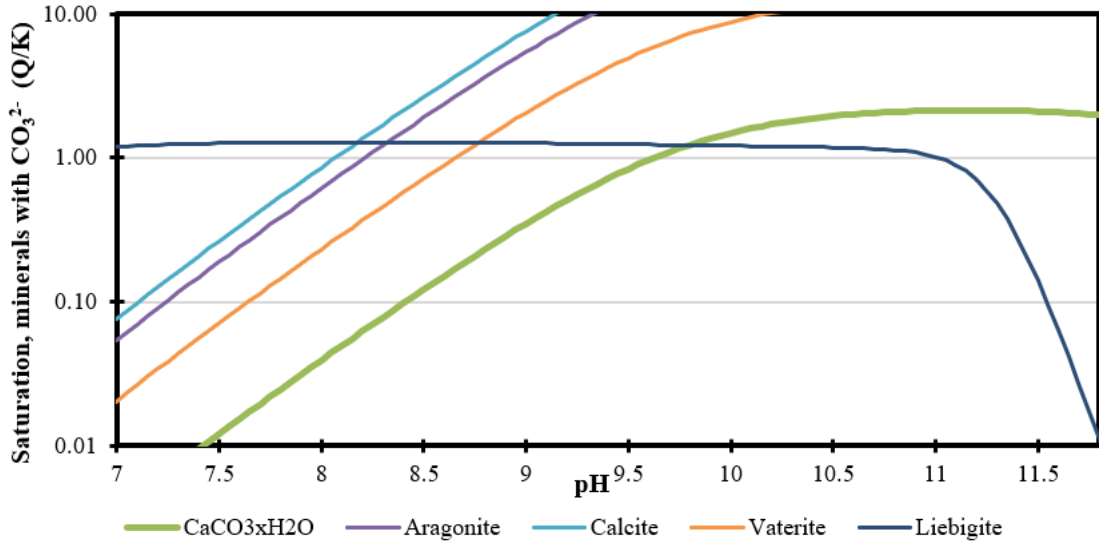


Figure 4.8. Saturation index of Ca-bearing mineral phases diagram plotted as a function of pH for 5.0% of NH₃ [3.1 mol/L NH_{3(aq)}] in SGW.

4.5 Conclusions

The work presented was part of an ongoing effort to understand and predict the fate of U at contaminated sites when alkaline NH₃ ammonia gas injection is chosen as a remediation technique. The focus of this study was to identify (1) mineral alteration of phyllosilicates and Hanford sediments after contact with 5% NH₃/95% N₂ gas treatment, (2) secondary precipitates, and (3) changes in the mobility of U. By using a wide range of characterization and spectroscopic techniques prior, during, and post-treatment, U behavior in the solid phase was monitored. These results are indicative of U removal due to multiple mechanisms, including:

- i. co-precipitation of U(VI) with secondary phases (e.g., CaCO₃ and Fe-oxides),
- ii. co-precipitation of reduced U(IV),

- iii. U precipitation (e.g., Na-boltwoodite or uranophane),
- iv. adsorption of U, and
- v. coating of U phases with secondary phases (e.g., Al/Si from incongruent dissolution and secondary precipitation).

The mechanisms aforementioned are contingent upon NH₃ gas leaving the system (i.e., pH 8). Co-precipitation mechanisms, such as CaCO₃ and Fe-oxide co-precipitation and incongruent dissolution phenomenon due to the aqueous phase being saturated with Si, Al, or similar ions, are primordial for immobilization. While Aim 1 concluded the incongruent dissolution phenomenon, characterization techniques, such as XRD, FTIR, EMPA, and SEM/TEM-EDS in Aim 2, proved the co-precipitation with secondary phases removal mechanism. For Aim 3, XANES analysis showed a significant fraction of reduced U(IV) for the illite mineral investigated ($26 \pm 11\%$) and CaCO₃ formed ($26 \pm 4\%$). Because experiments in this Aim were exposed to U, Fe-oxide impurities in clays along with the re-precipitated Al-Si aluminosilicates provided evidence for a valid U-sequestration mechanism. Lastly, non-radioactive low solubility minerals (e.g., cancrinite, sodalite, etc.) formation and significant Al/Si ratio phyllosilicate transformations during subsequent pH decrease are expected to coat the U phases present at the Hanford Site.

These removal mechanisms were supported by apparent partitioning coefficient (K_d) calculations and geochemical speciation. When describing the distribution of the contaminant at the liquid–solid interface, observation data from batch experiments showed K_d values during aeration treatment higher ($K_d > 107$ mL/g) than those of natural conditions ($K_d < 8.0$ mL/g). Further, simulation models predicted U- and Ca-bearing mineral phase upon NH₃ gas treatment, indicative of U removal at the investigated conditions.

Overall, this study demonstrated effective U removal and U-sequestration mechanisms from resulting precipitates. We hypothesized that the phyllosilicate minerals and Hanford Site sediments analyzed would be transformed to U-bearing phases and have CaCO₃ co-precipitated on the solid phase under conditions designed to mimic those under leaking high-level waste tanks. These batch experiments and predictive model simulations improve our understanding of U contaminant interactions in highly alkaline systems. Nonetheless, further studies are warranted to evaluate U fate and transport performance toward U reduction and immobilization in systematic studies.

4.6 References

- Abarca Betancourt, A. J. (2017). *The Stability of Uranium-Bearing Precipitates Created as a Result of Ammonia Gas Injections in the Hanford Site Vadose Zone*.
- Abdelouas, A. (2006). Uranium mill tailings: geochemistry, mineralogy, and environmental impact. *Elements*, 2(6), 335–341.
- Baeyens, B., & Bradbury, M. H. (2004). Cation exchange capacity measurements on illite using the sodium and cesium isotope dilution technique: effects of the index cation, electrolyte concentration and competition: modeling. *Clays and Clay Minerals*, 52(4), 421–431.
- Bethke, C. (2008). *Geochemical and biogeochemical reaction modeling* (2nd ed.). Oxford University Press.
- Bickmore, B. R., Nagy, K. L., Young, J. S., & Drexler, J. W. (2001). Nitrate-cancrinite precipitation on quartz sand in simulated Hanford tank solutions. *Environmental Science & Technology*, 35(22), 4481–4486.
- Boggs, M. A., Dai, Z., Kersting, A. B., & Zavarin, M. (2015). Plutonium (IV) sorption to montmorillonite in the presence of organic matter. *Journal of Environmental Radioactivity*, 141, 90–96.
- Boglaienko, D., Qafoku, O., Kukkadapu, R. K., Kovarik, L., Katsenovich, Y. P., Cherkasov, D. E., Emerson, H. P., & Levitskaia, T. G. (2021). Elemental iron: reduction of pertechnetate in the presence of silica and periodicity of precipitated nano-structures. *Environmental Science: Nano*.

- Buck, E. C., & McNamara, B. K. (2004). Precipitation of Nitrate– Cancrinite in Hanford Tank Sludge. *Environmental Science & Technology*, 38(16), 4432–4438.
- Cantrell, K. J., Deutsch, W. J., & Lindberg, M. J. (2011). Thermodynamic Model for Uranium Release from Hanford Site Tank Residual Waste. *Environmental Science & Technology*, 45(4), 1473–1480.
- Catalano, J. G., & Brown, G. E. (2005). Uranyl adsorption onto montmorillonite: Evaluation of binding sites and carbonate complexation. *Geochimica et Cosmochimica Acta*, 69(12), 2995–3005.
- Catalano, J. G., Heald, S. M., Zachara, J. M., & Brown, G. E. (2004). Spectroscopic and diffraction study of uranium speciation in contaminated vadose zone sediments from the Hanford site, Washington state. *Environmental Science & Technology*, 38(10), 2822–2828.
- Chapman, N., & Hooper, A. (2012). The disposal of radioactive wastes underground. In *Proceedings of the Geologists' Association* (Vol. 123, Issue 1, pp. 46–63). Geologists' Association.
- Chen, Shang, C., Shao, J., Zhang, J., & Huang, H. (2017). The application of iron-based technologies in uranium remediation: a review. *Science of the Total Environment*, 575, 1291–1306.
- Chipera, S. J., & Bish, D. L. (2001). Baseline studies of the clay minerals society source clays: powder X-ray diffraction analyses. *Clays and Clay Minerals*, 49(5), 398–409.
- Cole, H. (1970). Bragg's law and energy sensitive detectors. *Journal of Applied Crystallography*, 3(5), 405–406.
- Davis, J. A., Meece, D. E., Kohler, M., & Curtis, G. P. (2004). Approaches to surface complexation modeling of Uranium(VI) adsorption on aquifer sediments
1 Associate editor: J. Rustad. *Geochimica et Cosmochimica Acta*, 68(18), 3621–3641.
- Di Pietro, S. A., Emerson, H. P., Katsenovich, Y., Qafoku, N. P., & Szecsody, J. E. (2020). Phyllosilicate mineral dissolution upon alkaline treatment under aerobic and anaerobic conditions. *Applied Clay Science*, 189.
- Dong, W., Ball, W. P., Liu, C., Wang, Z., Stone, A. T., Bai, J., & Zachara, J. M. (2005). Influence of Calcite and Dissolved Calcium on Uranium(VI) Sorption to a Hanford Subsurface Sediment. *Environmental Science & Technology*, 39(20), 7949–7955.
- Duff, M. C., Coughlin, J. U., & Hunter, D. B. (2002). Uranium co-precipitation with iron oxide minerals. *Geochimica et Cosmochimica Acta*, 66(20), 3533–3547.

- Duff, M. C., Mason, C. F. V., & Hunter, D. B. (1998). Comparison of acid and base leach for the removal of uranium from contaminated soil and catch-box media. *Canadian Journal of Soil Science*, 78(4), 675–683.
- Edelstein, N., Katz, J. J., Fuger, J., & Morss, L. R. (2011). *The Chemistry of the Actinide and Transactinide Elements* (Third). Springer.
- Emerson, H. P., Di Pietro, S., Katsenovich, Y., & Szecsody, J. (2017). Effects of ammonium on uranium partitioning and kaolinite mineral dissolution. *Journal of Environmental Radioactivity*, 167.
- Emerson, H. P., Di Pietro, S., Katsenovich, Y., & Szecsody, J. (2018). Potential for U sequestration with select minerals and sediments via base treatment. *Journal of Environmental Management*, 223.
- Falini, G., Fermani, S., Gazzano, M., & Ripamonti, A. (1998). Structure and morphology of synthetic magnesium calcite. *Journal of Materials Chemistry*, 8(4), 1061–1065.
- Fusová, L. (2009). *Modification of the structure of Ca-montmorillonite*.
- Gallucci, M. (2020). What to do with 177 giant tanks of radioactive sludge. *IEEE Spectrum*, 57(5), 24–33.
- Grenthe, I., Wanner, H., & Forest, I. (1992). *Chemical thermodynamics of uranium*. North-Holland.
- Harvey, D. W. (2000). *History of the Hanford Site: 1943-1990*. Pacific Northwest National Laboratory (PNNL), Richland, WA.
- Hsi, C. D., & Langmuir, D. (1985). Adsorption of uranyl onto ferric oxyhydroxides: Application of the surface complexation site-binding model. *Geochimica et Cosmochimica Acta*, 49(9), 1931–1941.
- Jackson, M. L. (2005). *Soil chemical analysis: Advanced course* (Second). UW-Madison Libraries Parallel Press.
- Katsenovich, Y. P., Cardona, C., Szecsody, J., Lagos, L. E., & Tang, W. (2018). Assessment of calcium addition on the removal of U(VI) in the alkaline conditions created by NH₃ gas. *Applied Geochemistry*, 92, 94–103.
- Křepelová, A., Sachs, S., & Bernhard, G. (2006). Uranium (VI) sorption onto kaolinite in the presence and absence of humic acid. *Radiochimica Acta*, 94(12), 825–833.
- Langmuir, D. (1997). Aqueous geochemistry of uranium. *Aqueous Environmental Chemistry*, 494–512.

- Liao, R., Shi, Z., Chen, Y., Zhang, J., Wang, X., Hou, Y., & Zhang, K. (2020). Characteristics of uranium sorption on illite in a ternary system: effect of phosphate on adsorption. *Journal of Radioanalytical and Nuclear Chemistry*, 323(1), 159–168.
- Ling, & Zhang, W. (2015). Enrichment and Encapsulation of Uranium with Iron Nanoparticle. *Journal of the American Chemical Society*, 137(8), 2788–2791.
- Liu, C., Zachara, J. M., Qafoku, O., McKinley, J. P., Heald, S. M., & Wang, Z. (2004). Dissolution of uranyl microprecipitates in subsurface sediments at Hanford Site, USA. *Geochimica et Cosmochimica Acta*, 68(22), 4519–4537.
- Ma, R., Liu, C., Greskowiak, J., Prommer, H., Zachara, J., & Zheng, C. (2014). Influence of calcite on uranium(VI) reactive transport in the groundwater-river mixing zone. *Journal of Contaminant Hydrology*, 156, 27–37.
- Mashal, K., Harsh, J. B., & Flury, M. (2005). Clay mineralogical transformations over time in Hanford sediments reacted with simulated tank waste. *Soil Science Society of America Journal*, 69(2), 531–538.
- Mashal, K., Harsh, J. B., Flury, M., Felmy, A. R., & Zhao, H. (2004). Colloid formation in Hanford sediments reacted with simulated tank waste. *Environmental Science & Technology*, 38(21), 5750–5756.
- McKinley, Heald, S. M., Zachara, J. M., & Resch, C. T. (2002). The identification of uranium-bearing phases by X-ray microprobe, electron microprobe, and scanning electron microscopy. *InField Investigation Report for Waste Management Area B-BX-BY, River Protection Project (RPP). RPP-10098, D122–D129.*
- McKinley, J. P., Zachara, J. M., Wan, J., McCready, D. E., & Heald, S. M. (2007). Geochemical controls on contaminant uranium in vadose Hanford formation sediments at the 200 area and 300 area, Hanford Site, Washington. *Vadose Zone Journal*, 6(4), 1004–1017.
- Meece, D. E., & Benninger, L. K. (1993). The coprecipitation of Pu and other radionuclides with CaCO₃. *Geochimica et Cosmochimica Acta*, 57(7), 1447–1458.
- Meier, L. P., & Nüesch, R. (1999). The lower cation exchange capacity limit of montmorillonite. *Journal of Colloid and Interface Science*, 217(1), 77–85.
- Moyes, L. N., Parkman, R. H., Charnock, J. M., Vaughan, D. J., Livens, F. R., Hughes, C. R., & Braithwaite, A. (2000). Uranium uptake from aqueous solution by interaction with goethite, lepidocrocite, muscovite, and mackinawite: An X-ray absorption spectroscopy study. *Environmental Science & Technology*, 34(6), 1062–1068.

- Nicolas, H. G., Allen, S., La, D. Q., Tournassat, C., & Tinnacher, R. M. (2019). *Influence of Calcite on Uranium(VI) Sorption onto Montmorillonite Clay*.
- Payne, T. E., Lumpkin, G. R., & Waite, T. D. (1998). Uranium (VI) adsorption on model minerals. *Adsorption of Metals by Geomedia*, 75–97.
- Qafoku, Ainsworth, C. C., Szecsody, J. E., & Qafoku, O. S. (2003). Aluminum Effect on Dissolution and Precipitation under Hyperalkaline Conditions: I. Liquid Phase Transformations. *Journal of Environmental Quality*, 32(6), 2354–2363.
- Qafoku, N. P., Ainsworth, C. C., Szecsody, J. E., & Qafoku, O. S. (2004). Transport-controlled kinetics of dissolution and precipitation in the sediments under alkaline and saline conditions. *Geochimica et Cosmochimica Acta*, 68(14), 2981–2995.
- Qafoku, N. P., & Icenhower, J. P. (2008). Interactions of aqueous U (VI) with soil minerals in slightly alkaline natural systems. *Reviews in Environmental Science and Bio/Technology*, 7(4), 355–380.
- Qafoku, N. P., Zachara, J. M., Liu, C., Gassman, P. L., Qafoku, O. S., Smith, S. C. %J E. science, & technology. (2005). Kinetic desorption and sorption of U (VI) during reactive transport in a contaminated Hanford sediment. *Environmental Science & Technology*, 39(9), 3157–3165.
- Read, D., Lawless, T. A., Sims, R. J., & Butter, K. R. (1993). Uranium migration through intact sandstone cores. *Journal of Contaminant Hydrology*, 13(1–4), 277–289.
- Reeder, R. J., Nugent, M., Lamble, G. M., Tait, C. D., & Morris, D. E. (2000). Uranyl incorporation into calcite and aragonite: XAFS and luminescence studies. *Environmental Science & Technology*, 34(4), 638–644.
- Reynolds, J. G., Cooke, G. A., Page, J. S., & Warrant, R. W. (2018). Uranium-bearing phases in Hanford nuclear waste. *Journal of Radioanalytical and Nuclear Chemistry*, 316(1), 289–299.
- Sato, T., Murakami, T., Yanase, N., Isobe, H., Payne, T. E., & Airey, P. L. (1997). Iron nodules scavenging uranium from groundwater. *Environmental Science & Technology*, 31(10), 2854–2858.
- Schoonheydt, R. A., & Johnston, C. T. (2013). Surface and interface chemistry of clay minerals. In *Developments in clay science* (Vol. 5, pp. 139–172). Elsevier.
- Schott, J., Pokrovsky, O. S., & Oelkers, E. H. (2009). The link between mineral dissolution/precipitation kinetics and solution chemistry. *Reviews in Mineralogy and Geochemistry*, 70(1), 207–258.

- Serne, Last, G. V., Gee, G. W., Schaef, H. T., Lanigan, D. C., Lindenmeier, C. W., Lindberg, M. J., Clayton, R. E., Legore, V. L., & Orr, R. D. (2008). *Characterization of vadose zone sediment: Borehole 299-E33-45 near BX-102 in the B-BX-BY waste management area*. Pacific Northwest National Lab.(PNNL), Richland, WA (United States).
- Sheng, L., & Fein, J. B. (2014). Uranium reduction by *Shewanella oneidensis* MR-1 as a function of NaHCO₃ concentration: surface complexation control of reduction kinetics. *Environmental Science & Technology*, *48*(7), 3768–3775.
- Silva, R. J., & Nitsche, H. (1995). Actinide environmental chemistry. *Radiochimica Acta*, *70*(71), 377–396.
- Stumm, W., & Morgan, J. J. (1991). Aquatic chemistry. In *John Willey and Son, New York*. John Willey and Son.
- Su, C., & Suarez, D. L. (1997). In situ infrared speciation of adsorbed carbonate on aluminum and iron oxides. *Clays and Clay Minerals*, *45*(6), 814–825.
- Szecsody, Truex, M. J., Qafoku, N. P., Wellman, D. M., Resch, T., & Zhong, L. (2013). Influence of acidic and alkaline waste solution properties on uranium migration in subsurface sediments. *Journal of Contaminant Hydrology*, *151*, 155–175.
- Szecsody, Truex, M. J., Zhong, L., Johnson, T. C., Qafoku, N. P., Williams, M. D., Greenwood, W. J., Wallin, E. L., Bargar, J. D., & Faurie, D. K. (2012). Geochemical and Geophysical Changes during Ammonia Gas Treatment of Vadose Zone Sediments for Uranium Remediation. *Vadose Zone Journal*, *11*(4).
- Szecsody, Truex, M., Zhong, L., Williams, M., Resch, C., & McKinley, J. (2010). Remediation of Uranium in the Hanford Vadose Zone Using Gas-Transported Reactants : Laboratory-Scale Experiments. *Contract*, *January*, 65.
- Tombacz, E., Dobos, A., Szekeres, M., Narres, H. D., Klumpp, E., & Dekany, I. (2000). Effect of pH and ionic strength on the interaction of humic acid with aluminium oxide. *Colloid and Polymer Science*, *278*(4), 337–345.
- Tsarev, S., Collins, R. N., Ilton, E. S., Fahy, A., & Waite, T. D. (2017). The short-term reduction of uranium by nanoscale zero-valent iron (nZVI): role of oxide shell, reduction mechanism and the formation of U (V)-carbonate phases. *Environmental Science: Nano*, *4*(6), 1304–1313.
- Um, W., Wang, Z., Serne, R. J., Williams, B. D., Brown, C. F., Dodge, C. J., & Francis, A. J. (2009). Uranium phases in contaminated sediments below Hanford's U tank farm. *Environmental Science & Technology*, *43*(12), 4280–4286.

- Waite, T. D., Davis, J. A., Payne, T. E., Waychunas, G. A., & Xu, N. (1994). Uranium (VI) adsorption to ferrihydrite: Application of a surface complexation model. *Geochimica et Cosmochimica Acta*, 58(24), 5465–5478.
- Walls, J., Sharrard, C., Livens, F., Smith, J., Lloyd, J., Banford, A., Morris, K., Renshaw, J., Howard, B., & Pentreath, J. (2011). *Nuclear Power and the Environment*. Royal Society of Chemistry.
- Wan, J., Larsen, J. T., Tokunaga, T. K., & Zheng, Z. (2004). pH neutralization and zonation in alkaline-saline tank waste plumes. *Environmental Science & Technology*, 38(5), 1321–1329.
- Wang, Zachara, J. M., Gassman, P. L., Liu, C., Qafoku, O., Yantasee, W., & Catalano, J. G. (2005). Fluorescence spectroscopy of U(VI)-silicates and U(VI)-contaminated Hanford sediment. *Geochimica et Cosmochimica Acta*, 69(6), 1391–1403.
- Wellman, D. M., Gamerdinger, A. P., Kaplan, D. I., & Serne, R. J. (2008). Effect of particle-scale heterogeneity on Uranium(VI) transport in unsaturated porous media. In *Vadose Zone Journal* (Vol. 7, Issue 1, pp. 67–78).
- Yuan, K. (2015). *Electrochemical Investigations of Redox Reactions of Uranyl (VI) on Magnetite and Computational Modeling of the UO₂-HfO₂ Solid Solution*. Doctoral dissertation.
- Zachara, J., Brown, C., Christensen, J., Davis, J. A., Dresel, E., Kelly, S., Liu, C., McKinley, J., Serne, J., & Um, W. (2007). *A Site-Wide Perspective on Uranium Geochemistry at the Hanford Site*.
- Zhao, H., Deng, Y., Harsh, J. B., Flury, M., & Boyle, J. S. (2004). Alteration of kaolinite to cancrinite and sodalite by simulated Hanford tank waste and its impact on cesium retention. *Clays and Clay Minerals*, 52(1), 1–13.
- Zheng, Z., Zhang, G., & Wan, J. (2008). Reactive transport modeling of column experiments on the evolution of saline-alkaline waste solutions. *Journal of Contaminant Hydrology*, 97(1–2), 42–54.

CHAPTER V

General Conclusions

5 CHAPTER 5: GENERAL CONCLUSIONS

5.1 Conclusion Summary

Uranium is a risk-driving contaminant in groundwater and soil at U mining, milling, nuclear materials production, and disposal sites such as the U.S. DOE's Hanford Site. Reactive gases, such as NH_3 , may aid in sequestration of contaminants in the subsurface, especially in the vadose zone. In this study, we focused on the potential for NH_3 gas to immobilize U under conditions relevant to the Hanford Site's vadose zone. The injection of NH_3 gas creates hyperalkaline conditions that induce mineral dissolution and secondary precipitation that may immobilize U through complex adsorption, co-precipitation, and coating processes. In the present study, injection of reactive gases, such as NH_3 , was explored to create alkaline and reducing conditions, inducing sediment dissolution and precipitation processes that may decrease the amount of mobile U within the Hanford Site's vadose zone.

To begin, aluminosilicate minerals found across the Hanford Site, termed phyllosilicates, were selected to study their dissolution reactions. These minerals were exposed to anaerobic and aerobic conditions using comparative solutions (NH_4OH and NaOH). After a two-month contact-time period, our hypothesis was confirmed; incongruent dissolution phenomena occurred. The Al and Si atoms found in the minerals dissolved disproportionately, with Al detaching first and faster (< 240 h) than Si (> 1440 h). In addition, our results suggested formation of secondary precipitates based on incongruent dissolution observed in the aqueous phase with changes over time and solid phase characterization. Furthermore, alkaline treatments (NH_4OH versus NaOH) reacted differently with investigated phyllosilicate minerals. While mica minerals (illite and

muscovite) dissolved more with the strong base NaOH solution, montmorillonite dissolved more with weak base NH_4OH treatment, likely due to intercalation of the polyatomic cation NH_4^+ into the montmorillonite's expandable layers. Mica minerals lack expandable, hydration layers in their structure and, therefore, did not react as strongly with NH_4^+ .

To continue investigating NH_3 gas treatment, pure phyllosilicate clay minerals (illite and montmorillonite) in SGW were exposed to NH_3 gas. However, after a 12-h equilibration time, minerals were aerated to mimic a return to Hanford Site natural conditions at circumneutral pH. By utilizing various solid phase characterization techniques, Aim 2 experimentation showed significant physicochemical transformations in both minerals. We observed an increase in particle size and recrystallization of Al-OH in the phyllosilicate edges-sites as the pH was neutralized. These alterations led to co-precipitation processes and incongruent dissolution phenomena, which may increase U sequestration depending on where the U is when co-precipitation occurs.

Lastly, Aim 3 was an extension of Aim 2 experimentation; however, phyllosilicate minerals and Hanford Site sediments were exposed to U to identify the dominant phases with which U was associated. Geochemical software modeling predicted U-mineral formation at the investigated conditions in this research, including uranyl carbonate and silicate phases. Furthermore, although speciation models cannot account for co-precipitation processes, spectroscopic and crystallographic observations of the solid phases at circumneutral pH revealed CaCO_3 formation, a predominant mineral phase in a carbonate-rich Hanford Site vadose zone with incorporated U. In addition, significant U was observed in association with illite, including some reduced U(IV). If these phases were coated with Al-Si formed over time from incongruent dissolution of clays, U mobility

should be decreased significantly. Secondary precipitation, including calcite formation and incongruent dissolution phenomena, proved to be pathways to decrease U mobility as observed by apparent partitioning coefficient (K_d) values measured from batch experiments.

The results from this research show the scientific community that NH_3 gas injection at the Hanford Site's vadose zone is an innovative technology that may decrease the mobility of inorganic and radionuclide contaminants, particularly the mobile uranyl ion. This technology proves to be valuable for unsaturated areas where remedies are needed *in situ* and without the addition of liquid amendments.

5.2 Future Work

The proposed pathway for U immobilization and sequestration in the presence of NH_3 gas needs to be investigated further for diverse applications. Although the present study explored the use of NH_3 gas injection in batch-type experiments, future work should focus on studying column-type systems. Because they provide a higher solid to liquid ratio, sorption and U-bearing phase transformation processes may occur more quickly under saturated conditions due to the decreased porewater for ions to dissolve. A slow flow rate with significant mineral-water interface contact time (e.g., one pore volume per day) may help to induce secondary precipitation processes to a greater extent than observed in batch experiments. The decrease in headspace also maximizes the potential for creation of reducing conditions as the 5% NH_3 /95% N_2 gas mixture will more quickly displace air in the system.

Furthermore, future studies may identify solid phase characterization techniques which improve the resolution, quantification, and detection limits of the analytical

techniques used. For example, two-dimensional SEM-EDS images provide a ~ 0.5 nm resolution, while Atomic Force Microscopy (AFM) has a higher spatial resolution (< 0.1 nm), providing a three-dimensional surface profile. In addition, while semi-quantitative SEM-EDS and XRD analyses have a maximum penetration depth of $1.0 \mu\text{m}$ (10^3 nm) and $0.001 \mu\text{m}$ (1.0 nm) respectively, quantitative X-ray photoelectron spectroscopy (XPS) surface analysis is typically < 5.0 nm and is, therefore, better suited for compositional, chemical state, and surface complex analyses. Lastly, to improve U detection limits, the analytical application of Nanoscale Secondary Ion Mass-Spectrometry (nano-SIMS) would be beneficial as detection of low concentrations of U are challenging. This powerful technique analyzes the composition of solid surfaces, particularly important for the U-bearing mineral phases formed, with elemental detection limits in the ppb range.

The combination of small, one-dimensional columns and complementary characterization studies would provide additional details for understanding the interactions between U and Hanford Site sediments and U-bearing mineral formation with reactive NH_3 gas amendment.

A. Appendix

Mineral Dissolution and Precipitation Processes under Highly Alkaline Conditions

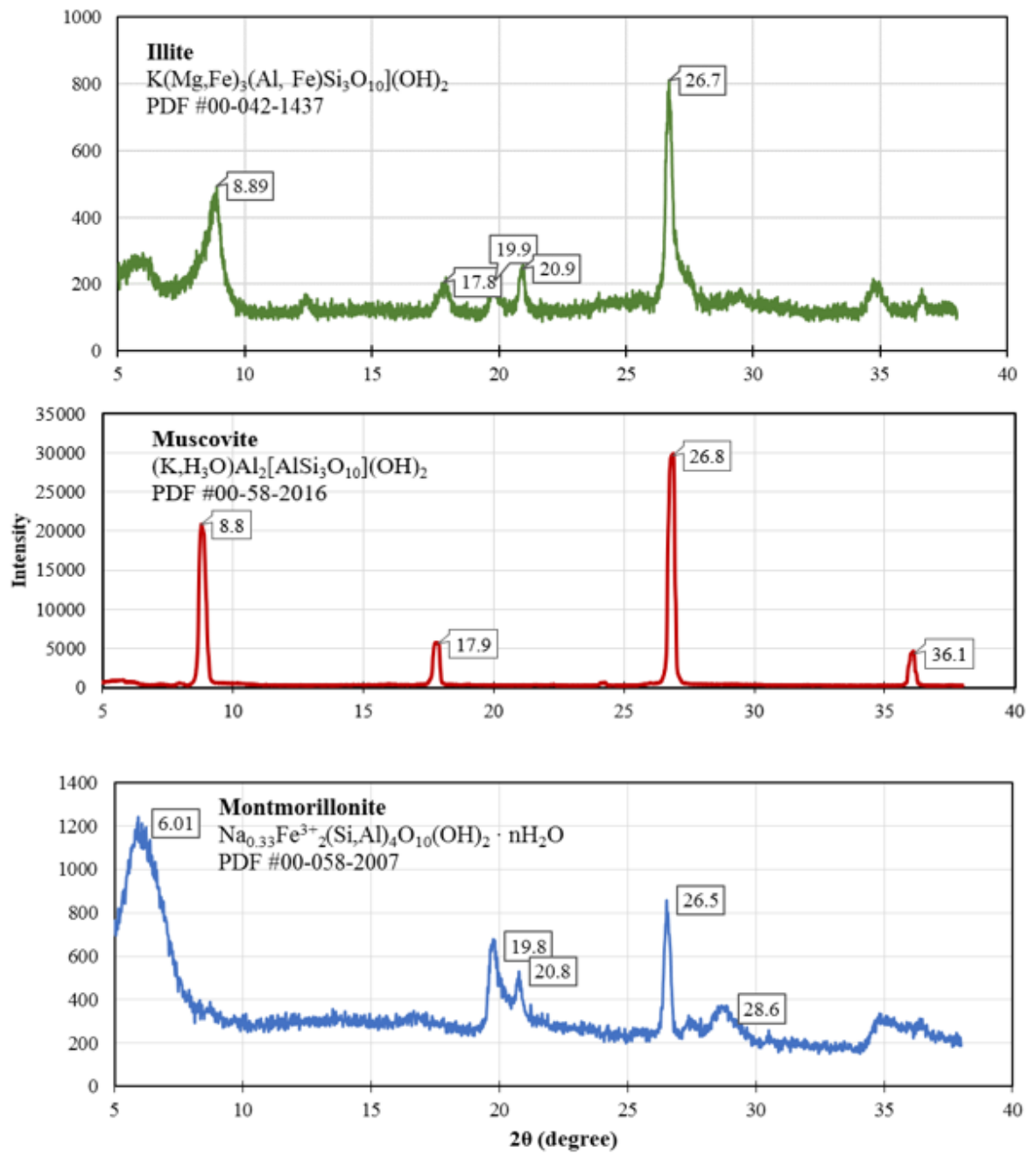


Figure A.1. XRD patterns for illite (green, top), muscovite (red, middle) and montmorillonite (blue, bottom). Note: major 2θ peak values are listed with reference to best fit PDF card.

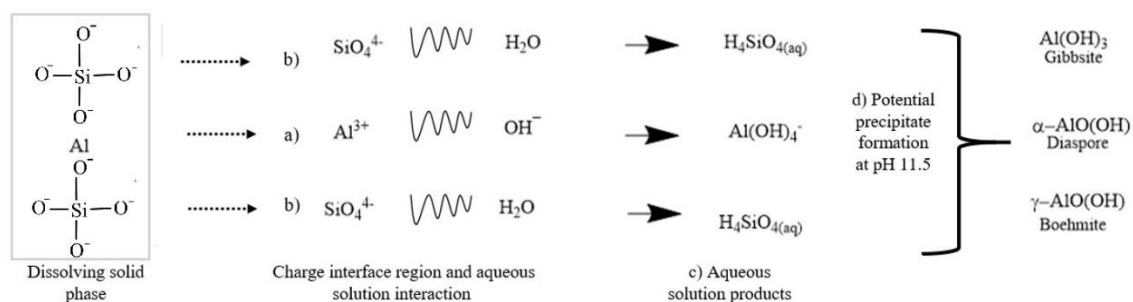


Figure A.2. The proposed mechanism of dissolution for phyllosilicates in alkaline solutions in three steps: a) individual Al atoms from the solid phase react with OH⁻ ions; b) silicate tetrahedra at the surface depart intact, and c) the products from a) and b) steps react in solution. At high pH, aluminosilicate formation such as those produced in d) can precipitate, according to our system (Crundwell, 2014).

Table A.1. Chemical Analysis (CEC and BET) and Theoretical Ratios for Minerals

Mineral	Chemical Formulae	Theoretical Al:Si	CEC (cmol/kg)	BET (m ² /g)*
Illite	K(Mg,Fe) ₃ (Al, Fe)Si ₃ O ₁₀ (OH) ₂	0.33	17.6	19.1
Muscovite	(K,H ₃ O)Al ₂ [AlSi ₃ O ₁₀](OH) ₂	1.0	16.2	0.096
Montmorillonite	Ca _{0.2} (Al,Mg,Fe) ₂ (Si ₄ O ₁₀)(OH) ₂ · nH ₂ O	0.5	9.73	23.8

Note*: Measurements from Emerson *et al.*, 2018

Table A.2. Pseudo second order dissolution rates as measured by monitoring of aqueous Si over time (rate law, standard deviation from linear regression, and R² values) for the minerals investigated (illite, muscovite, and montmorillonite) in 0.01 M NaOH and 3.1 M NH₄OH alkaline solutions under anaerobic and aerobic conditions

Treatment	Illite		Muscovite		Montmorillonite	
	<i>k</i> (±StDev) (L/μg-h)	R ²	<i>k</i> (±StDev) (L/μg-h)	R ²	<i>k</i> (±StDev) (L/μg-h)	R ²
Anaerobic, 3.1 M NH ₄ OH	-1.2±0.5x10 ⁻⁷	0.72	-8.9±4.7x10 ⁻⁸	0.65	-4.1±3.6x10 ⁻⁸	0.39
Anaerobic, 0.01 M NaOH	-3.6±1.8x10 ⁻⁸	0.66	-1.4±0.5x10 ⁻⁷	0.79	-3.4±0.5x10 ⁻⁸	0.98
Aerobic, 3.1 M NH ₄ OH	-7.9±3.8x10 ⁻⁸	0.68	-2.8±2.2x10 ⁻⁸	0.61	-8.9±6.6x10 ⁻⁸	0.48
Aerobic, 0.01 M NaOH	-6.4±4.1x10 ⁻⁸	0.55	-8.9±6.6x10 ⁻⁸	0.48	-6.4±4.1x10 ⁻⁸	0.55

Table A.3. Pseudo first order dissolution rates as measured by monitoring of aqueous Al over time (rate law, standard deviation from linear regression, and R^2 values) for the minerals investigated (illite, muscovite, and montmorillonite) in 0.01 M NaOH and 3.1 M NH_4OH alkaline solutions under anaerobic and aerobic conditions

Treatment	Illite		Muscovite		Montmorillonite	
	k ($\pm\text{StDev}$) (L/ $\mu\text{g-h}$)	R^2	k ($\pm\text{StDev}$) (L/ $\mu\text{g-h}$)	R^2	k ($\pm\text{StDev}$) (L/ $\mu\text{g-h}$)	R^2
Anaerobic, 3.1 M NH_4OH	-0.0010 \pm 0.0010	0.32	0.0009 \pm 0.0004	0.11	-0.0019 \pm 0.0014	0.49
Anaerobic, 0.01 M NaOH	-0.0016 \pm 0.0012	0.45	0.0013 \pm 0.0003	0.11	-0.0025 \pm 0.0019	0.47
Aerobic, 3.1 M NH_4OH	-0.0016 \pm 0.0013	0.43	0.0007 \pm 0.0006	0.05	-0.0023 \pm 0.0019	0.43
Aerobic, 0.01 M NaOH	-0.0015 \pm 0.0028	0.13	-0.0005 \pm 0.0002	0.88	-0.0019 \pm 0.0014	0.48

Table A.4. Pseudo second order dissolution rates as measured by monitoring of aqueous Al over time (rate law, standard deviation from linear regression, and R^2 values) for the minerals investigated (illite, muscovite, and montmorillonite) in 0.01 M NaOH and 3.1 M NH_4OH alkaline solutions under anaerobic and aerobic conditions

Treatment	Illite		Muscovite		Montmorillonite	
	k ($\pm\text{StDev}$) (L/ $\mu\text{g-h}$)	R^2	k ($\pm\text{StDev}$) (L/ $\mu\text{g-h}$)	R^2	k ($\pm\text{StDev}$) (L/ $\mu\text{g-h}$)	R^2
Anaerobic, 3.1 M NH_4OH	4.5 \pm 6.7 $\times 10^{-7}$	0.18	-7.8 \pm 0.1 $\times 10^{-7}$	0.15	1.2 \pm 1.6 $\times 10^{-6}$	0.22
Anaerobic, 0.01 M NaOH	4.9 \pm 3.3 $\times 10^{-7}$	0.52	-2.2 \pm 3.7 $\times 10^{-7}$	0.15	2.0 \pm 0.5 $\times 10^{-7}$	0.94
Aerobic, 3.1 M NH_4OH	1.1 \pm 0.8 $\times 10^{-6}$	0.49	-1.9 \pm 0.8 $\times 10^{-8}$	0.84	1.1 \pm 1.8 $\times 10^{-7}$	0.16
Aerobic, 0.01 M NaOH	2.5 \pm 0.1 $\times 10^{-6}$	0.02	2.8 \pm 0.1 $\times 10^{-6}$	0.02	3.8 \pm 1.9 $\times 10^{-7}$	0.67

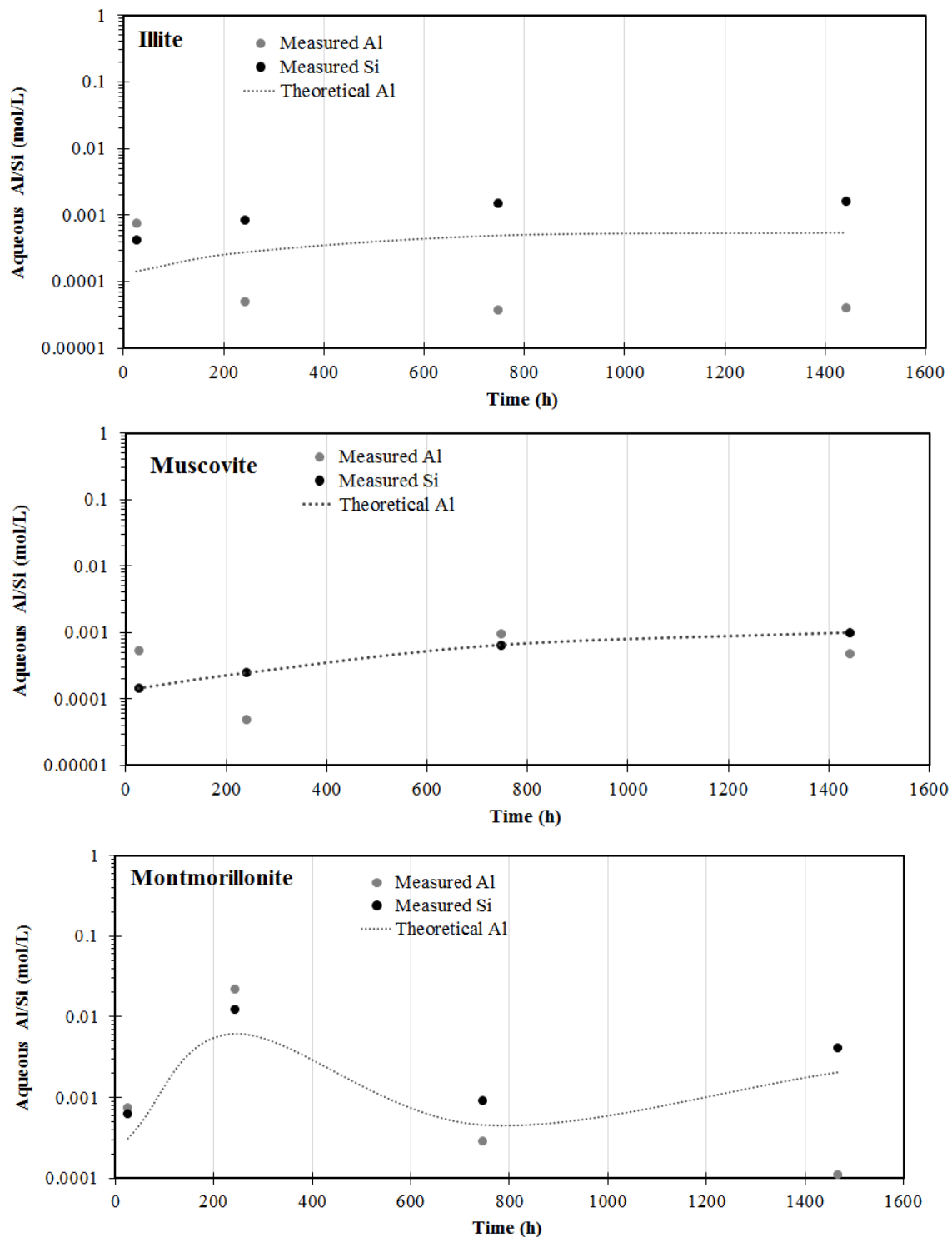


Figure A.3. Aqueous Si (black) and Al (gray), in mol/L after reaction of 33 g/L suspension of minerals [illite (top), muscovite (middle) and montmorillonite (bottom)] over time (24-, 240-, 745- and 1440-h) with 0.01 M NaOH under anaerobic conditions. Dashed lines represent theoretical Al dissolution based on triplicate measurements of Si in the aqueous phase.

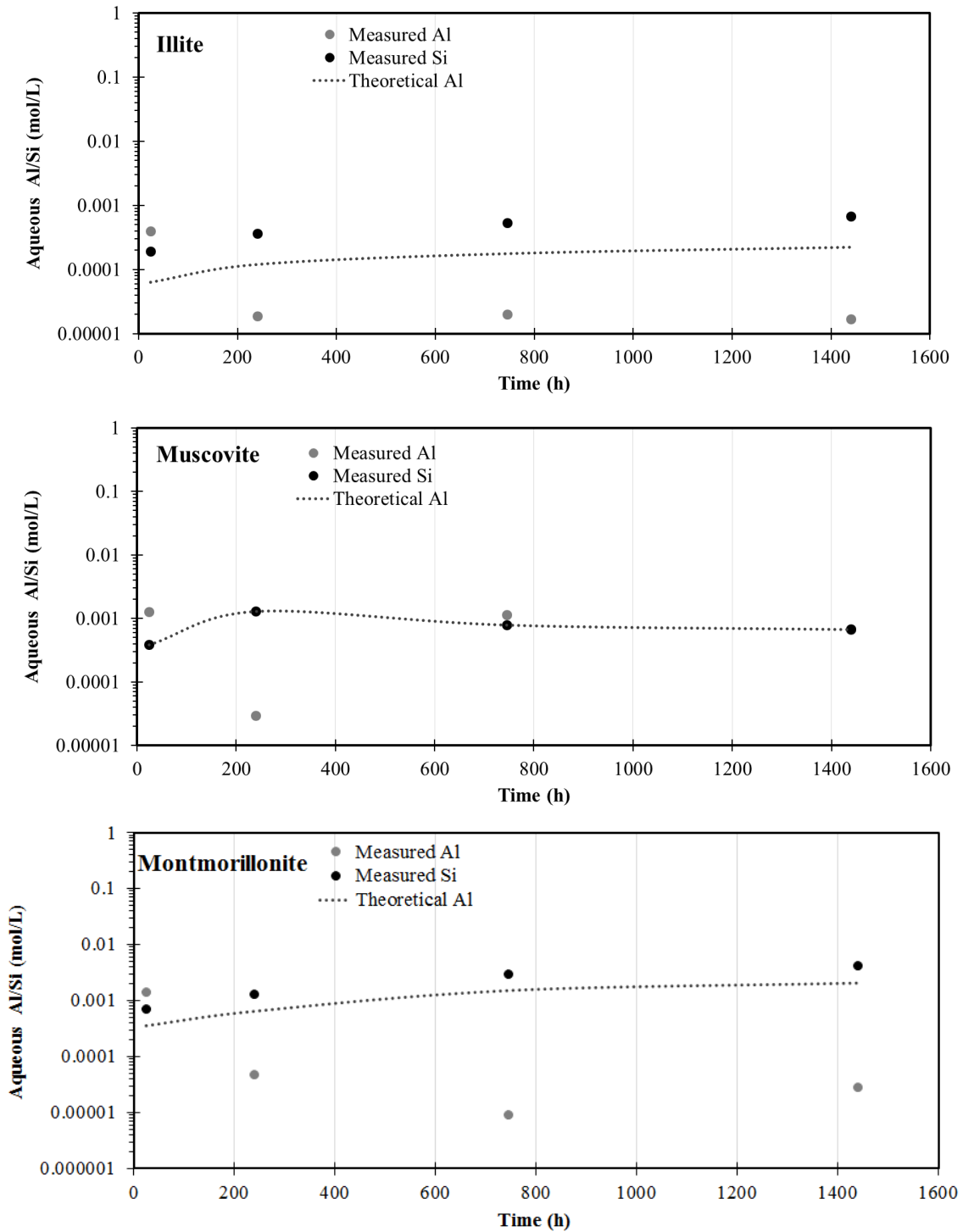


Figure A.4. Aqueous Si (black) and Al (gray), in mol/L after reaction of 33 g/L suspension of minerals [illite (top), muscovite (middle) and montmorillonite (bottom)] over time (24-, 240-, 745- and 1440-h) with 3.1 M NH_4OH under aerobic conditions. Dashed lines represent theoretical Al dissolution based on triplicate measurements of Si in the aqueous phase.

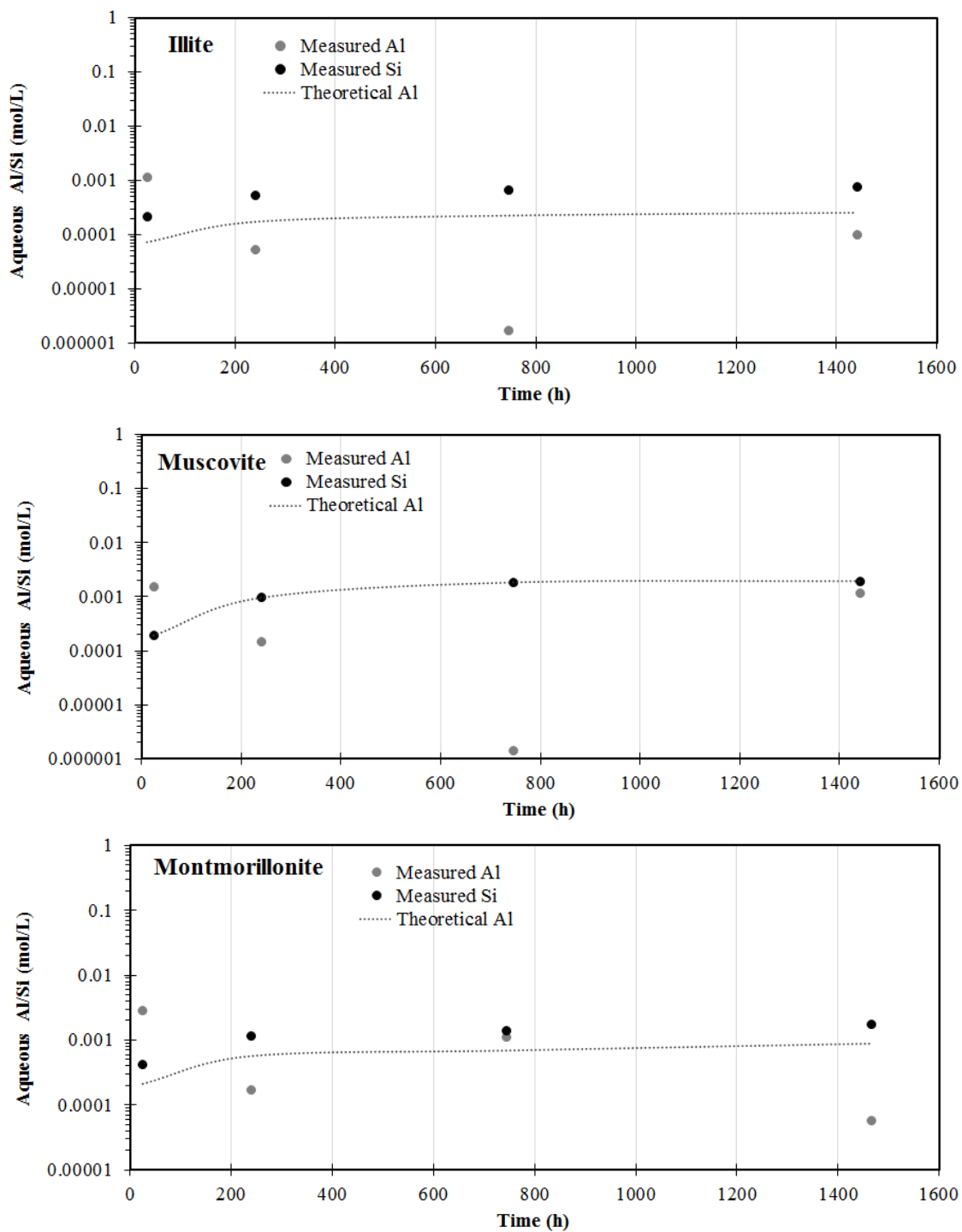


Figure A.5. Aqueous Si (black) and Al (gray), in mol/L after reaction of 33 g/L suspension of minerals [illite (top), muscovite (middle) and montmorillonite (bottom)] over time (24-, 240-, 745- and 1440-h) with 0.01 M NaOH under aerobic conditions. Dashed lines represent theoretical Al dissolution based on triplicate measurements of Si in the aqueous phase.

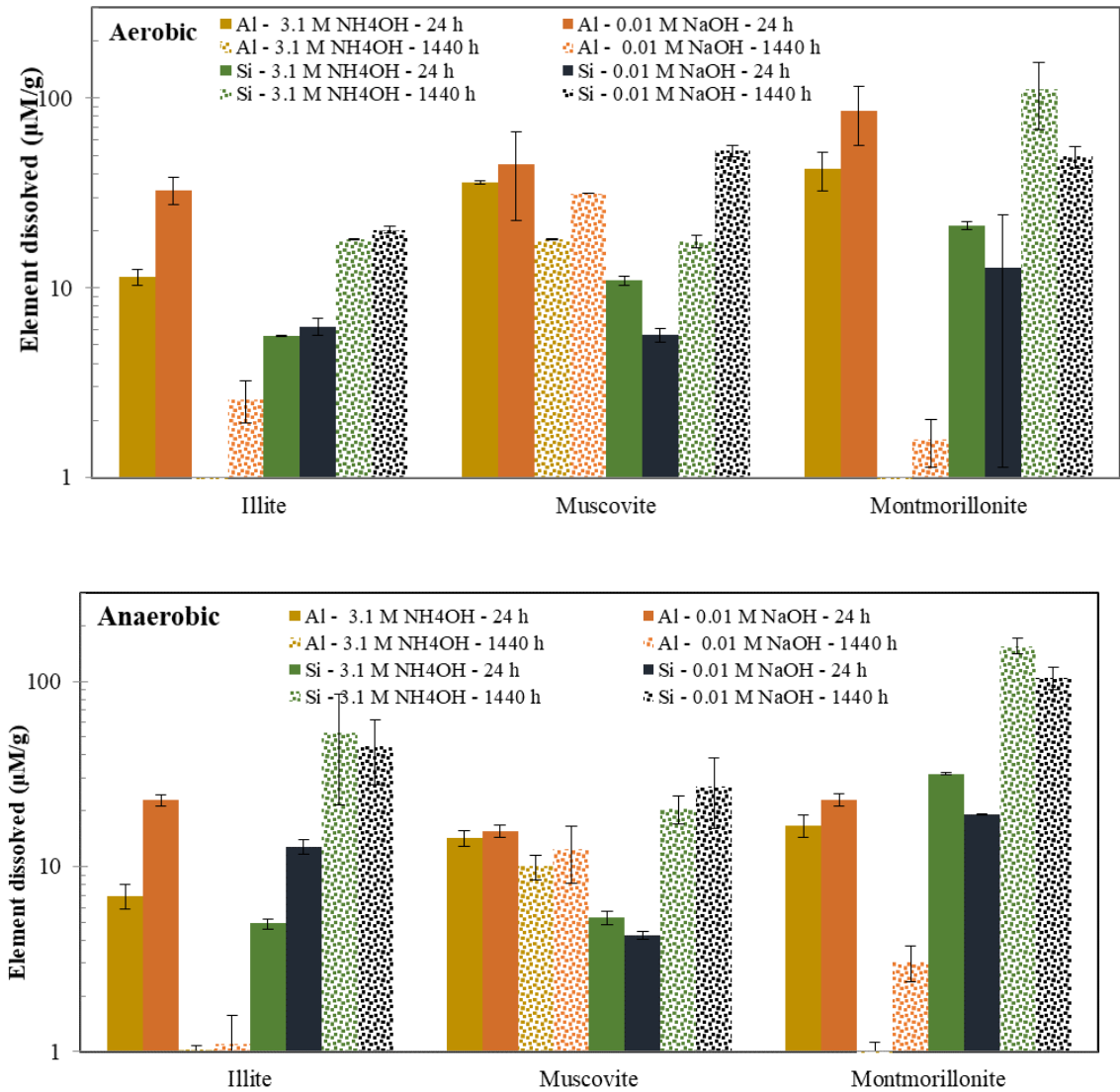


Figure A.6. Comparison of aqueous Al (orange) or Si (green), in $\mu\text{M/g}$, for minerals investigated at 24 h (solid) and 1440 h (pattern) contact-time via NaOH or NH_4OH treatment under aerobic (top) or anaerobic (bottom) conditions.

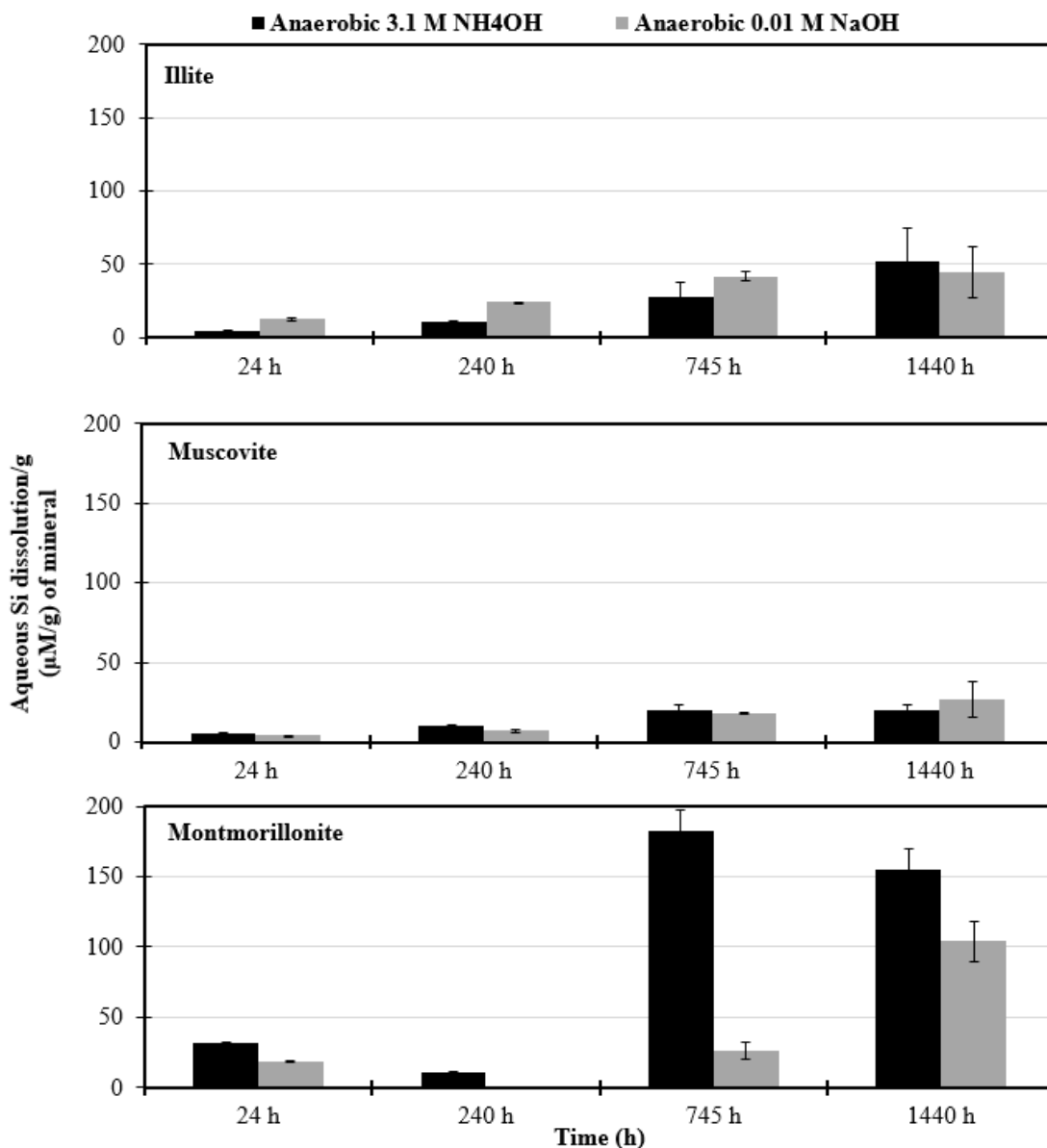


Figure A.7. Comparison of Si removal during alkaline treatments (3.1 M NH₄OH – black and 0.01 M NaOH – gray) for minerals (33g/L) illite (top), muscovite (middle) and montmorillonite (bottom) under anaerobic condition. Note: error bars are based on analysis of triplicate samples; montmorillonite at 240 h was unable to be sampled due to artifact problems.

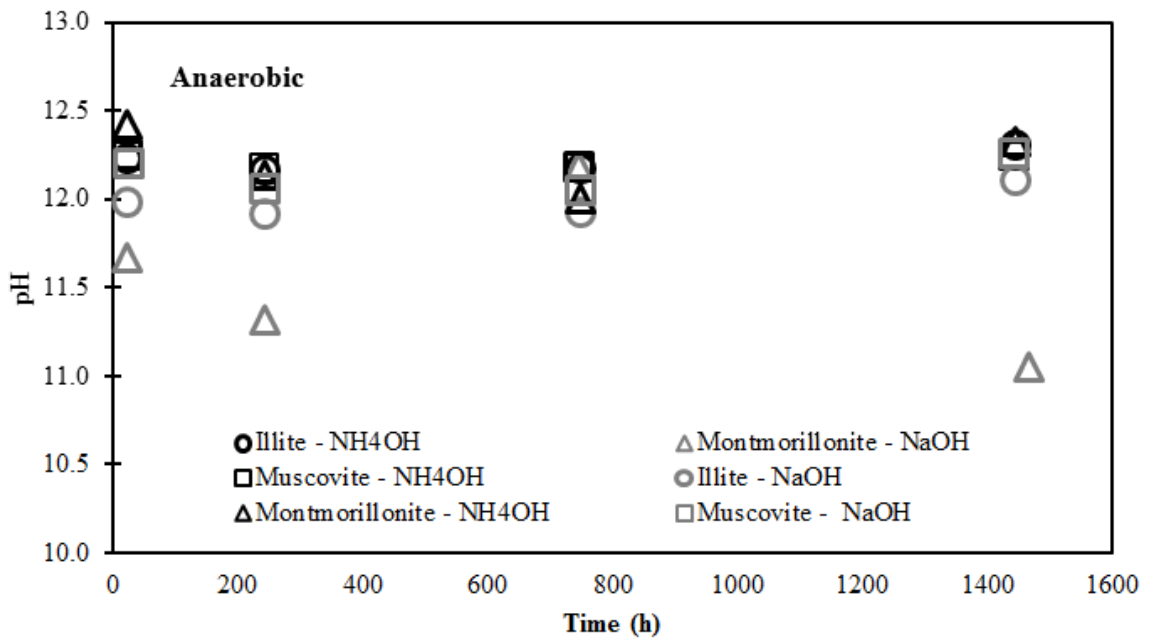
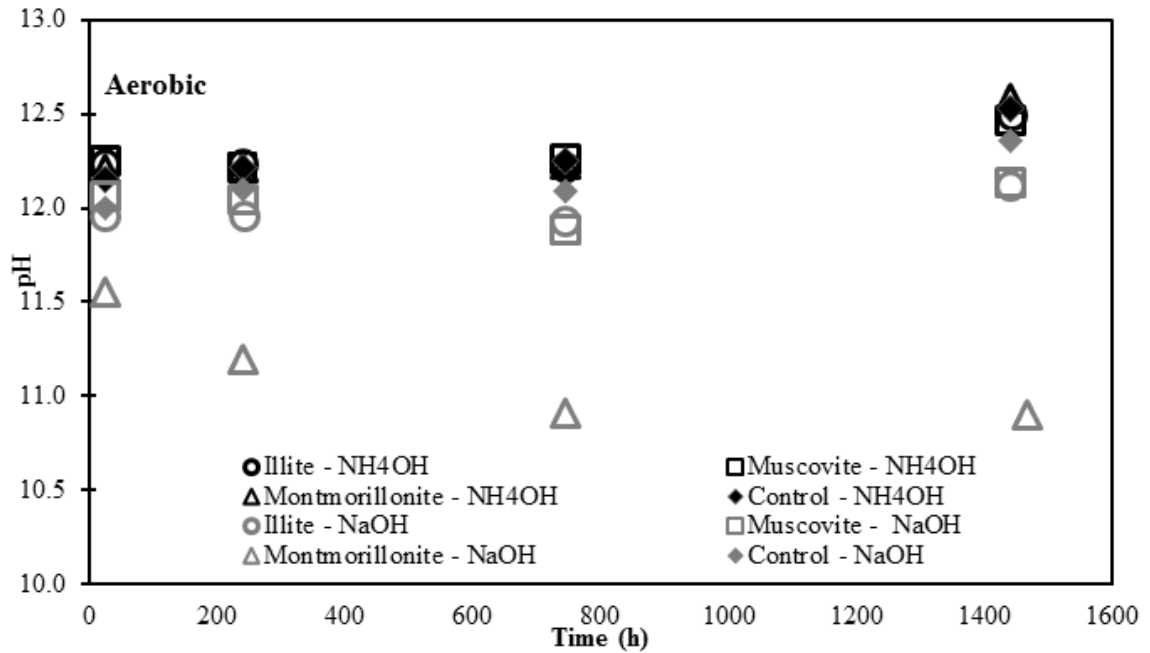


Figure A.8. pH measurements as a function of time for investigated minerals exposed to alkaline treatments (NaOH - gray and NH₄OH - black) under aerobic (top) and anaerobic conditions (bottom) for control (diamonds), illite (circles), muscovite (square), and montmorillonite (triangles).

Solid Phase Characterization Concept Maps

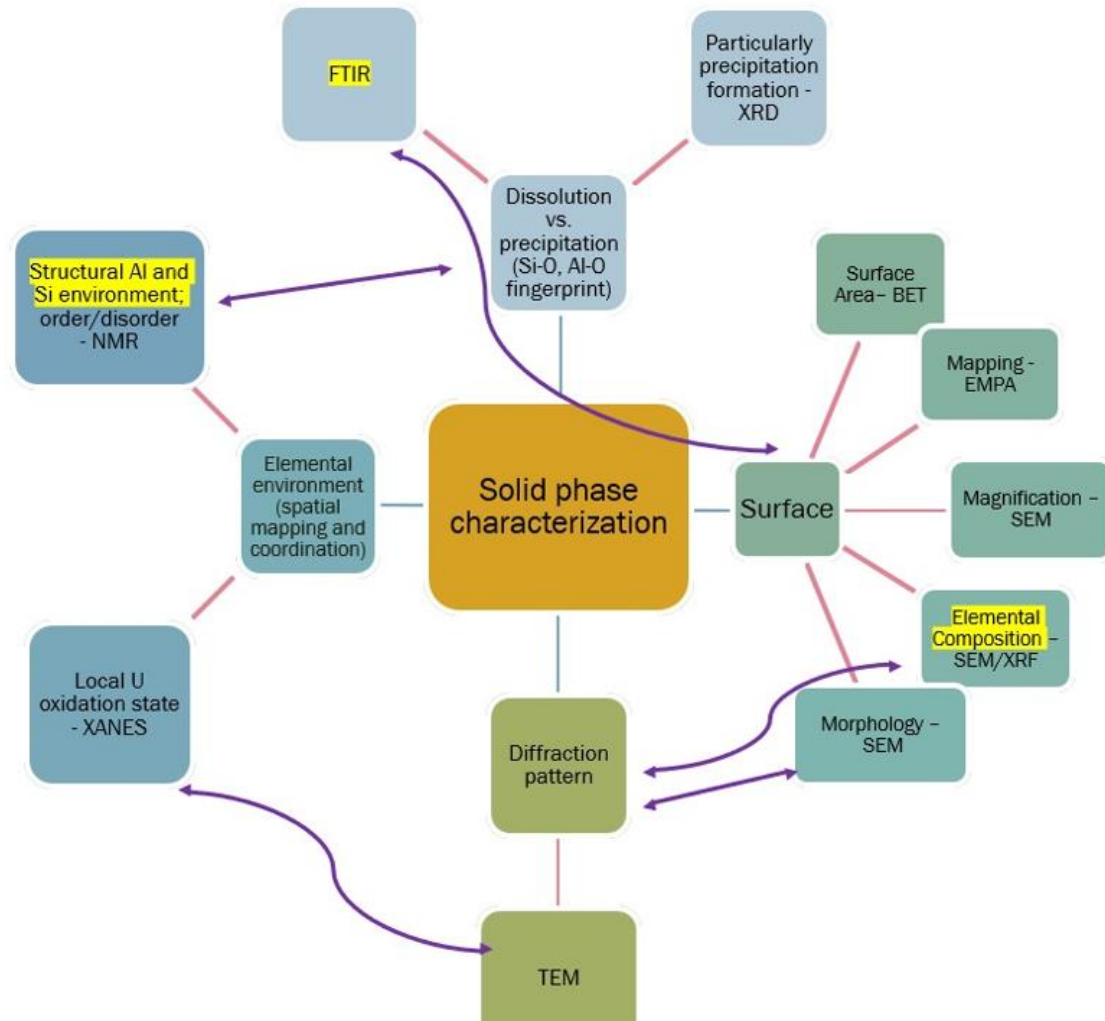


Figure A.9. Concept map identifying the differences and similarities between the various solid phase characterization techniques completed throughout this dissertation. Note: highlighted in yellow show the analytical techniques confirming incongruent dissolution phenomena and purple arrow show complementary characterization techniques.

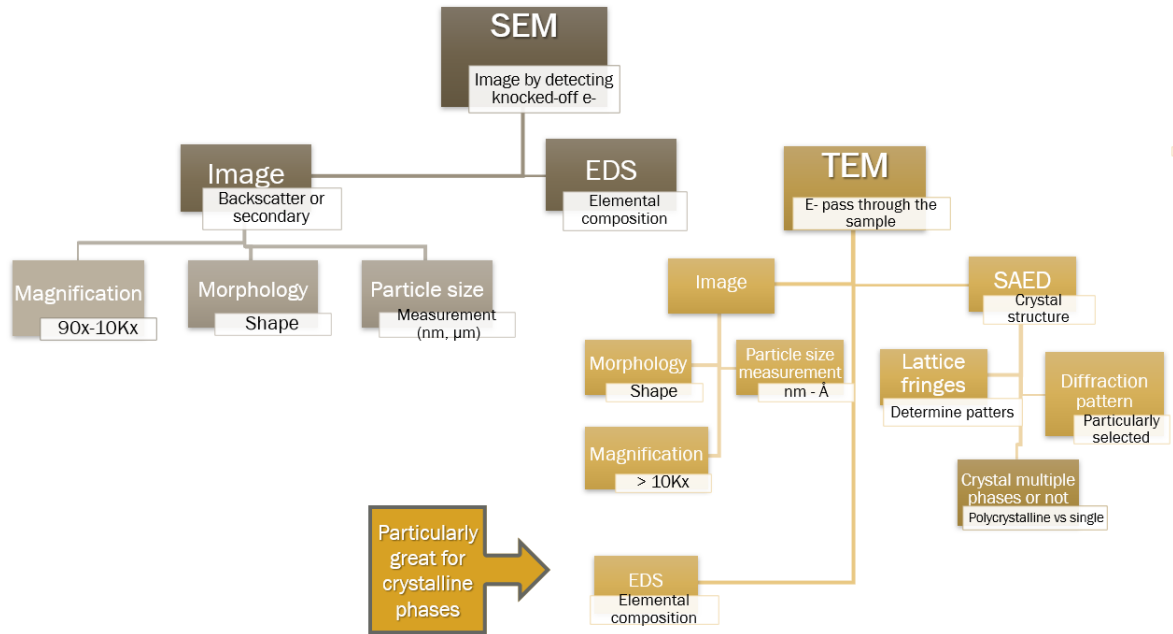


Figure A.10. Concept map identifying the differences between Scanning (SEM) and Transmission (TEM) electron microscopy.

Characterization of Physicochemical Mineral Phase Alterations with Treatment

Table A.5. SGW composition for batch protocol (7.2 mM total ionic strength)

Element	(mmol/L)
Na ⁺	1.1
K ⁺	0.22
Ca ²⁺	1.4
Mg ²⁺	0.6
HCO ₃ ⁻	1.32
Cl ⁻	3.9

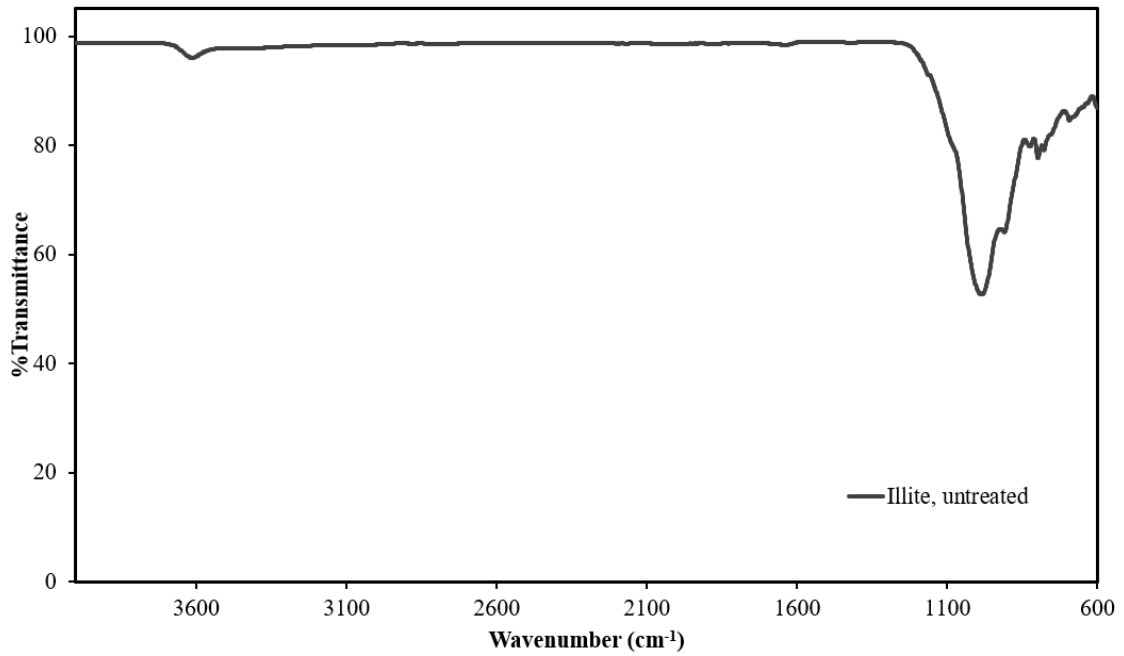


Figure A.11. X-ray diffraction pattern of untreated (control) illite clay (Silver Hill).

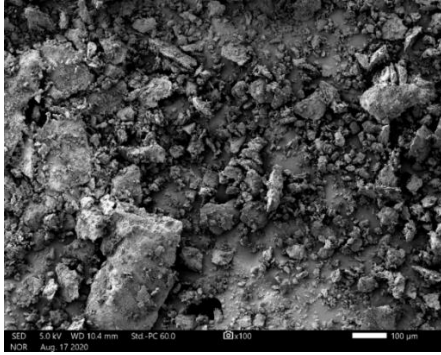
Table A.6. Indexed absorption bands for illite
(Clay Minerals Society, Cambrian Hole, Silver Hill Mount) FTIR spectra

Band	Wavenumber (cm⁻¹)	Solid Phase	Reference
Si-O-Al	693-695	Illite	(Jiang et al., 2008; Marsh et al., 2018b)
Si-O (\perp)	781-800	Quartz	(Mezni et al., 2011)
Si-O (\perp)	798	Quartz/Illite	(Marsh et al., 2018b; Mezni et al., 2011)
Si-O-Al	827-831	Illite	(Jiang et al., 2008; Marsh et al., 2018b)
C-O	880	Carbonate	(Barbosa et al., 2000)
Al-OH (\parallel)	901-912	Illite	(Marsh et al., 2018b; Öztop & Shahwan, 2006; Pironon et al., 2003)
Si-O-Al (\parallel)	981-987	Illite	(Marsh et al., 2018b; Öztop & Shahwan, 2006)
Si-O-Si (\perp)	1020-1080	Illite	(Konan et al., 2012; Marsh et al., 2018b)
Si-O (\perp)	1163	Illite	(Marsh et al., 2018b; Pironon et al., 2003)
C-O	1436	Carbonate	(Barbosa et al., 2000)
O-H (\parallel)	1650	Illite	(Konan et al., 2012)

\perp = stretching vibration, \parallel = bending vibration

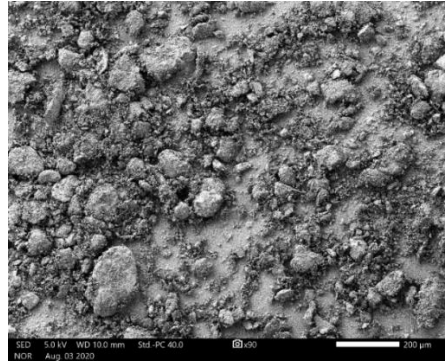
Illite – untreated control

100x



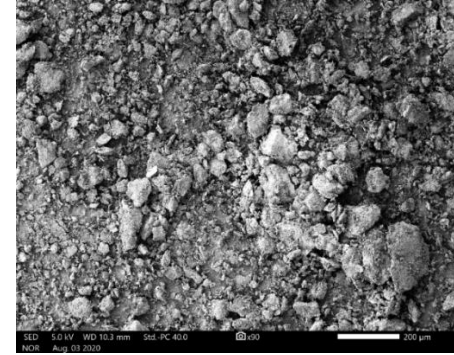
Illite – ammonia treated; pH 12

90x

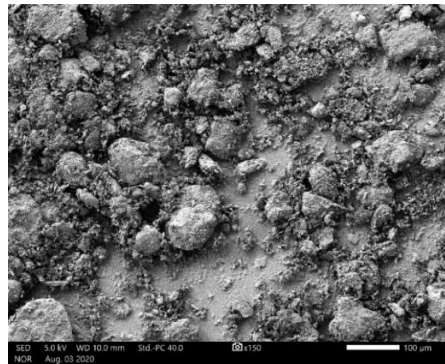


Illite – aerated treated; pH 8

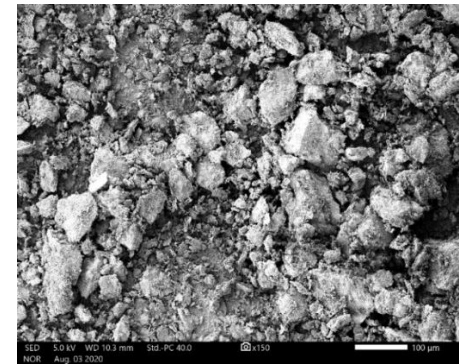
90x



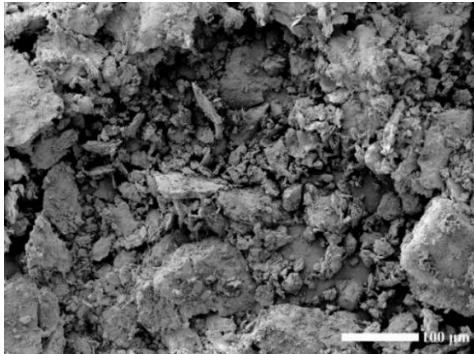
150x



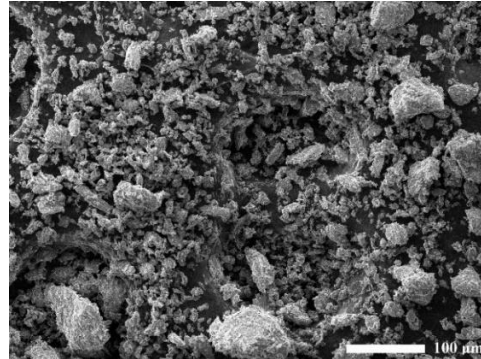
150x



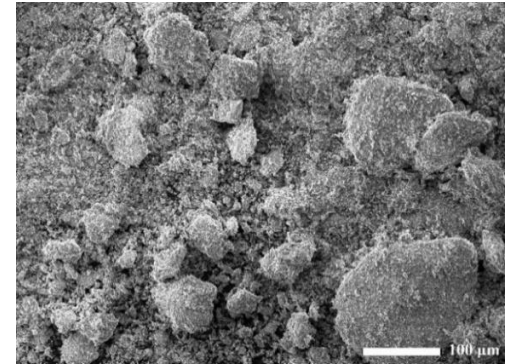
200x



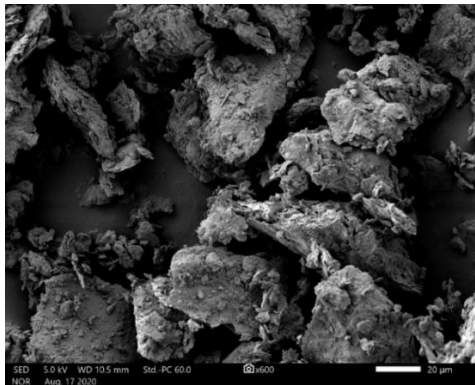
200x



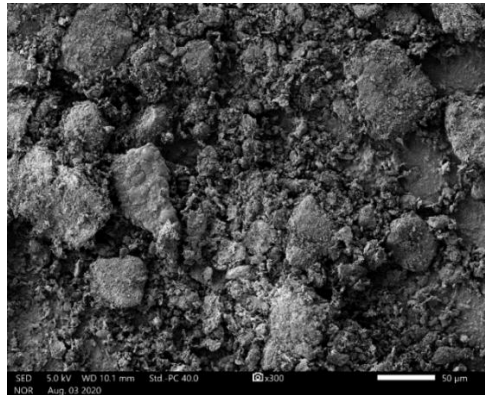
200x



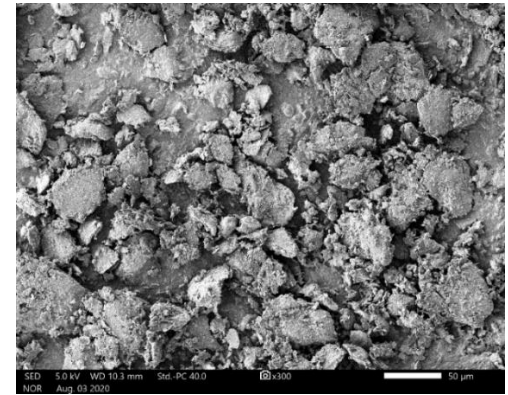
600x



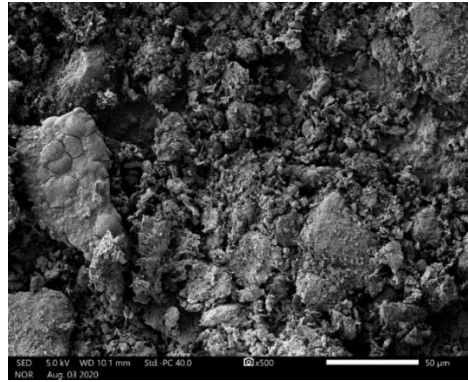
300x



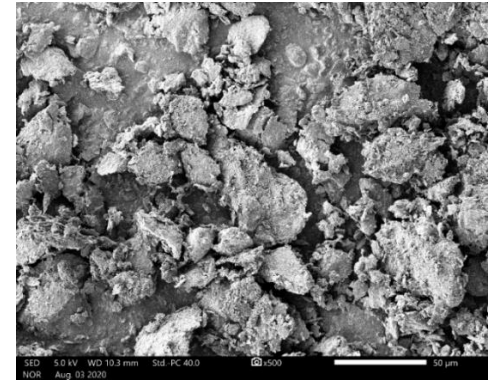
300x



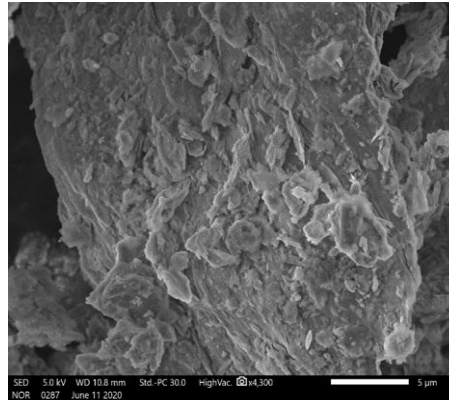
500x



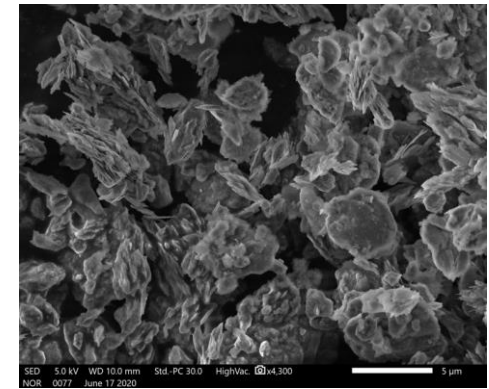
500x

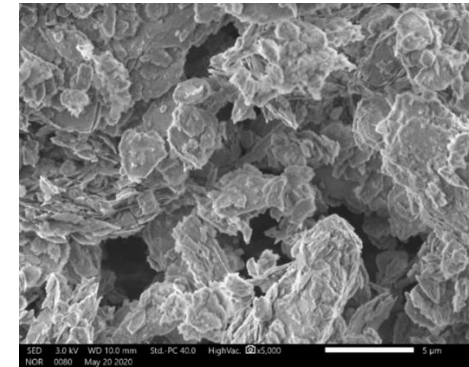
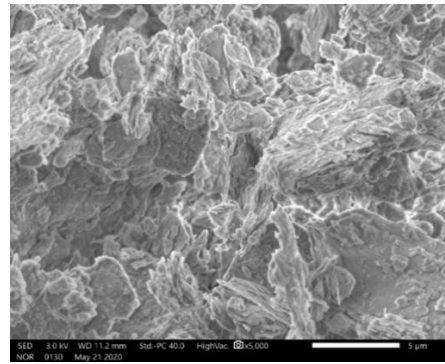


4300x

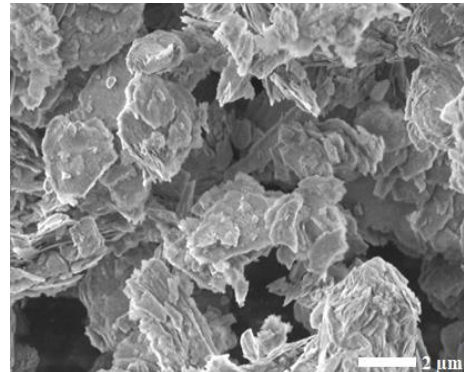


4300x





10000x



10000x

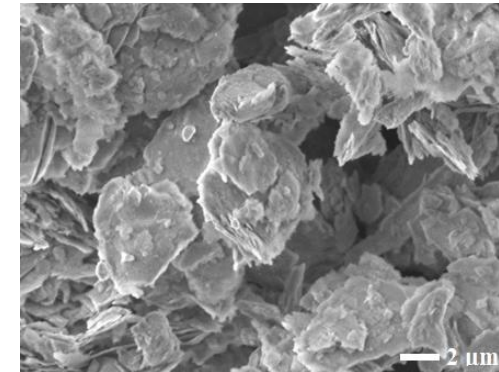


Figure A.12. SEM micrographs of untreated (left column) and treated illite (ammonia-middle column; aerated-right column) at various magnifications (90x, 150x, 200x, 300x, 500x, 4300x, and 10Kx).

Table A.7. Summary of descriptive statistics (ANOVA: Two-Factor with Replication) and particle size measurements of illite ammonia- and aerated- treated samples taken from magnification 1000x SEM images

	Location 1	Location 2	Location 3	Total		
<i>pH 12</i>						
Count	11	11	11	33		
Sum	192.6	166.4	134.8	493.8		
Average	17.5	15.1	12.3	14.96		
Variance	23.6	26.3	10.9	23.8		
Stdev				4.87		
<i>pH 8</i>						
Count	11	11	11	33		
Sum	230.7	185.1	192.4	608.2		
Average	21.0	16.8	17.5	18.4		
Variance	10.6	2.6	5.0	9.10		
Stdev				3.02		
<i>Total</i>						
Count	22	22	22			
Sum	423.3	351.5	327.2			
Average	19.2	16.0	14.9			
Variance	19.4	14.5	14.7			
ANOVA						
<i>Source of Variation</i>	SS	df	MS	F	<i>p</i> -value	F crit
Sample	198.2	1	198.2	15.0	0.0003	4.00
Columns	226.9	2	113.5	8.6	0.0005	3.15
Interaction	34.2	2	17.1	1.3	0.2808	3.15
Within	790.5	60	13.2			
Total	1249.8	65				

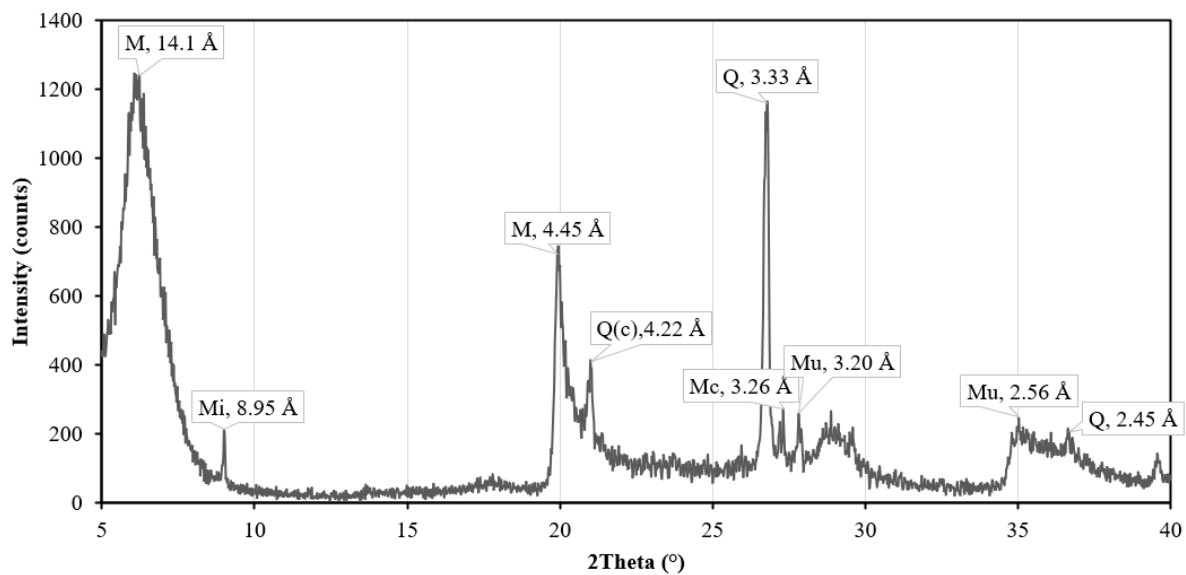
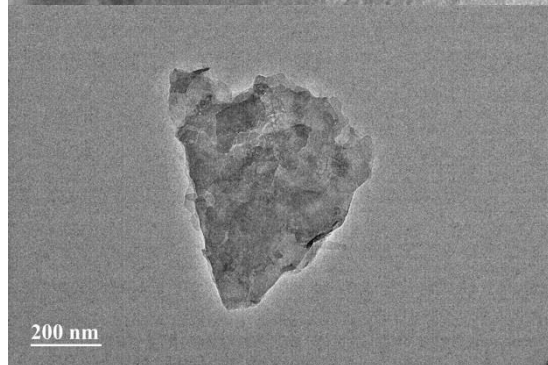
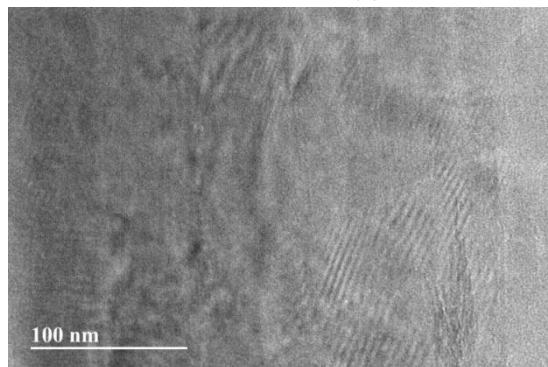


Figure A.13. X-ray diffraction pattern of montmorillonite clay (PDF: 01-076-8291). M, montmorillonite; Mi, mica; Q(c), quartz cristobalite; Mc, microcline; Mu, muscovite.

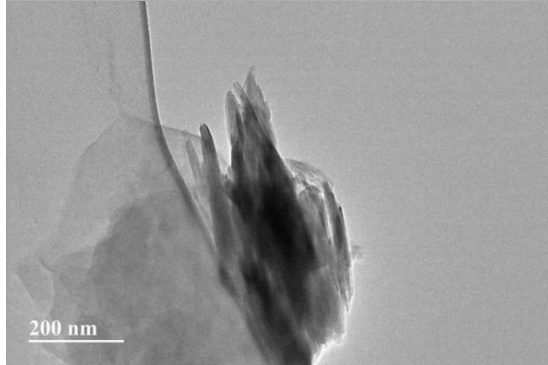
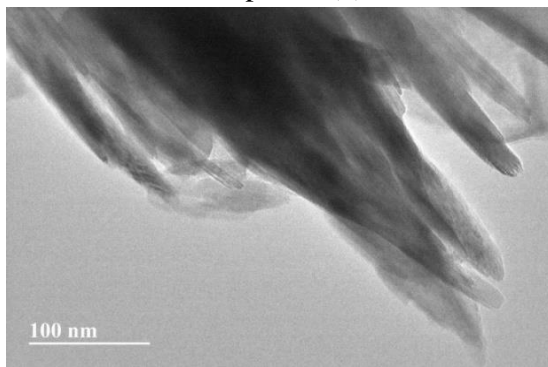
Table A.8. Indexed absorption bands for montmorillonite (Clay Minerals Society, Crook County, Wyoming) FTIR spectra.

Band	Wavenumber (cm⁻¹)	Solid Phase	Reference
Si-O-Si (∥)	480	Montmorillonite	(Ritz et al., 2011)
Si-O-Al (∥)	695	Montmorillonite	(Marsh et al., 2018b; Ritz et al., 2011)
Si-O-Al	696	Montmorillonite	(Marsh et al., 2018b; Ritz et al., 2011)
Si-O (⊥)	793-799	Quartz / Montmorillonite	(Hayati-Ashtiani, 2012; Marsh et al., 2018b)
Al-Mg-OH	836	Montmorillonite	(Hayati-Ashtiani, 2012)
Al-Fe-OH	875	Montmorillonite	(Hayati-Ashtiani, 2012)
C-O	880	Carbonate	(Marsh et al., 2018b)
Al-OH-Al (∥)	915-920	Montmorillonite	(Hayati-Ashtiani, 2012; Marsh et al., 2018b)
Si-O-Si (⊥)	1010-1031	Montmorillonite	(Marsh et al., 2018b; Wanyika, 2014)
C-O	1382-1430	Carbonate	(Hayati-Ashtiani, 2012; Ritz et al., 2011)
O-H (∥)	1629	Montmorillonite	(Marsh et al., 2018b; Wanyika, 2014)
Al-OH and Si-OH (⊥)	1644	Montmorillonite	(Ritz et al., 2011; Wanyika, 2014)
Al-OH (⊥)	3622	Montmorillonite	(Hayati-Ashtiani, 2012; Madejová et al., 1994; Wanyika, 2014)
O-H (⊥) interlayer cation	3620-3630	Montmorillonite	(Hayati-Ashtiani, 2012; Wanyika, 2014)

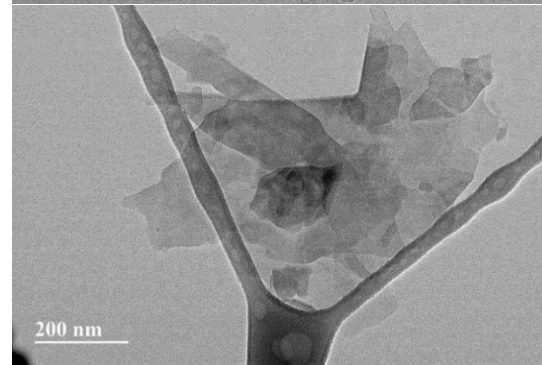
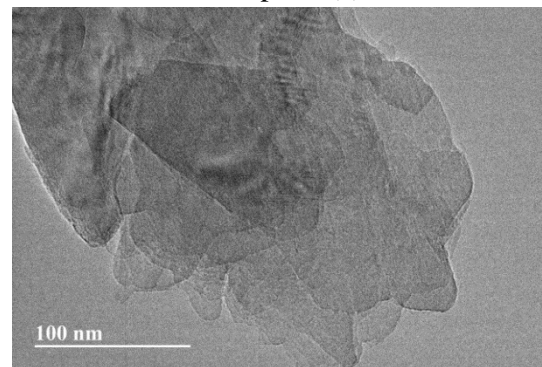
Illite untreated (a)



Illite pH 12 (b)



Illite pH 8 (c)



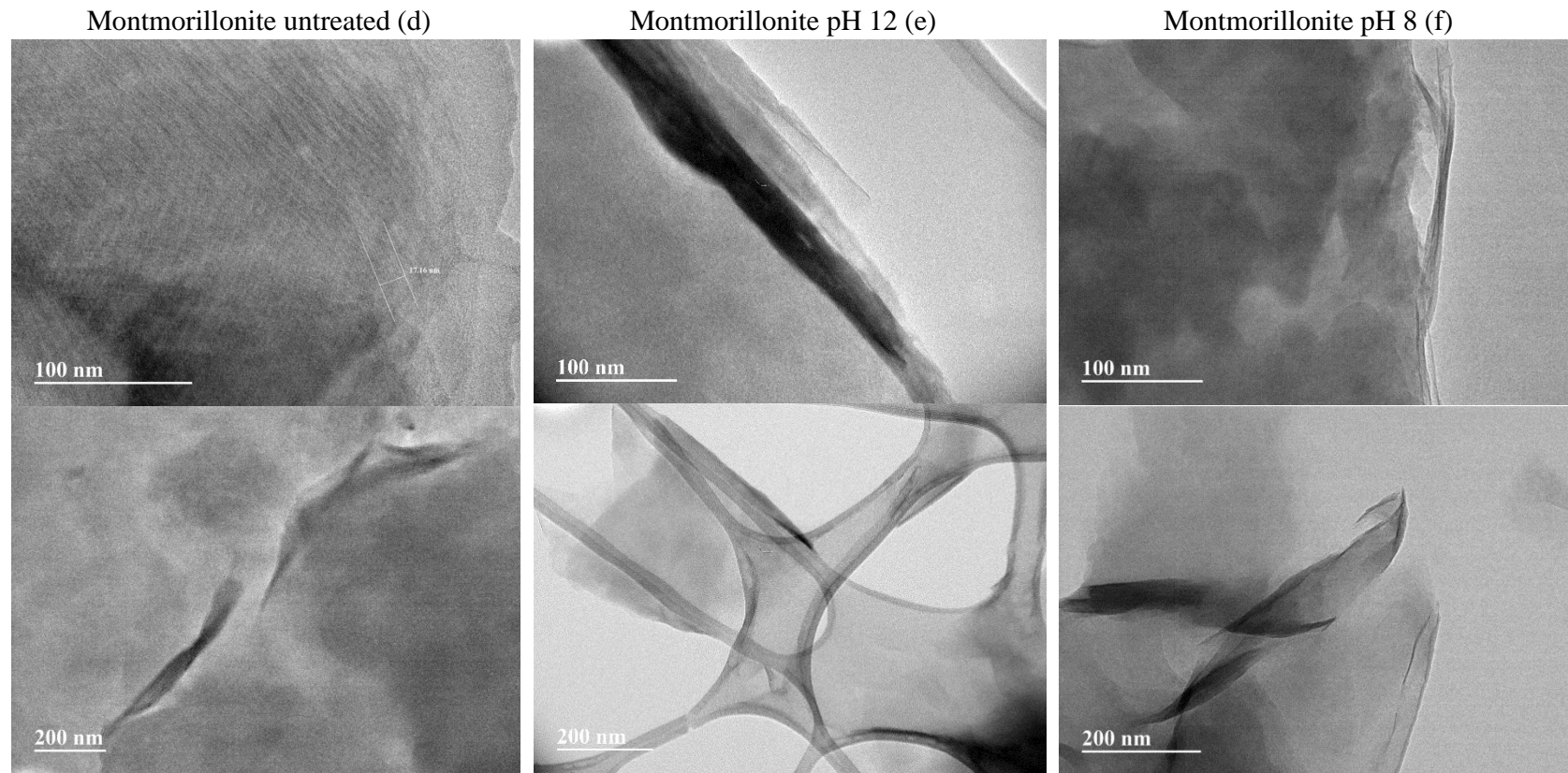


Figure A.14. Transmission Electron Microscope (TEM) micrographs of aluminosilicate minerals (illite, top; montmorillonite, bottom) untreated (a and d) and treated with 95% N₂/5% NH₃ gas for 30-day contact time in SGW solution (7.2 mM) at pH 12 (b and e) and 8 (c and f), ammonia- and aerated-treated, respectively.

References:

- Barbosa, MacKenzie, K. J. D., & Thaumaturgo, C. (2000). Synthesis and characterisation of materials based on inorganic polymers of alumina and silica: sodium polysialate polymers. *International Journal of Inorganic Materials*, 2(4), 309–317.
- Hayati-Ashtiani, M. (2012). Use of FTIR spectroscopy in the characterization of natural and treated nanostructured bentonites (montmorillonites). *Particulate Science and Technology*, 30(6), 553–564.
- Jiang, T., Li, G., Qiu, G., Fan, X., & Huang, Z. (2008). Thermal activation and alkali dissolution of silicon from illite. *Applied Clay Science*, 40(1), 81–89.
- Konan, Peyratout, C., Smith, A., Bonnet, J.-P., Magnoux, P., & Ayrault, P. (2012). Surface modifications of illite in concentrated lime solutions investigated by pyridine adsorption. *Journal of Colloid and Interface Science*, 382(1), 17–21.
- Madejová, J., Komadel, P., & Čičel, B. (1994). Infrared study of octahedral site populations in smectites. *Clay Minerals*, 29(3), 319–326.
- Marsh, A., Heath, A., Patureau, P., Evernden, M., & Walker, P. (2018). Alkali activation behaviour of un-calcined montmorillonite and illite clay minerals. In *Applied Clay Science* (Vol. 166, pp. 250–261).
- Mezni, M., Hamzaoui, A., Hamdi, N., & Srasra, E. (2011). Synthesis of zeolites from the low-grade Tunisian natural illite by two different methods. *Applied Clay Science*, 52(3), 209–218.
- Öztop, B., & Shahwan, T. (2006). Modification of a montmorillonite–illite clay using alkaline hydrothermal treatment and its application for the removal of aqueous Cs⁺ ions. *Journal of Colloid and Interface Science*, 295(2), 303–309.
- Pironon, J., Pelletier, M., De Donato, P., & Mosser-Ruck, R. (2003). Characterization of smectite and illite by FTIR spectroscopy of interlayer NH₄⁺ cations. *Clay Minerals*, 38(2), 201–211.
- Ritz, M., Vaculíková, L., & Plevová, E. (2011). *Application of infrared spectroscopy and chemometric methods to identification of selected minerals*.
- Wanyika, H. (2014). Controlled release of agrochemicals intercalated into montmorillonite interlayer space. *The Scientific World Journal*, 2014.

Determination of Solid Phases Speciation and Mobility of Uranium

Table A.9. Phyllosilicate minerals and Hanford sediments (~25 g/L) pH and ORP readings during 5% NH₃/95% N₂ and aeration treatments

Solid Phase	Loading (g/L)	pH initial	ORP (mV) initial	pH final	ORP (mV) final
Illite	25.01	10.86 ± 0.02	234.4 ± 12.4	8.88 ± 0.01	456.1 ± 11.5
Muscovite	25.09	10.77 ± 0.03	236.6 ± 11.3	8.54 ± 0.02	488.5 ± 5.3
Montmorillonite	25.00	10.94 ± 0.03	229.1 ± 11.4	8.75 ± 0.02	469.1 ± 7.5
Hanford Sediment	25.02	10.79 ± 0.01	238.5 ± 14.3	8.66 ± 0.03	485.0 ± 9.5

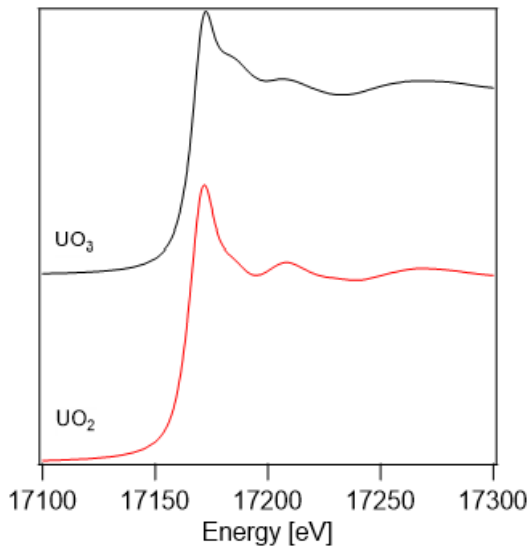


Figure A.15. Uranium L_{III}-edge XANES spectra of the reference compounds used for XANES LCA fitting. LCF fit shown in red for UO₂ and in black for UO₃.

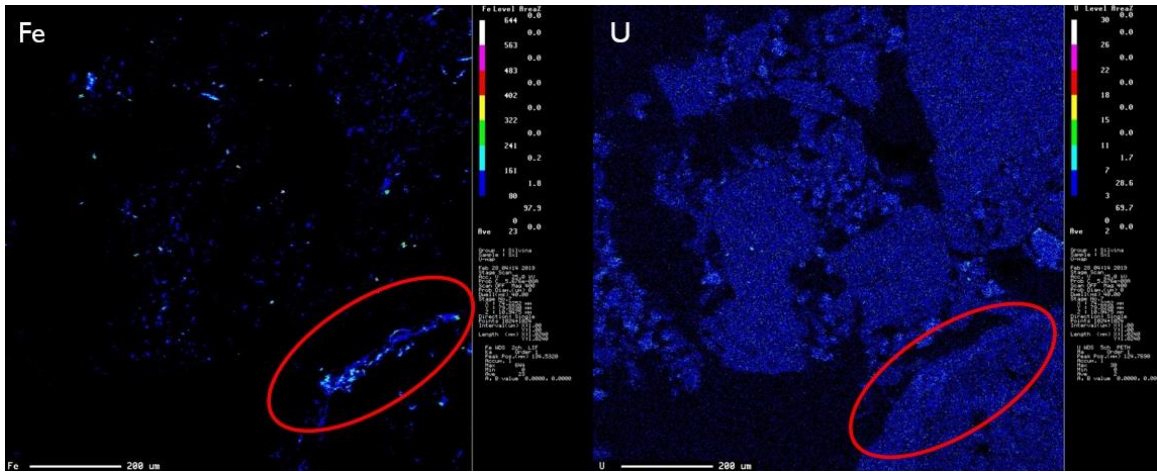
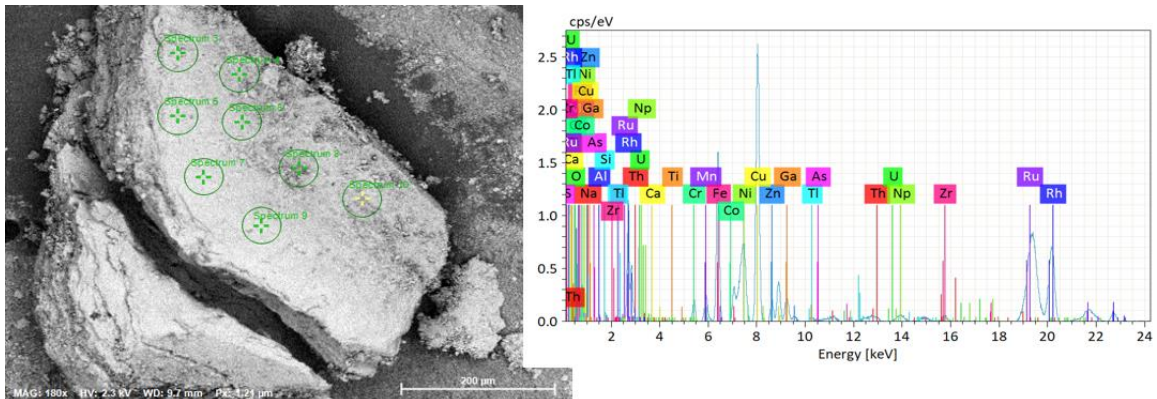


Figure A.16. EMPA micrograph and corresponding elemental maps for U and Fe showing a correlation on illite particles post-ammonia (5% NH₃/95% N₂) and aerated treatment in Experiment 3.

Table A.10. Hanford Sediment XRF-EDS Molar Quantity (normalized to MW) and Al/Si ratios for Experiment 2

Element	MW (g/mol)	Short Term	U-High Loading
Na	22.9	0.01	0.02
Mg	24.3	0.01	0.05
O	16.0	2.02	1.84
Al	27.0	0.92	0.15
Si	28.1	0.09	0.35
Ca	40.1	0.02	0.78
Fe	55.8	0.15	0.04
U	238	0.00	0.00
Al/Si	-	0.46 ± 0.40	0.44 ± 0.07



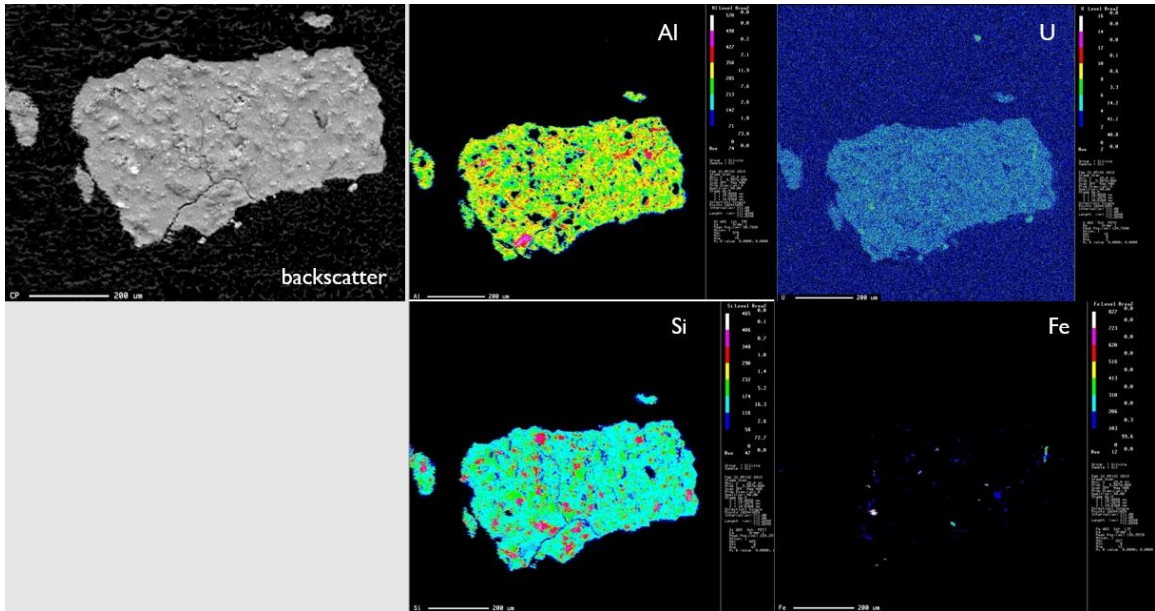


Figure A.17. EMPA backscatter micrograph and corresponding elemental maps for Al, U, Si, and Fe showing a correlation on illite particle post-ammonia (5% NH_3 /95% N_2) and aerated treatment in Experiment 3.

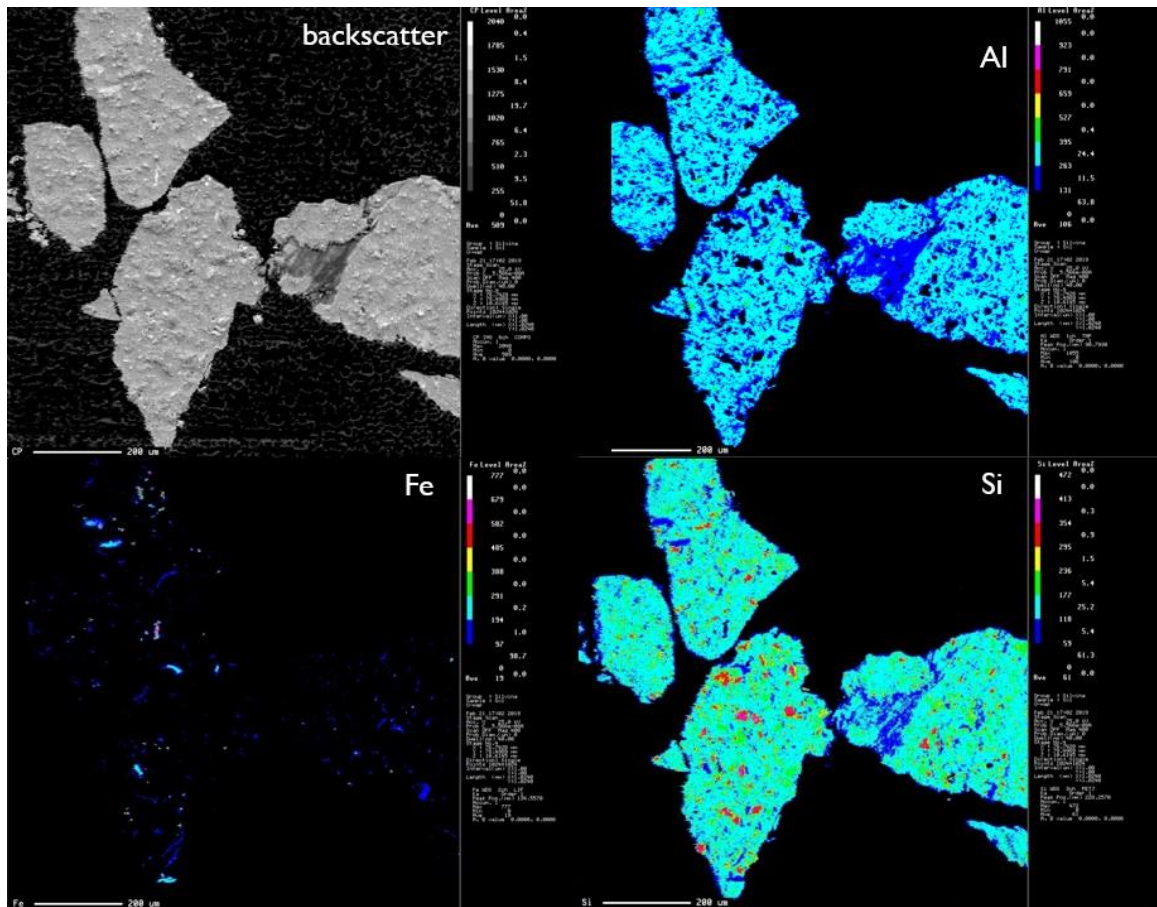


Figure A.18. EMPA backscatter micrograph and corresponding elemental maps for Al, Si, and Fe showing a correlation on illite particles post-ammonia (5% NH₃/95% N₂) and aerated treatment in Experiment 3.

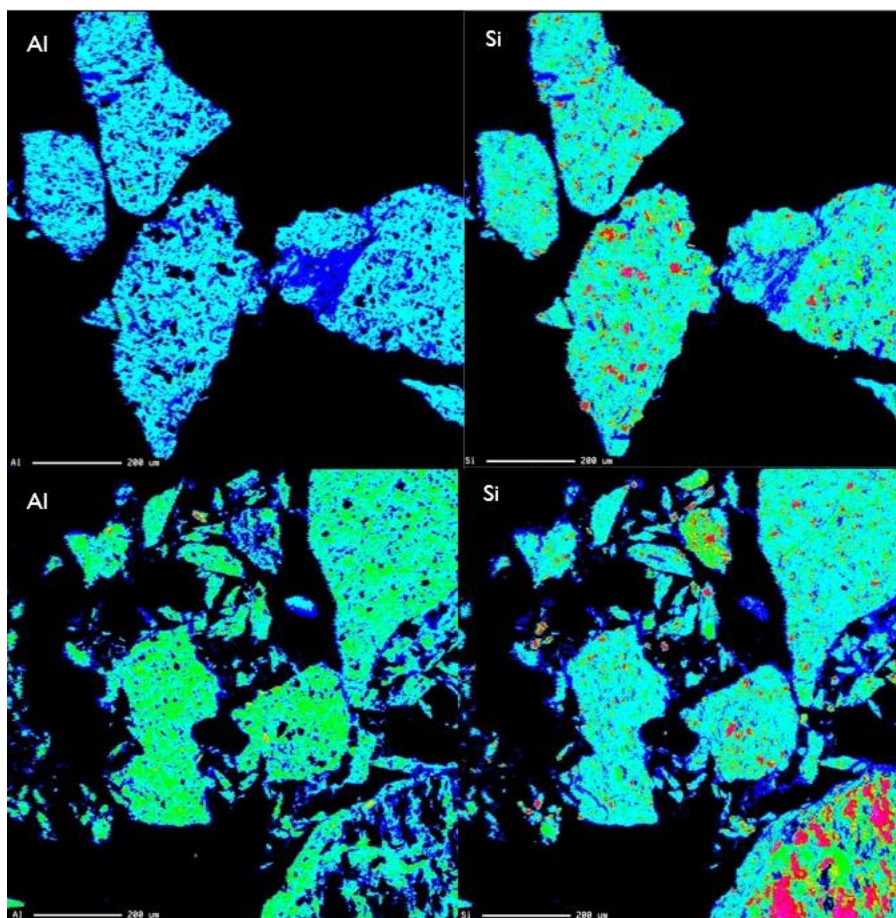


Figure A.19. EMPA micrographs and corresponding elemental maps for Al and Si showing a correlation on illite particles post-ammonia (5% NH₃/95% N₂) and aerated treatment in Experiment 3.

Table A.11. X-ray powder diffraction patterns for illite (IMt-2, Cambrian Hole, Silver Hill Mount, Clay Mineral Society) comparing *d*-spacing (in Å) and 2Theta (°) values for theoretical (obtained from the listed reference) and experimental measurements for untreated (control) and treatment (NH₃ and aerated at pH 12 and 8), respectively

Corresponding Peak	Theoretical		Experimental, control		Treated, pH 12		Treated & aerated, pH 8		Reference
	<i>d</i> (Å)	2Theta (°)	<i>d</i> (Å)	2Theta (°)	<i>d</i> (Å)	2Theta (°)	<i>d</i> (Å)	2Theta (°)	
Interlayer basal 001	10.1	8.76	10.1	8.71	10.1	8.73	10.1	8.77	(Marsh et al., 2018a; Moore & Reynolds Jr, 1989)
Kaolinite/Illite	7.13	12.4	7.06	12.5	7.07	12.5	7.11	12.4	(Marsh et al., 2018a; Smith, 2004)
Illite	4.99	17.8	4.93	18.0	4.94	18.0	4.98	17.8	(Marsh et al., 2018a)
Illite	4.51	19.7	4.51	19.7	4.51	19.7	4.51	19.7	(Moore & Reynolds Jr, 1989)
Quartz	4.25	20.9	4.25	20.9	4.23	21.0	4.25	20.9	(Dachille & Dent Glasser, 1959)
Calcite	3.86	23.0	-	-	-	-	3.85	23.1	(Swanson & Fuyat, 1953)
Quartz	3.34	26.6	3.32	26.8	3.33	26.8	3.34	26.7	(Dachille & Dent Glasser, 1959)
Microcline	3.26	27.3	3.26	27.3	3.27	27.3	3.27	27.2	(Blasi et al., 1987)
Calcite	3.04	29.4	3.04	29.4	3.03	29.4	3.02	29.5	(Swanson & Fuyat, 1953)
Illite	2.50	35.9	2.49	36.0	2.49	36.0	2.49	36.0	(Marsh et al., 2018a)
Calcite	2.50	36.0	-	-	-	-	2.49	36.0	(Swanson & Fuyat, 1953)
Calcite	2.29	39.4	2.28	39.5	2.28	39.5	2.28	39.5	(Swanson & Fuyat, 1953)

Table A.12. X-ray powder diffraction patterns for montmorillonite (SWy-2, Crook County, Wyoming, Clay Mineral Society) comparing *d*-spacing (in Å) and 2Theta (°) values for theoretical (obtained from the listed reference) and experimental measurements for untreated (control) and treatment (NH₃ and aerated at pH 12 and 8), respectively

Corresponding Peak	Theoretical		Experimental, control		Ammonia treated, pH 12		Treated & aerated, pH 8		Reference
	d(Å)	2Theta (°)	d(Å)	2Theta (°)	d(Å)	2Theta (°)	d(Å)	2Theta (°)	
Interlayer basal 001	15.0	5.89	14.14	6.24	14.52	6.08	14.7	6.00	(Chipera & Bish, 2001)
Mica	8.98	9.84	8.96	9.87	8.974	9.85	8.94	9.89	(Chipera & Bish, 2001)
Montmorillonite/ muscovite	4.49	19.76	4.45	19.93	4.47	19.8	4.46	19.9	(Blasi et al., 1987)
Quartz (cristobalite)	4.22	21.03	4.22	21.0	4.28	20.7	4.23	20.97	(Wong-Ng & Hubbard, 1987)
Calcite	3.84	23.12	-	-	3.83	23.2	3.83	23.19	(Falini et al., 1998)
Quartz	3.33	26.75	3.33	26.8	3.32	26.8	3.33	26.73	(Dachille & Dent Glasser, 1959).
Microcline	3.26	27.32	3.26	27.3	3.28	27.2	3.21	27.77	(Blasi et al., 1987)
Muscovite	3.20	27.83	3.20	27.8	3.21	27.8	3.2	27.77	(Smith, 2004)
Calcite	3.03	29.50	-	-	3.03	29.5	3.02	29.52	(Falini et al., 1998)
Calcite	2.83	31.57	-	-	2.84	31.5	2.84	31.52	(Falini et al., 1998)

References:

- Blasi, A., De Pol Blasi, C., & Zanazzi, P. F. (1987). A re-examination of the Pellotsalo microcline; mineralogical implications and genetic considerations. *The Canadian Mineralogist*, 25(3), 527–537.
- Chipera, S. J., & Bish, D. L. (2001). Baseline studies of the clay minerals society source clays: powder X-ray diffraction analyses. *Clays and Clay Minerals*, 49(5), 398–409.
- Dachille, F., & Dent Glasser, L. S. (1959). High pressure forms of BPO₄ and BAsO₄; quartz analogues. *Acta Crystallographica*, 12(10), 820–821.
- Falini, G., Fermani, S., Gazzano, M., & Ripamonti, A. (1998). Structure and morphology of synthetic magnesium calcite. *Journal of Materials Chemistry*, 8(4), 1061–1065.
- Gallucci, M. (2020). What to do with 177 giant tanks of radioactive sludge. *IEEE Spectrum*, 57(5), 24–33.
- Marsh, A., Heath, A., Patureau, P., Evernden, M., & Walker, P. (2018). Alkali activation behaviour of un-calcined montmorillonite and illite clay minerals. *Applied Clay Science*, 166, 250–261.
- Moore, D. M., & Reynolds Jr, R. C. (1989). *X-ray Diffraction and the Identification and Analysis of Clay Minerals*. (Second). Oxford University Press (OUP).
- Smith, S. R. (2004). *Geochronology and geochemistry of rare-element pegmatites from the Superior Province of Canada (Ontario)*.
- Swanson, H. E., & Fuyat, R. K. (1953). Calcite. *Standard X-Ray Diffraction Patterns*, 539, 52–53.
- Wong-Ng, W., & Hubbard, C. R. (1987). Standard reference materials for X-ray diffraction Part II. Calibration using d-spacing standards. *Powder Diffraction*, 2(4), 242–248.
- Zachara, J., Brown, C., Christensen, J., Davis, J. A., Dresel, E., Kelly, S., Liu, C., McKinley, J., Serne, J., & Um, W. (2007). *A Site-Wide Perspective on Uranium Geochemistry at the Hanford Site*.

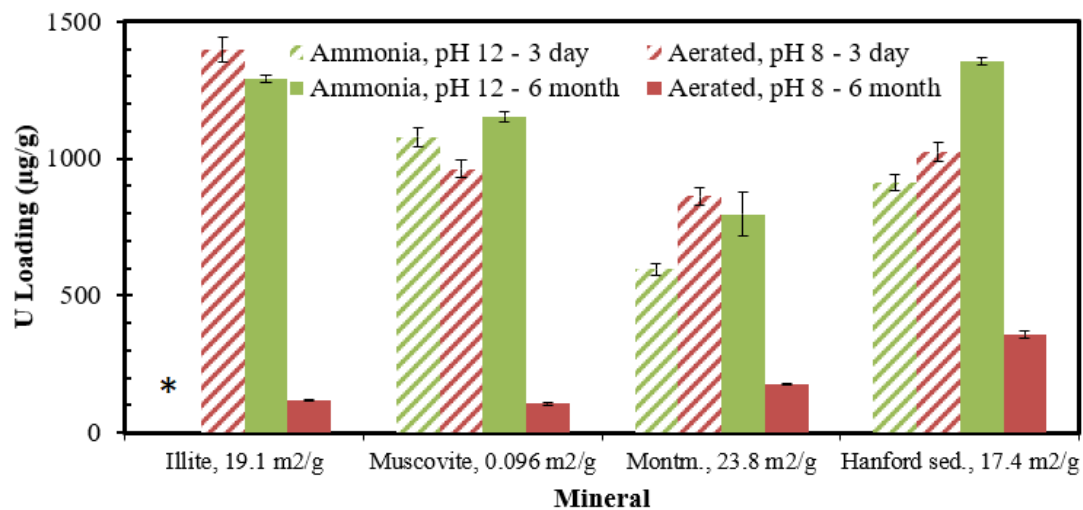


Figure A.20. U loading ($\mu\text{g/g}$) of phyllosilicate minerals and Hanford Site sediments upon ammonia (green) or aerated (red) treatment during three-day (pattern) or six-month (solid) contact time for Experiment 3. Notes: surface area in m^2/g represented next to the solid phase; *: there was no measurement recorded for illite 3-day, ammonia treatment

VITA

SILVINA ANALIA DI PIETRO

- 1990 Born: Buenos Aires, Argentina
- 2008-2010 A.A., Chemistry, *Robert “Bob” Elmore* Honors Institute
Broward College
Davie, FL
- 2010-2012 B.S., Chemistry, Honors College
Florida International University
Miami, FL
- 2015 Acceptance into the DOE-FIU Science
and Technology Workforce Development Program
- 2016 *Roy G. Post* Foundation Graduate Student Level Award
- 2018 *Innovations* Nuclear Technology R&D Award
- 2018 M.S., Chemistry, Environmental Track
Florida International University
Miami, FL
- 2018-2021 Doctoral Candidate
Florida International University
Miami, Florida
- 2021 U.S. Delegate to the *International Younger Chemists
Network* for the IUPAC U.S. National Committee

PUBLICATIONS AND PRESENTATIONS

Di Pietro, S.A., Emerson, H.P., Katsenovich, Y. “Illite Physicochemical Transformation upon NH₃ Gas Treatment”. *Waste Management Symposia* – Phoenix, Arizona (virtual). March, 2021.

Di Pietro, S.A., Emerson, H.P., Katsenovich, Y., Qafoku, N., Szecsody, J., “Effects of Variable Redox Conditions and Alkaline Treatment in Phyllosilicate Minerals” *Clay Mineral Society* – Richland, WA (virtual). October, 2020. Oral presentation.

Di Pietro, S.A., Emerson, H.P., Katsenovich, Y., Qafoku, N., Szecsody, J., (2020) “Phyllosilicate Mineral Dissolution upon Alkaline Treatment under Aerobic and Anaerobic Conditions,” *Applied Clay Science*, 189: 105520.

Szecsody, J., Emerson, H.P., Pearce, C.I., Gartman, B.N., Resch, C.T., Di Pietro, S.A., (2020) “In Situ Reductive Dissolution to Remove Precipitated Iodine-129 from Aquifer Sediments,” *Journal of Environmental Radioactivity*, 216: 106182.

Di Pietro, S.A., Emerson, H.P., Katsenovich, Y., “Phyllosilicate mineral dissolution upon variable alkaline treatment and redox conditions.” *American Chemical Society – San Diego, CA, August, 2019. Oral presentation.*

Di Pietro, S.A., Joseph, C., Zavarin, M., “Can We Isolate Nuclear Waste? Neptunium (IV) Diffusion Rates through Bentonite Clay” *Lawrence Livermore National Laboratory Summer Interns Poster Symposium – Livermore, CA, August, 2019. Poster presentation.*

Szecsody, J., Truex, M., Qafoku, N., McKinley, J., Ivarson, K., Di Pietro, S.A., (2019) “Persistence of Chromate in Vadose Zone and Aquifer Sediments in Hanford, Washington,” *Science of the Total Environment*, 676, 482-492.

Emerson, H.P., Di Pietro, S.A., Katsenovich, Y., and Szecsody, J., (2018) “Uranium Immobilization in the Presence of Minerals Following Remediation via Base Treatment with Ammonia Gas,” *Journal of Environmental Management*, 223, 108-114.

Di Pietro, S.A., Emerson, H.P., Katsenovich, Y. “Potential Impacts to Local Mineralogy from Remediation with Ammonia Gas.” *American Chemical Society – Boston, MA, August, 2018. Oral presentation.*

Di Pietro, S.A., Emerson, H.P., Katsenovich, Y., Szecsody, J. “Effects of Ammonia and Variable Redox Conditions on Mineral Dissolution.” *American Chemical Society – San Francisco, CA, April, 2017. Oral presentation.*

Di Pietro, S.A., Emerson, H.P., Katsenovich, Y. “Ammonia Gas Treatment for Uranium Immobilization at US DOE Hanford Site.” *Waste Management Symposia – Phoenix, Arizona, March, 2017. Oral presentation. Full paper in the Waste Management Symposia proceedings.*

Emerson, H.P., Di Pietro, S.A., Katsenovich, Y., and Szecsody, J., (2016) “Effects of Ammonia on Uranium Partitioning and Kaolinite Mineral Dissolution,” *Journal of Environmental Radioactivity*, 167, 150-159.